

KATHOLIEKE UNIVERSITEIT LEUVEN
FACULTEIT TOEGEPASTE WETENSCHAPPEN
DEPARTEMENT ELEKTROTECHNIEK
Kasteelpark Arenberg 10, 3001 Leuven (Heverlee)

ADVANCED SIGNAL PROCESSING APPLIED TO IN-VIVO SPECTROSCOPY AND HEART RATE VARIABILITY

Promotor:
Prof. dr. ir. S. Van Huffel

Proefschrift voorgedragen tot
het behalen van het doctoraat
in de toegepaste wetenschappen

door

Geert MORREN

Mei 2004

2

.

KATHOLIEKE UNIVERSITEIT LEUVEN
FACULTEIT TOEGEPASTE WETENSCHAPPEN
DEPARTEMENT ELEKTROTECHNIEK
Kasteelpark Arenberg 10, 3001 Leuven (Heverlee)

ADVANCED SIGNAL PROCESSING APPLIED TO IN-VIVO SPECTROSCOPY AND HEART RATE VARIABILITY

Jury:
Prof. Dr. ir. J. Berlamont, voorzitter
Prof. Dr. ir. S. Van Huffel, promotor
Prof. Dr. H. Devlieger
Prof. Dr. ir. D. Vandermeulen
Prof. Dr. ir. R. Sepulchre (ULG Liège)
PD. Dr. sc. tech. M. Wolf (ETH Zürich)
Prof. Dr. P. Casaer
Prof. Dr. A. Aubert

Proefschrift voorgedragen tot
het behalen van het doctoraat
in de toegepaste wetenschappen

door

Geert MORREN

U.D.C. 681.3*I5 Mei 2004

© Katholieke Universiteit Leuven – Faculteit Toegepaste Wetenschappen
Arenbergkasteel, B-3001 Heverlee (Belgium)

Alle rechten voorbehouden. Niets uit deze uitgave mag vermenigvuldigd en/of openbaar gemaakt worden door middel van druk, fotocopie, microfilm, elektronisch of op welke andere wijze ook zonder voorafgaande schriftelijke toestemming van de uitgever.

All rights reserved. No part of the publication may be reproduced in any form by print, photoprint, microfilm or any other means without written permission from the publisher.

D/2004/7515/35

ISBN 90-5682-497-X

Voorwoord

Bij het beëindigen van dit doctoraat wil ik enkele mensen bedanken.

Vooreerst gaat mijn dank uit naar mijn promotor, Prof. Sabine Van Huffel, voor de mogelijkheid die zij mij bood in haar onderzoeksgroep te doctoreren, en voor de begeleiding gedurende de voorbije vier jaren.

Verder wil ik ook de leden van de begeleidingscommissie, Prof. Hugo Devlieger, Prof. Dirk Vandermeulen en Prof. Rodolphe Sepulchre, bedanken voor het op zeer korte tijd nalezen van een eerste versie van dit proefschrift, en de terechte en constructieve opmerkingen dienaangaande.

Mijn dank gaat ook uit naar de voorzitter, Prof. Jean Berlamont, en de leden van de jury, PD. Martin Wolf, Prof. Paul Casaer en Prof. André Aubert, voor hun bereidwillige medewerking.

Dr. Gunnar Naulaers en Dr. Hans Daniëls wil ik bedanken voor de goede samenwerking met de afdeling Neonatologie van U.Z. Leuven. Zonder de metingen die jullie mij bezorgden, en aanpasten naar mijn wensen, was dit werk niet mogelijk geweest. Ook de verhelderende uitleg en de discussies erover, heb ik steeds zeer gewaardeerd. Ik bedank tevens Prof. Hugo Devlieger en Prof. Paul Casaer voor hun inbreng tijdens diverse vergaderingen.

I would like to thank PD. Martin Wolf, not only for being a member of the jury, but also for providing the fNIRS data. I appreciated your interesting comments regarding the interpretation of the data and the results. Although it was mainly via e-mail, I really enjoyed the smooth collaboration.

Verder dank ik de talrijke collega's, waar ik steeds met mijn vragen terecht kon, in het bijzonder Philippe en Lieven. Ook alle administratieve en technische collega's wil ik bedanken voor de hulp bij allerhande praktische problemen.

Ik bedank de K.U. Leuven voor de financiering van het onderzoek.

Mijn bureaugenoten Pieter, Wim en Jean-Michel zijn door de jarenlange samenwerking eerder vrienden dan collega's. Ik dank jullie voor de goede verstandhouding, zowel op het werk als daarbuiten. Ook de overige leden van SISTA, en in het bijzonder BIOMED, wil ik bedanken voor de aangename sfeer in onze onderzoeksgroep.

Ik bedank ook mijn ouders voor de kansen die ik gekregen heb.

En tenslotte Lara, om er te zìjn, en mij en mijn afwezigheid te verdragen: bedankt!

Geert Morren, Mei 2004

Abstract

In this thesis, three biomedical applications of signal processing are discussed.

The problem of estimating the parameters of exponentially damped sinusoidal signals in the presence of noise, is encountered in many applications including magnetic resonance spectroscopy (MRS). It is shown how, in the case of oversampled signals, data decimation can be utilized to reduce the computational complexity of subspace-based parameter estimation algorithms, while retaining the same statistical accuracy. From the Hankel total least squares (HTLS) method, three variants that use data decimation are derived and their performance is compared using Monte Carlo simulations with reference signals and simulated MRS signals.

Near-infrared spectroscopy (NIRS) is an optical technique that can be used to analyze human tissue non-invasively. From attenuation changes of light that has passed through tissue, concentration changes of oxygenated and deoxygenated hemoglobin can be calculated. The value of NIRS for the monitoring of the cerebral circulation and oxygenation in preterm neonates is explored in several studies to which we contributed. Another application, functional NIRS, relies on the changes of the optical properties of brain tissue related to functional activation. Two types of changes are observed: the fast signal, caused by light scattering, directly related to neuronal activity and the slow signal, due to light absorption, related to hemodynamic changes in the activated area. As the fast signal is much smaller than the slow signal, it can not be directly observed in NIRS signals. Using adaptive filtering and independent component analysis (ICA), however, we are able to detect the fast signal in the motor cortex during a finger tapping exercise.

The third application deals with the analysis of neonatal heart rate variability (HRV) to predict abnormal cardiorespiratory events. Standardized parameters as well as recently introduced methods are used to quantify different aspects of HRV. Special attention is paid to detrended fluctuation analysis (DFA), a method which characterizes the scaling behaviour of a time series. The methodology for calculating all HRV parameters is fine-tuned for our neonatal heart

rate data. All HRV parameters are calculated for a number of preterm neonates, divided in three age-matched groups according to the occurrence of abnormal cardiorespiratory events during the polysomnography and the eventual home monitoring. The statistical significance of the differences between the three groups is discussed. The values of the HRV parameters obtained in the present study as well as the differences between behavioural states, are compared to results reported in literature.

Korte Inhoud

In deze thesis worden drie biomedische toepassingen van signaalverwerking besproken.

Het bepalen van de parameters van een modelfunctie bestaande uit een som van exponentieel gedempte sinusoïden in de aanwezigheid van ruis is een probleem dat voorkomt in diverse toepassingen waaronder magnetische resonantie spectroscopie (MRS). Er wordt aangetoond hoe data decimatie kan benut worden om de rekenkost van deelruimte-gebaseerde parameterschattingsmethodes te verlagen zonder de nauwkeurigheid van de schattingen te verminderen, als de bemonsteringsfrequentie voldoende groot is. Er worden drie varianten van de HTLS methode (Hankel totale kleinste kwadraten) afgeleid die gebruik maken van data decimatie. De performantie van de verschillende algoritmes wordt vergeleken op basis van Monte Carlo simulaties met referentiesignalen en gesimuleerde MRS signalen.

Nabij-infrarood spectroscopie is een optische techniek die kan gebruikt worden om biologisch weefsel niet-invasief te onderzoeken. Uit de verzwakking van licht dat door het weefsel gegaan is, kunnen veranderingen in de concentratie van geoxygeneerd en gedeoxygeneerd hemoglobine berekend worden. De waarde van NIRS voor de monitoring van de cerebrale circulatie en oxygenatie bij pasgeborenen wordt bestudeerd in een aantal studies. Een andere toepassing van NIRS, functionele NIRS, berust op de veranderingen in optische eigenschappen van hersenweefsel ten gevolge van hersenactiviteit. Daarmee gaan twee soorten optische signalen gepaard: het neuronale signaal, veroorzaakt door verstrooiing en een rechtstreeks gevolg van de activering van de hersencellen, en het hemodynamische signaal, veroorzaakt door absorptie en een gevolg van de toename in bloedtoevoer naar het geactiveerde hersengebied. Omdat het neuronale signaal veel kleiner is dan het hemodynamische signaal en de ruis, is het neuronale signaal niet direct waarneembaar in de NIRS metingen. Door gebruik te maken van adaptieve filtering en onafhankelijke componenten analyse (ICA), zijn we er echter in geslaagd het neuronale signaal te detecteren in de motor cortex.

In de derde toepassing wordt de hartritmevariabiliteit (HRV) van prematuren geanalyseerd met de bedoeling om abnormale cardiorespiratoire gebeurtenissen te voorspellen. Zowel standaard HRV parameters als nieuwe methodes worden gebruikt om diverse aspecten van de HRV te kwantificeren. De DFA methode, die de schaalinvariantie van tijdreeksen karakteriseert, wordt in detail geanalyseerd. De methodologie van elke methode wordt aangepast aan onze specifieke hartritmsignalen. Alle HRV parameters worden berekend voor een aantal prematuren, opgedeeld in 3 groepen naargelang het voorkomen van abnormale cardiorespiratoire gebeurtenissen tijdens de polysomnografie en thuismonitoring. De HRV parameters worden vergeleken met waarden uit de literatuur, en de verschillen tussen de drie groepen worden statistisch geanalyseerd.

Glossary

Mathematical Notation

$\mathbf{v}$	vector $\mathbf{v}$
$\mathbf{M}$	matrix $\mathbf{M}$
$\mathbf{M}^T$	transpose of matrix $\mathbf{M}$
$\mathbf{M}^*$	complex conjugate of matrix $\mathbf{M}$
$\mathbf{M}^H = (\mathbf{M}^*)^T$	Hermitian transpose of matrix $\mathbf{M}$
$\mathbf{M}^{-1}$	inverse of matrix $\mathbf{M}$
$\mathbf{M}^\dagger$	pseudo–inverse of matrix $\mathbf{M}$
$\det \mathbf{M}$	determinant of matrix $\mathbf{M}$
$\mathrm{diag}\{\mathbf{v}\}$	square diagonal matrix with vector $\mathbf{v}$ as diagonal
$\mathbf{X}(k:l,:)$	rows k up to l of matrix $\mathbf{X}$
$\mathbf{X}(:,k:l)$	columns k up to l of matrix $\mathbf{X}$
$\mathbf{v}(m)$	m–th element of vector $\mathbf{v}$
$\mathbf{M}(m,n)$	element on the m–th row and n–th column of matrix $\mathbf{M}$
x^*	complex conjugate of x
$\mathrm{conj}(\cdot)$	complex conjugation
$\hat{x}$	estimate of x
$\lvert\cdot\rvert$	absolute value
$\bar{\cdot}$	mean value
$\mathcal{E}\{\cdot\}$	expectation operator
σ_x^2	variance of x
σ_x	standard deviation of x
$a \ll b$	a is much smaller than b
$a \gg b$	a is much larger than b
$a \approx b$	a is approximately equal to b
$[\cdot]$	concentration

Fixed Symbols

A	light attenuation
B	differential pathlength factor
C_i	concentration of chromophore i
C_{xy}	measure of coherence in a specific frequency range
$C_{xy}(f)$	coherence function of signals $x(k)$ and $y(k)$
D	diffusion coefficient (Chapter 3)
D	decimation factor (Chapter 2)
G	scattering term in the modified Beer-Lambert law
$[H]$	hemoglobin concentration in large vessel blood sample
H	self-similarity parameter, Hurst exponent (Chapter 4)
I_0	intensity of incident light
I	intensity of emerging light
K	model order (Chapter 2)
K	constant reflecting the molecular weight of hemoglobin, the brain tissue density and the large vessel-tissue ratio, used for the calculation of cerebral blood flow and volume (Chapter 3)
L	number of lags
M	filter order (adaptive noise canceller)
N	number of data points
$P_{xx}(f)$	power spectral density of $x(k)$
$P_{yy}(f)$	power spectral density of $y(k)$
$P_{xy}(f)$	cross power spectral density of $x(k)$ and $y(k)$
R_{xy}	correlation coefficient between signals x and y
$R(l,t)$	intensity of reflected light at a distance l and time t
$S(r,t)$	photon source
a_i	amplitude of signal pole i
c	speed of light in tissue
c_i	complex amplitude of signal pole i
d	interoptode distance
d_i	damping factor of signal pole i
$e(k)$	error signal at time k (adaptive noise canceller)
f	frequency
f_i	frequency of signal pole i
f_s	sampling frequency
g	scattering anisotropy factor
m	number of rows of the data matrix
n	number of chromophores
$n(k)$	noise at time k
$n_r(k)$	noise reference at time k (adaptive noise canceller)
$n_x(k)$	noise in observed signal at time k (adaptive noise canceller)
$n_f(k)$	filter output at time k (adaptive noise canceller)

s	signal of interest
$x(k)$	observed signal at time k
$y(k)$	observed signal at time k
z_i	signal pole i
z_i'	decimated signal pole i
α	DFA scaling exponent
α_i	specific extinction coefficient of chromophore i
β	spectral index
γ	long-term correlations exponent
Δt	sampling interval
$\delta(k)$	Dirac impulse at $k = 0$
μ	stepsize (adaptive noise canceller)
μ_a	absorption coefficient
μ_s	scattering coefficient
μ_{eff}	effective attenuation coefficient
ϕ_i	phase of signal pole i
$\phi(r,t)$	diffuse photon fluence rate at position r and time t
σ_ν	standard deviation of noise
$\omega = 2\pi f$	pulsation
$\mathbf{A}$	mixing matrix
$\mathbf{I}_N$	$N \times N$ identity matrix
$\mathbf{R}_\mathbf{x} = \mathcal{E}\{\mathbf{x}^*\mathbf{x}^T\}$	autocorrelation matrix corresponding to vector $\mathbf{x}$
$\mathbf{W}$	whitening matrix
$\mathbf{X}$	data matrix
$\mathbf{w}(k)$	filter weights
$\mathbf{x}$	data sequence
$\mathbf{x}_d$	decimated data sequence

Acronyms and Abbreviations

AC	Amplitude
ALTE	Apparent life threatening event
ANC	Adaptive noise cancellation
bpm	beats per minute
CA	Conceptional age
CBF	Cerebral blood flow
CBV	Cerebral blood volume
CCD	Charge coupled device
cf.	`confer` : compare with
CPC_x	Common power coefficient
CPR	Cardiopulmonary resuscitation
CTG	Cardiotocography

$CtOx$	Cytochrome oxydase
CW	Continuous wave
DC	Mean intensity
DFA	Detrended fluctuation analysis
ECG	Electrocardiogram
EEG	Electroencephalogram
e.g.	`exempli gratia` : for example
EMG	Electromyogram
EOG	Electro-oculogram
Eq.	equation
EROS	Event-related optical signal
ESPRIT	Estimation of signal parameters via rotational invariance techniques
fNIRS	Functional near infrared spectroscopy
FFT	Fast Fourier transform
FiO_2	fractional inspired oxygen concentration
FIR	Finite impulse response
FU	Follow-up
GA	Gestational age
Hb	deoxygenated hemoglobin
HbO_2	oxygenated hemoglobin
HF	High frequency power
HFN	Normalized high frequency power
HR	Heart Rate
HRV	Heart Rate Variability
HTLS	Hankel total least squares
i.e.	`id est` : that is
ICA	Independent component analysis
ICG	Indocyanine green
IVH	Intraventricular haemorrhage
LED	Light emitting diode
LF	Low frequency power
LFN	Normalized low frequency power
LMS	Least mean square adaptive filter
LS	Least squares
MAP	Mean arterial blood pressure
MBLL	Modified Beer-Lambert law
MEG	Magnetoencephalogram
MRS	Magnetic resonance spectroscopy
MSE	Mean squared error
NICU	Neonatal Intensive Care Unit
NIR	Near infrared
NIRS	Near infrared spectroscopy
NLMS	Normalized least mean square adaptive filter
NNS	Non-nutritive sucking

$PaCO_2$	Partial arterial CO_2 pressure
PaO_2	Partial arterial oxygen pressure
PC	Personal computer
PH	Phase
PCA	Principal component analysis
PMA	Postmenstrual age
PMT	Photomultiplier tube
PS	Polysomnography
PVL	Periventricular Leucomalacia
PWR	Total power (Chapter 4)
RMSE	Root mean squared error
RMSSD	Root mean squared differences of RR intervals
SAA	Sample asymmetry analysis
SAA-R	Sample asymmetry analysis ratio
SaO_2	peripheral oxygen saturation
SDANN	Standard deviation of the average normal RR intervals calculated over periods of 5 minutes
SDNN	Standard deviation of normal RR intervals
SNR	Signal-to-noise ratio
SOBI	Second-order blind identification
SRS	Spatially resolved spectroscopy
SVD	Singular value decomposition
SWO	Singuliere waarden ontbinding
TI	Triangular index
TLS	Total least squares
TOI	Tissue oxygenation index
TPSF	Temporal point spread function
TRS	Time-resolved spectroscopy
ULF	Ultra low frequency power
UZ	Universitaire ziekenhuizen
vgl.	vergelijking
VLBW	Very low birth weight
VLF	Very low frequency power
vs.	versus
w.r.t.	with respect to

Contents

Voorwoord **i**

Abstract **iii**

Korte Inhoud **v**

Glossary **vii**

Contents **xiii**

Samenvatting **1**

1 Introduction **31**

1.1 Biomedical signal processing 31

1.2 Chapter by chapter overview 33

2 Subspace-based parameter estimation methods using data decimation **37**

2.1 Introduction 37

2.2 HTLS 39

2.3 Decimative HTLS 42

2.3.1 Decimated data matrices 43

2.3.2 D order shift 45

2.4 Computational complexity 46
2.5 Numerical Examples 46
2.5.1 Two peak reference signal 46
2.5.2 Simulated MRS signals 51
2.6 Conclusions 60

3 Near-infrared spectroscopy **63**
3.1 Introduction 64
3.1.1 Physical principles 64
3.1.2 Models 65
3.1.3 Instrumentation 68
3.1.4 Clinical applications 69
3.2 Monitoring of cerebral circulation and oxygenation in neonates 70
3.2.1 Cerebral TOI in prematurely born infants 72
3.2.2 Cerebral circulation and oxygenation during rewarming of neonates 73
3.2.3 Cerebral autoregulation 74
3.3 Functional monitoring 80
3.3.1 Introduction 80
3.3.2 Measurements 82
3.3.3 Raw signals 84
3.3.4 Filtering 88
3.3.5 Independent component analysis (ICA) 96
3.3.6 Discussion 109
3.4 Conclusions 112

4 Heart rate variability of neonates **115**
4.1 Introduction 115

4.1.1 Polysomnography and evaluation of cardiorespiratory control in neonates . . . 115
4.1.2 Heart Rate Variability . . . 117
4.2 Neonatal heart rate data . . . 118
4.3 Standard time- and frequency-domain analysis of HRV . . . 121
4.3.1 Basic concepts . . . 122
4.3.2 Methodology . . . 123
4.3.3 Standard HRV parameters . . . 129
4.4 Fractal analysis of neonatal HRV . . . 129
4.4.1 Basic concepts . . . 129
4.4.2 Detrended fluctuation analysis (DFA) . . . 133
4.4.3 Methodology . . . 135
4.4.4 DFA parameters of HRV . . . 149
4.5 Sample asymmetry analysis . . . 149
4.5.1 Basic concepts . . . 149
4.5.2 Methodology . . . 150
4.6 Classification AA, AN, NN neonates . . . 151
4.6.1 Subjects . . . 151
4.6.2 Measurements . . . 152
4.6.3 Results . . . 153
4.6.4 Discussion . . . 158
4.7 Conclusion . . . 162

5 Conclusions and further research **165**

Bibliography **171**

Appendices **193**

A Relationship between detrended fluctuation analysis (DFA) and spectral analysis 193

A.1 Fluctuation function of a single sinusoid 193

A.2 Fluctuation function of arbitrary signals 198

B Alternative estimators of the fractal exponent 200

B.1 Frequency domain methods 200

B.2 Wavelet-based methods 207

C Effect of ECG sampling rate on HRV parameters 208

List of publications **211**

Curriculum Vitae **213**

Samenvatting

Gevorderde signaalverwerking voor in-vivo spectroscopie en hartritmevariabiliteit

Hoofdstuk 1: Inleiding

In deze thesis worden drie toepassingen van biomedische signaalverwerking besproken. Elke fysische grootheid die verandert in functie van de tijd, of een andere onafhankelijke veranderlijke, kan beschouwd worden als een signaal. Biomedische signalen bevatten informatie over de onderliggende fysiologische processen. Een stijging van de lichaamstemperatuur kan bijvoorbeeld wijzen op een infectie. Het doel van de signaalverwerking kan algemeen omschreven worden als het duidelijker maken van die informatie voor een waarnemer. Concreet kan dat gaan om:

- het filteren van de signalen om ruis of artefacten te verwijderen;
- het nauwkeurig bepalen van klinisch relevante parameters;
- classificatie voor diagnostische doeleinden;
- ...

Voor deze taken zijn verscheidene signaalverwerkingstechnieken beschikbaar uit diverse disciplines. In deze thesis is er gekozen voor een probleemgerichte aanpak. In elk hoofdstuk, worden uitgaande van een bepaald probleem, de gebruikte technieken uitgelegd, samen met de redenen waarom ze toegepast worden en de daarbij gemaakte veronderstellingen.

Hoofdstuk 2: Deelruimte-gebaseerde parameterschattingsmethoden met data decimatie

Inleiding

In vele toepassingen van digitale signaalverwerking, waaronder magnetische resonantie spectroscopie (MRS), wordt een modelfunctie bestaande uit een som van exponentieel gedempte sinusoïden gebruikt. Het signaal $x(k)$ wordt gemodelleerd als een som van K exponentieel gedempte sinusoïden en additieve witte ruis $n(k)$:

$$x(k) = \sum_{i=1}^{K} a_i e^{j(\phi_i)} e^{(j2\pi f_i - d_i)k/f_s} + n(k), \qquad k = 0, 1, \ldots, N-1 \tag{1}$$

waarin a_i de amplitude voorstelt, ϕ_i de fase, f_i de frequentie en d_i de demping van component i, en f_s de bemonsteringsfrequentie. Bij MRS signalen, leveren deze parameters rechtstreeks informatie over de moleculen van het onderzochte organisme: de frequentie f_i van een spectrale component kenmerkt de identiteit van de molecule, de demping d_i kenmerkt de mobiliteit van de overeenstemmende molecule en de amplitude a_i is rechtstreeks evenredig met de concentratie van de molecule. Het probleem bestaat er dus in deze parameters zo nauwkeurig mogelijk te bepalen op basis van een reeks van N opgemeten datapunten $x(k), k = 0, 1, \ldots, N-1$. Hierbij wordt verondersteld dat het aantal componenten K a priori gekend is. Eens de zogenaamde signaalpolen $z_i = e^{(j2\pi f_i - d_i)/f_s}$ gekend zijn, kunnen de amplitudes en fases bepaald worden door oplossing van een lineair stelsel. Het probleem bestaat dus voornamelijk uit de schatting van de signaalpolen z_i.

Hoewel er verscheidene technieken bestaan om dit probleem aan te pakken, beperken we ons tot de zogenaamde deelruimte-gebaseerde methoden, die gebruik maken van de eigenwaarden ontbinding van de covariantiematrix in een signaal-deelruimte en een ruis-deelruimte. Meer bepaald zullen we gebruik maken van het HTLS algoritme [211], een variant van het gekende ESPRIT algoritme [183, 182]. We leiden drie varianten van het HTLS algoritme af die gebruik maken van data decimatie.

HTLS

Beschouw de volgende Hankel matrix $\mathbf{X}$ met m rijen die alle data punten $x(k),\ k = 0, \ldots, N-1$ bevat:

$$\mathbf{X} = \begin{bmatrix} x(0) & x(1) & \ldots & x(N-m) \\ x(1) & x(2) & \ldots & x(N-m+1) \\ \vdots & \vdots & \ddots & \vdots \\ x(m-1) & x(m) & \ldots & x(N-1) \end{bmatrix} \tag{2}$$

In de veronderstelling dat er geen ruis is, kan deze matrix met behulp van het model (1) geschreven worden als een product van Vandermonde matrices:

$$\begin{aligned}\mathbf{X} &= \begin{bmatrix} 1 & 1 & \dots & 1 \\ z_1 & z_2 & \dots & z_K \\ \vdots & \vdots & \ddots & \vdots \\ {z_1}^{m-1} & {z_2}^{m-1} & \dots & {z_K}^{m-1} \end{bmatrix} \times \begin{bmatrix} c_1 & 0 & \dots & 0 \\ 0 & c_2 & \dots & 0 \\ \vdots & \vdots & \ddots & \vdots \\ 0 & 0 & \dots & c_K \end{bmatrix} \\ &\quad \times \begin{bmatrix} 1 & z_1 & \dots & {z_1}^{N-m} \\ 1 & z_2 & \dots & {z_2}^{N-m} \\ \vdots & \vdots & \ddots & \vdots \\ 1 & z_K & \dots & {z_K}^{N-m} \end{bmatrix} \\ &\equiv \mathbf{SCT}^T \end{aligned} \tag{3}$$

Hieruit zouden de signaalpolen z_i en de complexe amplitudes c_i rechtstreeks bepaald kunnen worden. Er bestaan echter geen algoritmes om rechtstreeks deze Vandermonde ontbinding te berekenen. Daarom wordt in het HTLS algoritme gebruik gemaakt van de singuliere waarden ontbinding van $\mathbf{X}$ en de volgende verschuivingsinvariante structuur van $\mathbf{S}$ om de signaalpolen te bepalen:

$$\mathbf{S}^1 = \mathbf{S}_1\mathbf{Z} \tag{4}$$

waarbij met $\mathbf{S}^1$, $\mathbf{S}_1$ de matrix $\mathbf{S}$ zonder de bovenste, respectievelijk de onderste rij aangeduid wordt, en $\mathbf{Z}$ een $(K \times K)$ diagonaal matrix bestaande uit de K signaalpolen $z_i,\ i = 1, \dots, K$ voorstelt.

Decimatie

Data decimatie kan op verschillende manieren toegepast worden in het HTLS algoritme. Enerzijds kan HTLS toegepast worden op een matrix, die opgebouwd is uit verschillende gedecimeerde signalen. Anderzijds kan de verschuivingsinvariantie tussen de matrix $\mathbf{S}$ zonder respectievelijk de D bovenste en D onderste rijen benut worden. Hoewel dit geen data decimatie in de strikte zin van het woord is, gebruiken we die term hier toch omdat beide methodes schattingen geven van de gedecimeerde signaalpolen. Nadat de signaalpolen geschat zijn, worden de fases en amplitudes zoals steeds bepaald als de kleinste kwadraten oplossing van het stelsel (1), waarin z_k vervangen is door de schattingen $\hat{z}_k$.

Van de originele tijdreeks $\mathbf{x} = [x(0), x(1), \dots, x(N{-}1)]$, kunnen D verschillende gedecimeerde tijdreeksen gevormd worden:

$$\mathbf{x}_d = [x(d), x(D+d), \dots, x((N/D{-}1)D+d)] \tag{5}$$

$$\equiv [x_d(0), x_d(1), \dots, x_d(N/D-1)] \quad d = 0, 1, \dots, D{-}1 \tag{6}$$

met D de decimatie factor, gekozen zodat $|f_i| < f_{sample}/(2D),\ \ i = 1, 2, \ldots, K$ om vouwvervorming te vermijden. Met behulp van het model (1) kan dit geschreven worden als:

$$x_d(k) = \sum_{i=1}^{K} c_i z_i^{(Dk+d)} + n(Dk+d) \tag{7}$$

$$= \sum_{i=1}^{K} (c_{id})(z_i')^k + n(Dk+d), \qquad k = 0, 1, \ldots, N/D-1 \tag{8}$$

met $z_i' \equiv z_i^D,\ i{=}1,\ldots,K$ and $c_{id} \equiv c_i z_i^d,\ i{=}1,\ldots,K,\ d{=}0,\ldots,D{-}1$.

De Vandermonde ontbinding van een Hankel matrix $\mathbf{X}_d$, opgebouwd op basis van een gedecimeerde tijdreeks $\mathbf{x_i}$ zoals in vgl. (2), kan dus geschreven worden als:

$$\mathbf{X}_d = \begin{bmatrix} 1 & 1 & \ldots & 1 \\ z_1' & z_2' & \ldots & z_K' \\ \vdots & \vdots & \ddots & \vdots \\ {z_1'}^{m-1} & {z_2'}^{m-1} & \ldots & {z_K'}^{m-1} \end{bmatrix} \times \begin{bmatrix} c_{1d} & 0 & \ldots & 0 \\ 0 & c_{2d} & \ldots & 0 \\ \vdots & \vdots & \ddots & \vdots \\ 0 & 0 & \ldots & c_{Kd} \end{bmatrix}$$
$$\times \begin{bmatrix} 1 & z_1' & \ldots & {z_1'}^{N/D-m} \\ 1 & z_2' & \ldots & {z_2'}^{N/D-m} \\ \vdots & \vdots & \ddots & \vdots \\ 1 & z_K' & \ldots & {z_K'}^{N/D-m} \end{bmatrix} \tag{9}$$

$$\equiv \mathbf{S}\mathbf{C}_d\mathbf{T}^T \tag{10}$$

Vermits deze vergelijking volledig analoog is aan vgl. (3), is het duidelijk dat HTLS toegepast op de matrix $\mathbf{X}_d$ schattingen $\hat{z}_i'$ oplevert van de gedecimeerde signaalpolen z_i', van waaruit de echte signaalpolen z_k eenvoudig kunnen berekend worden. Omdat de matrix $\mathbf{X}_d$ maar een fractie (N/D) van de beschikbare data bevat, zullen deze schattingen echter statistisch minder nauwkeurig zijn. Twee verschillende uitbreidingen worden voorgesteld die alle datapunten benutten.

Uit vgl. (9) is het duidelijk dat alle matrices $\mathbf{X}_d,\ \ d = 0, 1, \ldots, D-1$ dezelfde kolomruimte hebben en bijgevolg dezelfde verschuivingsinvariantie. Bijgevolg kan de matrix $\mathbf{X}_{stack}$ ontbonden worden als volgt:

$$\mathbf{X}_{stack} \equiv \begin{bmatrix} \mathbf{X}_0 & \mathbf{X}_1 & \ldots & \mathbf{X}_{D-1} \end{bmatrix} \tag{11}$$

$$= \mathbf{S} \begin{bmatrix} \mathbf{C}_0\mathbf{T}^T & \mathbf{C}_1\mathbf{T}^T & \ldots & \mathbf{C}_{D-1}\mathbf{T}^T \end{bmatrix} \tag{12}$$

Hieruit blijkt dat ook $\mathbf{X}_{stack}$ dezelfde verschuivingsinvariante structuur bezit. HTLS toegepast op $\mathbf{X}_{stack}$ resulteert dus in dezelfde gedecimeerde signaalpolen.

Omdat in dit geval echter alle data benut worden, zullen de schattingen statistisch nauwkeuriger zijn. Deze methode, verder *HTLSDstack* genoemd, is het datamatrix equivalent van het decimatieve ESPRIT algoritme dat gebruikt maakt van de gemiddelde covariantiematrix van verschillende gedecimeerde tijdreeksen [196, 82].

Een variant hierop maakt gebruik van de volgende datamatrix:

$$\begin{aligned} \mathbf{X}_{sum} &\equiv \mathbf{X}_0 + \mathbf{X}_1 + \ldots + \mathbf{X}_{D-1} && (13) \\ &= \mathbf{S}\left[\ \mathbf{C}_0\mathbf{T}^T + \mathbf{C}_1\mathbf{T}^T + \ldots + \mathbf{C}_{D-1}\mathbf{T}^T\ \right] && (14) \end{aligned}$$

Ook hier is het duidelijk dat $\mathbf{X}_{sum}$ dezelfde verschuivingsinvariantie bezit als de matrices $\mathbf{X}_d,\ \ d = 0, 1, \ldots, D-1$, terwijl alle datapunten gebruikt worden. Merk op dat deze methode, verder aangeduid met *HTLSDsum*, neerkomt op het toepassen van HTLS op de tijdreeks die bekomen wordt door in de originele tijdreeks telkens D opeenvolgende datapunten op te tellen.

Een andere methode, DESE ("DEcimative Spectral Estimation"), schat ook de gedecimeerde signaalpolen hoewel er geen gebruik gemaakt wordt van gedecimeerde tijdreeksen [65]. DESE schat de gedecimeerde signaalpolen uitgaande van de originele datamatrix $\mathbf{X}$ op basis van de verschuivingsinvariantie tussen de matrix $\mathbf{S}$ zonder respectievelijk de D bovenste en D onderste rijen. De niet-decimatieve versie van DESE (*D=1*) is identiek aan de "matrix pencil"methode [94]. Wij passen deze werkwijze toe op HTLS om de verschillende decimatiemethoden te kunnen vergelijken zonder rekening te moeten houden met andere verschillen tussen de methoden.

Uit vgl. (3) is het duidelijk dat er een verschuivingsinvariante eigenschap bestaat tussen de matrix $\mathbf{S}$ zonder respectievelijk de D bovenste en D onderste rijen:

$$\mathbf{S}^D = \mathbf{S}_D\mathbf{Z}' \tag{15}$$

waarin $\mathbf{S}^D$, $\mathbf{S}_D$ de matrix $\mathbf{S}$ zonder respectievelijk de D bovenste en D onderste rijen voorstelt, en $\mathbf{Z}'$ is a $(K \times K)$ een diagonaal matrix bestaande uit de K gedecimeerde signaalpolen $z'_i,\ i = 1, \ldots, K$. Verder is HTLSDdese identiek aan HTLS. Deze versie wordt verder gerefereerd als *HTLSDdese*.

Rekenkost

De rekenkost van de voorgestelde algoritmes wordt hoofdzakelijk bepaald door de 2 singuliere waarden ontbindingen (SWO): de SWO van datamatrix $\mathbf{X}$ (SWO1) en een SWO om de totale kleinste kwadraten oplossing te berekenen van het verschuivingsinvariantie-stelsel (SWO2). Over het algemeen is de rekenkost van SWO1 veel groter dan die van SWO2. Bij de vergelijking van de verschillende algoritmes, beperken we ons tot een vergelijking van de dimensies van de matrices waarvan de SWO berekend wordt, zoals weergegeven in

Tabel 1. Voor elk algoritme is de rekenkost vooral afhankelijk van het aantal rijen m van de datamatrix $\mathbf{X}$. Vermits over het algemeen $m \gg D$, vermindert de rekenkost van HTLSDstack en HTLSDsum met toenemende decimatiefactor D, terwijl de rekenkost van HTLSDdese amper beïnvloed wordt door D.

Tabel 1: Dimensies van de matrices waarvan de SWO de rekenkost van de algoritmes bepaalt, in functie van m (aantal rijen van de datamatrix) en D (decimatiefactor).

	SWO1	SWO2
HTLSDstack	$(m) \times (N - (m-1)D)$	$(m-1) \times (2K)$
HTLSDsum	$(m) \times (N/D - (m-1))$	$(m-1) \times (2K)$
HTLSDdese	$(m) \times (N - (m-1))$	$(m-D) \times (2K)$

Numerieke voorbeelden

Het eerste numerieke voorbeeld bestaat uit het schatten van de frequenties van twee ongedempte sinusoïden in de aanwezigheid van witte ruis. De gemiddelde fout op de schattingen van de frequenties in functie van de signaal-ruisverhouding (SNR) is weergegeven in Figuur 1, voor elke methode met decimatiefactor 10 en zonder decimatie. De belangrijkste conclusies die we uit deze simulaties kunnen trekken zijn:

- Voor elke methode is onder een bepaalde SNR, de gemiddelde fout op de frequentieschattingen groter dan het verschil in frequentie tussen beide sinusoïden. Dit komt overeen met het geval waarin beide frequenties niet onderscheiden kunnen worden, m.a.w. waarbij slechts ééén frequentieschatting in de buurt van de exacte frequenties ligt terwijl de andere schatting ver van de juiste frequentie verwijderd is (zie Fig. 2.2).
- Voor gelijkblijvende m, neemt de nauwkeurigheid van HTLSDstack en HTLSDsum toe met toenemende decimatiefactor D, terwijl de nauwkeurigheid van HTLSDdese enkel vergroot bij lage SNR, waarbij de frequenties niet kunnen onderscheiden worden.
- Voor gelijkblijvende D, neemt de nauwkeurigheid toe met toenemende m (zolang tenminste $m \leq N/2$), en bijgevolg toenemende rekenkost.

Bijkomende experimenten met verschillende m en D tonen aan dat de nauwkeurigheid van HTLSDstack en HTLSDsum enkel afhankelijk is van het pro-

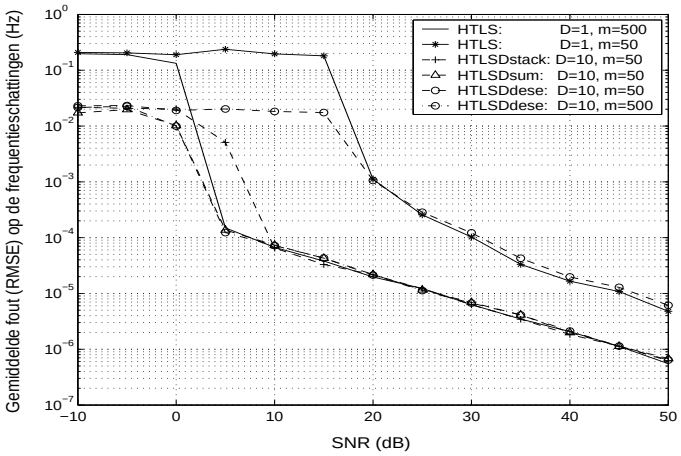

Figuur 1: Gemiddelde fout in functie van de signaal-ruisverhouding voor HTLS zonder decimatie (volle lijn) en de verschillende HTLS versies met decimatiefactor 10 (HTLSDstack (+), HTLSDsum (△) en HTLSDdese (o)); m stelt het aantal rijen van de datamatrix voor.

dukt mD, als de SNR voldoende hoog is om beide frequenties te onderscheiden. Verder wordt aangetoond dat, voor een gegeven modelorde K en eenzelfde aantal datapunten N, de hoogste nauwkeurigheid voor HTLSDstack en HTLSDsum bereikt wordt wanneer de matrices $\mathbf{X}_d$ zo vierkant mogelijk zijn ($m = \frac{N}{2D}$), terwijl dit voor HTLSDdese en HTLS het geval is wanneer de matrix $\mathbf{X}$ zo vierkant mogelijk is ($m = \frac{N}{2}$) (zie Fig. 2.3). Wanneer we de rekenkost van de verschillende algoritmes vergelijken voor deze optimale waarden van m, blijkt dat voor HTLSDstack en HTLSDsum het aantal rijen van de matrix van SWO1 vermindert met een factor D, terwijl de dimensies van deze matrix voor HTLSDdese dezelfde zijn als voor HTLS (zonder decimatie). Hieruit volgt dat de nauwkeurigste schattingen tegen een zo laag mogelijke rekenkost bekomen worden met HTLSDstack en HTLSDsum met optimale m waarde ($m = N/(2D)$) en waarbij D zo groot mogelijk gekozen wordt zonder vouwvervorming te veroorzaken ($|f_i| < f_{sample}/(2D),\ \ k = 1, 2, \ldots, K$).

In de tweede reeks numerieke experimenten worden de parameters van gesimuleerde MRS signalen, met 5 (zie Tabel 2.4) of 11 pieken (zie Tabel 2.5), geschat met de verschillende methodes, waarbij telkens de dimensie (m) gebruikt wordt die de hoogste nauwkeurigheid geeft. De performantie van de methodes wordt vergeleken aan de hand van de robuustheid, gedefinieerd als het percentage van de gevallen waarin alle pieken geïdentificeerd worden binnen bepaalde grenzen, en de nauwkeurigheid, gedefinieerd als de vierkantswortel van de gemiddelde kwadratische fout (RMSE) van de parameterschattingen. In het voorbeeld met 5 pieken, blijkt HTLSDsum iets robuuster dan de overige

methodes, die ongeveer even robuust zijn (zie Fig. 2.6). De parameterschattingen met HTLSDsum van de piek met de hoogste frequentie zijn echter minder nauwkeurig dan die van de overige methodes (zie Fig. 2.8). Anderzijds blijkt de nauwkeurigheid van HTLSDstack voor dichtbij elkaar liggende pieken ook iets lager dan die van de overige methodes (zie Figure 2.7). Wat betreft het voorbeeld met 11 pieken, blijkt de robuustheid van alle methodes gelijkaardig te zijn (zie Fig. 2.10). In dit geval, blijkt de nauwkeurigheidheid van HTLSDstack over het algemeen iets groter dan die van de overige methodes, hoewel de verschillen meestal beperkt blijven tot enkele percenten (zie Fig. 2.11). Enkel de schatting van de piek met de hoogste frequentie met HTLSDsum is beduidend minder nauwkeurig dan de overige methodes (zie Fig. 2.12).

Conclusies

Bij voldoende hoge bemonsteringsfrequentie, kan data decimatie gebruikt worden om de rekenkost van deelruimte-gebaseerde parameterschattingsmethoden te verlagen zonder de nauwkeurigheid te verminderen.

Hoofdstuk 3 : Nabij-infrarood spectroscopie

Inleiding

Nabij-infrarood spectroscopie (NIRS) is een optische techniek waarmee biologisch weefsel niet-invasief kan onderzocht worden. Uit de verzwakking van licht dat door het weefsel gestuurd wordt, kunnen bepaalde eigenschappen van het weefsel bepaald worden. De twee belangrijkste vormen van interactie tussen nabij-infrarood licht en biologisch weefsel zijn absorptie en verstrooiing.

De *absorptie* van biologisch weefsel is vrij laag in het nabij-infrarode gebied (650 - 1000 nm). Bovendien blijft de bijdrage van de meeste componenten tot de absorptie, en dus tot de lichtverzwakking, constant. De concentratie van twee belangrijke lichtabsorberende componenten, namelijk geoxygeneerd en gedeoxygeneerd hemoglobine, varieert echter in de tijd, als functie van bloedtoevoer, oxygenatie en metabolisme. Op basis van de gekende absorptiekarakteristiek van beide componenten kunnen, uitgaande van de opgemeten veranderingen in lichtverzwakking, de veranderingen in concentratie van beide componenten afgeleid worden.

Een ander effect is *verstrooiing*, dat veroorzaakt wordt door verschillen in brekingsindex tussen diverse bestanddelen van het weefsel. In vergelijking met absorptie, is de verstrooiing groot maar relatief constant in de tijd. Veranderingen in verstrooiing kunnen veroorzaakt worden door veranderingen in hemoglobineconcentraties, maar ook door bijvoorbeeld hersenactiviteit. Veranderingen in verstrooiing dragen wel veel minder bij tot de verandering in lichtverzwakking dan veranderingen in absorptie.

Er bestaan verschillende modellen om de concentraties van de verschillende componenten te berekenen uitgaande van de opgemeten lichtverzwakking. Het meest eenvoudige model is gebaseerd op de Beer-Lambert wet, waarbij de verstrooiing constant verondersteld wordt. Een meer nauwkeurige methode maakt gebruik van de diffusievergelijking om de propagatie van fotonen in een verstrooiend medium te beschrijven.

De NIRS instrumentatie kan opgedeeld worden in twee types, naargelang het NIR licht dat gebruikt wordt. Bij zogenaamde "continuous wave"(CW) NIRS, waarbij de intensiteit van de lichtbron constant is, kan men enkel de verzwakking van het licht meten. Bij "time-resolved"(TRS) NIRS anderzijds, wordt ook de tijd die het licht nodig heeft om door het weefsel te gaan gemeten worden. Hiervoor wordt gebruikt gemaakt van korte lichtpulsen (tijdsdomein TRS) of van lichtbronnen waarvan de intensiteit sinusoïdaal gemoduleerd wordt (frequentiedomein TRS) (zie Fig. 3.2). Met deze bijkomende informatie kunnen absorptie en verstrooiing afzonderlijk gekwantificeerd worden.

Monitoring van de hersencirculatie en -oxygenatie bij pasgeborenen

Een veelbelovende toepassing van NIRS is de monitoring van de hersencirculatie en -oxygenatie bij pasgeborenen. Aangezien NIRS hiervoor nog niet routinematig in de klinische praktijk gebruikt wordt, is het meeste onderzoek gericht op de validatie en evaluatie van NIRS. In dit kader worden in samenwerking met de afdeling neonatologie van de Universitaire Ziekenhuizen Leuven (Gasthuisberg) verschillende studies gevoerd. Hierbij wordt een commercieel CW-NIRS toestel gebruikt waarmee concentratieveranderingen van HbO_2, Hb en de zogenaamde tissue oxygenation index (TOI), een maat voor de oxygenatie, kunnen gemeten worden.

In een eerste studie wordt de TOI van de hersenen gemeten op de eerste drie levensdagen bij prematuur geboren baby's. TOI blijkt een stabiele parameter te zijn die voornamelijk de cerebrale veneuze zuurstofsaturatie weerspiegelt. De TOI neemt toe tijdens de eerste drie levensdagen van premature n [149].

In een tweede studie wordt het effect van het opwarmen van prematuur geboren baby's met hypothermie op de hersencirculatie onderzocht. De hersencirculatie wordt continu gemeten tijdens het opwarmen met behulp van NIRS. Er worden geen negatieve effecten van het opwarmen op de hersencirculatie vastgesteld [147].

In een derde, exploratieve studie wordt de mogelijkheid om de cerebrale autoregulatie van premature n te evalueren met behulp van NIRS onderzocht. Cerebrale autoregulatie is het mechanisme waarbij de bloeddoorstroming van de hersenen (CBF) constant gehouden wordt tijdens veranderingen van de arteriële bloeddruk (MAP). Wanneer dit mechanisme niet goed werkt, zoals bij sommige premature n het geval is, is er een verhoogd risico op onder andere hersenbloedingen. De simultane en continue meting van MAP en CBF kan dus informatie verschaffen over de cerebrale autoregulatie. Gelijklopende veranderingen in MAP en CBF wijzen immers op een zwakke cerebrale autoregulatie. Omdat, bij constante perifere zuurstofsaturatie, een schatting van de verandering in CBF kan gemaakt worden op basis van de concentratieveranderingen van HbO_2 en Hb, namelijk $\Delta HbD = \Delta HbO_2 - \Delta Hb$ [207], kan NIRS gebruikt worden voor de evaluatie van cerebrale autoregulatie. Bij enkele prematuur geboren baby's werden daarom gelijktijdig MAP, SaO_2 en ΔHbD gemeten. De overeenstemming tussen MAP en ΔHbD wordt gekwantificeerd met drie verschillende methodes. Naast de gekende methodes zoals de correlatiecoëfficiënt en coherentie-analyse, wordt ook een nieuwe methode, HTLS-SEP, voorgesteld. Deze methode is gebaseerd op een modellering van de signalen met exponentieel gedempte sinusoïden, waarbij dezelfde parameters voor beide signalen gebruikt worden. De bijdrage van deze gemeenschappelijke componenten tot de totale variantie van het HbD signaal wordt gebruikt als maat voor de overeenstemming tussen beide signalen. In Fig. 2 is een voorbeeld weergegeven van

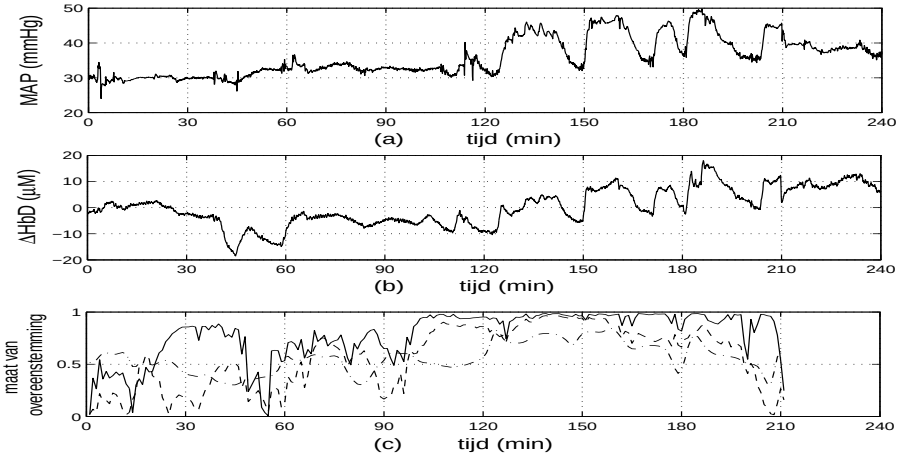

Figuur 2: Simultane veranderingen van MAP (a) and HbD (b) in een prematuur geboren baby, en de overeenkomstige maten voor de evaluatie van cerebrale autoregulatie (c): R_{xy} (streeplijn), C_{xy} (streep-punt lijn) en CPC_x (volle lijn).

opgemeten veranderingen in MAP en HbD, samen met de verschillende maten voor de evaluatie van cerebrale autoregulatie.

De eerste resultaten suggereren dat de correlatiecoëfficiënt en HTLS-SEP beter de overeenstemming tussen MAP en HbD weergeven. Een uitgebreidere follow-up studie is echter noodzakelijk om de verschillende methodes te analyseren en te vergelijken met het oog op de evaluatie van cerebrale autoregulatie.

Functionele metingen van hersenactiviteit

Inleiding

Een andere toepassing van NIRS situeert zich in het domein van de functionele metingen van hersenactiviteit. Hersenactiviteit veroorzaakt veranderingen in de optische eigenschappen van de hersenen die kunnen gemeten worden met NIRS. Naargelang de responsietijd, kunnen twee signalen onderscheiden worden. Het snelle *neuronale signaal*, met een responsietijd in de grootteorde van milliseconden, wordt veroorzaakt door veranderingen in de verstrooiingseigenschappen van de neuronen, en is dus rechtstreeks verbonden met de hersenactiviteit. Het trage *hemodynamische signaal* anderzijds, met een responsietijd in de grootteorde van seconden, is een gevolg van de toename in bloedtoevoer naar het geactiveerde gebied. Aangezien de toename in bloedtoevoer een groter gebied bestrijkt dan enkel de geactiveerde neuronen, is het neuronale signaal beter

gelokaliseerd. Daartegenover staat dat de amplitude van het neuronale signaal veel kleiner is dan het hemodynamische signaal, en daarom zeer moeilijk te detecteren is. Het doel van deze studie is de detectie van het neuronale signaal in de motor cortex, veroorzaakt door beweging met de hand. Deze beweging bestaat uit het naar elkaar brengen en weer verwijderen van de vingertoppen, inclusief de duim, op een vast ritme ("finger tapping"). We zoeken dus een component in de NIRS signalen die gecorreleerd is met de frequentie waarmee de hand beweegt. Deze studie gebeurde in samenwerking met het Laboratory for Fluorescence Dynamics van de University of Illinois at Urbana-Champaign, waar de metingen verricht werden.

Metingen

De metingen zijn uitgevoerd met frequentie-domein NIRS apparatuur, waarbij sinusoïdaal gemoduleerd NIR licht gebruikt wordt. De verschillen in gemiddelde intensiteit (DC), amplitude (AC) en fase (PH) tussen het invallende licht en het gemeten licht worden rechtstreeks geanalyseerd. Hierbij wordt gebruik gemaakt van een sensor met 4 lichtbronnen (laser diodes) en 4 detectors, geplaatst op een cirkel met diameter 3.2 cm (zie Fig. 3.7). Om het licht van de verschillende bronnen te kunnen onderscheiden worden de lichtbronnen beurtelings aangestuurd. De bemonsteringsfrequentie van een complete cyclus, waarin alle 48 parameters (AC, DC en PH voor 16 bron-detector paren) gemeten worden, bedraagt 96 Hz. Naast de NIRS-metingen, worden ook de ademhaling, de arteriële pulsaties (pulsoximeter) en een signaal synchroon met de handbeweging (mechanisch) gemeten.

De sensor wordt geplaatst boven de motor cortex contralateraal aan de bewegende hand. De frequentie van de handbeweging wordt aangegeven met een metronoom. Het protocol bestaat uit een rustperiode van 1 minuut, gevolgd door afwisselende rust- en stimulatie-periodes van 20 s (meestal 8), en tenslotte nog een rustperiode van 1 minuut. In totaal werden de metingen van 14 normale, gezonde vrijwilligers geanalyseerd.

De grootste fluctuaties in de AC- en DC-signalen zijn de arteriële pulsaties (zie Fig. 3.8). Dit blijkt ook uit het spectrum van een typisch DC-signaal, zoals weergegeven in Fig. 3, waar de grootste pieken overeenkomen met het hartritme en harmonischen daarvan. Verder zijn er ook een piek bij de ademhalingsfrequentie en een piek bij 0.12 Hz, gerelateerd aan de Mayer, zichtbaar. Tenslotte is er ook een kleine piek bij 0.025 Hz, overeenkomend met een periode van 40 s, zichtbaar. Deze piek, ten gevolge van het trage hemodynamische signaal, is een eerste indicatie dat de metingen in het juiste gebied gebeurd zijn. Bij de frequentie van de handbeweging is evenwel geen piek zichtbaar. Omdat de AC-signalen grotendeels dezelfde informatie bevatten als de DC-signalen maar een lagere signaal-ruisverhouding, worden de AC-signalen niet verder geanalyseerd. In de PH-signalen, die informatie leveren over de tijd die de fotonen

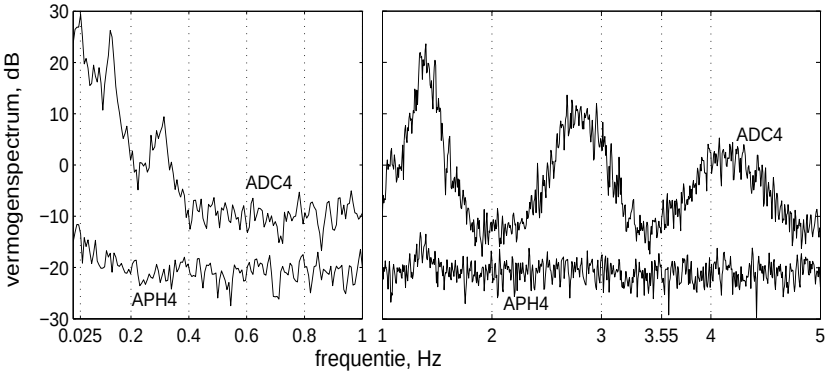

Figuur 3: Vermogenspectrum van typische DC- en PH-signalen (ADC4 en APH4). De pieken in het spectrum van ADC4 komen overeen met het hemodynamische signaal (0.025 Hz), Mayer golven (0.12 Hz), ademhaling (0.3 Hz) en arteriële pulsaties (1.4 Hz en hogere harmonischen). Er is geen piek bij de frequentie van de handbeweging (3.55 Hz). In het power spectrum van APH4, is er enkel een kleine piek ten gevolge van de arteriële pulsaties zichtbaar. Opmerking: de spectra werden verticaal verschoven om de figuur te verduidelijken.

nodig hebben om de detector te bereiken, is de ruis nog groter.

Filteren

Omdat de amplitude van het neuronale signaal zeer klein is ten opzichte van de andere fysiologische signalen zoals arteriële pulsaties en ruis worden de NIRS signalen eerst gefilterd. De laag- en hoogfrequente fysiologische stoorsignalen worden eerst verwijderd met een conventioneel banddoorlaatfilter met afsnijfrequenties van 1 Hz en 10 Hz. Aangezien de frequentie van de hartbeweging meestal tussen de tweede en derde harmonische van de hartfrequentie ligt, en beide frequenties enigszins variëren in functie van de tijd, is het niet mogelijk de fluctuaties ten gevolge van de arteriële pulsaties te verwijderen met een filter met een vaste doorlaatband. Daarom wordt gebruik gemaakt van een adaptief filter, waarvan de adaptatie gebaseerd is op het genormaliseerd kleinste kwadraten algortime (NLMS), in de standaard configuratie voor interferentieonderdrukking (interference cancelling) (zie Fig. 3.13). Het primaire signaal, dat dient als gewenste responsie voor het filter, is in dit geval het NIRS signaal dat zowel het neuronaal signaal als de ruis (arteriële pulsaties) bevat. Het pulsoximeter-signaal, dat enkel de arteriële pulsaties bevat, wordt gebruikt als ruisreferentie. In sommige metingen, waarvan het pulsoximeter onbruikbaar was omwille van verzadiging, werd evenwel een ander filter gebruikt, dat beschreven is in [73]. Het effect van het adaptief filter wordt geïllustreerd in

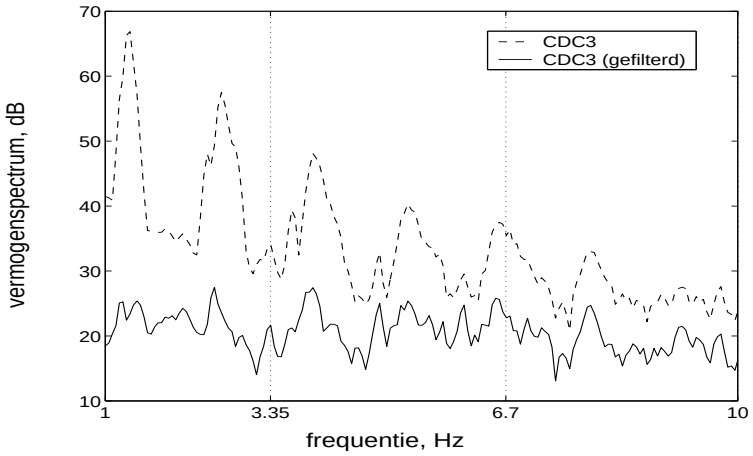

Figuur 4: Vermogenspectrum van een typisch DC-signaal voor en na de adaptieve filtering. Opmerking: de spectra werden verticaal verschoven om de figuur te verduidelijken.

Fig. 4 waarin het spectrum van een typisch DC-signaal voor en na de filtering vergeleken wordt.

In het spectrum van het gefilterde signaal is een zeer kleine piek zichtbaar bij de frequentie van de handbeweging (3.35 Hz), al zou deze moeilijk kunnen onderscheiden worden zonder voorkennis van de bewegingsfrequentie. Om na te gaan of deze piek effectief veroorzaakt wordt door de handbeweging, wordt het vermogen bij de bewegingsfrequentie vergeleken tijdens rust- en stimulatieperiodes. Het blijkt dat er in meerdere signalen statistisch significante verschillen zijn (zie Tabel 3.2).

Onafhankelijke componenten analyse (ICA)

Bij de voorgaande analyse werd voorkennis over zowel de bewegingsfrequentie als het begin en einde van elke stimulatie-periode gebruikt. Zonder deze voorkennis kan het neuronale signaal evenwel niet gedetecteerd worden in individuele NIRS-signalen. Daarom wordt de informatie in de verschillende NIRS-signalen gecombineerd om een duidelijker neuronaal signaal te bekomen. De methode die daarvoor gebruikt wordt is onafhankelijke componenten analyse (ICA), een techniek waarmee statistisch onafhankelijke bronsignalen kunnen gereconstrueerd worden op basis van een aantal geobserveerde lineaire combinaties van deze bronsignalen. Wiskundig kan dit als volgt uitgedrukt worden:

$$\mathbf{x}(k) = \mathbf{y}(k) + \mathbf{n}(k) = \mathbf{A}\mathbf{s}(k) + \mathbf{n}(k), \tag{16}$$

waarin $\mathbf{x}(k)$ en $\mathbf{n}(k)$ vectoren van lengte m (het aantal lichtbundels) zijn die respectievelijk de observaties en additieve ruis voorstellen, en waarin $\mathbf{s}$ een vector van lengte n is die de bronsignalen bevat. Het doel van ICA is om de matrix $\mathbf{A}$ en/of de bronsignalen $\mathbf{s}$ te bepalen wanneer enkel de observaties $\mathbf{x}$ gegeven zijn. De voornaamste veronderstelling die hierbij gemaakt wordt is dat de bronsignalen statistisch onafhankelijk zijn. Omdat het neuronale signaal ten gevolge van de handbeweging onafhankelijk verondersteld wordt van de andere fysiologische signalen en de ruis, gaan we ervan uit dat ICA kan gebruikt worden om het neuronale signaal af te zonderen als een van de bronsignalen. In de meeste ICA algoritmes wordt het probleem opgelost in twee stappen. In de eerste stap wordt een $n \times m$ matrix $\mathbf{W}$ berekend zodat de getransformeerde observaties $\mathbf{z}(k) = \mathbf{W}\mathbf{y}(k)$ onderling ongecorreleerd zijn en eenheidsvariantie hebben, m.a.w. $\mathcal{E}\{\mathbf{W}\mathbf{y}(k)\mathbf{y}^*(k)\mathbf{W}^T\} = \mathbf{I}_n$. In deze stap, die overeen komt met principale componenten analyse (PCA), kan ook een dimensiereductie van de data doorgevoerd worden. In de tweede stap, dient dan nog een orthogonale $n \times n$ matrix $\mathbf{U}$ bepaald te worden zodat $\mathbf{A} = \mathbf{W}^\dagger\mathbf{U}$ (waarin het superscript † de Moore-Penrose pseudo-inverse voorstelt). Meestal wordt hogere orde informatie gebruikt om $\mathbf{U}$ te berekenen. Voor tijdsgecorreleerde signalen kan $\mathbf{U}$ echter ook bepaald worden op basis van covariantiematrices met verschillende tijdsververschuivingen (waarbij dus enkel tweede orde informatie gebruikt wordt). Aangezien de optische signalen duidelijk tijdsgecorreleerd zijn, wordt een dergelijke algoritme, meer bepaald SOBI [19], gebruikt. In dit algoritme wordt een set van covariantiematrices met verschillende tijdsverschuivingen gelijktijdig gediagonaliseerd. Op die manier wordt opgelegd dat de covarianties met verschillende tijdsverschuivingen nul zijn, wat nodig is om statistisch onafhankelijke signalen te verkrijgen.

Voor elke meting, wordt SOBI toegepast op zowel de set van gefilterde DC-signalen als op de set van gefilterde PH-signalen. De volledige signalen die alle rust- en stimulatie-perioden omvatten, meestal bestaande uit 40000 datapunten, worden daarbij gebruikt. Er worden telkens evenveel bronsignalen geschat als er observaties zijn, namelijk 16 behalve in enkele gevallen waar één of twee optische signalen onbruikbaar waren omwille van verzadiging. Uit het vermogenspectrum van een van de IC's berekend uit de set van gefilterde DC-signalen, weergegeven in Fig. 5, blijkt duidelijk dat deze IC het neuronale signaal bevat. De twee grootste pieken in het spectrum liggen bij de bewegingsfrequentie (3.35 Hz) en de tweede harmonische (6.7 Hz). De overige IC's bevatten de residu's van de arteriële pulsaties en/of ruis. De piek bij de bewegingsfrequentie is duidelijker dan in de spectra van de gefilterde DC-signalen of in de spectra van de IC's berekend uit de set van ongefilterde DC-signalen. Als we het vermogen bij de bewegingsfrequentie vergelijken tijdens rust- en stimulatie-periodes, blijkt dat er in 9 van de 12 DC-metingen statistisch significante verschillen zijn in een van de IC's (zie Tabel 3.3). In de PH-metingen worden slechts in één meting een statistisch significant verschil waargenomen.

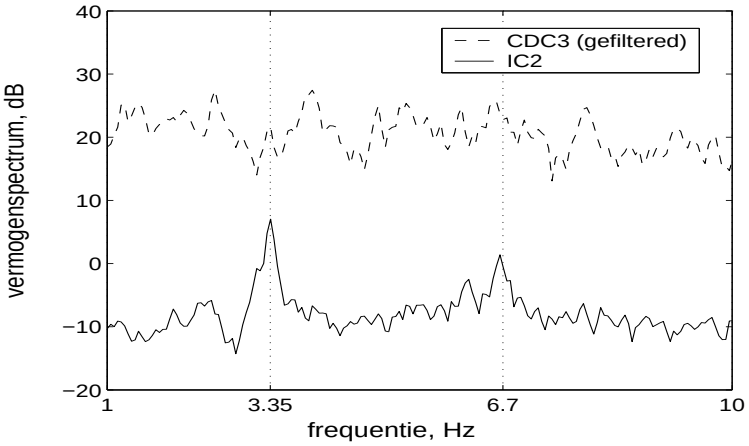

Figuur 5: Vermogenspectrum van een gefilterd DC-signaal, en de IC die het neuronale signaal bevat, berekend uit de set van gefilterde DC-signalen. Opmerking: de spectra werden verticaal verschoven om de figuur te verduidelijken.

Op basis van de IC's kunnen ook de individuele stimulatie-periodes gedetecteerd worden zonder voorkennis van de bewegingsfrequentie. In het spectrogram van IC2, weergegeven in Fig. 6, waarbij willekeurige vensters van 4 s (d.w.z. niet exact samenvallend met de stimulatieperioden) kunnen alle stimulatie-periodes behalve de eerste duidelijk geïdentificeerd worden.

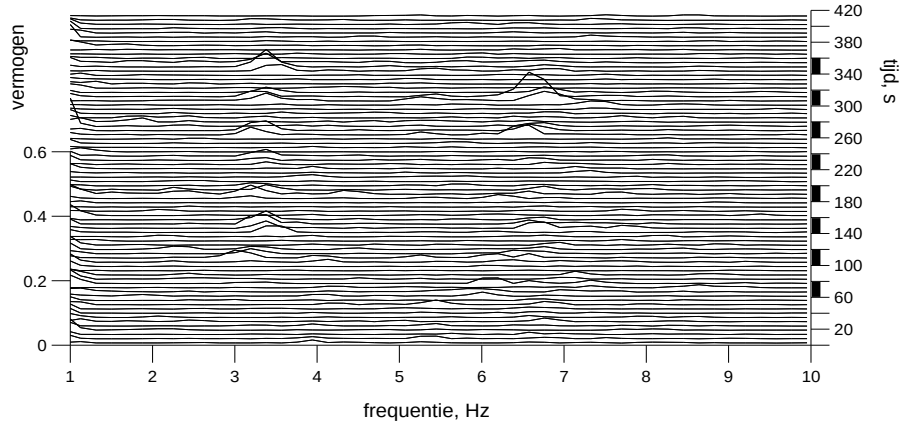

Figuur 6: Spectrogram van IC2 berekend uit de set gefilterde DC-signalen. De stimulatie-periodes zijn aangeduid met de zwarte vakjes naast de tijdsas.

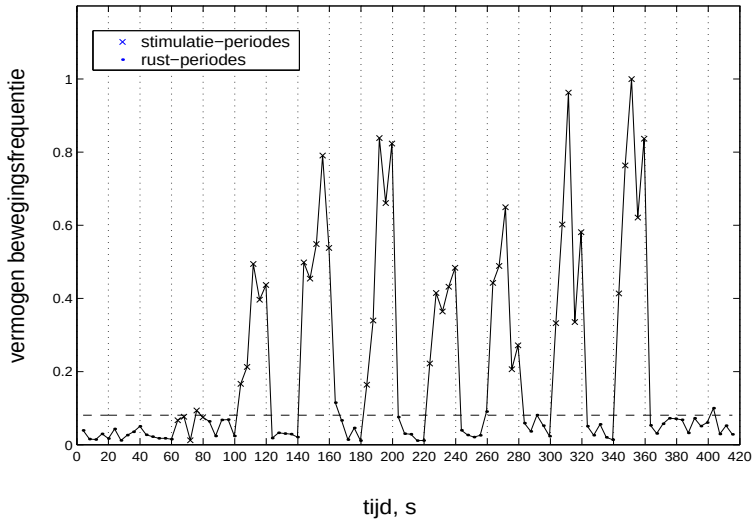

Figuur 7: Vermogen van IC2 bij de bewegingsfrequentie in functie van de tijd (niet-overlappende segmenten van 4 s). De IC's werden berekend uit de set van gefilterde DC-signalen. De streeplijn stelt het drempelniveau voor dat gebruikt werd voor de detectie.

Om op een meer objectieve manier te bepalen welke stimulatie-periodes geïdentificeerd kunnen worden, enkel op basis van de optische signalen, wordt de volgende eenvoudige procedure gevolgd. Het vermogen bij de bewegingsfrequentie wordt berekend voor willekeurige, opeenvolgende tijdsvensters van 4 s. De bewegingsfrequentie wordt in dit geval afgeleid uit het optische signaal zelf als het maximum van het spectrum in het beschouwde frequentiegebied. Het gemiddelde vermeerderd met tweemaal de standaarddeviatie van het vermogen bij de bewegingsfrequentie tijdens de eerste rustperiode van 1 minuut, wordt gebruikt als drempelwaarde. Een stimulatie-periode wordt beschouwd als zijnde gedetecteerd wanneer de drempel minstens 3 maal overschreden wordt gedurende de stimulatie-periode. Uit Fig. 7 blijkt dat op deze manier elke stimulatie-periode behalve de eerste gedetecteerd wordt in het spectrogram van Fig. 6. Ook voor de overige metingen komen de op deze manier gedetecteerde periodes goed overeen met de periodes die in het spectrogram op het zicht kunnen geïdentificeerd worden. In de 9 DC-metingen waarin een significante IC gevonden werd, kunnen op deze manier 67 van de 78 stimulatie-periodes gedetecteerd worden.

Discussie

In 9 van de 14 metingen, wordt in de DC-signalen een significant neuronaal signaal gevonden. Dat niet in alle gevallen een neuronaal signaal gevonden werd is te verklaren door het feit dat het neuronaal signaal sterk gelokaliseerd is en dat de sensor, die vrij klein is, in die gevallen vermoedelijk niet helemaal correct gepositioneerd was. Wat betreft PH-metingen, wordt slechts in 1 geval een significant neuronaal signaal geobserveerd. Het feit dat het neuronale signaal zeer lokaal is, m.a.w. dat het niet in alle lichtbundels geobserveerd wordt, wijst er ook op dat het niet veroorzaakt is door een mechanische koppeling tussen de beweging van de hand en de optische sensor. Onze resultaten bevestigen de resultaten van een vorige studie, op vijf van de hier geanalyseerde metingen, waarin het neuronale signaal gedetecteerd op basis van de kruiscorrelatie tussen de optische signalen en het bewegingssignaal berekend over de volledige duur van de meting [227]. Een belangrijk verschil met onze studie is dat individuele stimulatie-periodes kunnen geïdentificeerd worden in de optische signalen op zich.

Er zijn totnogtoe weinig studies verschenen die de niet-invasieve detectie van dit type neuronale signaal beschrijven. Gratton et al. beschrijven de detectie van het neuronale signaal in de PH-metingen, maar niet in de DC-metingen, bij verschillende soorten stimuli [74, 79, 78, 177, 50, 77]. Steinbrink et al., en Franceschini et al. daarentegen detecteerden een neuronaal signaal in de DC-metingen met CW-NIRS [193, 66]. Een gedetailleerde vergelijking van deze studies is echter moeilijk omwille van verschillen in stimuli, instrumentatie, enz. Een methodologisch verschil met onze studie bestaat erin dat in de voorgaande studies de signalen uitgemiddeld worden over een groot aantal stimulatie-periodes. In ons geval zou dit echter niet effectief zou zijn omdat de bewegingsfrequentie, in tegenstelling tot de stimulatiefrequentie bij bvb. een visuele stimuli, niet helemaal constant is. Door gebruik te maken van gevorderde signaalverwerking, bekomen we echter toch een neuronaal signaal waarin bovendien individuele stimulatie-periodes kunnen geïdentificeerd worden.

Op basis van studies op neuronaal niveau en invasieve studies met proefdieren, veronderstellen alle bovenvermelde auteurs dat het neuronaal signaal veroorzaakt wordt door verstrooiing. Op basis van de studies met in-vivo metingen bij mensen, kan het echter niet uitgesloten worden dat het neuronale signaal veroorzaakt wordt door absorptie. Verder onderzoek waarbij het neuronaal signaal zowel in DC- als in PH-signalen gedetecteerd wordt, kan hierover uitsluitsel brengen.

Conclusies

Door gebruik te maken van adaptieve filtering en onafhankelijke componenten analyse, kan hersenactiviteit gedetecteerd worden in de motor cortex op basis van functionele NIRS metingen.

Hoofdstuk 4: Hartritmevariabiliteit bij pasgeborenen

Inleiding

Het cardiorespiratoire systeem van pasgeborenen die behoren tot een specifieke risicogroep, zoals premature n of baby's die een schijnbaar levensbedreigende gebeurtenis (ALTE) doorgemaakt hebben, wordt geëvalueerd met behulp van polysomnografie. Polysomnografie is de continue, simultane meting van verscheidene fysiologische parameters zoals elektrocardiogram (ECG), ademhaling, perifere zuurstofsaturatie (SaO_2), EMG, EEG en EOG. In de Universitaire Ziekenhuizen Leuven, worden jaarlijks bij honderden pasgeborenen zulke polysomnografie opgemeten, hoofdzakelijk bij premature n, ALTE-kinderen of kinderen van ongeruste ouders. Naargelang het aantal en de ernst van de apnees (ademhalingsstoornissen) en bradycardies (hartritmedalingen) wordt de polysomnografie als normaal of abnormaal beschouwd. Kinderen met een abnormale polysomnografie worden thuis verder opgevolgd met een cardiorespiratoire monitor. Afhankelijk van de resultaten van de polysomnografie (PS) en de thuismonitoring (FU) kunnen dus 3 groepen onderscheiden worden: NN (normale PS, normale FU), AN (abnormale PS, normale FU) en AA (abnormale PS, abnormale FU). Het doel van deze studie is om te onderzoeken of abnormale cardiorespiratoire gebeurtenissen kunnen voorspeld worden op basis van het hartritme tijdens de polysomnografie in een periode zonder abnormale gebeurtenissen. Meer bepaald gaan we na of de 3 hoger vermelde groepen kunnen onderscheiden worden op basis van de hartritmevariabiliteit tijdens de polysomnografie. De onderliggende hypothese is dat abnormaliteiten in het autonome zenuwstelsel, dat instaat voor de cardiorespiratoire controle, niet alleen door abnormale bradycardieën weerspiegeld worden, maar ook door meer subtiele veranderingen in het hartritme.

Het hartritme is in normale toestand immers niet constant maar verandert continu onder invloed van het parasympathische (vertragend effect) en sympathische zenuwstelsel (versnellend effect). De analyse van hartritmevariabiliteit (HRV) is een niet-invasieve manier om de werking van het autonome zenuwstelsel te bestuderen. Sinds de beschrijving van de eerste klinische toepassing van HRV in 1965 [91], wordt HRV onderzocht in diverse klinische omstandigheden [10, 17, 152, 188, 16, 201, 96]. Uit verscheidene studies blijkt dat een verminderde HRV dikwijls gepaard gaat met pathologische condities van het hart of het autonoom zenuwstelsel [120].

Het meest elementaire hartritmesignaal is de reeks van intervallen tussen opeenvolgende hartslagen. Aangezien de hartslagen gedetecteerd worden op basis van de R-pieken in het ECG, dat de elektrische activiteit van het hart weergeeft, wordt dit signaal verder ook RR-interval reeks genoemd. Er bestaan verscheidene methodes om HRV te kwantificeren op basis van een hartritmesignaal. De

eenvoudigste maten voor HRV zijn tijdsdomein parameters zoals de variantie. Met frequentiedomein parameters, zoals de energie in een bepaald frequentiebereik, kunnen korte en lange-termijn HRV beter gescheiden worden. Een aantal tijds- en frequentiedomein parameters werden gestandaardiseerd in 1996. Daarnaast worden de laatste jaren ook een aantal nieuwere methodes, vaak met oorsprong in niet-lineaire systeem-theorie, toegepast voor de kwantificatie van HRV, zoals de Lyapunov exponent, de correlatie-dimensie en fractale analyse [71, 26, 169, 35, 233, 165]. Vooral deze laatste methode, die de kwantificatie van de zelfgelijkenis of de schaalinvariantie van tijdreeksen beoogt, is een veelbelovende methode gebleken in diverse studies [26, 233, 165, 97, 184, 118]. In deze studie zullen zowel de standaard HRV-parameters en enkele nieuwe methodes waaronder fractale analyse toegepast worden op de neonatale hartritmesignalen. Voor de nieuwere methodes wordt bovendien het effect van typische patronen in hartritmesignalen in detail onderzocht, om inzicht te krijgen in de performantie en interpretatie van deze methodes.

Hartritme bij pasgeborenen

Verschillende fysiologische factoren zoals ademhaling veroorzaken ritmische fluctuaties in het hartritme. De invloed van de ademhaling op het hartritme is gekend als "respiratoire sinus aritmie"(RSA): het hartritme stijgt bij het inademen en daalt bij het uitademen [205, 191, 161]. Omdat de ademhalingsfrequentie bij pasgeborenen (0.6-1.2 Hz) soms groter is dan de helft van het hartritme (2-2.6 Hz) wordt RSA niet altijd waargenomen bij pasgeborenen (Nyquist frequentie). Het hartritme wordt ook beïnvloed door andere effecten van de ademhaling, zoals apnees (adempauzes) en periodische ademhaling [41, 69]. In de meeste hartritmesignalen zijn ook fluctuaties met frequentie rond 0.1 Hz aanwezig. Hoewel de oorsprong hiervan nog niet juist gekend is, wordt deze dikwijls toegeschreven aan de baroreceptor reflex [161]. Fluctuaties met nog lagere frequenties worden veroorzaakt door onder andere thermoregulatie en fysische activiteit [102].

Het hartritme is ook afhankelijk van zowel de postmenstruele als de postnatale leeftijd. Het hartritme bij de geboorte neemt af met toenemende postmenstruele leeftijd, en ligt rond de 120 bpm bij normale, voldragen pasgeborenen [36]. Postnataal neemt het hartritme toe tijdens de eerste levensweken en neemt daarna stelselmatig af tot ongeveer 70 bpm bij volwassenen [144]. Het gemiddelde hartritme tijdens de onderzochte polysomnografieën is 150 bpm. De hartritmevariabiliteit bij de geboorte neemt toe met toenemende postmenstruele leeftijd [38, 192]. Postnataal neemt HRV af tijdens de eerste levensweken, en neemt achteraf toe [108]. Ook het slaapstadium waarin de baby zich bevindt, beïnvloedt het hartritme: tijdens rustige slaap (QS) is het hartritme lager en HRV geringer dan tijdens dan tijdens actieve slaap (AS) [161, 181].

Een ander typisch fenomeen dat voorkomt in hartritmesignalen zijn "spikes",

plotse en kortstondige veranderingen in hartritme (zie bijvoorbeeld Fig. 4.1(c)). Er zijn 2 soorten spikes: hartritmestoornissen die slechts een of twee hartslagen duren, ofwel korte hartritmevertragingen, die meestal 5 tot 20 hartslagen duren. Vermits het hartritmesignaal bepaald wordt op basis van de intervallen tussen opeenvolgende R-pieken in het ECG, leiden fouten bij de piekdetectie (gemiste of valse R-pieken) ook tot spikes in de RR interval reeks.

Standaard tijds- en frequentie-domein analyse van HRV

De volgende gestandaardiseerde tijdsdomein HRV parameters worden gebruikt [201]:

1. SDNN: de standaarddeviatie van de (normale) RR intervallen als maat voor globale HRV;
2. TI: de triangulaire index, gedefinieerd als het totaal aantal RR intervallen gedeeld door het maximum van het histogram, een maat voor globale HRV;
3. SDANN: de standaarddeviatie van de gemiddelde RR intervallen berekend op opeenvolgende periodes van 5 minuten, als maat voor HRV met periode langer dan 5 minuten;
4. RMSSD: de vierkantswortel van het gemiddelde van de gekwadrateerde verschillen tussen opeenvolgende RR intervallen, als maat voor korte termijn HRV.

Spectrale analyse van het hartritmesignaal is de basis voor de frequentiedomein HRV parameters. Deze zijn gedefinieerd -voor volwassenen- als de energie in de volgende frequentiegebieden: ULF (< 0.003 Hz), VLF (0.003 to 0.04 Hz), LF (0.04 to 0.15 Hz) en HF (0.15 to 0.4 Hz) [201]. Deze frequentiegebieden kunnen geassocieerd worden met verschillende fysiologische invloeden: HF bevat bijvoorbeeld de invloed van de ademhaling (RSA). Aangezien de ademhalingsfrequentie en het hartritme bij baby's veel hoger zijn dan bij volwassenen wordt in deze studie het HF frequentiegebied uitgebreid tot 0.15 - 1.5 Hz.

Alle hogervermelde HRV parameters berekend op basis van de gehele RR interval reeksen worden verder globale HRV parameters genoemd. Aangezien het slaapstadium een belangrijke invloed heeft op het hartritme, worden de HRV parameters ook berekend op afzonderlijke periodes van rustige en actieve slaap. De subscripts "QS1", "AS1", "QSX" en "ASX"duiden aan dat een bepaalde HRV parameter berekend is op respectievelijk de eerste QS periode, de eerste AS periode, alle QS periodes en alle AS periodes tijdens de polysomnografie. TI, SDANN en ULF worden alleen berekend op de gehele tijdreeksen omdat de afzonderlijke QS en AS-periodes te weinig RR intervallen bevatten voor een nauwkeurige schatting van deze parameters.

Een niet te verwaarlozen verschil tussen de hartritmesignalen in deze studie en de voorschriften van de Task Force heeft te maken met de bemonsteringsfrequentie van het ECG [201]. Aangezien de RR intervallen bepaald worden op basis van de R-pieken in het ECG, bepaalt de bemonsteringsfrequentie van het ECG de nauwkeurigheid van de RR interval reeks (zie Fig. 4.2). Aangezien de bemonsteringsfrequentie bij een polysomnografie normaal 100 Hz bedraagt, kunnen de RR intervallen slechts tot op 0.01 s bepaald worden. Dit veroorzaakt een vertekening (bias) van de HRV parameters (zie Fig. 4.3). De fout kan echter gemodelleerd worden als witte ruis gefilterd met eindige impulsrespons filter (met transfertfunctie $H(z) = 1 - z$). Op basis daarvan worden correcties afgeleid om de vertekening van de HRV parameters te compenseren. Aan de hand van ECG metingen met een bemonsteringsfrequentie van 1000 Hz, wordt aangetoond dat deze correcties nauwkeurige resultaten geven (zie Appendix C).

Fractale analyse van HRV

De laatste jaren zijn verscheidene publicaties verschenen over het fractale karakter van fysiologische signalen. Hiermee wordt de zelfgelijkenis of schaalinvariantie bedoeld, die wiskundig als volgt uitgedrukt wordt:

$$x(k) =_d c^H x(k/c), \forall c > 0 \tag{17}$$

waarin $0 < H < 1$ de zelfgelijkenis-parameter of Hurst-coëfficiënt voorstelt en $=_d$ de gelijkheid van distributie, aangezien het hier niet om exacte, maar statistische zelfgelijkenis gaat. Bijgevolg is elke statistische parameter m_k van een zelfgelijkende tijdreeks met lengte k evenredig met k^H:

$$m_k =_d p\, k^H \tag{18}$$

met p een constante. Het logaritme hiervan geeft:

$$log(m_k) =_d log(p) + H log(k) \tag{19}$$

Vermits de statistische parameters zoals de variantie afhankelijk zijn van de schaal, zijn zelfgelijkende signalen niet-stationair. De incrementen van zelfgelijkende tijdreeksen kunnen wel stationair zijn. Men spreekt dan van zogenaamde "H-sssi"processen. Voor elke waarde van H bestaat er juist n Gaussiaans H-sssi proces, aangeduid als fractionele Browniaanse beweging (fBm). De incrementen van fBm, fractionele Gaussiaanse ruis (fGn) genoemd, hebben lange-termijn correlaties als $H > 1/2$. Met lange-termijn correlaties wordt bedoeld dat de autocorrelatie zo langzaam afneemt met toenemende tijdsverschuiving, dat deze geen eindig som heeft (zie vgl. 4.5). Als $H = 1/2$ dan is de tijdreeks ongecorreleerd, m.a.w. witte Gaussiaanse ruis, en als $H < 1/2$ dan spreekt men van anti-correlaties. De spectrale dichtheid van fGn is evenredig is met $(1/f)^\beta$ in de omgeving van de oorsprong ($f \to 0$), met een spectrale index $-1 < \beta < 1$. Hoewel de spectrale dichtheid van fBm niet gedefinieerd

is (niet-stationair), kan het aangetoond worden dat het periodogram van fBm een gelijkaardige schaaleigenschap bezit, met $1 < \beta < 3$ (zie Fig. 4.4).

Fractale signalen kunnen dus beschreven worden door de zelfgelijkenis parameter H samen met de classificatie van het signaal als fGn of fBm, of door de spectrale index β of andere equivalente parameters. Er bestaan verschillende methodes om deze parameter te schatten van een gegeven tijdreeks. Detrended fluctuation analysis (DFA) bepaalt een zelfgelijkenis parameter, de schaalexponent, op basis van de schaaleigenschappen van de variantie, m.a.w. het verloop van de variantie in functie van de lengte van het beschouwde segment. Het DFA algoritme bestaat uit de volgende stappen:

1. Integreer de tijdreeks $x(k), k = 1, \ldots, N$: $y(k) \equiv \sum_{i=1}^{k} x(i), k = 1, \ldots, N$.
2. Verdeel $y(k)$ in niet-overlappende segmenten van lengte n.
3. Verwijder de (lineaire) trend van $y(k)$ in elk segment: $y_d(k)$.
4. Berekend de variantie $F(n)$ van de tijdreeks $y_d(k)$ voor de beschouwde segment-lengte (of schaal) n: $F(n) = \sqrt{\frac{1}{N} \sum_{i=k}^{N} (y_d(k))^2}$.
5. Herhaal de vorige stappen voor verschillende schalen n om de volledige fluctuatie functie $F(n)$ te berekenen.

Voor een zelfgelijkende tijdreeks is F(n) een machtsfunctie van n: $F(n) \propto n^{\alpha}$, zoals aangegeven in Fig. 8. De schaalexponent α kan geschat worden door lineaire regressie van $F(n)$ t.o.v. n in logaritmische coördinaten. De schaalexponent is equivalent met de Hurst-coëfficiënt (voor fGn $\alpha = H$, voor fBm $\alpha = H + 1$) en de spectrale index β ($\alpha = (\beta + 1)/2$).

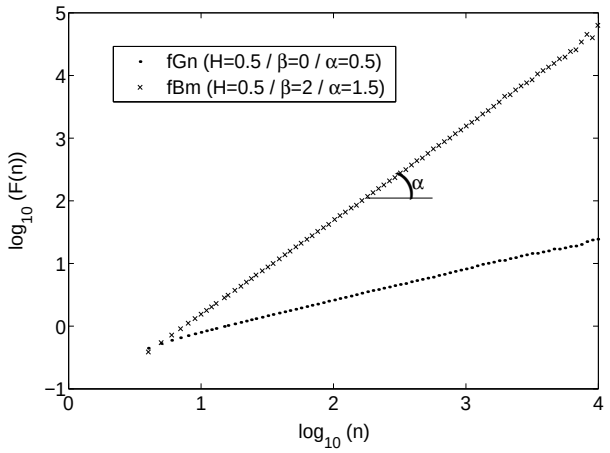

Figuur 8: Fluctuatie functie van fractionale Gaussiaanse ruis (fGn) en fractionale Browniaanse beweging (fBm) met $H = 0.5$

De toepassing van DFA op hartritmesignalen wordt in detail onderzocht. Met een methode op basis van zgn. surrogaat-data [168], tonen we aan dat de schaalexponent α niet constant is in de tijd. De grootste variaties zijn gerelateerd met verschillen in slaapstadium, zoals te zien is in Fig. 9.

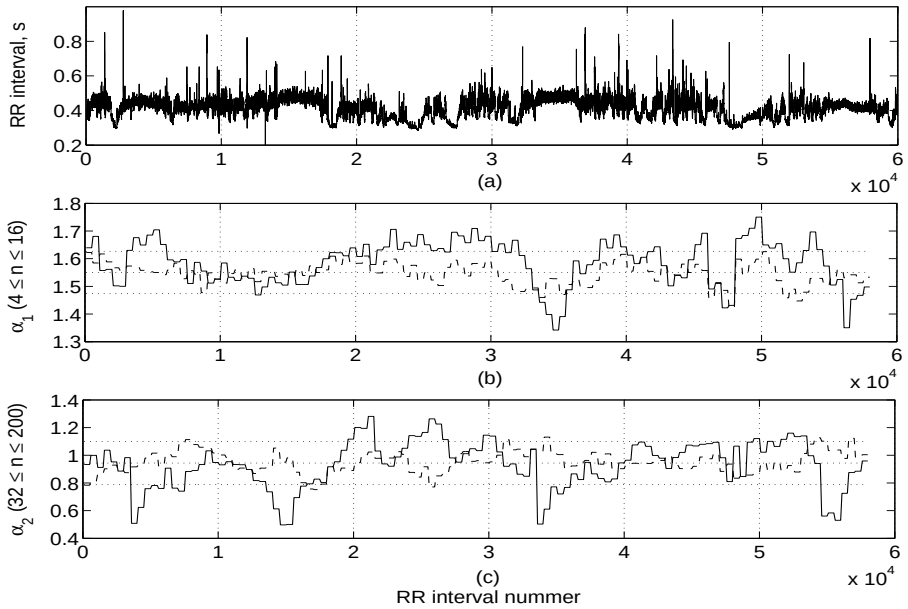

Figuur 9: (a) RR interval reeks en de schaalexponenten (b) α_1 ($4 \leq n \leq 16$) and (c) α_2 ($32 \leq n \leq 200$) berekend op segmenten van $N = 2000$ RR intervallen in functie van de tijd. De horizontale puntlijnen in (b) en (c) geven de gemiddelde schaalexponent van de surrogaat data, en het gemiddelde $\pm$ 2 $\times$ standaarddeviatie.

Het effect van spikes op de schaaleigenschappen van hartritmesignalen wordt geanalyseerd. Hartritmestoornissen veroorzaken een toename in F(n) voor de kleinste schalen, zoals weergegeven in Fig. 10(c), en bijgevolg een onderschatting van de schaalexponent op kleine schalen. Korte hartritmevertragingen veroorzaken een toename in F(n) op iets grotere schalen, overeenkomend met de duur van de hartritmevertraging, zoals weergegeven in Fig. 10(d). Aangezien zelfs een beperkt aantal spikes, de schaaleigenschappen op kleine schaal beïnvloeden, is het beter deze hartritmevertragingen te verwijderen (bvb. door interpolatie) alvorens de schaalexponent te schatten met DFA (zie ook Fig. 4.8).

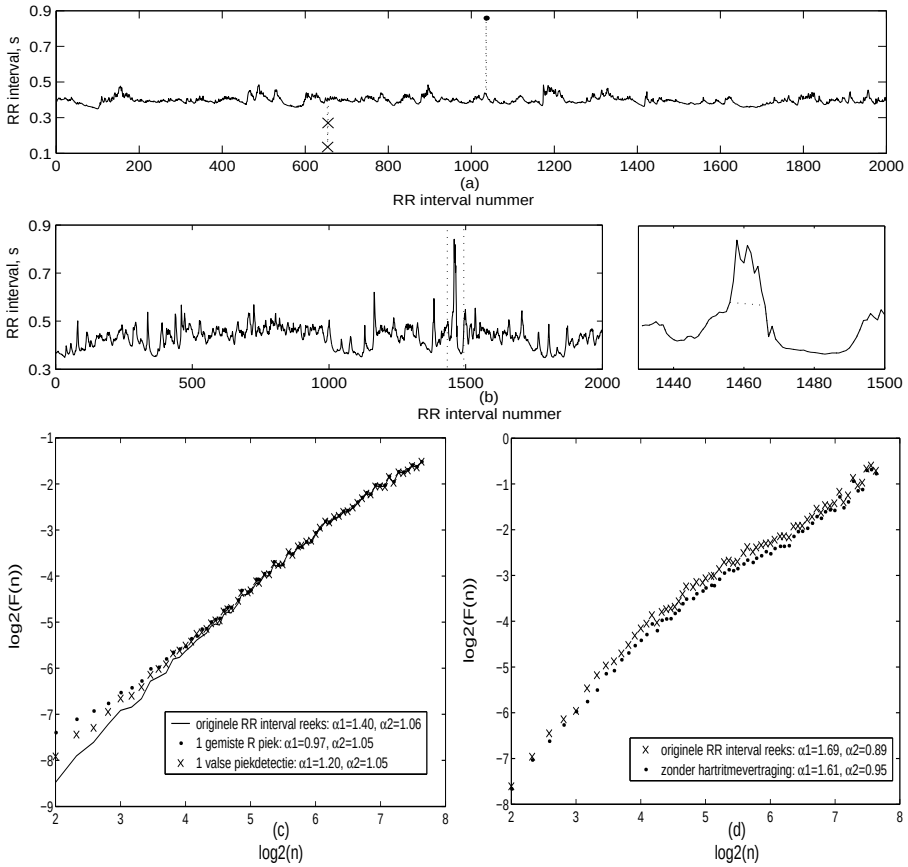

Figuur 10: (a) RR interval reeks bestaande uit $N = 2000$ RR intervallen met 1 foutief gedetecteerde piek (gemiste R piek of valse detectie), (b) Effect van 1 foutief gedetecteerde piek op de schaaleigenschappen, (c) RR interval reeks bestaande uit $N = 2000$ RR intervallen met 1 hartritmevertraging, (d) Effect van 1 hartritmevertraging op de schaaleigenschappen.

Ook het effect van periodische fluctuaties wordt onderzocht. Deze veroorzaken een knik in de fluctuatie functie F(n) bij de schaal overeenkomend met de periode van de fluctuaties (zie Fig. 4.10). De knik die in de fluctuatie functie van de meeste hartritmesignalen voorkomt, kan aldus gerelateerd worden aan fysiologische invloeden zoals bijvoorbeeld de Mayer waves in Fig. 11 (zie ook Fig. 4.11, Fig. 4.13 en Fig. 4.14). Aangezien dergelijke fluctuatie functies niet goed kunnen beschreven worden met een enkele schaalexponent, worden in dit geval meerdere (2 of 3) schaalexponenten geschat, elk over een verschillende bereik van schalen. Deze schaalexponenten komen echter niet overeen met de schaaleigenschappen van een eventuele fractale component in het signaal. Daarom wordt ook nog een globale schaalexponent geschat waarbij een zo groot mogelijk aantal schalen gebruikt worden.

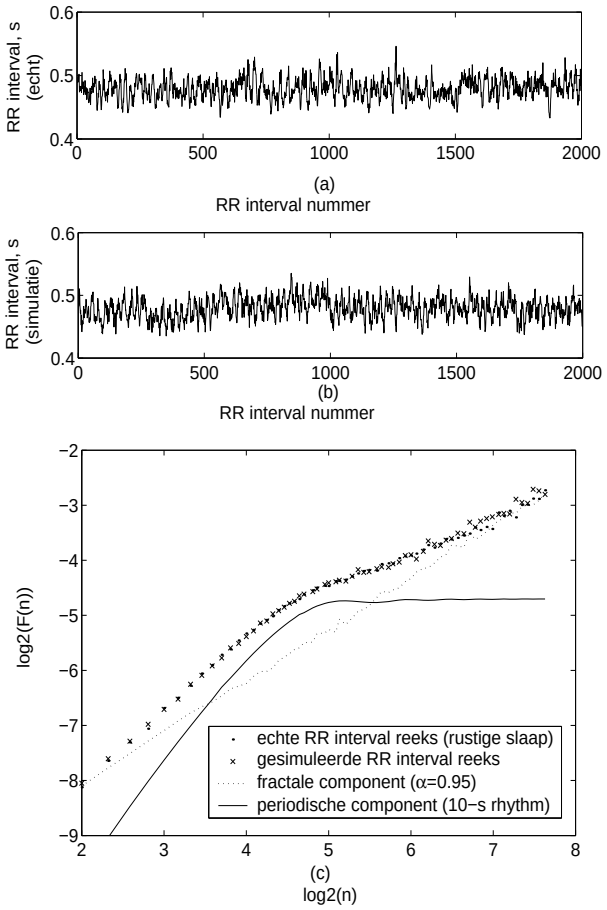

Figuur 11: (a) segment van 2000 RR intervallen tijdens rustige slaap, (b) gesimuleerde RR interval reeks tijdens rustige slaap, (c) schaaleigenschappen van de echte RR interval reeks, de gesimuleerde RR interval reeks, en de fractale en periodische component van het gesimuleerde signaal.

Tenslotte wordt ook voor DFA een correctie afgeleid om het effect van de lage bemonsteringsfrequentie op de fluctuatie functie te compenseren (zie Fig. 4.15). Er wordt aangetoond dat deze correctie zelfs voor de kleinste schalen, waar de afwijking het grootst is, zeer nauwkeurige resultaten geeft (zie appendix C). Analoog aan de standaard HRV parameters, worden de DFA parameters berekend op zowel de volledige RR interval reeksen als gedurende afzonderlijke slaapstadia.

Sample asymmetrie analyse

Zoals hoger vermeld komen in de meeste hartritmesignalen een aantal kleine hartritmevertragingen voor die niet als abnormaal beschouwd worden volgens de criteria voor de beoordeling van de polysomnografie. Aangezien deze hartritmevertragingen niettemin een klinische betekenis kunnen hebben, wordt tenslotte nog een HRV parameter voorgesteld om deze hartritmevertragingen te kwantificeren. Hiervoor wordt de zogenaamde "sample asymmetrie analyse"(SAA) gebruikt, een methode die de asymmetrie van het histogram van alle RR intervallen ten opzichte van een willekeurig referentiepunt, in ons geval de mediaan, kwantificeert zoals aangegeven in Fig. 12 [111]. SAA wordt toegepast op de volledige RR interval reeksen. Aangezien de histograms berekend worden op intervallen van 10 ms, stelt zich hier geen probleem met de lage bemonsteringsfrequentie van het ECG.

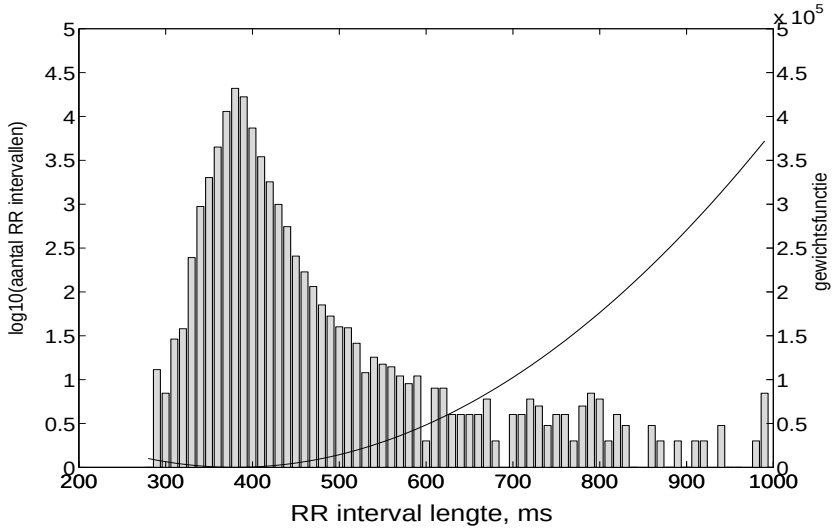

Figuur 12: Sample asymmetrie analyse van de RR interval reeks van prematuur AA5 (R=6.09).

Classificatie van AA, AN, NN pasgeborenen

Voor deze studie werden polysomnografieën van prematuren opgemeten in U.Z. Leuven tussen 2000 en 2003 gebruikt. De prematuren werden ingedeeld in 3 groepen naargelang de evaluatie van de polysomnografie en de thuismonitoring. Er waren 39 prematuren met een abnormale polysomnografie, waarvan er 15 ook abnormale cardiorespiratoire gebeurtenissen tijdens de thuismonitoring meemaakten. Enkele polysomnografieën met veel artefacten in het ECG

werden niet geanalyseerd. Aangezien de leeftijd een belangrijke factor is die mee het hartritme bepaalt, werden AA en AN groepen samengesteld uit premature met gelijkaardige leeftijd. De AA en AN groepen bevatten ieder 10 premature. Uit de NN groep werden ook 10 premature geselecteerd met vergelijkbare leeftijd. De gemiddelde conceptionele leeftijd op het tijdstip van de polysomnografie bedroeg 36.4 weken voor de NN groep, 36.3 weken voor de AN en 36.4 weken voor de AA. De gemiddelde postmenstruele leeftijd is 32.3 weken, 31.9 weken en 32.3 weken voor respectievelijk de NN, AN en AA groep (zie Tabel 4.1).

De RR intervallen werden bepaald door een automatisch piekdetectie algoritme. Elke RR interval reeks werd manueel gecontroleerd op foute detecties en gecorrigeerd waar nodig (op basis van het ECG). De gemiddelde duur van de polysomnografieën bedraagt 8 uur, hetgeen overeenkomt met ongeveer 75000 RR intervallen. Naast het ECG werden tijdens de polysomnografieën ook nog de ademhaling, de perifere zuurstofsaturatie (SaO_2), EMG, EEG en EOG opgemeten. Op basis van deze signalen werd het onderscheid gemaakt tussen rustige en actieve slaap. Alle rustige slaap-periodes van elke polysomnografie werden geanalyseerd. Voor elke rustige slaap-periode werd ook een periode van actieve slaap geselecteerd voor analyse.

Alle hoger vermelde HRV parameters werden eerst berekend op de volledige RR interval reeksen (zie Tabel 4.2). De groepen werden paarsgewijs vergeleken voor elke HRV parameter met behulp van de Wilcoxon rang-som test. Geen enkele globale standaard of DFA parameter is significant verschillend in de 3 groepen. SAA-R is groter voor AA dan voor AN en NN, maar enkel het verschil tussen AA en AN is significant. Er is een grote overlapping tussen de individuele SAA-R waarden van de 3 groepen (zie Fig. 4.18).

De HRV parameters werden ook bepaald voor alle rustige en actieve slaap-periodes per polysomnografie (zie Tabel 4.3). Er zijn geen significante verschillen in de standaard tijdsdomein HRV parameters. Tijdens actieve slaap is LF kleiner bij AA dan bij NN en AN hoewel enkel het verschil tussen AA en NN significant is. Tijdens rustige slaap is HFN groter bij AA dan bij NN ($p = 0.05$) en AN (n.s.), en (LF/HF) kleiner bij AA dan bij NN (n.s.) en AN ($p = 0.05$). Ook de schaalexponent α_1 is kleiner bij AA dan bij NN (n.s.) en AN ($p = 0.05$). Voor elke HRV parameter met significante verschillen tussen de groepen, is er steeds een grote overlapping tussen de individuele parameterwaarden van de 3 groepen (zie Fig. 4.19).

De HRV parameters werden ook bepaald voor de eerste QS en AS periode afzonderlijk (zie Tabel 4.4). De resultaten zijn vergelijkbaar met de gemiddelde waarden per slaapstadium. Tijdens de eerste QS periode is de schaalexponent α_2 groter bij AA dan bij AN en NN. Beide verschillen zijn significant, maar er is nog steeds een grote overlapping tussen de individuele waarden van elke groep.

Gezien het geringe aantal prematuren in elke groep, dienen de resultaten van de statistische testen met enige omzichtheid geïnterpreteerd worden. Het verschil in SAA-R suggereert dat AA prematuren meer kleine hartritmevertragingen hebben dan AN en NN prematuren. Tijdens rustige slaap, schijnt er bij AA prematuren ook een relatief grotere HF component te zijn dan in de AN en NN groep (lagere LFN, hoger HFN, lager LF/HF). De verschillen in schaalexponenten tijdens rustige slaap bij AA prematuren (lagere α_1, hogere α_2) kunnen eveneens verklaard worden door de relatief kleinere LF. Voor alle HRV parameters wordt er een grote variabiliteit binnen eenzelfde groep waargenomen. Daardoor is er een grote overlapping van de individuele parameterwaarden van de verschillende groepen, en kunnen de 3 groepen niet onderscheiden worden op basis van de besproken HRV parameters. Hoewel vergelijkingen bemoeilijkt worden door verschillen in methodologie en patiëntgegevens, komen de waarden van de HRV parameters uit deze studie vrij goed overeen met de literatuur. Ook de geobserveerde verschillen in de HRV parameters tussen actieve en rustige slaap bevestigen resultaten uit de literatuur.

Conclusies

De hartritmevariabiliteit van prematuren tijdens een polysomnografie werd geanalyseerd met de bedoeling om eventuele abnormale cardiorespiratoire gebeurtenissen te voorspellen. De standaard tijds- en frequentiedomein HRV parameters, DFA en SAA werden gebruikt om verschillende aspecten van de HRV te kwantificeren. Omwille van het geringe aantal prematuren is het moeilijk om statistische conclusies te trekken. Hoewel er schijnbaar wel kleine verschillen zijn in sommige HRV parameters, kunnen de 3 groepen niet onderscheiden worden door de grote overlapping van de individuele parameterwaarden.

Chapter 1

Introduction

In this chapter, the field of biomedical signal processing is briefly introduced, and a chapter by chapter overview of the thesis is presented.

1.1 Biomedical signal processing

In this thesis, three applications of biomedical signal processing are discussed. Any physical quantity that varies as a function of time, or any other independent variable, can be considered as a signal. Biomedical signals reflect physiological processes in living, biological systems. An archetype of a biomedical signal is the body temperature: a rise in temperature could indicate an infection. The physical quantities in biomedical signals can be of many different types, including magnetic, optical and electrical. Despite the wide variety of biomedical signals, most of them share some characteristics. These are often related to the limitations imposed on the measurement system to disturb the patient as little as possible. For example, as noninvasive measurements are preferable in view of patient safety, some parameters have to be inferred from indirect measurements, which are more likely to be contaminated with noise. In this context, not only instrumentation noise, but any physiological interference that is not relevant for the parameter under observation is considered as noise. For in-vivo measurements, it is not possible to isolate the system of interest, and therefore the signals produced by that system are also influenced by the many interactions among the physiological systems. For active measurements, which require external stimuli to be applied to the subject, there are severe energy limitations for the input stimuli, which again limits the signal to noise ratio.

All treatment of signals that occurs between the data acquisition and the interpretation by an observer is considered as signal processing. In general, the aim of biomedical signal processing is to enhance/extract the relevant information in/from the measured signals. Depending on the application, this could be one or more of the following:

- reduction of noise and artifacts, e.g. to reveal information from signals that is not apparent by eye;
- identification and separation of desired and unwanted components;
- accurate, objective quantification of clinical parameters, e.g. metabolite concentrations in magnetic resonance spectroscopy;
- detection of physiological events or states, e.g. for patient monitoring;
- data reduction to retain only the most clinically relevant data;
- classification, e.g. for diagnosis
- ...

Although the separation might be somewhat artificial, usually four steps can be discriminated in the processing of biomedical signals, which are shown in Fig. 1.1. Depending on the application and the aim of the signal processing, however, some steps could be omitted.

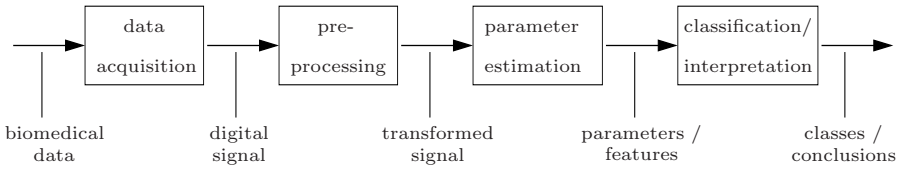

Figure 1.1: General biomedical signal processing scheme.

In our scheme, the *data acquisition* includes not only the data acquisition at the sensor level, but also eventual analog processing and the analog to digital conversion. In the *preprocessing* step, the digital signals are transformed to improve the parameter estimation or feature extraction in the next step. The *parameter estimation* consists of the extraction of clinically relevant features or parameters from the transformed signals. In the *classification / interpretation* step, these parameters are used for human or computer-aided decision making.

The work presented in this thesis, is focused mainly on the preprocessing and parameter estimation steps for specific biomedical applications. A wide variety of techniques is available from diverse application domains. Various filtering techniques -simple, optimal, adaptive- are available to reduce the noise and/or artifacts. Signal transformations such as the Fourier transform are also often used as preprocessing. In the case of multichannel data, techniques such as principal or independent component analysis can be used for data reduction.

These techniques are used in Chapters 3 and 4 as preprocessing. The parameter estimation is in many cases model-based, i.e. an appropriate model is assumed for the given data and the parameters describing the model are determined such that the model fits the given data as closely as possible. In some cases, however, parameters can also be calculated directly from the (transformed) signals. Both types of parameter estimation are used in this thesis.

Rather than starting with an overview of all techniques used in this work, a problem-based approach is followed. In each chapter, the techniques used to analyze the (biomedical) problem under consideration, are presented together with the rationale for using them and the underlying assumptions.

1.2 Chapter by chapter overview

In Chapter 2, the problem of estimating the parameters of exponentially damped sinusoidal signals in the presence of noise is considered. This model is used in magnetic resonance spectroscopy (MRS) to quantify metabolite concentrations. The focus is on subspace-based methods used to estimate the model parameters. Our contribution consists in showing how, in the case of oversampled signals, data decimation can be employed to reduce the computational complexity of subspace-based algorithms while retaining the same statistical accuracy. Three variants of the HTLS algorithm (Hankel total least squares) using data decimation are derived. Monte Carlo simulations on reference signals and simulated MRS signals are performed to analyze the statistical accuracy and robustness of each method. These results are published in the papers [137] and [136]. It should be noted that, when using real data, additional preprocessing steps are necessary prior to the parameter estimation to deal with deviations from the analytical model function (due to eddy currents, magnetic field inhomogeneities, etc.) and for the removal of unwanted components (e.g. residual water). After the preprocessing, the noise levels usually encountered in real data are still higher than those used in our simulations. Therefore, in practice, optimization based parameter estimation algorithms are used that are more robust and accurate than HTLS due to the imposition of additional biochemical prior knowledge. The MRS signals, however, are well suited for our purpose, i.e. evaluating the performance of the HTLS-versions using data decimation for the estimation of multiple, closely spaced peaks in the presence of noise. Moreover, as the same model is encountered in many other applications, the use of the presented technique is not restricted to MRS.

Chapter 3 deals with two applications of near-infrared spectroscopy (NIRS), an optical technique that can be used to analyze human tissue non-invasively due to the relatively good transparency of biological tissue in the near-infrared range. The first application is the monitoring of cerebral circulation and oxy-

genation in neonates. As oxygenated and deoxygenated hemoglobin are the most important light absorbing compounds in tissue, the concentration changes of these compounds can be determined from the changes in light attenuation. Under certain conditions, other parameters such as cerebral blood flow (CBF) and cerebral blood volume (CBV) can be estimated from these concentration changes as well. We contributed to clinical studies exploring the value of NIRS for the monitoring of cerebral oxygenation in preterm neonates. The results hereof are published in [149],[147], [150] and [148]. In another study, the use of NIRS for the assessment of cerebral autoregulation in neonates is investigated. This is done by quantifying the concordance between changes in mean arterial blood pressure (MAP) and HbD, a measure of CBF derived from NIRS data. In this context, a new method to quantify the concordance between two signals was proposed and compared to correlation and coherence analysis. The results of this study are published in [138] and [139]. Note that, in this application, the parameters are extracted from the relation between two signals. The second application of NIRS, functional monitoring of brain activity, also involves multichannel signal processing. Functional NIRS relies on the changes of the optical properties of the brain tissue related to functional activation. Two types of changes can be observed: the fast signal presumably caused by light scattering, which is directly related to neuronal activity, and the slow signal due to light absorption, related to hemodynamic changes in the activated area. The problem is that the fast signal is much smaller than the slow signal, and is actually buried in the noise. Note that the hemodynamic signal, which is the signal of interest in the neonatal application of NIRS, is considered as noise in this study. By applying appropriate signal processing techniques, we are able to detect the fast signal in the motor cortex during a finger tapping exercise. Adaptive filtering is used to reduce the noise in each channel individually. Independent component analysis is applied to the filtered signals to separate the fast signal due to the neuronal activity. These results are published in [141] and [142].

In Chapter 4, the analysis of neonatal heart rate variability is treated. The main goal of this study is to investigate if abnormal cardiorespiratory events can be predicted from the heart rate recorded during a polysomnography. Heart rate variability, which consists of the analysis of the fluctuations in heart rate, is considered as a non-invasive marker of autonomic activity. The properties and determinants of neonatal HR and HRV are discussed, and the differences in comparison with adults are pointed out. The determination of the heart rate signals from the ECG recordings, using filtering and peak detection, is the first step of the preprocessing. From the resulting heart rate signal, several parameters are determined to quantify different aspects or features of HRV. For some of these HRV parameters, the heart rate signal was transformed prior to the parameter estimation. Both commonly used, standard HRV parameters as well as recently introduced methods are used. As the standard HRV parameters were defined for adults, the methodology is adapted to account for

the differences between neonatal and adult heart rate. Besides the standard HRV parameters, two recently introduced signal analysis methods are applied to neonatal heart rate data. Detrended fluctuation analysis (DFA), a method which characterizes the scaling behaviour of a time series with one or more scaling exponents, is analyzed and its relation with spectral analysis is established. The methodology of applying DFA to neonatal RR interval series is investigated, specifically with respect to the time constancy of the scaling exponents and the effect of typical spikes (ectopic beats, HR decelerations) and periodical fluctuations on the scaling behaviour. The application of DFA to neonatal heart rate data and the sensitivity to the above mentioned patterns are described in the papers [135] and [134]. In order to quantify the number and amplitude of the HR decelerations, sample asymmetry analysis (SAA) is used. SAA is a measure based on the asymmetry of the histogram of the RR intervals around the median RR interval. Another aspect that needs consideration is the relatively low sampling rate of the ECG recordings during normal polysomnographies. As the beat-to-beat heart rate is determined from the R-peaks in the ECG, the accuracy of the heart rate is limited by the sampling frequency of the ECG. The effect of the ECG sampling rate on the HRV parameters is analyzed. Based on the statistical properties of the errors in the RR intervals, correction factors are introduced to compensate for the bias introduced by the low ECG sampling rate. A set of ECGs are recorded at a higher sampling rate, to verify the accuracy of the proposed corrections. All HRV parameters above are applied to RR interval series derived from the ECG of preterm neonates, recorded during polysomnographies at the University Hospitals Gasthuisberg. According to the evaluation of the polysomnography (PS) and the eventual home monitoring (follow-up - FU), the infants are divided into three groups: NN (normal PS, normal FU), AN (abnormal PS, normal FU) and AA (abnormal PS, abnormal FU). It is investigated whether these three groups can be distinguished using the proposed HRV parameters. The statistical significance of the differences between the three groups is determined. Although the statistical tests should be interpreted with some caution due to the small number of subjects, it is suggested that there are differrences in some HRV parameters between the three groups. Owing to the large variability of the HRV parameters within each group, however, there is a large overlap between the individual parameter values of each group, making the classification of the preterm infants based on the HRV parameters impossible.

Chapter 2

Subspace-based parameter estimation methods using data decimation

The problem of estimating the parameters of exponentially damped sinusoidal signals in the presence of noise is considered. More specifically, the effect of data decimation on the statistical accuracy and computational complexity of subspace-based parameter estimation methods is investigated. The exponentially damped sinusoidal model appears in many applications such as radar, system identification, speech processing and magnetic resonance spectroscopy (MRS). Since our interest in the problem originated from the latter application, the work presented here is mainly based on Monte-Carlo simulation experiments inspired by MRS. The presented techniques are, however, not restricted to MRS but can be applied in other domains as well.

2.1 Introduction

In various applications of digital signal processing, including MRS, exponentially damped sinusoids are used as a model function [213]. The signal $x(k)$ is represented as a sum of K exponentially damped sinusoids, contaminated by additive white noise $n(k)$:

$$x(k) = \sum_{i=1}^{K} c_i z_i^k + n(k), \qquad k = 0, 1, \ldots, N-1 \tag{2.1}$$

with complex amplitudes $c_i,\ i = 1, \ldots, K$

$$c_i = a_i e^{j(\phi_i)} \tag{2.2}$$

and signal poles $z_i,\ i = 1, \ldots, K$

$$z_i = e^{(j2\pi f_i - d_i)/f_s} \tag{2.3}$$

where a_i represents the amplitude, ϕ_i the phase, f_i the frequency and d_i the damping factor of component i, and f_s is the sampling frequency. In MRS signals, a_i is related to the concentration of the component and f_i characterizes it, while d_i provides information about its mobility and molecular environment. The problem consists in estimating the amplitudes a_i, phases ϕ_i, frequencies f_i and damping factors d_i given a set of N data points $x(k), k = 0, 1, \ldots, N-1$. Since the number of components present in the compound under analysis is usually known a priori in MRS, we assume that the number of sinusoids K, also referred to as the model order, is given. If this is not the case, the model order can be determined using several methods such as Akaike's information criterion or Rissanen's minimum description length [5, 178]. If the poles z_i are known, the estimation of complex amplitudes c_i reduces to a linear least squares problem. We will address the estimation of the poles z_i, also referred to as harmonic retrieval.

Various techniques have been applied to the harmonic retrieval problem, including maximum likelihood methods [197], linear prediction methods [112], subspace-based methods [24] and higher-order statistics [157]. The focus of our work is on the subspace-based methods, which have their origin in Pisarenko's method for harmonic retrieval [170] and rely on the eigenvalue decomposition (EVD) of the sample covariance matrix into a signal subspace and a noise subspace. A widely used subspace-based algorithm is ESPRIT [183], which exploits an underlying rotational invariance of signal subspaces spanned by two temporally displaced data sequences. Two versions of the ESPRIT-algorithm appeared in the literature, relying on either the least-squares (LS) [183] or the total least squares (TLS) [182] technique. The data matrix equivalent of ESPRIT-TLS, which is based on the singular value decomposition of the data matrix rather than on the eigenvalue decomposition of the sample covariance matrix, is known as HTLS (Hankel TLS) in the MRS-literature [211]. Several closely related algorithms such as the matrix pencil method (MATPEN) have been proposed [94].

It is known that subspace-based parameter estimation techniques perform poorly when applied to closely spaced sinusoids [198]. Therefore, in recent publications different approaches based on data decimation were proposed in order to increase the performance of these subspace-based methods [196, 82]. The idea was to artificially increase the frequency separation by downsampling (decimating) the signal by a factor D, while making sure that no aliasing is introduced.

The method proposed in [196] calculates the average of the sample covariance matrices of the decimated sequences, which is then used to estimate the decimated signal poles by means of the ESPRIT-TLS algorithm. The method presented in [82] is essentially identical since it uses the same covariance matrix, but calculated in a slightly different way. Another recently proposed method, called DESE (DEcimative Spectral Estimation), also makes use of the full data set, while it imposes almost no constraints on the size of the data matrix with respect to the decimation factor D [65]. Since DESE uses the original (not decimated) data matrix as input, it is not a "decimative" approach in the true sense of the word. On the other hand, the algorithm yields estimates of the decimated signal poles, and therefore it was included in this study. The non-decimative version of DESE (*D=1*) is identical to the matrix pencil method [94].

In this chapter, three decimative versions of the HTLS method [211] are derived. The first version, HTLSDstack, is the "data matrix" counterpart of the decimative ESPRIT-TLS algorithm presented in [196] and [82]. The second version, HTLSDsum, is a variant of the first one. The third version, HTLSDdese, was derived by applying the approach used in DESE [65] to the HTLS method. Comparing different decimative versions of one and the same basic subspace-based algorithm (i.e. HTLS), allows us to focus on the differences between the decimative approaches, without the need to take into account the differences between the subspace-based estimation methods themselves (ESPRIT, MATPEN, HTLS, ...). Similar conclusions hold for the decimative approaches applied to the other subspace-based estimators.

The basic HTLS algorithm is presented in the section 2.2, and the decimative versions are derived in section 2.3. The computational complexity of the three decimative versions is compared in section 2.4. In section 2.5, the statistical accuracy of the different methods is compared using numerical experiments.

2.2 HTLS

Consider the following Hankel data matrix with m rows constructed from the data sequence $x(k),\ k = 0, \ldots, N-1$:

$$\mathbf{X} = \begin{bmatrix} x(0) & x(1) & \ldots & x(N-m) \\ x(1) & x(2) & \ldots & x(N-m+1) \\ \vdots & \vdots & \ddots & \vdots \\ x(m-1) & x(m) & \ldots & x(N-1) \end{bmatrix} \tag{2.4}$$

Assuming noiseless data, the model of Eq. (2.1) reduces to

$$x(k) = \sum_{i=1}^{K} c_i z_i^k, \qquad k = 0, 1, \ldots, N-1 \tag{2.5}$$

and it can easily be seen that the data matrix $\mathbf{X}$ can be written in terms of Vandermonde matrices:

$$\begin{aligned} \mathbf{X} &= \begin{bmatrix} 1 & 1 & \ldots & 1 \\ z_1 & z_2 & \ldots & z_K \\ \vdots & \vdots & \ddots & \vdots \\ {z_1}^{m-1} & {z_2}^{m-1} & \ldots & {z_K}^{m-1} \end{bmatrix} \times \begin{bmatrix} c_1 & 0 & \ldots & 0 \\ 0 & c_2 & \ldots & 0 \\ \vdots & \vdots & \ddots & \vdots \\ 0 & 0 & \ldots & c_K \end{bmatrix} \\ &\quad \times \begin{bmatrix} 1 & z_1 & \ldots & {z_1}^{N-m} \\ 1 & z_2 & \ldots & {z_2}^{N-m} \\ \vdots & \vdots & \ddots & \vdots \\ 1 & z_K & \ldots & {z_K}^{N-m} \end{bmatrix} \\ &\equiv \mathbf{S}\mathbf{C}\mathbf{T}^T \end{aligned} \tag{2.6}$$

From this Vandermonde decomposition, the signal poles z_i and complex amplitudes c_i can immediately be derived. However, to our knowledge no algorithms exist that compute the Vandermonde decomposition directly. Therefore, the parameters have to be determined indirectly. From Eq. (2.6) it is clear that $\mathbf{S}$ exhibits the shift-invariance property:

$$\mathbf{S}^1 = \mathbf{S}_1 \mathbf{Z} \tag{2.7}$$

where $\mathbf{S^1}$, $\mathbf{S_1}$ stands for the matrix $\mathbf{S}$ with its top, respectively bottom row deleted, and $\mathbf{Z}$ is a $(K \times K)$ diagonal matrix composed of the K signal poles $z_i,\ i = 1, \ldots, K$.

Since $\mathbf{X}$ has exactly rank K, the singular value decomposition (SVD) of $\mathbf{X}$ has the following form:

$$\mathbf{X} = \mathbf{U}_K \mathbf{\Sigma}_K \mathbf{V}_K^H \tag{2.8}$$

with $\mathbf{U}_K \in \mathbb{C}^{m \times K}$, $\mathbf{\Sigma}_K \in \mathbb{C}^{K \times K}$ and $\mathbf{V}_K \in \mathbb{C}^{(N-m+1) \times K}$. It can be inferred that $\mathbf{S}$ spans the same column space as $\mathbf{U}_K$, and hence they are equal up to a multiplication by a non-singular matrix $\mathbf{Q} \in \mathbb{C}^{K \times K}$, i.e.:

$$\mathbf{U}_K = \mathbf{S}\mathbf{Q} \tag{2.9}$$

Using Eq. (2.9), the shift-invariance property of Eq. (2.7) translates to:

$$\mathbf{U}_K^1 = \mathbf{U}_{K1}\mathbf{Q}^{-1}\mathbf{Z}\mathbf{Q} \equiv \mathbf{U}_{K1}\mathbf{Z}_Q \tag{2.10}$$

where $\mathbf{U}_K^1$, $\mathbf{U}_{K1}$ stands for the matrix $\mathbf{U}_K$ with its top, respectively bottom row deleted.

Hence, by truncating the SVD of $\mathbf{X}$ and setting up Eq. (2.10), $\mathbf{Z}_Q \equiv \mathbf{Q}^{-1}\mathbf{Z}\mathbf{Q}$ can be calculated. Since the eigenvalues of $(\mathbf{Q}^{-1}\mathbf{Z}\mathbf{Q})$ and $\mathbf{Z}$ are equal, the signal poles can be determined. From these signal poles z_i, the frequencies f_i and damping factors d_i are easily calculated. Given the signal poles z_i, the complex amplitudes c_i are obtained as the LS solution to Eq. (2.5). From the complex amplitudes c_i, the phases ϕ_i and amplitudes a_i are easily derived.

For noisy data, $\mathbf{X}$ has not rank K, and there is no exact solution $(\mathbf{Z}_Q)$ of the shift-invariance property in $\mathbf{U}_K$ anymore. However, $\mathbf{X}$ can be approximated by its truncated SVD

$$\mathbf{X} = \mathbf{U}\mathbf{\Sigma}\mathbf{V}^H \approx \mathbf{U}_K\mathbf{\Sigma}_K\mathbf{V}_K^H = \mathbf{X}_K, \tag{2.11}$$

where $\mathbf{U}_K$, $\mathbf{V}_K$ are the first K columns of $\mathbf{U}$, respectively $\mathbf{V}$ and $\mathbf{\Sigma}_K$ is the leading $K \times K$ submatrix of $\mathbf{\Sigma}$. $\mathbf{X}_K$ has rank K, but does not have the Hankel structure anymore. Therefore, there is no exact solution $\mathbf{Z}_Q$ of the shift-invariance property in $\mathbf{U_K}$, and the set of equations

$$\mathbf{U}_K^1 \approx \mathbf{U}_{K1}\mathbf{Z}_Q \tag{2.12}$$

is solved in a total least squares (TLS) sense to estimate $\mathbf{Z}_Q$ [212]. The TLS solution is given by

$$\hat{\mathbf{Z}}_Q = -\hat{\mathbf{V}}_{12}\hat{\mathbf{V}}_{22}^{-1} \tag{2.13}$$

in which $\hat{\mathbf{V}}_{12}$ and $\hat{\mathbf{V}}_{22}$ are obtained from the SVD of the augmented data matrix:

$$\begin{bmatrix} \mathbf{U}_K^1 & \mathbf{U}_{K1} \end{bmatrix} = \hat{\mathbf{U}}\hat{\mathbf{\Sigma}}\hat{\mathbf{V}}^H \tag{2.14}$$

with

$$\hat{\mathbf{V}} = \begin{bmatrix} \hat{\mathbf{V}}_{11} & \hat{\mathbf{V}}_{12} \\ \hat{\mathbf{V}}_{21} & \hat{\mathbf{V}}_{22} \end{bmatrix} \tag{2.15}$$

Alternatively, Eq. (2.12) could be solved in a LS sense. The corresponding algorithm is known as HSVD. The eigenvalues of the matrix $\hat{\mathbf{Z}}_Q$ are the estimates $\hat{z}_i$ of the signal poles z_i, which in turn yield the desired estimates $\hat{f}_i$ and $\hat{d}_i$ of the frequencies f_i and damping factors d_i. Estimates $\hat{a}_i$ and $\hat{\phi}_i$ of the amplitudes a_i and phases ϕ_i are determined by filling in the obtained poles into Eq. (2.5) and solving the resulting equations in a LS sense.

The original description of the ESPRIT(-LS) algorithm [183] is essentially the same as the HSVD algorithm, the only difference being that the EVD of the sample covariance matrix $\mathbf{R} = \frac{1}{N}\mathbf{X}\mathbf{X}^H$ is used instead of the SVD of the data matrix $\mathbf{X}$. Similarly, HTLS is the data matrix counterpart of the ESPRIT-TLS algorithm [182]. The SVD approach avoids squaring the data and is therefore preferable from a numerical point of view.

The HTLS algorithm can be summarized as follows:

Step 1: Arrange the data points $x(k),\ k = 0, \ldots, N-1$ in a Hankel matrix $\mathbf{X}$ of dimensions $m \times (N-m+1)$ with $m \geq K$ and $N-m > K$ as in Eq. (2.4).

Step 2: Compute the SVD of $\mathbf{X}$ and truncate $\mathbf{X}$ to rank K: $\mathbf{X} = \mathbf{U}\mathbf{\Sigma}\mathbf{V}^H \approx \mathbf{U}_K\mathbf{\Sigma}_K\mathbf{V}_K^H = \mathbf{X}_K$, where $\mathbf{U}_K$ and $\mathbf{V}_K$ are respectively the first K columns of $\mathbf{U}$ and $\mathbf{V}$, $\mathbf{\Sigma}_K$ is the leading $(K \times K)$ submatrix of $\mathbf{\Sigma}$ and $\mathbf{V}^H$, respectively $\mathbf{V}_K^H$ represents the hermitian conjugate of $\mathbf{V}$, respectively $\mathbf{V}_K$.

Step 3: Impose the shift-invariance property and solve the following overdetermined set of equations in a TLS sense:

$$\mathbf{U}_K^1 \approx \mathbf{U}_{K1}\mathbf{Z}_Q. \tag{2.16}$$

The eigenvalues of $\mathbf{Z}_Q$ are the estimates $\hat{z}_i, i = 1, \ldots, K$ of the signal poles z_i, from which the estimates $\hat{f}_i$ and $\hat{d}_i$ of the frequencies f_i and damping factors d_i are easily obtained.

Step 4: Fill in the signal pole estimates $\hat{z}_i$ into the model function of Eq. (2.5) and solve the obtained system of N equations in a LS sense to determine the estimates $\hat{c}_i, i = 1, \ldots, K$ of the complex amplitudes. From these, the estimates $\hat{\phi}_i$ and $\hat{a}_i$ of the phases ϕ_i and amplitudes a_i are easily derived.

2.3 Decimative HTLS

Data decimation can be applied to the HTLS algorithm in two different ways. The first approach consists in applying HTLS to a data matrix, constructed from several decimated sequences. In the second approach, the original (not decimated) data matrix is used to estimate the decimated signal poles by exploiting the shift-invariance property between its D order lower shift (top D rows deleted) and D order upper shift (bottom D rows deleted) equivalents. The latter approach is not decimation in the true sense of the word since it does not use decimated sequences. However, since both approaches give estimates of the decimated signal poles, both approaches are referred to as "decimative" in this paper. In both cases, after the estimation of the signal poles, the phases and amplitudes are calculated as the least squares solution to Eq. (2.5), with z_k replaced by the estimates $\hat{z}_k$. Since the first approach gives rise to two different versions of the HTLS algorithm, as shown below, we end up with 3 decimative versions of HTLS.

2.3.1 Decimated data matrices

From the original data sequence $\mathbf{x} = [x(0), x(1), \ldots, x(N-1)]$, D different decimated sequences are formed:

$$\begin{aligned} \mathbf{x}_d &= [x(d), x(D+d), \ldots, x((N/D-1)D+d)] && (2.17) \\ &\equiv [x_d(0), x_d(1), \ldots, x_d(N/D-1)] \quad d = 0, 1, \ldots, D-1 && (2.18) \end{aligned}$$

with D the decimation factor, chosen such that $|f_i| < f_{sample}/(2D)$, $i = 1, 2, \ldots, K$ in order to avoid aliasing. Using the model of Eq. (2.5) this can be written as:

$$\begin{aligned} x_d(k) &= \sum_{i=1}^{K} c_i z_i^{(Dk+d)} + n(Dk+d) && (2.19) \\ &= \sum_{i=1}^{K} (c_{id})(z_i')^k + n(Dk+d), \qquad k = 0, 1, \ldots, N/D-1 && (2.20) \end{aligned}$$

with $z_i' \equiv z_i^D$, i=1,...,K and $c_{id} \equiv c_i z_i^d$, i=1,...,K, d=0,...,D−1.

Hence, the Vandermonde decomposition of a Hankel data matrix $\mathbf{X}_d$ constructed from a noiseless decimated sequence $\mathbf{x_i}$ can be written as:

$$\begin{aligned} \mathbf{X}_d &= \begin{bmatrix} x_d(0) & x_d(1) & \ldots & x_d(N/D-m) \\ x_d(1) & x_d(2) & \ldots & x_d(N/D-m+1) \\ \vdots & \vdots & \ddots & \vdots \\ x_d(m-1) & x_d(m) & \ldots & x_d(N/D-1) \end{bmatrix} \\ &= \begin{bmatrix} 1 & 1 & \ldots & 1 \\ z_1' & z_2' & \ldots & z_K' \\ \vdots & \vdots & \ddots & \vdots \\ {z_1'}^{m-1} & {z_2'}^{m-1} & \ldots & {z_K'}^{m-1} \end{bmatrix} \times \begin{bmatrix} c_{1d} & 0 & \ldots & 0 \\ 0 & c_{2d} & \ldots & 0 \\ \vdots & \vdots & \ddots & \vdots \\ 0 & 0 & \ldots & c_{Kd} \end{bmatrix} \\ &\quad \times \begin{bmatrix} 1 & z_1' & \ldots & {z_1'}^{N/D-m} \\ 1 & z_2' & \ldots & {z_2'}^{N/D-m} \\ \vdots & \vdots & \ddots & \vdots \\ 1 & z_K' & \ldots & {z_K'}^{N/D-m} \end{bmatrix} && (2.21) \\ &\equiv \mathbf{S}\mathbf{C}_d\mathbf{T}^T && (2.22) \end{aligned}$$

Note the similarity between Eq. (2.6) and Eq. (2.21). This shows that HTLS applied to the matrix $\mathbf{X}_d$, containing noisy data points x_i, yields the estimates $\hat{z}_i'$ of the decimated signal poles z_i'. The signal poles z_k can be estimated by taking the Dth-root of $\hat{z}_i'$.

The matrix $\mathbf{X}_d$, however, only contains a fraction of the available data points, i.e. N/D of the N data points. It is clear that the use of all data points will

yield better results from a statistical point of view. In order to make use of all decimated sequences, two different extensions of HTLS are described below.

HTLSDstack

To explain the first method, it is assumed again that the decimated time series $\mathbf{x}_d,\ d = 0, 1, \ldots, D-1$ are noiseless. Equation (2.21) shows that the matrices $\mathbf{X}_d,\ d = 0, 1, \ldots, D-1$ have the same column space and thus share the same shift-invariance property. As a consequence, the matrix $\mathbf{X}_{stack}$ can be decomposed as follows:

$$\begin{aligned} \mathbf{X}_{stack} &\equiv \left[\begin{array}{cccc} \mathbf{X}_0 & \mathbf{X}_1 & \ldots & \mathbf{X}_{D-1} \end{array}\right] && (2.23) \\ &= \mathbf{S}\left[\begin{array}{cccc} \mathbf{C}_0\mathbf{T}^T & \mathbf{C}_1\mathbf{T}^T & \ldots & \mathbf{C}_{D-1}\mathbf{T}^T \end{array}\right] && (2.24) \end{aligned}$$

Therefore, still in the noiseless case, not only the column space of $\mathbf{X}_d,\ d = 0, 1, \ldots, D-1$, but also that of $\mathbf{X}_{stack}$ share the same shift-invariance property. Applying HTLS to $\mathbf{X}_{stack}$ or any matrix $\mathbf{X}_d$ will therefore yield the same set of (decimated) signal poles. If the time series $\mathbf{x}_d,\ d = 0, 1, \ldots, D-1$ are noisy, it is better from a statistical point of view to include all available data points. Hence, HTLS applied to $\mathbf{X}_{stack}$ will yield more accurate estimates of the (decimated) signal poles. In the remainder of this paper, this method is referred to as HTLSDstack.

Some interesting observations can be made with respect to HTLSDstack. First of all, HTLSDstack can be seen as a special case of the multichannel HTLS method [214], where the different channels correspond to the decimated time series. Furthermore, it should be noted that HTLSDstack is the "data matrix" counterpart of the decimative ESPRIT-TLS algorithm that acts on the corresponding averaged sample covariance matrix $\mathbf{R}$. This can be derived from the observation that the averaged sample covariance matrix $\mathbf{R}$ used in [196], can be written as follows:

$$\begin{aligned} \mathbf{R} = \frac{1}{D}\sum_{d=0}^{D-1}\mathbf{R}_d &= \frac{1}{D}\left[\begin{array}{cccc} \mathbf{X_0} & \mathbf{X}_1 & \ldots & \mathbf{X}_{D-1} \end{array}\right]\left[\begin{array}{c} \mathbf{X}_0^H \\ \mathbf{X}_1^H \\ \vdots \\ \mathbf{X}_{D-1}^H \end{array}\right] && (2.25) \\ &= \frac{1}{D}\mathbf{X}_{stack}\mathbf{X}_{stack}^H && (2.26) \end{aligned}$$

where $\mathbf{R}_d = \mathbf{X}_d\mathbf{X}_d^H,\ d = 0, 1, \ldots, D-1$ represents the sample covariance matrix of the decimated sequence $\mathbf{x}_d$. HTLS can also be applied to matrices in which the data is arranged differently. In [82], for example, the covariance matrix is calculated from a data matrix that is equal to $\mathbf{X}_{stack}$ up to a permutation of the columns. Since the obtained covariance matrix is identical to $\mathbf{R}$, the methods proposed in [196] and [82] are essentially equivalent. More general, all matrices with the same column space yield identical results.

HTLSDsum

To explain the second method we start again from the noiseless case. From Eq. (2.21) it is clear that:

$$\begin{aligned} \mathbf{X}_{sum} &\equiv \mathbf{X}_0 + \mathbf{X}_1 + \ldots + \mathbf{X}_{D-1} && (2.27) \\ &= \mathbf{S}\left[\ \mathbf{C}_0\mathbf{T}^T + \mathbf{C}_1\mathbf{T}^T + \ldots + \mathbf{C}_{D-1}\mathbf{T}^T\ \right] && (2.28) \end{aligned}$$

As a consequence, $\mathbf{X}_{sum}$ and the matrices $\mathbf{X}_d,\ d = 0, 1, \ldots, D-1$ share the same invariant structure. If the matrices $\mathbf{X}_d$ and hence $\mathbf{X}_{sum}$ contain noisy measurements, HTLS can be applied to $\mathbf{X}_{sum}$ to obtain estimates of the decimated signal poles and complex amplitudes. Note that this scheme comes down to applying HTLS to the sequence obtained by summing every D consecutive points of the original sequence.

2.3.2 D order shift

Another recently proposed method, called DESE ("DEcimative Spectral Estimation"), also yields estimates of decimated signal poles [65]. Since it does not use decimated data sequences, it is not necessary to reduce the size of the Hankel matrix with increasing decimation factor D. DESE uses the original, not decimated data matrix $\mathbf{X}$ to estimate the decimated signal poles by exploiting the shift-invariance property between its D order lower shift (top D rows deleted) and D order upper shift (bottom D rows deleted) equivalents. The non-decimative version of DESE (*D=1*) is identical to MATPEN [94]. In this work, the same approach was applied to HTLS. This version is referred to as HTLSDdese.

From Eq. (2.6) it is clear that there also exists a shift-invariance property between the D order lower shift and D order upper shift equivalents of $\mathbf{S}$:

$$\mathbf{S}^D = \mathbf{S}_D\mathbf{Z}' \tag{2.29}$$

where $\mathbf{S}^D$, $\mathbf{S}_D$ stands for the matrix $\mathbf{S}$ with the top, respectively bottom D rows deleted, and $\mathbf{Z}'$ is a $(K\times K)$ diagonal matrix composed of the K decimated signal poles $z'_i,\ i = 1, \ldots, K$. Hence, HTLSDdese is identical to HTLS as outlined in section 2.2, except for step 3 where instead of Eq. (2.16) the following set of equations is solved in a TLS sense:

$$\mathbf{U}_K^D \approx \mathbf{U}_{KD}\mathbf{Z'}_Q \tag{2.30}$$

The decimated signal poles can be estimated as the eigenvalues of $\mathbf{Z'}_Q$.

2.4 Computational complexity

In this section the effect of varying D and m on the computational cost is discussed. The computational complexity of the presented algorithms consists mainly of two singular value decompositions: the SVD of the data matrix $\mathbf{X}$ in step 2, referred to as SVD1, and an SVD to calculate the TLS solution of Eq. (2.16) in step 3, referred to as SVD2. The computational aspects of these SVDs will not be discussed in detail, since there exist various algorithms, each with specific properties, that can be applied to all of these decimative algorithms. Efficient implementations exploit the Hankel structure, and compute only a partial SVD (K singular vectors). However, it is clear that, for a given model order K, the dimensions of the matrices whose SVDs are calculated are important factors determining the computational cost. These dimensions are shown in Table 2.1 for the different algorithms. Usually, the computational cost of SVD1 is much higher than that of SVD2.

Table 2.1: Dimensions of the matrices whose SVDs determine the main computational cost of the algorithms, as a function of m (the number of rows of the data matrix).

	SVD1	SVD2
HTLSDstack	$(m) \times (N-(m-1)D)$	$(m-1) \times (2K)$
HTLSDsum	$(m) \times (N/D-(m-1))$	$(m-1) \times (2K)$
HTLSDdese	$(m) \times (N-(m-1))$	$(m-D) \times (2K)$

For all three algorithms, the computational cost mainly depends on the parameter m, the number of rows of the data matrix $\mathbf{X}$. As m is usually much larger than D ($m \gg D$), increasing the decimation factor D reduces the computational cost of HTLSDstack and HTLSDsum while it has little effect on the computational cost of HTLSDdese.

2.5 Numerical Examples

2.5.1 Two peak reference signal

Undamped sinusoids

The first numerical example consists in estimating the frequencies of two, closely spaced undamped sinusoids contaminated by Gaussian white noise. The

exact parameter values of the sinusoids are given in Table 2.2.

Table 2.2: Exact parameter values of the undamped, two peak reference signal.

peak i	f_i(Hz)	d_i(rad/s)	a_i	ϕ_i
1	0.02	0	1	0
2	0.0205	0	1	0

A Monte-Carlo simulation consisting of 40 independent trials is performed, each with $N = 1000$ data points. The results are shown in Fig. 2.1, where the averaged root mean squared error $(0.5 \times (RMSE1 + RMSE2))$ of the frequency estimates has been plotted versus the signal-to-noise ratio (SNR), both for decimation by a factor of 10 and without decimation. Here, $RMSE1$ and $RMSE2$ denote the respective root mean squared errors for the frequency estimates of the two sinusoids.

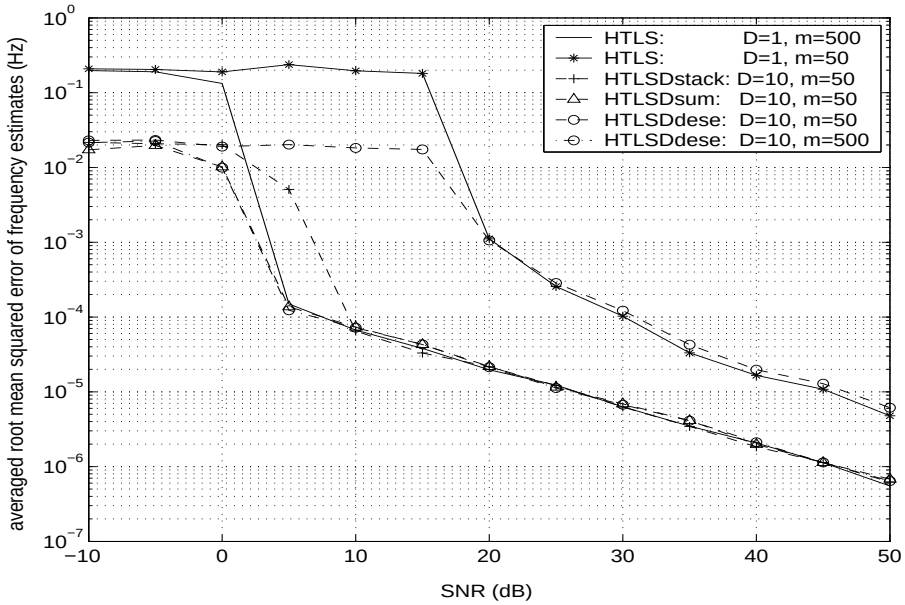

Figure 2.1: Averaged root mean squared error $(0.5\times(RMSE1+RMSE2))$ *versus SNR for HTLS without decimation (solid lines) and the different decimative HTLS-versions (HTLSDstack (+), HTLSDsum (△) and HTLSDdese (o)) with decimation factor* $D = 10$*; m denotes the number of rows in the Hankel data matrix under consideration.*

The following observations can be made:

- In all curves, the averaged root mean square error (RMSE) remains relatively constant up to a certain SNR level. In this low SNR-range, the averaged RMSE is, depending on the method and the number of rows m, of the order of 0.01 to 0.1. The error on the frequency estimates is thus much larger than the frequency separation between the two sinusoids, i.e. 0.0005. This means that the algorithm fails to estimate the frequency of both sinusoids separately. This typically corresponds to the case where one frequency estimate is in the neighborhood of the true frequencies, but the other estimate is far from the true frequencies, as illustrated in Fig. 2.2. When the SNR is high enough to separate both sinusoids, the averaged RMSE suddenly drops to a level of the order of the frequency separation. When the SNR is further increased, the frequency estimates become gradually more accurate.

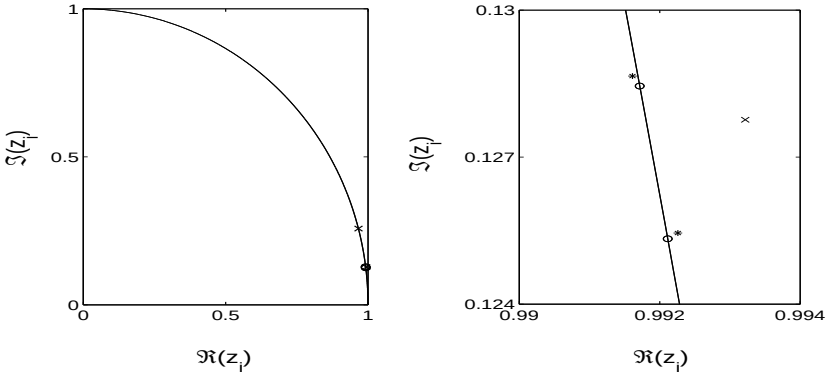

Figure 2.2: Example of the estimates of the signal poles: the true signal poles are indicated with a circle (o), the estimates in the presence of noise with SNR=0 dB are indicated with a cross (×) and the estimates in the presence of noise with SNR=20 dB with an asterix (*). The right figure is an enlargement of the left figure in the neighborhood of the true frequencies.

- Comparing the curves with $m = 50, D = 1$ and $m = 50, D = 10$ in Fig. 2.1, it is observed that increasing the decimation factor (while keeping m constant) improves the accuracy significantly, both for HTLSDstack and HTLSDsum. The accuracy of HTLSDstack and HTLSDsum is comparable for high signal-to-noise ratio (SNR), while HTLSDsum is slightly better for low SNR. For HTLSDdese, increasing the decimation factor D only improves the accuracy at very low SNR ($< 20dB$), where the estimates are practically meaningless since the RMSE of the frequency estimates is larger than the frequency separation between the two sinusoids.

- Comparing the curves with $m = 50, D = 1$ and $m = 500, D = 1$, it is seen that for constant D, the accuracy of the frequency estimates increases with increasing m ($m \leq N/2$), and hence increasing computational cost, as also observed in [211].

- Comparing the curve with $m = 500, D = 1$ and those of HTLSDstack and HTLSDsum with $m = 50$, $D = 10$, it can be noted that in order to obtain a comparable accuracy without decimation, the number of rows of the data matrix should be increased with a factor 10. More generally, experiments with HTLSDstack and HTLSDsum showed that, if the SNR is high enough to obtain meaningful estimates, the statistical accuracy of the decimative methods remains the same as long as the product mD is kept constant.

In the current setting (given model order K, given number of data points N), the only parameter to be fixed is the number of rows m of the data matrix. Simulations with varying m are performed in order to determine the number of rows for which the highest statistical accuracy is achieved. Figure 2.3 shows the averaged root mean square error as a function of m for two different SNRs (10 dB and 30 dB). On the left, the results for HTLSDstack and HTLSDsum are shown. Since both methods use decimated ($D = 10$) data sequences, the range of m-values is limited to $N/D - 1$ (=99). On the right, the results for HTLSDdese and HTLS without decimation are shown. For these methods, m is only limited to N–D–1 (=994) respectively N–1 (=999). For HTLSDstack and HTLSDsum, the highest statistical accuracy is achieved for square decimated data matrices $\mathbf{X}_d$, i.e. for $m = \frac{N}{2D}$. The exact value of m, however, is not critical because there is a relatively large range of m values for which the accuracy is approximately the same. This range increases with increasing SNR, in our simulations from $40 < m < 60$ for SNR=10 dB to $30 < m < 70$ for SNR=30 dB, but is always centered around $m = \frac{N}{2D}$. Therefore, this is considered as the optimal m-value. For HTLSDdese and HTLS without decimation, similar results are obtained: the highest accuracy is achieved when the original data matrix $\mathbf{X}$ is square, i.e. for $m = \frac{N}{2}$.

Looking back at Fig. 2.1, it is clear now that whatever decimation factor is chosen, the statistical accuracy of the decimated versions HTLSDstack, HTLSDsum and HTLSDdese is comparable to the highest statistical accuracy that can be obtained with HTLS when the optimal matrix dimensions (i.e. the parameter m) are chosen. There is, however, an important difference between these HTLS versions, namely that HTLSDstack and HTLSsum offer a computational advantage over HTLS without decimation and HTLSDdese. This is shown in Table 2.3, where the dimensions of the data matrices determining the computational cost are compared for the optimal m values (i.e. in order to obtain the highest statistical accuracy). Since $N \gg D$, the computational complexity of both HTLSDstack and HTLSDsum decreases with a factor D

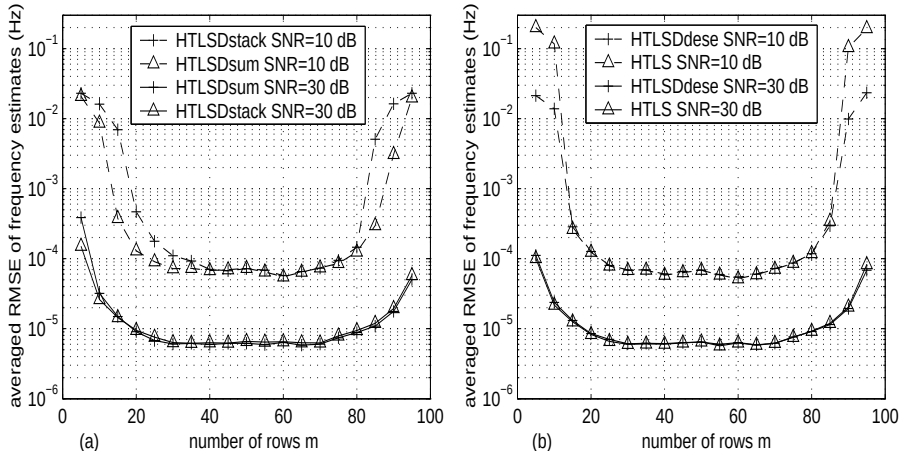

Figure 2.3: Averaged root mean squared error ($0.5\times(RMSE1+RMSE2)$*) versus SNR for HTLS without decimation (solid lines) and the different decimative HTLS-versions (HTLSDstack (+), HTLSDsum (△) and HTLSDdese (o)) with decimation factor* $D = 10$*; m denotes the number of rows in the Hankel data matrix under consideration.*

whereas the computational complexity of HTLSDdese remains approximately the same upon changing D, as shown in Table 2.3. Therefore, we conclude that the highest statistical accuracy at the lowest computational cost is achieved by the HTLSDstack and HTLSDsum versions with D as high as possible taking into account the requirements to avoid aliasing, i.e. $|f_i| < f_{sample}/(2D),\ \ k = 1, 2, \ldots, K)$ and the optimal m value ($m = N/(2D)$).

Table 2.3: Dimensions of the matrices whose SVDs determine the main computational cost of the algorithms, for optimal m (the number of rows of the data matrix), i.e. $m = N/2D$ *for HTLSDstack and HTLSDsum and* $m = N/2$ *for HTLSDdese.*

	SVD1	SVD2
HTLSDstack	$(\frac{N}{2D}) \times (\frac{N}{2} + D)$	$(\frac{N}{2D} - 1) \times (2K)$
HTLSDsum	$(\frac{N}{2D}) \times (\frac{N}{2D} + 1)$	$(\frac{N}{2D} - 1) \times (2K)$
HTLSDdese	$(\frac{N}{2}) \times (\frac{N}{2} + 1)$	$(\frac{N}{2} - D) \times (2K)$

2.5.2 Simulated MRS signals

The second example consists of estimating the parameters of signals simulating typical ^{31}P MRS signals. White Gaussian noise whose real and imaginary components have standard deviation σ_ν was added to the signals. The number of data points is $N = 128$. The optimal matrix dimensions are used for all algorithms, i.e. $m = N/2$ for HTLS and HTLSDdese, and $m = N/(2D)$ for HTLSDstack and HTLSDsum. (Relative) root mean square errors (RMSE) of the estimates of all signal parameters are calculated from 2000 noise realizations (excluding failures) for different noise levels σ_ν. A failure occurs when not all peaks are resolved within specified intervals lying symmetrically around the exact frequencies, or when the estimated damping factor is negative. The halfwidths of the intervals are based on Cramer-Rao lower bound considerations. To ensure that the RMSE was calculated on exactly the same noise realizations for the different methods, all noise realizations that failed for any method are excluded for the calculation of the RMSE. Although the exclusion of failures is not statistically sound, the same procedure is applied in [211] and is mainly justified from the MRS application as follows. In MRS spectroscopic data measurements, each peak of interest characterizes a certain metabolite and is expected to appear around an approximately known frequency. This information allows us to decide whether a run is successful or not. The corresponding parameter estimates only contain useful metabolite information when a peak estimate is found within the expected frequency interval. Therefore, failures should be excluded in our RMSE computation since it does not make sense to compare the parameters of a peak of interest with those of a noise peak that might appear far away from the expected frequency region. This procedure allows us to point out which method provides the best parameter estimates when the peaks can be resolved.

It is worth noting that the noise levels used in our simulation are lower than those usually encountered in real data. In practice, optimization based quantification algorithms are used that are more robust and accurate than HTLS due to the imposition of additional biochemical prior knowledge [213]. The MRS signals are, however, well suited for our purpose, i.e. evaluating the performance of the decimative HTLS-versions for the estimation of multiple, closely spaced peaks in the presence of noise.

Five peak simulated MRS signal

The first signal is a representative example simulating a typical ^{31}P MRS signal of perfused rat liver. The exact parameters of the fifth-order model function are given in Table 2.4. The theoretical spectrum of the noiseless signal is displayed in Fig. 2.4, from negative to positive frequency. The halfwidths of the intervals around each frequency for the determination of the number of failures, are respectively 82, 82, 82, 43 and 82 Hz. These values are derived

Table 2.4: Exact parameter values of the simulated 5 peak ^{31}P MRS signal.

peak i	f_i(Hz)	d_i(rad/s)	a_i	ϕ_i
1	-1379	208	6.1	15
2	-685	256	9.9	15
3	-271	197	6.0	15
4	353	117	2.8	15
5	478	808	17.0	15

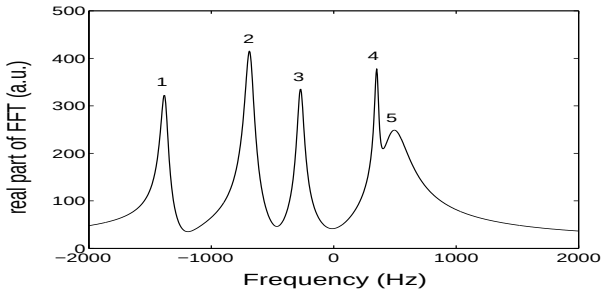

Figure 2.4: FFT of the simulated 5 peak ^{31}P MRS signal

from the Cramer-Rao bounds of peaks 4 and 5 at the noise standard deviation where these intervals touch each other. The signal used for our Monte Carlo experiments, consisting of only $N = 128$ data points, is shown in Fig. 2.5 together with its FFT. The signal contaminated with noise with $\sigma_\nu = 2$ and

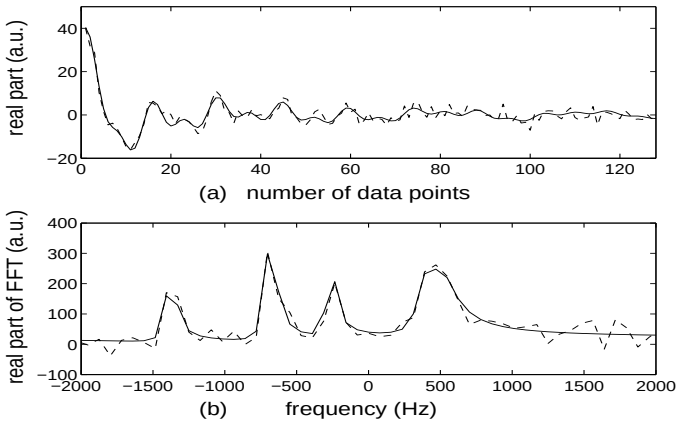

Figure 2.5: (a) Simulated 5 peak ^{31}P MRS signal and (b) its corresponding FFT (real part). The full line represents the exact signal. The dashed line represents the signal to which noise with $\sigma_\nu = 2$ is added.

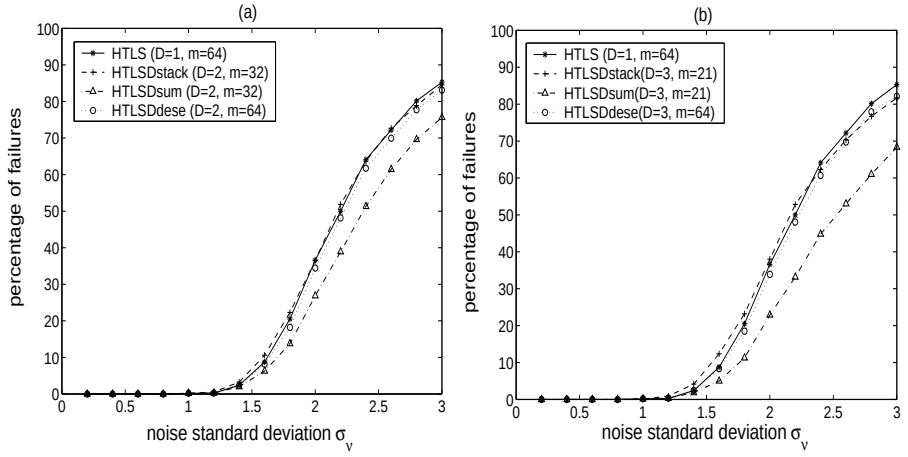

Figure 2.6: Percentage of times that HTLS and its decimative versions (with (a) $D = 2$ and (b) and $D = 3$) fail to resolve all peaks of the simulated 5 peak ^{31}P MRS signal as a function of the noise standard deviation σ_ν: HTLS (*), HTLSDstack (+), HTLSDsum ($\triangle$) and HTLSDdese (o)).

the corresponding FFT are also shown. Note that peak 4 and peak 5 can not be distinguished in the FFT due to the low frequency resolution, even without noise. Since the data was sampled at 10 kHz and the highest frequency in the signal is 1379 Hz, the highest decimation factor that does not cause aliasing is $D = 3$.

The percentage of failures as a function of the noise level σ_ν is shown in Fig. 2.6. The failure rate of HTLSDsum is lower than that of the other methods, which all have similar failure rates, irrespective of the decimation factor D. The difference in failure rate between HTLSDsum and the other methods increases with increasing noise level σ_ν. For large noise levels, HTLSDsum with decimation factor $D = 3$ has up to 7% less failures than HTLSDsum with $D = 2$, which has in turn about 10% less failures than the other methods. It was observed that the occurence of a failure is usually due to the fact that peaks 4 and 5 are fitted by only one peak, while an additional noise peak appears far away from the exact frequencies. So, only HTLSDsum seems to improve the ability to resolve closely spaced peaks.

Figure 2.7 shows the (relative) root mean square errors of the parameter estimates of one of the overlapping peaks (peak 5) obtained with HTLS without decimation and the decimative methods with $D = 2$. For low noise levels ($\sigma_\nu \leq 1$), the RMSE of the frequency estimates is comparable for all methods (differences smaller than 3% percent). For larger noise levels, the RMSE of the frequency estimate of HTLSDstack is 5% to 10% larger than that of the other methods, which all have comparable accuracy. The same behavior is observed

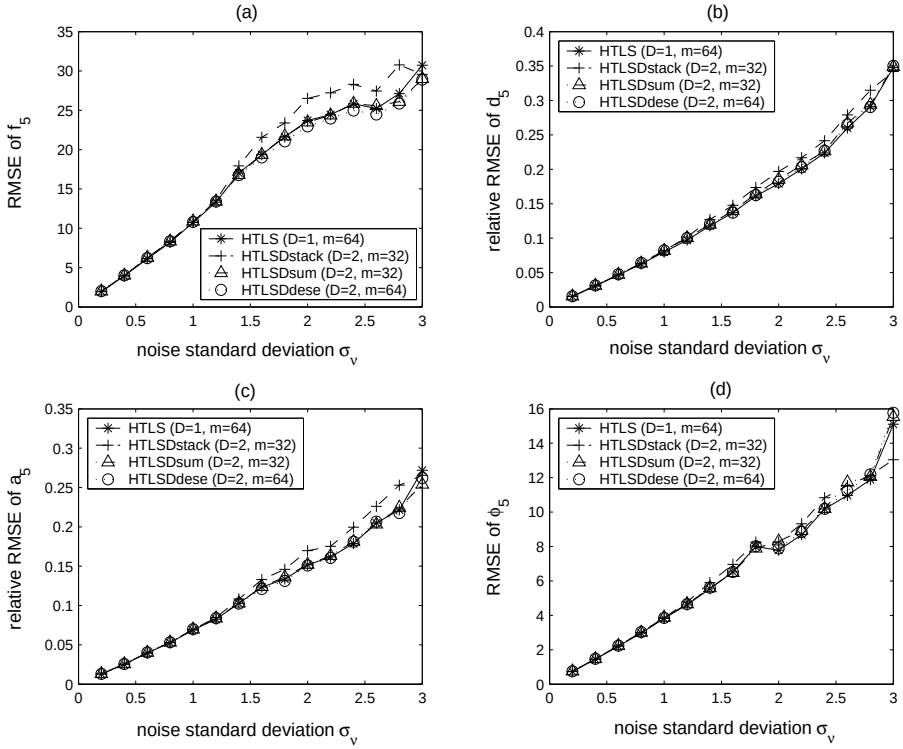

Figure 2.7: (Relative) root mean-squared error of HTLS and decimative ($D = 2$) estimates of (a) frequency f_5, (b) damping factor d_5, (c) amplitude a_5 and (d) phase ϕ_5 of the simulated 5 peak ^{31}P MRS signal.

for the RMSE of the damping factors and also for the amplitudes and phases. Note that the noise level where the RMSE of HTLSDstack starts to increase w.r.t. the RMSE of the other methods ($\sigma_\nu = 1$) coincides with the noise level where failures start to occur.

The RMSEs of the parameter estimates of peak 4 are very similar to that of peak 5, i.e. the RMSE of HTLSDstack is 5 to 10% larger than that of the other methods, which have comparable accuracy. For peaks 2 and 3, the differences between the RMSE of the parameter estimates of all methods are negligible. The RMSE of the frequency estimates of peak 1, which has the highest frequency and is therefore the limiting factor for D, is shown in Fig. 2.8. It is observed that the RMSE of HTLSDsum with $D = 2$ is about 10% higher than that of the other methods irrespective of the noise level, which again have very similar RMSEs. The RMSEs of the other parameter estimates are very similar to that of the frequency and are therefore not shown.

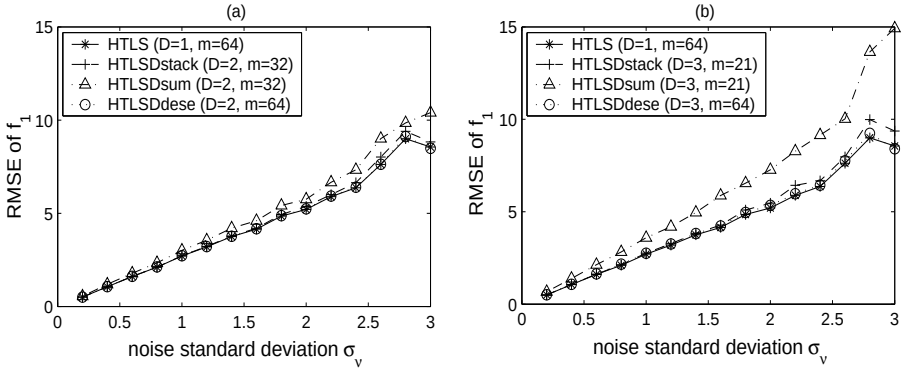

Figure 2.8: Root mean-squared error of HTLS and decimative estimates of frequency f_1 with decimation factor (a) $D = 2$ and (b) $D = 3$.

Comparing the estimates of the decimative methods with $D=2$ and $D=3$, it is found that, in general, the RMSE increases with increasing decimation factor. The differences are usually limited to a few percent, except for those methods and peaks with a significantly lower accuracy (i.e. HTLSDstack for peaks 4 and 5, and HTLSDsum for peak 1). The RMSE of the frequency estimates of peak 1, obtained with $D = 3$, is shown in Fig. 2.8. The lower accuracy of HTLSDsum is more pronounced with $D = 3$. In the latter case, the RMSE is up to 40% higher than that of the other methods.

Eleven peak simulated MRS signal

The second simulated MRS signal was derived from an in vivo ^{31}P spectrum measured in the human brain. The exact parameters of this eleventh-order model are given in Table 2.5. The halfwidths of the intervals around each

Table 2.5: Exact parameter values of the simulated 11 peak ^{31}P MRS signal.

peak	f_i(Hz)	d_i(rad/s)	a_i	ϕ_i
1	-86	50	75	135
2	-70	50	150	135
3	-54	50	75	135
4	152	50	150	135
5	168	50	150	135
6	292	50	150	135
7	308	50	150	135
8	360	25	150	135
9	440	285.7	1400	135
10	490	25	60	135
11	530	200	500	135

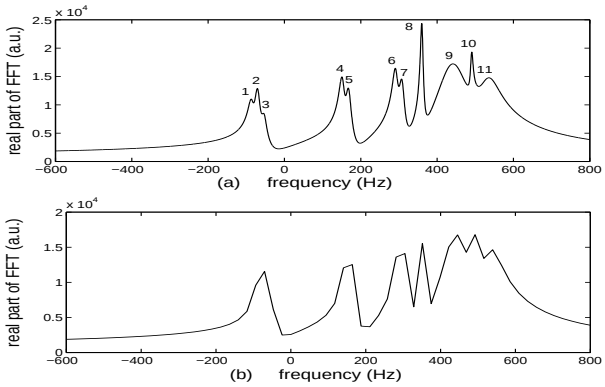

Figure 2.9: (a) Theoretical spectrum of the simulated 11 peak ^{31}P MRS signal (b) FFT of the 128 data points used for the simulations.

frequency for the determination of the number of failures, are respectively 8.6, 7.3, 8.6, 3.2, 3.2, 3.4, 3.6, 7.4, 5.5, 2.3 and 7.7 Hz for peak 1 to 11. These values are derived from the Cramer-Rao bounds on the frequencies at that noise standard deviation where the two intervals of two neighboring peaks in the triplet (i.e. peaks 1, 2 and 3) touch. The theoretical spectrum of the noiseless signal is shown in Fig. 2.9(a). It is again observed that several closely spaced peaks can not be distinguished in the FFT of 128 data points that were used for the Monte Carlo simulations, as shown in Fig. 2.9(b). Since the sampling frequency is 3 kHz and the highest frequency in the signal 530 Hz, the maximum decimation factor was $D = 2$.

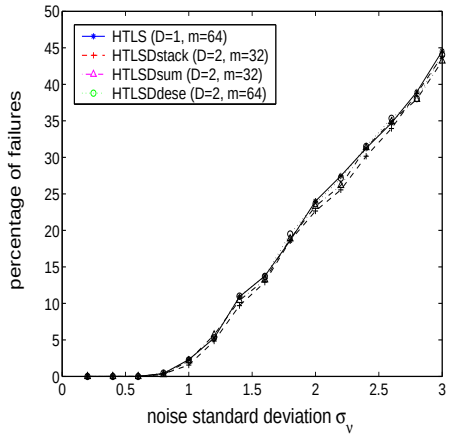

Figure 2.10: Percentage of times that HTLS and its decimative versions (with $D = 2$) fail to resolve all peaks of the simulated 11 peak ^{31}P MRS signal as a function of the noise standard deviation σ_ν: HTLS (*), HTLSDstack (+), HTLSDsum ($\triangle$) and HTLSDdese (o)).

The percentage of failures for HTLS without decimation and the decimative algorithms with $D = 2$ is shown in Fig. 2.10. It is seen that the failure rates of all HTLS-versions are comparable [1]. Overall, HTLSDstack has the lowest percentage of failures, but the difference with HTLS, which has the highest failure rate, is less than 2%.

The RMSE of the frequency estimates of peak 3, of which the parameters are the most difficult to estimate, is plotted as a function of σ_ν in Fig. 2.11. It is seen that the accuracy of all methods is comparable when for each method the optimal matrix dimensions m are used. Overall, the frequency estimates obtained with HTLSDstack are the most accurate. The RMSE of the frequency

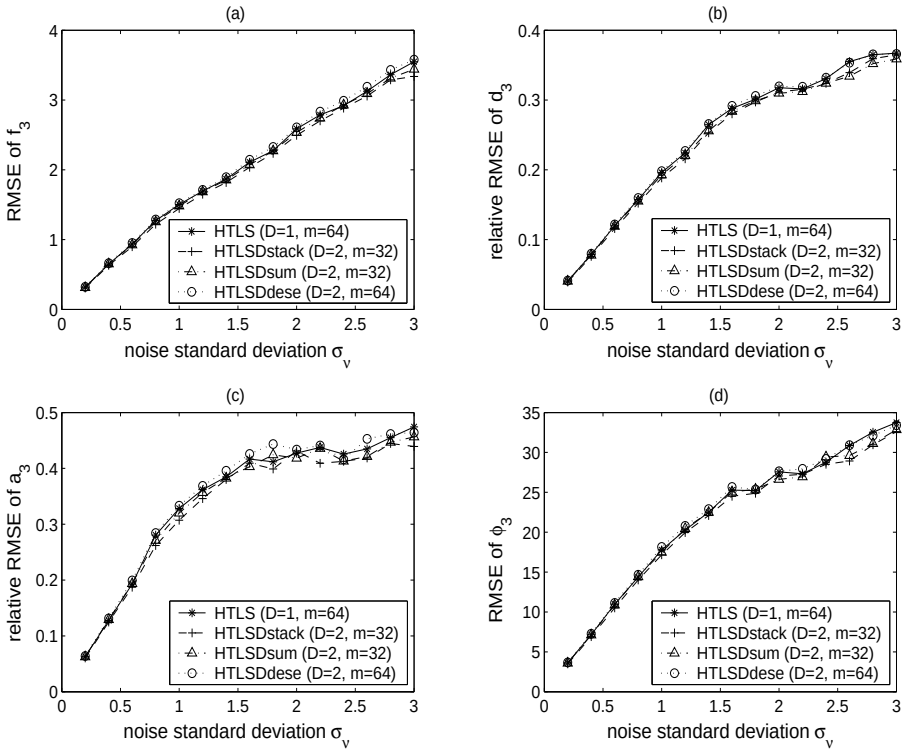

Figure 2.11: (Relative) root mean-squared error of (decimative) HTLS ($D = 2$) estimates of (a) frequency f_3, (b) damping factor d_3, (c) amplitude a_3 and (d) phase ϕ_3 of the simulated 11 peak ^{31}P MRS signal.

[1] The original DESE algorithm, presented in [65], has less failures than HTLSDstack and HTLSDsum. This is partly due to the differences between the HTLS and MATPEN algorithms.

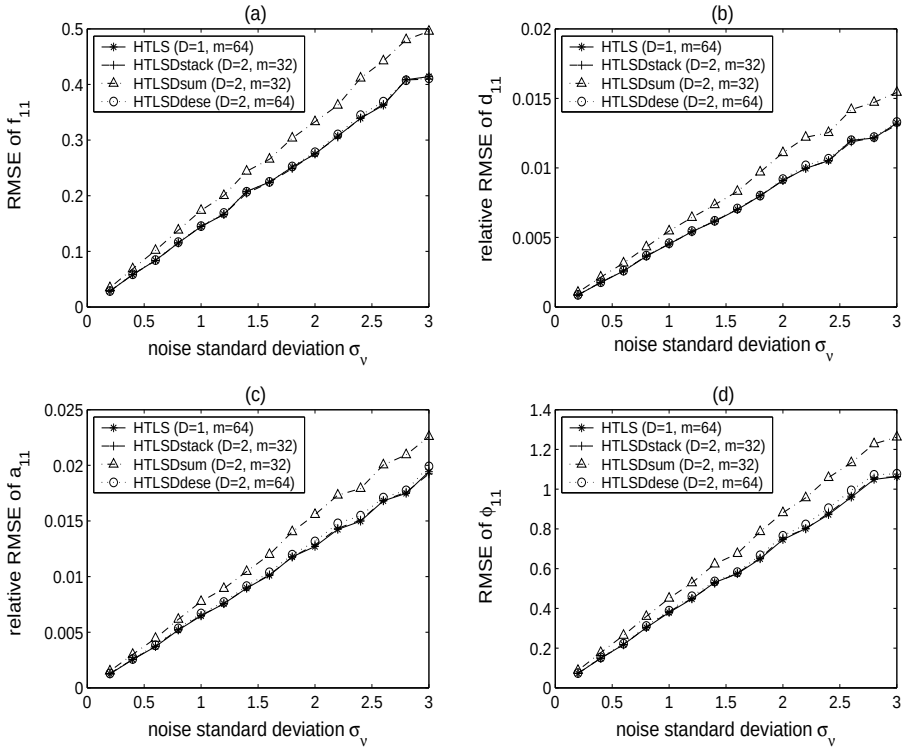

Figure 2.12: (Relative) root mean-squared error of (decimative) HTLS ($D = 2$) estimates of (a) frequency f_{11}, (b) damping factor d_{11}, (c) amplitude a_{11} and (d) phase ϕ_{11} of the simulated 11 peak ^{31}P MRS signal.

estimates of HTLS and HTLSDsum are on average 2% to 3% higher, and that of HTLSDdese up to 5%. The RMSE of the estimates of the other parameters are very similar to that of the frequency estimates.

The results for the other peaks are similar, although the RMSE of HTLSDsum increases with increasing frequency. The parameter estimates for peaks 9, 10 and 11, which are closest to the Nyquist frequency, obtained with HTLSDsum are clearly less accurate than those obtained with the other methods. The RMSE of the frequency estimate of HTLSDsum is about 20% higher than that of HTLSDstack, irrespective of the noise level, as shown in Fig. 2.12(a). This decreased accuracy is also reflected in the estimates of the other parameters, as shown in Fig. 2.12(b-d).

Computational complexity

Some simple tests using the counter of floating point operations (flops) in Matlab illustrate the dependence of the computational cost of each algorithm on D and m, as shown in Table 2.6. Although more efficient implementations are possible for each algorithm (exploiting the Hankel matrix structure, using partial SVD algorithms, etc.), the effect of varying D and/or m on the computational burden will qualitatively be the same as indicated in Table 2.6.

Table 2.6: Computational complexity of the algorithms, for different D and m values, expressed as flops/10^6.

	D	m	5 peak signal	11 peak signal
HTLS	1	64	13.0	12.3
HTLSDstack	2	32	5.0	4.0
HTLSDsum	2	32	2.9	1.9
HTLSDdese	2	64	13.0	12.3
HTLSDstack	3	21	n.a.[a]	2.3
HTLSDsum	3	21	n.a.[a]	0.8
HTLSDdese	3	64	n.a.[a]	11.7

[a] n.a. means not available: for HTLSDstack and HTLSDsum, m must be smaller than N/D.

For each method and decimation factor, the optimal matrix dimensions were used. The number of flops were calculated both for the 5 peak and the 11 peak simulated MRS signal. The differences between the 5 peak and 11 peak signals are small because the model order K only affects the computational cost of SVD2 (in Table 2.3), which is usually much smaller than that of SVD1. As expected, the computational cost is mainly determined by the number of rows m of the data matrix. Therefore, the computational cost of HTLSDstack and HTLSDsum are much lower than that of HTLS without decimation and HTLSDdese. HTLSDsum is faster than HTLSDstack, while the difference in computational cost between HTLS and HTLSDdese is small. For example, estimating the parameters of the 5 peak simulated ^{31}P MRS signal with HTLSDstack, respectively HTLSDsum with $D = 2$ is 3 or 6 times faster than without decimation. For a decimation factor $D = 3$, HTLSDstack and HTLSDsum are respectively 6 and 15 times faster than HTLS without decimation. For HTLSDdese, only for $D = 3$, a small reduction of the computational cost of about 5% compared to HTLS without decimation is observed.

2.6 Conclusions

The problem of estimating the parameters of exponentially damped sinusoidal signals in the presence of noise is considered. Three subspace-based methods using data decimation were derived from the HTLS algorithm [211], the data matrix equivalent of the well known ESPRIT algorithm [182]. HTLSDstack uses a concatenation of Hankel matrices constructed from the different decimated sequences as data matrix. This method corresponds to the decimative ESPRIT versions presented in [196, 82]. HTLSDsum uses the average of the Hankel matrices of each decimated sequence as data matrix, which comes down to applying HTLS on the signal obtained by summing every D consecutive data points of the original signal. HTLSDdese uses the original, not decimated data matrix to estimate the decimated signal poles by exploiting the shift-invariance property between its D order lower shift (top D rows deleted) and D order upper shift (bottom D rows deleted) equivalents.

The computational complexity and statistical accuracy of the different methods are compared. Increasing the decimation factor D reduces the computational cost of HTLSDsum and HTLSDstack, while it has little effect on the computational cost of HTLSDdese. Monte Carlo simulations on reference signals and simulated MRS signals are used to analyze the statistical accuracy and percentage of failures of each method. It is shown that the number of rows of the data matrix is by far the most important factor determining the statistical accuracy of the parameter estimates. The optimal matrix dimensions are determined for each method. It can be concluded that square data matrices give the best parameter estimates. For the optimal matrix dimensions, HTLSDsum is faster than HTLSDstack, which in turn is faster than HTLSDdese.

Simulated MRS signals were used to evaluate the performance of the decimative HTLS-versions for the estimation of multiple, closely spaced exponentially damped sinusoids in the presence of noise. For the simulated 5 peak MRS signal, the percentage of failures (i.e. when two closely spaced peaks are fitted by only one peak, while an additional noise peak is introduced) of HTLSDsum is lower than that of the other methods, which have comparable failure rates. However, the statistical accuracy of the parameter estimates of the peak with the highest frequency obtained with HTLSDsum is also lower compared to the other methods. Overall, HTLS without decimation yields the most accurate estimates although the differences with HTLSDstack and HTLSDsum are small. The computational cost of HTLSDstack is however 3 (for $D = 2$) to 6 (for $D = 3$) times lower. For the simulated 11 peak MRS signal, the percentage of failures of HTLS and all its decimative versions are very similar. The statistical accuracy of HTLSDstack is a few percent higher than that of HTLS without decimation and HTLSDdese. The statistical accuracy of HTLSDsum for the parameter estimates of the high frequency peaks is up to 20% lower than that of HTLSDstack.

In summary, it can be concluded that decimation as applied in HTLSDstack yields as good estimates as the best possible ones without decimation at a much lower computational cost. The computational cost of HTLSDsum is even lower, but the statistical accuracy of the parameter estimates of the peaks close to the Nyquist frequency is also lower. The decimative approach HTLSDdese does not offer any computational advantage, while its statistical accuracy did not prove to be higher than that of the other algorithms.

Chapter 3

Near-infrared spectroscopy

In its most general sense, near-infrared spectroscopy (NIRS) can be described as a technique to analyze matter by studying its interaction with light in the near-infrared range (650 nm-1000 nm). The application of NIRS to human tissue in vivo was introduced by Jöbsis, in 1977, for the non-invasive monitoring of tissue oxygenation [104]. The use of NIRS in humans relies on the relatively good transparency of biological tissue in the near-infrared range. As NIR light can penetrate several centimeters into the tissue, some of the optical properties of the tissue can be measured non-invasively. NIRS has been oriented towards use for clinical monitoring of tissue oxygenation, in particular to study cerebral hemodynamics in infants. In recent years, however, NIRS has also been proposed as a method to study brain activity non-invasively, a technique which is referred to as functional NIRS (fNIRS).

In the first, introductory section, the physical principles, models, technologies and applications of NIRS are briefly described. In the two following sections, the applications we have been working on are treated in detail. Section 3.2 summarizes the studies that were performed in collaboration with the department of Paediatrics of the University Hospital Leuven regarding the cerebral circulation and oxygenation in neonates. Section 3.3 discusses the use of NIRS for functional monitoring. These data were obtained from the laboratory for fluorescence dynamics of the university of Illinois at Urbana-Champaign.

3.1 Introduction

3.1.1 Physical principles

The two most important types of interaction of NIR light and biological tissue are absorption and scattering. Changes in either property of the tissue will result in changes in the attenuation and the transit time of the light passing through the tissue.

Absorption

Human tissues contain various light absorbing substances that are present in sufficient quantities to contribute significantly to the attenuation of transmitted NIR light. Such compounds, which absorb light in the spectral region of interest, are called chromophores. Each chromophore is characterized by its absorption spectrum describing the level of absorption at each wavelength. The relatively good transparency of biological tissue is actually due to the relatively low absorption of most compounds in the NIR frequency range (650 nm - 1000 nm). The concentration (and hence the light absorption) of several compounds such as water remain approximately constant with time, and therefore their contribution to the total light attenuation can also be considered constant. More interesting, however, are those compounds whose concentration change with time, according to blood supply, oxygenation status and metabolism. The most important of such chromophores are: oxygenated hemoglobin (HbO_2), deoxygenated hemoglobin (Hb) and cytochrome oxidase ($CtOx$). The varying concentration of these chromophores result in changes in light attenuation with time, hence providing information on the tissue oxygenation status.

Scattering

Scattering of light in tissue is caused by mismatched refractive indices at microscopic levels, for example at membrane boundaries of cells or between intra- and extracellular fluid, and at macroscopic levels, for example between soft tissue and bone. Compared to absorption, the light attenuation due to scattering is high but relatively constant in time. Changes in hemoglobin concentrations induce changes in the scattering of the tissue, but these contribute much less to the total light attenuation than the corresponding absorption changes. In the brain, neuronal activity changes the scattering properties, as explained in section 3.3, but these changes are also much smaller than the absorption changes.

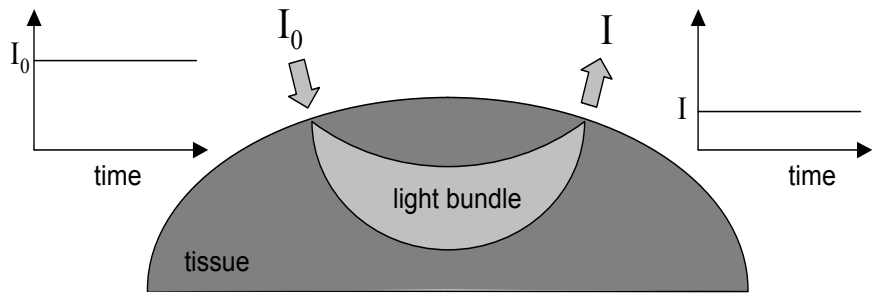

Figure 3.1: Schematic representation of the sample volume (light bundle) when source and detector are placed on the same surface. The incoming light (source) has intensity I_o, the emerging light (detector) is attenuated and has intensity I.

Sample Volume

Although the absorption is relatively low in biological tissue, it is still difficult for NIR light to penetrate more than a few centimeter. Due to the high scattering, however, a detector, placed a few centimeters from the source on the same surface, can collect light that has passed through the tissue beneath the optodes. Assuming homogeneous tissue, the sample volume corresponds to a banana-shaped volume beneath the optodes [28], as schematically shown in Fig. 3.1.

Using a more sophisticated head model, including skin, skull, cerebrospinal fluid (CSF) and brain tissue, a somewhat different sample volume was calculated [155]. The depth of penetration mainly depends on the interoptode distance. Experiments on phantoms indicate that the average depth reached in the skull is approximately half the interoptode distance [80].

3.1.2 Models

Modified Beer-Lambert law

Different models can be used to calculate chromophore concentration changes from the measured light attenuation changes. The simplest model, used in most commercial clinical NIRS devices, is based on a modification of the Beer-Lambert law to take into account scattering effects:

$$log(I_o/I) = A = (\sum_{i=1}^{n} \alpha_i \times C_i) \times d \times B + G \tag{3.1}$$

with:
I_o = intensity of the incident light (source) at a certain wavelength;
I = intensity of the emerging light (detector) at a certain wavelength;

A = attenuation;
n = number of chromophores;
α_i = (wavelength dependent) specific extinction coefficient of chromophore i;
C_i = concentration of chromophore i;
d = interoptode distance (between light source and detector);
B = differential pathlength factor, accounting for the increase in pathlength between source and detector for light being scattered;
G = term due to light scattering loss.

As the term G due to the scattering losses is unknown, it is not possible to calculate absolute chromophore concentrations from the absolute attenuation measured. However, since the changes in scattering (G) are usually negligible compared to the absorption changes, it is possible to determine changes in the concentration from the changes in attenuation. To this end, the differential pathlength factor B, or the pathlength ($B \times d$) must be known. There are several methods to measure the pathlength ($B \times d$). The two most important are briefly described below. One method is based the measurement of the mean transit time of a short laser pulse travelling through the tissue [49]. The other method, which is actually the frequency-domain counterpart of the first, makes use of intensity-modulated light and measures the phase shift between the incident and emerging light [55]. However, as most commercially available NIRS systems can not measure the actual pathlength, B is usually set to a fixed value in clinical studies. Typical values of the differential path length factor B are available from the literature for different types of tissue, wavelengths and ages of the subjects [55, 54, 230]. By setting up Eq. (3.1) for n (or more) wavelengths and solving this set of equations simultaneously, the absolute concentration changes of each chromophore can be calculated. Besides the assumption of negligible scattering changes, the assessment of chromophore concentration changes based on the modified Beer-Lambert law (MBLL) implicitly assumes that the sample volume itself and the changes within are homogeneous. Due to the latter assumption, which is clearly not correct, the MBLL approach is limited to the assessment of global absorption or concentration changes. The standard MBLL analysis can not accurately quantify even relative changes in hemoglobin concentrations for a focal hemodynamic change, for example caused by brain activity [27].

Diffusion equation

To overcome the limitations of the MBLL approach, which can only determine concentration changes, other techniques have been proposed that allow absolute determination of blood oxygenation. These methods rely on the diffusion approximation describing the propagation of photons in a highly scattering medium such as living tissue [100]:

$$\frac{1}{c}\frac{\delta\phi(r,t)}{t} = \nabla[D(r)\nabla\phi(r,t)] - \mu_a(r)\phi(r,t) + S(r,t) \tag{3.2}$$

with:
$\phi(r,t)$ = diffuse photon fluence rate at position r and time t;
c = speed of light in the tissue;
$D(r)$ = the diffusion coefficient: $D(r) = (3(\mu_a(r) + (1-g)\mu_s(r)))^{-1}$;
$\mu_a(r)$ = the absorption coefficient;
$\mu_s(r)$ = the scattering coefficient;
$S(r,t)$ = the photon source;
g = the scattering anisotropy factor (mean cosine of the scattering angle).

For a semi-infinite, homogeneous half-space geometry, it can be shown that the solution of Eq. (3.2) for an impulse input is given by:

$$R(l,t) = \frac{z_0}{(4\pi Dc)^{3/2}} t^{-5/2} exp(-\mu_a ct) exp(\frac{-(l^2 + z_0^2)}{4Dct}) \tag{3.3}$$

with $R(l,t)$ = the intensity of the reflected light at a distance l and time t and $z_0 = ((1-g)\mu_s)^{-1}$.

From this equation, absolute measures of oxygenation can be determined in different ways. Time-resolved methods, either in time-domain or in frequency-domain, are able to separate the contributions of absorption and scattering to the intensity attenuation. In the time-domain, μ_a and μ_s can be estimated by fitting the measured temporal response to a short input laser pulse propagating through the tissue to Eq. (3.3) [159]. By determining μ_a for multiple wavelengths, absolute values of chromophore concentrations can be estimated. Frequency-domain methods obtain equivalent data by using sinusoidally intensity-modulated light as opposed to pulsed light. From measurements of mean intensity, amplitude and phase of the transmitted light, μ_a and μ_s can be determined [63, 110]. Spatially-resolved methods (SRS), on the other hand, measure the diffuse back-reflected light at multiple sensors. From the spatial variation of the light, the effective attenuation coefficient $\mu_{eff} = (3\mu_a(\mu_a + \mu_s'))^{1/2} \approx (3\mu_a\mu_s'))^{1/2}$ (for a highly scattering medium) can be determined. By using multiple wavelengths and assuming a linear wavelength dependence of the scattering coefficient μ_s, relative chromophore concentrations can be estimated [125]. The ratios of these relative concentrations can in turn be used as absolute measures. Note that these methods also assume that the tissue is homogeneous and semi-infinite in extent. While the latter assumption may be reasonable for small source/detector spacing the first assumption may again lead to unreliable signals in the case of localized hemodynamic changes [126]. For more complex geometries and/or heterogeneous media the diffusion approximation can be solved numerically or other models can be used. In order to obtain accurate quantification of focal hemodynamic changes, multiple source-detector pairs combined with more advanced models and/or image reconstruction techniques are necessary [27, 9].

3.1.3 Instrumentation

The technology used in NIRS systems includes low-power light sources, usually laser diodes or LEDs, and light measurement devices such as photomultiplier (PMT) tubes and charge-coupled device (CCD) cameras or light sensitive diodes. NIR light is guided to and from the tissue by optical fibers. Depending on the type of NIR light used, NIRS systems can be divided in two categories.

Continuous wave NIR spectroscopy

The simpler and less expensive systems are of the continuous wave (CW) type, which use constant light sources. Therefore, only the wavelength dependent attenuation of the emerging light can be measured. If the differential path length factor is estimated, absolute changes in chromophore concentrations can be calculated using the MBLL for simple geometries. Based on the diffusion approximation, and using multiple sensors (SRS), it is also possible to compute relative concentrations of chromophores [125].

Time resolved NIR spectroscopy

Time resolved spectroscopy (TRS) uses non-continuous light sources. In addition to the attenuation of the light, TRS can take into account information about the transit time (time of flight) of the photons through the tissue. This allows to separate the contribution of absorption and scattering to the intensity attenuation. TRS can be performed in either the time-domain or the frequency domain, as illustrated in Fig. 3.2.

In *time-domain TRS*, ultrashort laser pulses (picosecond order) are used as input to the tissue, and the emerging light intensity is measured as a function of time. From the temporal profile of the intensity of the transmitted light, called the temporal point spread function (TPSF), values of μ_a and μ_s' can be obtained using either the MBLL or the diffusion approximation [49, 159].

In *frequency-domain TRS*, the intensity of the light source is sinusoidally modulated. The intensity (DC), modulation depth or amplitude (AC) and the phase shift (PH) of the emerging light relative to the source light is measured. Estimates of μ_a and μ_s' can be determined by fitting the frequency-domain data, which is the Fourier transform equivalent of the TPSF, to a diffusion approximation model [63]. Various other implementations of this technique exist for quantifying tissue properties [62, 110].

Frequency-domain TRS systems are less expensive and allow faster data acquisition than time-domain TRS systems [76]. With time-domain TRS systems on the other hand, additional information is available from the TPSF, which can be useful for imaging applications [89].

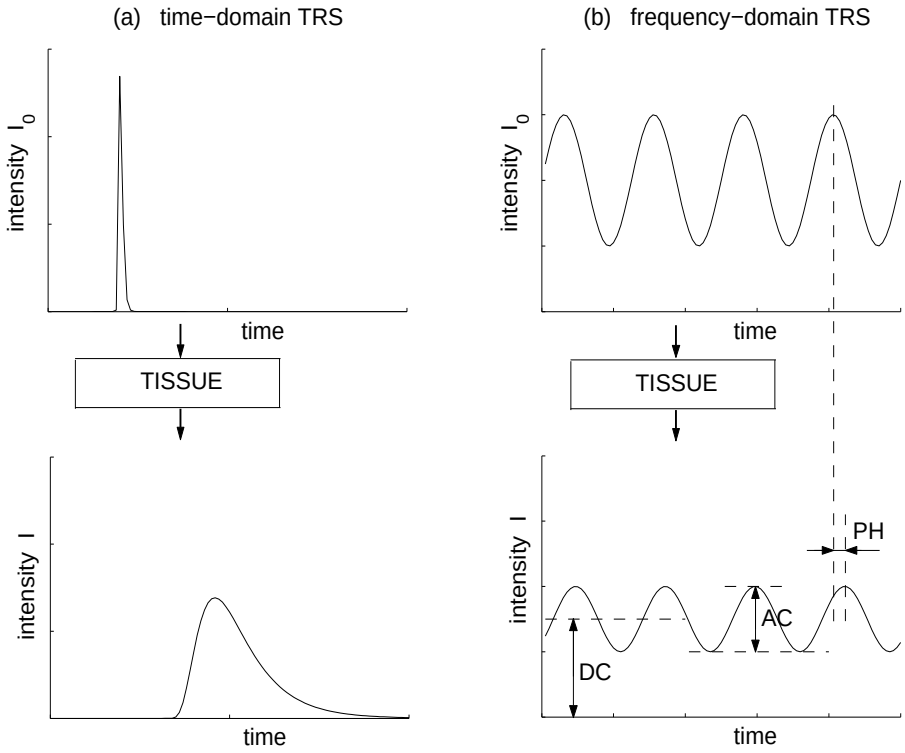

Figure 3.2: Two types of time-resolved NIRS instrumentation: (a) time-domain TRS and (b) frequency-domain TRS.

3.1.4 Clinical applications

NIR spectroscopy is mainly used in clinical studies to monitor, continuously and non-invasively, the oxygenation and hemoglobin concentrations in human tissue. The major application is the study of the brain, especially in neonates [4, 221], although it can be applied to other tissues which are close beneath the skin such as muscles [172, 46] or the liver [202, 222]. Using similar instrumentation, with multiple sensors and detectors, imaging is also possible. Clinical applications of NIR imaging include breast cancer screening (optical mammography) [84, 206] and brain, possibly functional, imaging [85, 92]. In this section, only the applications we contributed to will be discussed, namely the monitoring of cerebral oxygenation in neonates and monitoring of brain activity (functional monitoring).

3.2 Monitoring of cerebral circulation and oxygenation in neonates

Disturbances of the cerebral circulation and oxygen delivery play an important role in the genesis of cerebral complications in prematurely born infants such as intraventricular haemorrhage (IVH) and periventricular leucomalacia (PVL) [145]. Since NIRS allows non-invasive, continuous monitoring of several cerebral circulation parameters at the bedside, it is considered as a promising tool which could help the neonatologist in preventing cerebral complications [4, 221]. In collaboration with the Department of Paediatrics of the University Hospitals Leuven (Gasthuisberg), different studies regarding the clinical use and validation of NIRS have been conducted.

A commercial continuous wave NIRS device (NIRO-300®, Hamamatsu Photonics, Hamamatsu, Japan) is used in all these studies. The NIRO-300 uses 4 pulsed laser diodes to generate light at 4 different wavelengths (775, 810, 850 and 910 nm). The laser diodes sequentially irradiate the skin through the same emitter which is made from a fiber bundle. The pulse width of each laser diode is about 100 ns and the repetition rate is 2 kHz. The total average power of the irradiation to the skin is about 1 mW and classified as laser Class 1. Three closely spaced photodiodes measure the attenuation as a function of source-detector distance. The following parameters, obtained with the NIRO-300, are used:

- *Concentration changes of HbO_2, Hb and $CtOx$.*
  From the light attenuation in the middle detector (at the four different wavelengths), absolute concentration changes in oxygenated (HbO_2) and deoxygenated (Hb) hemoglobin and cytochrome oxidase ($CtOx$) are calculated using the MBLL. The differential pathlength factor is set to 4.39, according to time-of-flight measurements in post-mortem infant human brain [230, 20].

- *Cerebral blood flow (CBF) and cerebral blood volume (CBV)*
  Absolute values of CBF and CBV can be obtained indirectly from CW NIRS data. From the concentration changes in HbO_2 (and Hb) following a change in SaO_2, induced by changing the oxygen administration (FiO_2), CBF or CBV can be calculated using the Fick principle [57, 225, 229]. Several validation studies have been performed for these methods [30, 190, 70, 226, 132, 29, 12]. An alternative to this method consists in using indocyanine green (ICG) as tracer (instead of HbO_2) [158]. These methods, however, have two disadvantages. First, the necessary manipulation of the patient (for example the increase in oxygen administration to provoke a sudden change in HbO_2) is often difficult in babies. Secondly, these methods only provide single measurements and

do not allow continuous monitoring. To overcome these limitations, other parameters are often used that reflect changes in CBF or CBV.

A measure of the changes in CBF (ΔCBF) is ΔHbD, the difference between the concentration changes of oxygenated and deoxygenated hemoglobin:

$$\Delta[HbD] \equiv \Delta[HbO_2] - \Delta[Hb], \tag{3.4}$$

which can be continuously measured with NIRS. A strong correlation between ΔHbD and ΔCBF, determined by radioactive microspheres, was found during hypotension in piglet experiments during which the arterial oxygen saturation (SaO_2) did not change appreciably [207]. Further research is needed, however, to determine under which circumstances $\Delta[HbD]$ is a good measure of ΔCBF.

Changes in CBV (ΔCBV), on the other hand, are proportional to the changes in total hemoglobin concentration:

$$\Delta CBV = \frac{K(\Delta[HbO_2] + \Delta[Hb])}{[H]}, \tag{3.5}$$

where K is a constant reflecting the molecular weight of hemoglobin, the brain tissue density and the large vessel-tissue hematocrit ratio and $[H]$ is the hemoglobin concentration in a large vessel blood sample [4].

- *Tissue oxygenation index (TOI).*
  From the differences in attenuation between the 3 detectors, at different distances from the light source, relative hemoglobin concentrations are calculated, i.e. the relative proportions of HbO_2 and Hb, as explained in section 3.1.2 (SRS). This is sufficient for the quantification of the TOI:

$$TOI \equiv \frac{[HbO_2]}{[HbO_2] + [Hb]}, \tag{3.6}$$

  which is used as a measure of (cerebral) hemoglobin oxygen saturation. TOI is a parameter that can not only be monitored continuously, but since it is an absolute value it can also be measured and compared on different occasions within the same individual.

These NIRS parameters were complemented with measurements of ECG, heart rate, respiration, invasive arterial blood pressure (MAP) and peripheral oxygen saturation (SaO_2). All data are recorded at a sampling frequency of 100 Hz by a data acquisition system CODAS (CODAS®, Dataq Instruments, USA) and stored on a PC. All signals except those from the NIRO-300 are analog and digitized afterwards by the CODAS-system. The NIRO-300 signals are digital with a sampling rate of 6 Hz. They are converted to analog signals with a sample-and-hold function before their introduction in the CODAS-system.

3.2.1 Cerebral TOI in prematurely born infants

The aim of this study was to determine normal values of cerebral TOI in prematurely born infants. Fifteen patients with a mean postmenstrual age (PMA) of 28 weeks (range 25-30 weeks) were included in the study. Infants with abnormal brain ultrasound were excluded. TOI was measured in the first three days of life. TOI was measured the first time within 6 hours after birth for at least 30 minutes. The second and third measurement were performed respectively 24 and 48 hours later. The optodes were placed at the right frontoparietal side with 4 cm interoptode distance. Several other parameters were measured simultaneously: SaO_2, $PaCO_2$, PaO_2, pH, mean arterial blood pressure (MAP), heart rate and hemoglobin concentrations.

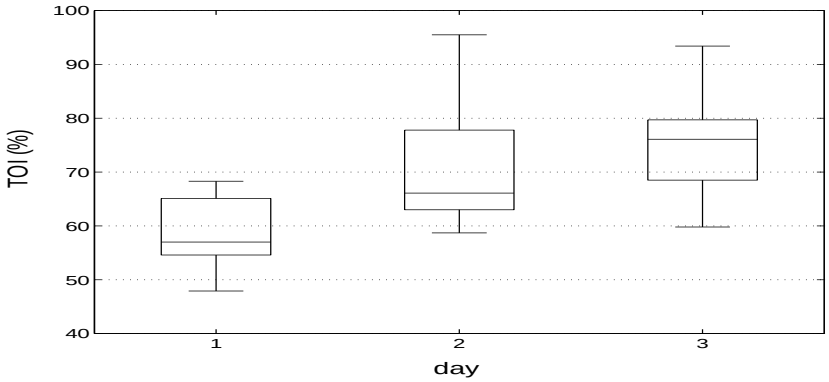

Figure 3.3: Box-and-whisker plot of TOI on the first 3 days of life of prematurely born infants.

Figure 3.3 shows a box-and-whisker plot of the TOI values on the first 3 days of life. The median (95% confidence interval) TOI was 57.0% (54.0%-65.7%) on day 1, 66.1% (61.9%-82.2%) on day 2 and 76.1% (67.8%-80.1%) on day 3. The mean standard deviation of the TOI values was 2.2%. An ANOVA-test showed a significant difference at the $p < 0.001$ level between the three days. A Student-Newman-Keuls test for all pairwise comparisons showed a significant increase in TOI from day 1 to day 2 and day 3, but not from day 2 to day 3. No correlation was found between TOI and PMA, SaO_2, MAP, $PaCO_2$, PaO_2 or hemoglobin concentration after multiple regression.

These results suggest an increase in cerebral hemoglobin oxygen saturation in the first three days of life, which is in line with the observed increase in cerebral blood flow in prematurely born infants [129]. The values of TOI at the second and third day agree with reported values of TOI in adults [173, 186, 131, 151]. An important confounding factor in this study is a low $PaCO_2$ value on the

first day, which could partly explain the lower CBF, although no correlation was found between TOI and $PaCO_2$. The combination of low $PaCO_2$ with low blood pressure may explain a lower CBF and hence a greater oxygen uptake with a lower venous saturation.

In conclusion, these findings suggest that TOI measured in prematurely born infants is a stable parameter reflecting the cerebral venous oxygen saturation. This was later validated in an animal study, where the TOI of the brain was found to be very well correlated with the venous oxygen saturation in the jugular bulb [146]. Continuous measurements over several days might detect periods of low cerebral oxygenation and high risk for neurological complications.

3.2.2 Cerebral circulation and oxygenation during rewarming of neonates

Very low birth weight (VLBW) babies are at increased risk of hypothermia in the first days of life as they have reduced vasomotor response to cold stress. Hypothermia has in turn been related to several cerebral complications [52]. In this study, the effect of rewarming on the cerebral circulation and oxygenation of VLBW babies with hypothermia was investigated. It was hypothesized that the increase in cerebral metabolism, due to the increased temperature, would cause an increase in CBF while the cerebral hemoglobin oxygen saturation would remain constant. Without adequate increase in CBF, due to peripheral vasodilatation, cerebral hemoglobin oxygen saturation will decrease which can lead to cerebral complications.

Eight subjects with a median (minimum and maximum) gestational age of 26 weeks (23-30 weeks) and median postnatal age of 0 days (0-6 days) were included. The median birth weight was 690 gram (505-1320 gram). The median temperature when the measurements started was 33.2℃ (30-35℃). Rewarming was done in an incubator. The NIRO-300 was used to measure TOI and changes in hemoglobin concentrations, from which ΔCBV and ΔHbD were calculated. Heart rate (HR), SaO_2 and MAP were measured simultaneously.

The evolution of ΔCBV and ΔHbD as a function of the temperature during rewarming of VLBW preterms is shown in Fig. 3.4. An increase in CBV (mean 0.77 ml/100g tissue, 95% CI: 0.19-1.36 ml/100g tissue) was observed in all subjects, which confirms other studies reporting a similar increase in CBV [210, 53, 61]. More interestingly, an increase in TOI and HbD was found in 4 patients, while in the 4 other patients, a decrease in TOI and HbD was found. Retrospective study revealed that the first group had important signs of peripartal asphyxia shown by CTG, low Apgar scores and an increased lactate level after birth. The concordant changes in CBV, TOI and HbD may reflect a reperfusion phenomenon in peripartal asphyxia patients. TOI was lower in this group at the start of the measurement and did not differ in comparison with the

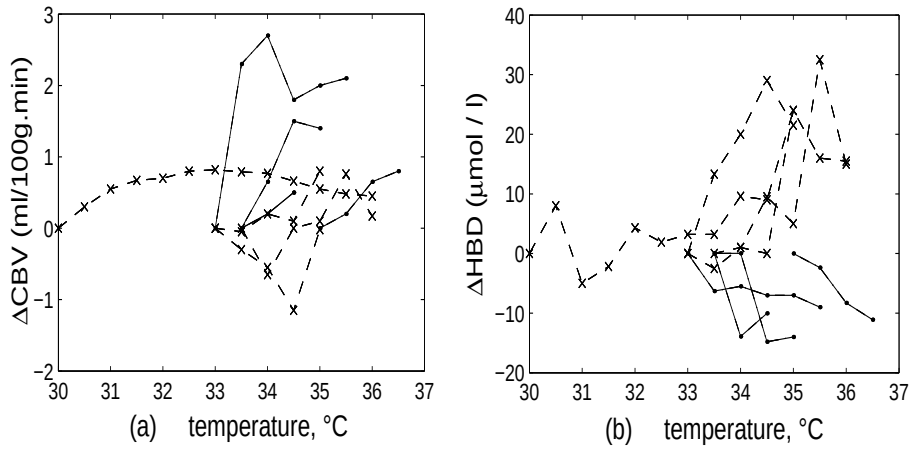

Figure 3.4: Changes in (a) ΔCBV and (b) ΔHbD during rewarming in asphyxiated (dashed line) and non-asphyxiated (solid line) VLBW preterms.

second group anymore after rewarming, suggesting that we measured a recovery of the cerebral hemoglobin oxygen saturation after a hypoxic moment. In the second group of patients, without signs of peripartal asphyxia, an increase in CBV was observed while TOI did not change significantly, suggesting a normal coupling. HbD decreased, mainly due to an increase in Hb, suggesting that oxygen consumption increased due to the increased metabolism.

In conclusion, no negative effects of rewarming on the cerebral oxygenation of very premature infants were found. Cerebral complications, described in babies with hypothermia, are more likely the consequence of peripartal asphyxia and not of the rewarming procedure itself. Larger studies are needed, however, to confirm these hypotheses.

3.2.3 Cerebral autoregulation

Some important forms of brain injury in premature infants are caused in considerable part by disturbances in CBF. Premature infants are particularly vulnerable for the development of disturbances in CBF because cerebral autoregulation, the mechanism by which CBF is maintained constant despite alterations in mean arterial blood pressure (MAP), is either defective or absent in at least some of the infants [117, 171]. Recently, a method has been proposed to detect whether cerebral autoregulation is working properly. The study suggests that concordant changes in MAP and cerebral intravascular oxygenation (HbD), measured non-invasively by NIRS, reflect impaired cerebral autoregulation [208]. Consequently, premature infants with impaired cerebrovascular

autoregulation could be identified by simultaneous, continuous measurements of ΔHbD and MAP. We performed an observational study where MAP, ΔHbD and SaO_2 were measured simultaneously in prematurely born infants.

Methods

The concordance between ΔMAP and ΔHbD was quantified using three different measures, briefly described below.

Correlation

The most straightforward way to quantify the concordance between two signals $x(k)$ and $y(k)$ is the correlation coefficient R_{xy}, estimated as:

$$R_{xy} = \frac{\sum_{k=1}^{N}(x(k)-\bar{x})(y(k)-\bar{y})}{\sqrt{\sum_{k=1}^{N}(x(k)-\bar{x})^2 \sum_{k=1}^{N}(y(k)-\bar{y})^2}} \tag{3.7}$$

where N is the number of samples considered and $\bar{x}, \bar{y}$ stands for the mean of $x(k)$, respectively $y(k)$. If one is only interested in the correlation in a specific frequency band, the signals can be filtered with a band-pass filter containing the frequency band of interest before calculating the correlation coefficient.

Coherence

Another way to quantify the correlation in a frequency specific manner is based on the coherence function, defined as:

$$C_{xy}(f) = \frac{|P_{xy}(f)|^2}{P_{xx}(f)P_{yy}(f)} \tag{3.8}$$

where $P_{xy}(f)$ is the cross power spectral density of $x(k)$ and $y(k)$, and $P_{xx}(f)$, $P_{yy}(f)$ the power spectral densities of $x(k)$, respectively $y(k)$. The spectral density functions can be estimated using Welch's method [109]. The coherence function is a measure of the linear dependence between the signals $x(k)$ and $y(k)$ at a given frequency. A coherence of 1 indicates perfect frequency specific correlation, a coherence 0 indicates a complete lack of frequency specific correlation. To obtain a measure of the coherence over a specific frequency band, the coherence function is averaged over that frequency band.

HTLS-SEP

This is a novel method based on the idea to fit one linear model to two signals. Only if the two signals have the same dynamical properties (or, in other words, have common signal poles), the determined system will be able to explain both signals sufficiently well. Mathematically, this is expressed in the proposed

model of $x(t)$ and $y(t)$, which consists of a sum of K exponentially damped sinusoids:

$$x(k) = \sum_{i=1}^{K} c_i^x z_i^k + n_1(k),\ k = 0, 1, \ldots, N-1 \tag{3.9}$$

$$y(k) = \sum_{i=1}^{K} c_i^y z_i^k + n_2(k),\ k = 0, 1, \ldots, N-1 \tag{3.10}$$

where $n_1(k)$ and $n_2(k)$ represent the noise; $z_i,\ i = 1, \ldots, K$ the signal poles as in Eq. (2.3); and c_i^x, respectively $c_i^y,\ i = 1, \ldots, K$ the complex amplitudes associated with $x(k)$ respectively $y(k)$ as in Eq. (2.2). Note that the two signals $x(k)$ and $y(k)$ are modeled with the same signal poles $z_i,\ i = 1, 2, \ldots, K$ (meaning that they share the dynamical properties of one linear system) but with different complex amplitudes.

To determine the common poles, a subspace-based approach is used. First, Hankel matrices H_x and H_y are constructed from $x(k)$ respectively $y(k)$, according to Eq. (2.4). To determine the common subspace C of H_x and H_y, matrices X and Y must be calculated such that:

$$H_x X = H_y Y \equiv C \tag{3.11}$$

Rewriting this condition as:

$$[H_x\ -H_y] \begin{bmatrix} X \\ Y \end{bmatrix} = 0 \tag{3.12}$$

shows that X and Y can be derived from the null space of the block Hankel matrix $[H_x\ H_y]$, which can be calculated using a simple SVD.

The common poles are estimated using the subspace-based algorithm called HTLS explained in section 2.2 [211]. The phases and amplitudes are estimated for $x(k)$ and $y(k)$ separately as the least squares solutions to the models Eq. (3.9) and Eq. (3.10), with the frequencies and damping factors replaced by their estimates. Note that it is implicitly assumed that both signals are related by means of a linear model. However if the relation is almost linear, the nonlinear model can be approximated by a linear one and the technique can still be applied.

Using all estimated parameters, the part of $x(k)$ and $y(k)$ common to both signals can be reconstructed, yielding $x_c(k)$ and $y_c(k)$. The common part $x_c(k)$ will only be a good fit of $x(k)$, when $x(k)$ and $y(k)$ have common signal poles. The ratio of the energy of the common part to the sum of the energy of the common part and the energy of the residual $x_r(k)$ ($x_r(k) \equiv x(k) - x_c(k)$) is used as measure of the importance of the common part:

$$CPC_x = \frac{\sum_{k=0}^{N-1} (\hat{x}_c(k))^2}{\sum_{k=0}^{N-1} (\hat{x}_c(k))^2 + \sum_{k=0}^{N-1} (\hat{x}_r(k))^2} \tag{3.13}$$

If the signals consist only of common poles, then CPC_x approaches one; if there are no common poles CPC_x, then will be close to zero. If the signals are normalized (zero mean, unit standard deviation), CPC_x can also be regarded as a measure of the mean squared error of $\hat{x}_c(k)$ with respect to $x(k)$, since:

$$CPC_x \approx 1 - \frac{1}{N} \sum_{k=0}^{N-1} x_r(k)^2 \tag{3.14}$$

Similarly, $\hat{y}_c(k)$, $\hat{y}_r(k)$ and CPC_y can be defined.

Experimental results

From several premature infants, MAP, SaO_2 and ΔHbD were measured simultaneously at the University Hospital Leuven. ΔHbD was calculated as the difference between the concentration changes of HbO_2 and Hb, measured using CW NIRS (NIRO-300, Hamamatsu). From the original data recorded at 100 Hz, the average values for non-overlapping 5-second intervals were calculated (0.2 Hz). This sampling frequency is still high enough, since the main physiological importance can be attributed to the frequency band of 0 - 0.01 Hz (i.e. changes occurring over several minutes) [208].

As the concordance between the signals might vary as a function of time, a sliding window approach was used: the presented measures were calculated on 30-minute recordings (i.e. 360 samples), and plotted against the starting time of the 30-minute window. In this way it is possible to track the changes of the measures over time.

For the correlation coefficient, we used the 5-second averaged values without filtering. When the signals are low-pass filtered to the frequency range of interest (0 - 0.01 Hz), the correlation coefficient is only slightly higher in strongly correlated windows, but also higher in uncorrelated windows. Therefore, the correlation coefficient of the unfiltered signals is more sensitive to discriminate between correlated and uncorrelated windows.

Several parameters have an influence on the estimation of the spectra for the calculation of the coherence function. In the first place, the length of the segments, used for the spectral estimation using Welch's method, and the number of overlapping points between consecutive segments. The shorter the segments, the more periodograms can be averaged and hence the lower the variance of the estimates of the spectra, but also the lower the frequency resolution. Experiments with varying segment lengths showed that segments of 144 data points give the best results (the frequency resolution is then 0.0014 Hz). The overlap was set to half the segment length. The average of the coherence function over the frequency band of interest (0 - 0.01 Hz) was used as measure of coherence, and is referred to as C_{xy} in the remainder of this paper. Before calculating the FFT of each segment, the mean was removed and a Hanning window applied.

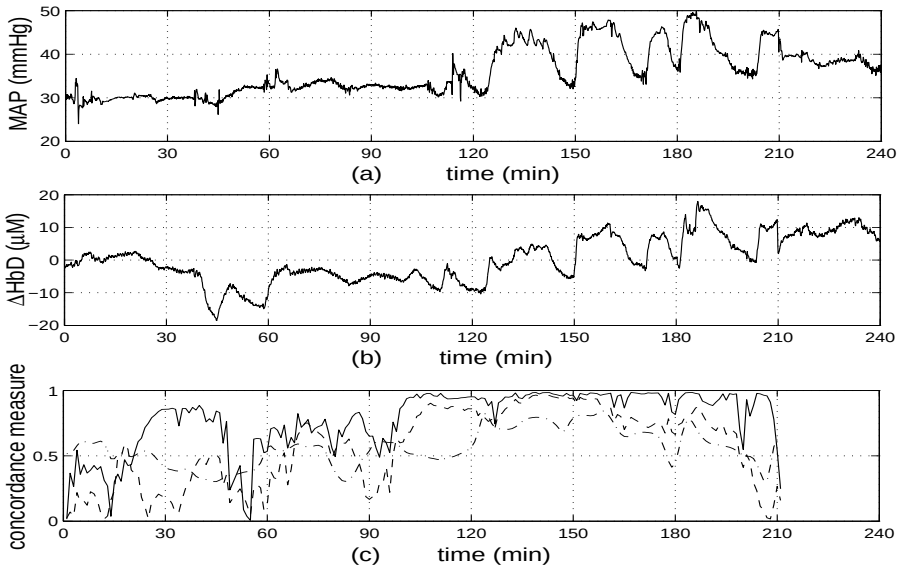

Figure 3.5: Simultaneous changes in MAP (a) and ΔHbD (b) in a premature infant, with corresponding measures of concordance (c): R_{xy} (dashed line), C_{xy} (dash-dotted line) and CPC_x (solid line).

The main problem for the HTLS-SEP method is the determination of the model order K of the common subspace, which is twice the number of frequency components. As K is not known a priori, the following procedure is used. First, $x(k)$ and $y(k)$ are modelled with $K = 2$. Then, as long as both e_x, defined as the mean of $|x(k) - \hat{x}(k)|$ over the 30-minute window, and e_y, being the mean of $|y(k) - \hat{y}(k)|$ over the same period, decreases, K is increased with 2. If either e_x or e_y increases, the procedure is stopped. The model of ΔHbD with the previous value of K is then used to calculate CPC_x by means of Eq. (3.14). The rationale for this approach is that as long as common components are added to the model, both signals will be better fitted. Before the modelling, the signals of the 30-minute windows are normalized to zero mean and unit standard deviation.

An example of the measurements on a premature infant are shown in Fig. 3.5, together with the corresponding measures. The total length of the measurement is four hours. The MAP signal shows only modest fluctuations during the first two hours. There is also modest variability in ΔHbD during the first two hours, except between the 40th and 60th minute, where ΔHbD clearly decreases. However, this decrease is accompanied by a decrease in SaO_2, as can be seen in Fig. 3.6. Fig. 3.6 also shows MAP and ΔHbD during the 30-

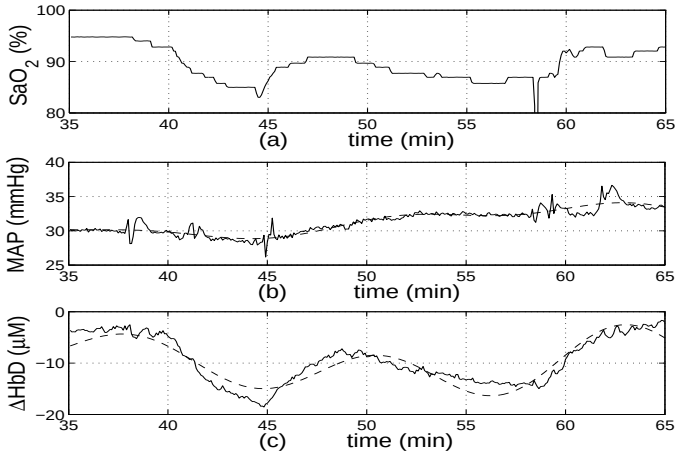

Figure 3.6: Simultaneous changes in SaO_2 (a), MAP (b) and ΔHbD (c) in the premature infant of Fig. 3.5 between the 35th and 65th minute. The original signals (solid line) are displayed together with the modelled signals (dashed line). The model order K was 4. The different measures are: $R_{xy} = 0.26$, $C_{xy} = 0.39$ and $CPC_x = 0.86$.

minute window containing this decrease, together with the models of MAP and ΔHbD. As the condition of constant SaO_2 does not hold, ΔHbD can not be assumed to be proportional to ΔCBF during this period, and therefore it is difficult to interprete the results. The analysis of this 30-minute window results in low correlation R_{xy} and coherence C_{xy} (0.26 and 0.39 respectively), but a high value for CPC_x (0.86). This might indicate that the dynamics of SaO_2 is not only reflected in HbD, but also in MAP although to a lesser degree. A possible explanation is that the infant might have had an open ductus Botalli, causing decreases in oxygenation which are often accompanied by decreases in blood pressure. During the last two hours of the recording, large spontaneous fluctuations in MAP are associated with parallel changes in ΔHbD, while SaO_2 remains constant. This is a case of impaired cerebrovascular autoregulation. During this period, CPC_x (close to 1) and R_{xy} (about 0.8) are higher than C_{xy}, suggesting that CPC_x and R_{xy} are more sensitive in order to detect impaired autoregulation. To make a meaningful comparison of these methods, however, a larger study is necessary. In a follow-up study, the predictive value of the measures with respect to subsequent brain injuries statistically could also be evaluated.

3.3 Functional monitoring

3.3.1 Introduction

Brain activity induces changes in the brain tissue that can be measured non-invasively with various techniques relying on different physical principles. The two following categories of techniques are most frequently used [37].

Initially, only electrophysiological methods such as electroencephalography (EEG) and magnetoencephalography (MEG) allowed non-invasive functional studies of the human brain. EEG and MEG measure the changes in respectively electrical and magnetic fields produced in the brain, and are therefore directly coupled to neuronal activity. Since the transmission of electrical and magnetic fields to the sensors is effectively instantaneous (only limited by the speed of light), these techniques have a very good temporal resolution. The accurate localization of the activated brain areas based on EEG/MEG data alone remains a difficult problem, however, because the so-called inverse problem of estimating the current sources based on EEG/MEG recordings only is fundamentally ill-posed [43]. This means that for any distribution of EEG/MEG recorded, there are many possible configurations of current sources within the brain consistent with the data, a principle which was already pointed out in 1853 by Helmholtz [86].

During the past decade, modern imaging techniques such as functional magnetic resonance imaging (fMRI) and positron emission tomography (PET) have dominated the field [209]. Both techniques rely on the measurement of variables related to hemodynamic and metabolic events induced by brain activity. Since the hemodynamic response to neuronal activity takes place over several seconds, the temporal resolution that can be obtained with these techniques is limited. On the other hand, these techniques allow localization of brain activity with a high spatial resolution, for fMRI up to 1 mm [209].

In the last few years, efforts have been done to combine high-quality localization information, provided by PET or fMRI, with high-quality temporal data, generated by EEG or MEG [43, 220]. On the other hand, also recently, NIRS has been proposed as a method to study brain activity non-invasively. Functional NIRS (fNIRS) relies on the changes of the optical properties of the brain tissue related to functional activation. These changes can be divided, according to their large difference in response time, into fast neuronal changes and slow hemodynamic changes.

- *Fast neuronal signal*
  The fast neuronal signal, with a response time on the order of milliseconds, relies on optical changes directly related to neuronal activity. Neuronal activity leads to small changes in the optical properties of the neurons, presumably in the scattering of the neuronal membranes. These

changes can be measured with NIRS and yield an optical signal that corresponds to the electrical and magnetic signal measured with EEG and MEG.

Several studies on the origin of the fast signal in single nerve cells, animals and humans can be found in the literature [39, 195, 200, 185, 81, 176, 123, 74, 79, 77, 177, 50, 193, 227, 228].

Cohen [39] and Stepnoski [195] observed changes in birefringence in the membrane of nerve cells simultaneous to the action potential. The decrease in birefringence causes an increase in light scattering [195]. Tasaki found that thermal (heat production), mechanical (swelling) and optical (birefringence) changes in the axon were simultaneous to the action potential and related to a sudden swelling of the gel layer in the neuronal membrane [200]. However, it is difficult to extrapolate the cited data on single nerve cell preparations to in vivo measurements in humans.

Salzberg studied the neurohypophysis of mice and reported large and rapid decreases in light scattering, which accompanied the secretion of nerve terminals [185]. Further work has been done in animals, e.g. on the open cat cortex [81, 176, 123]. Grinvald reported a decrease in reflected light 200 ms after the onset of whisker stimulation [81]. Rector found a decrease in reflected light synchronous to the electrical signal [176]. Both findings can be interpreted as a decrease in light scattering or an increase in light absorption. Malonek reported an increase in light scattering 200 ms after the onset of the stimulation [123].

In humans, Gratton [74, 79, 77], Rinne [177] and DeSoto [50] reported increases in the phase of a frequency-domain NIRS instrument, which can be interpreted as an increase in light scattering or in absorption. Steinbrink [193] as well as Wolf [227, 228] report a decrease in the intensity of the light, also suggesting an increase in light scattering or absorption.

- *Slow hemodynamic signal*
  The slow hemodynamic signal, with a response time on the order of seconds, can be attributed to changes in absorption that are mostly produced by hemodynamic and oxygenation changes, which occur in active areas of the brain due to neurovascular coupling. This effect has been extensively studied in human adults [218, 153]. In short, the neuronal activity increases the oxygen consumption, which in turn leads to an increase in blood flow to provide more oxygen. In adults, the increase in blood flow overcompensates for the consumed oxygen, resulting in a net oxygenation increase in the activated area. The increase in blood flow affects the oxy- (HbO_2) and deoxyhemoglobin (Hb) concentrations, i.e. the HbO_2 concentration increases and the Hb concentration decreases. The changes in hemoglobin concentrations can be measured using NIRS, MRI or PET. The slow hemodynamic signal originates from the cortex, which was confirmed by a simultaneous comparison of NIRS to MRI [204] and PET [219].

Besides the differences in time scale, there are other important differences between the fast and the slow optical signal. The slow hemodynamic-related absorption changes are much larger than the fast neuronal scattering changes, and therefore easier to observe. On the other hand, since the increase in blood flow affects blood vessels in a larger volume of tissue than the volume of the activated neurons, the fast signal is more localized than the slow signal.

NIRS allows thus the simultaneous measurement of both optical changes directly related to neuronal activity, and the hemodynamic changes. Therefore, it is a unique approach to study neurovascular coupling [218], combining subcentimeter spatial localization with millisecond temporal resolution [75]. Some important advantages of NIRS are that it is non-invasive and can be used at the bedside, and therefore can be combined with other techniques such as EEG, MEG or fMRI. Due to the limited penetration of light into living tissue, however, only superficial layers of the brain can be reached with NIRS.

This section deals with the detection of the fast neuronal signal in NIRS measurements of the motor cortex. Since the stimulation is a finger tapping exercise, the goal of this study is to detect a component in the optical signals which is correlated with the tapping frequency. Therefore, the DC, AC and PH signals of a frequency-domain NIRS instrument were directly analyzed (without modelling to determine concentrations or absorption coefficients).

3.3.2 Measurements

Subjects

Three female and 11 male healthy adult volunteers (between 19 and 55 years) were included in this study. All except one were right handed. Written informed consent was obtained from all subjects prior to the measurements. The subject data is summarized in Table 3.1.

Instrumentation

For the NIRS measurements, a frequency-domain NIRS system (Oxy-Imager, ISS Champaign, IL, USA) was used. Laser diodes, whose intensity was modulated at 110 MHz, were used as light sources. For this instrument and this application, the largest source of noise is shot noise, which results from the quantum nature of the light detection. Since higher light intensity is the only way to improve the signal-to-noise ratio (SNR) concerning the shot noise, the light of four laser diodes was combined to achieve higher light intensity at each source location. The power output of each laser diode was 5 mW, which is laser class 3a. The light was guided to the tissue by optical fibers of 0.4 mm core diameter. The emerging light, which has passed through the tissue, was collected by fibers of 3 mm core diameter. Photomultiplier tubes (PMT) were

Table 3.1: Subject data

subject no.	sex	age	hand	mean heart rate (Hz)	mean tapping frequency (Hz)	no. of tapping periods
1	M	22	right	1.05	2.65	8
2	M	45	right	1.20	2.97	8
3	M	55	right	1.33	3.35	8
4	M	28	right	1.30	2.92	8
5	M	44	right	1.37	3.33	8
6	M	22	left	1.16	2.84	8
7	F	30	right	1.10	2.66	8
8	M	19	right	1.18	2.82	8
9	M	35	right	1.40	3.55	16
10	M	19	right	0.92	2.91	8
11	M	22	right	1.05	2.50	8
12	F	26	right	1.20	3.05	6
13	F	37	left	1.05	2.80	8
14	M	38	right	1.05	2.65	8

used as detectors. The gain of the PMTs was modulated at 110.0005 Mhz to demodulate the high frequency. Since the component at the mismatch frequency of 5 kHz carries all the information of mean intensity (DC), amplitude of the oscillations (AC) and phase (PH), the output of the PMT was low-pass filtered with a cut-off at 10 kHz. The filtered signal was processed by a computer in order to determine AC, DC and PH.

A special sensor consisting of four crossed source-detector pairs arranged on a circle with diameter 3.2 cm, as shown in Fig. 3.7, was used. The path of the light, penetrating from source to detector, forms a banana shape, and is referred to as a light bundle [154]. The geometry of the sensor was optimized to penetrate the region of interest with a high number of light bundles. To distinguish the light of the four source locations, the laser diodes were multiplexed. At each of the four detectors (A,B,C,D), the intensity (DC), amplitude (AC) and phase (PH) of the modulated optical signal were measured. The sample rate for a complete cycle, which measures all 48 parameters (AC, DC and PH for 16 source-detectors pairs), was 96.1539 Hz.

In addition, the arterial pulsations, the respiration and a signal synchronous to the finger tapping were measured simultaneously with the optical data. A pulse oximeter (N200, Nellcor Incorporated), attached to the middle finger of the left hand if the tapping was performed with the right hand and vice versa, measured the arterial pulsations and the peripheral oxygen saturation (SaO_2). The respiratory signal was obtained from a breathing belt fixed around the

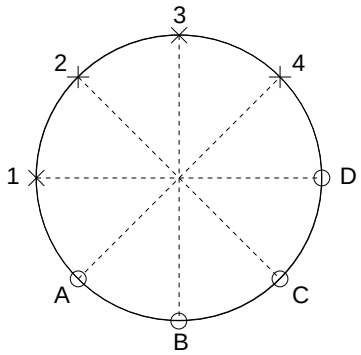

Figure 3.7: Configuration of the NIRS sensor with 4 sources (x) and 4 detectors (o) arranged on a circle with diameter 3.2cm. The sensor was placed above the motor cortex (C3 position).

chest. Using a strain gauge (New Life Technologies), a signal proportional to the tension in the belt is derived. An electronic device registered the tapping movement. The amplitude of this signal was independent of the amplitude of the finger movement.

Protocol

The sensor, consisting of the four crossed source detector pairs, was placed above the motor cortex (C3 position according to the international 10/20 system [103]), contralateral to the hand performing the finger tapping exercise. By a metronome, the tapping frequency was set at approximately 2.5 times the heart rate of the subject. The measurement protocol consisted of a 1-minute pre-exercise period (baseline), a 5-minute stimulation run with alternating rest- and tapping (with the whole hand) periods of 20 s each (corresponding to a frequency of 0.025 Hz), and a 1-minute after-exercise period (baseline). For two subjects, the stimulation runs had different durations. Overall, there were 14 subjects: 12 with stimulation runs of 8 tapping periods, one with 16 tapping periods and one with 6 tapping periods, as indicated in Table 3.1. The subjects were supine in a quiet and dark room, and wearing safety goggles during the whole measurement. The protocol was approved by the institutional Review Board of the University of Illinois at Urbana-Champaign (IRB#94125).

3.3.3 Raw signals

Figure 3.8 shows examples of all measured signals. The upper three figures are the different optical signals from detector C and source 3: (a) CDC3, (b) CAC3 and (c) CPH3. The lower three figures show the additional measurements: (d) arterial pulsations, (e) respiration and (f) tapping.

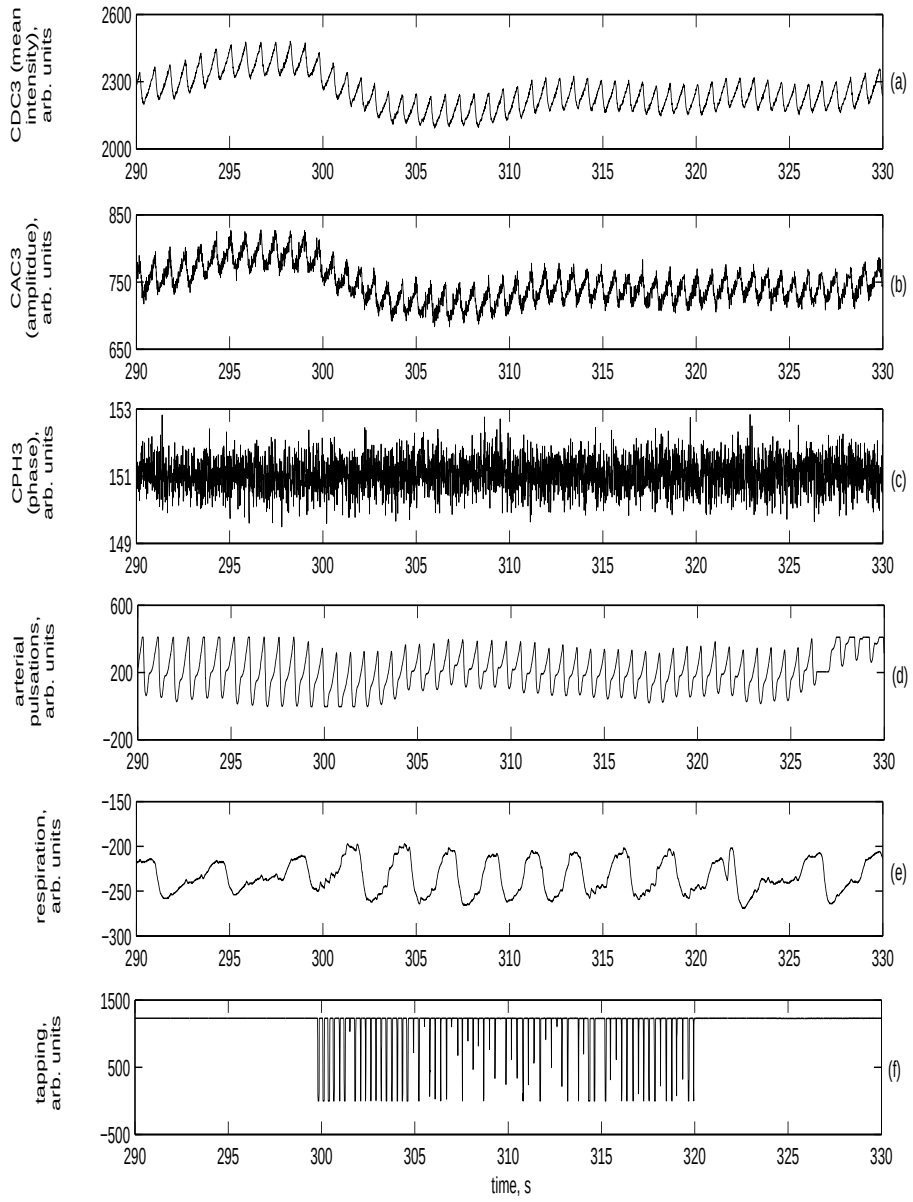

Figure 3.8: Representative fragments of different signals of subject 3: (a) mean intensity signal CDC3 (detector C, source 3), (b) amplitude signal CAC3 (detector C, source 3) (c) phase signal CPH3 (detector C, source 3), (d) arterial pulsations recorded with a pulse oximeter, (e) respiration signal recorded with a strain gauge and (f) tapping signal which is low when the fingers are touching each other.

The CDC3-signal shown in Fig. 3.8(a) is representative for the other DC-signals, although the signal strength depends on the distance between source and detector and differs between subjects. The dominant frequency with a period of approximately 0.75 s (corresponding to a frequency of 1.3 Hz) is due to the arterial pulsations.

The power spectrum of another representative DC-signal (ADC4 of subject 9) was estimated using Welch's method [109] with non-overlapping windows of 15000 samples (156 s), and is shown in Fig. 3.9. A signal of the longer measurement of subject 9 was used for Fig. 3.9 since this allowed us to average several periodograms of longer windows. In the power spectrum of ADC4, the dominant frequencies between 1 Hz and 5 Hz are the heart rate (arterial pulsations), around 1.4 Hz, and its harmonics. As the heart rate is not perfectly constant during the whole measurement, the peaks are smeared out. At the tapping frequency (3.55 Hz), no peak can be distinguished. There are also peaks in the lower frequency range (below 1 Hz). The peak around 0.3 Hz is due to the respiration. This peak, however, is not always present in the power spectra of the optical signals. The peaks around 0.12 Hz are related to Mayer waves, which have been observed by many researchers although their origin is not yet exactly determined [95]. The peak at 0.025 Hz, corresponding to a period of 40 s, is due to the slow hemodynamic signal. This is a first indication that the measurements are done over the activated region of the brain.

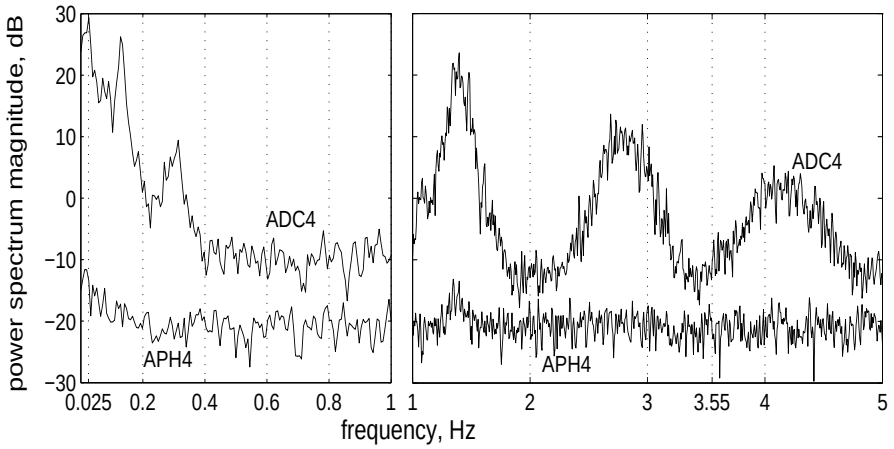

Figure 3.9: Power spectrum of representative DC- and PH-signals (ADC4 and APH4 of subject 9). The peaks in the power spectrum of the ADC4 are due to the slow hemodynamic signal (0.025 Hz), Mayer waves (0.12 Hz), respiration (0.3 Hz) and arterial pulsations (1.4 Hz and harmonics). At the tapping frequency (3.55 Hz), no peak can be distinguished. In the power spectrum of APH4, only a small peak at the heart rate can be observed. Note: the spectra were shifted vertically in order to obtain a clear figure.

Fig. 3.10 shows the spectrogram of CDC3, calculated as the short time Fourier transforms (STFT) on non-overlapping windows of 4 seconds. The spectrogram is completely dominated by the arterial pulsations: no peaks can be observed at the tapping frequency or its harmonics. The spectrogram also shows that the heart rate varies slightly throughout the measurement.

The AC-signal shown in Fig. 3.8(b) (CAC3) is very similar to the corresponding DC-signal, although it is somewhat more noisy. From the theory of photon migration it is known that the DC- and AC-signals contain mainly the same information, but the SNR of the AC-signals is smaller. Therefore, the AC-signals were not analyzed in this study.

The PH-signals are much more noisy than the DC- or AC-signals, as shown in Fig.3.8(c). In the power spectrum of APH4, also shown in Fig. 3.9, only a peak at the heart rate can be observed, which is usually smaller than the corresponding peak in the DC-signals. In many cases the noise in the phase signal is so large that even this peak can not be detected. The spectrograms

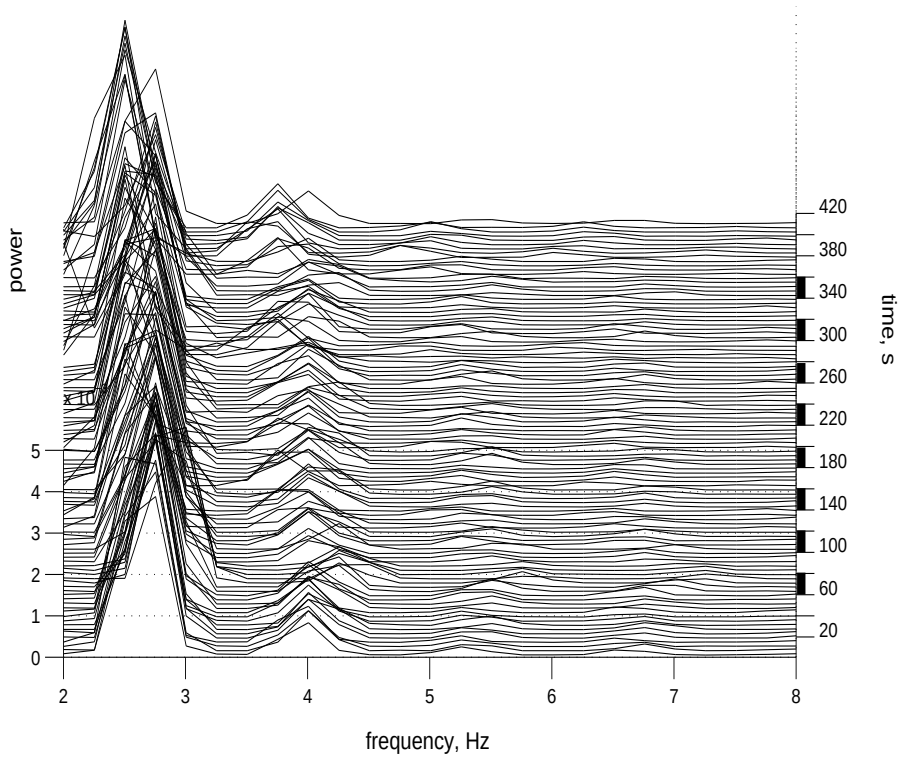

Figure 3.10: Spectrogram of CDC3. The tapping periods are marked by the black squares parallel to the time axis.

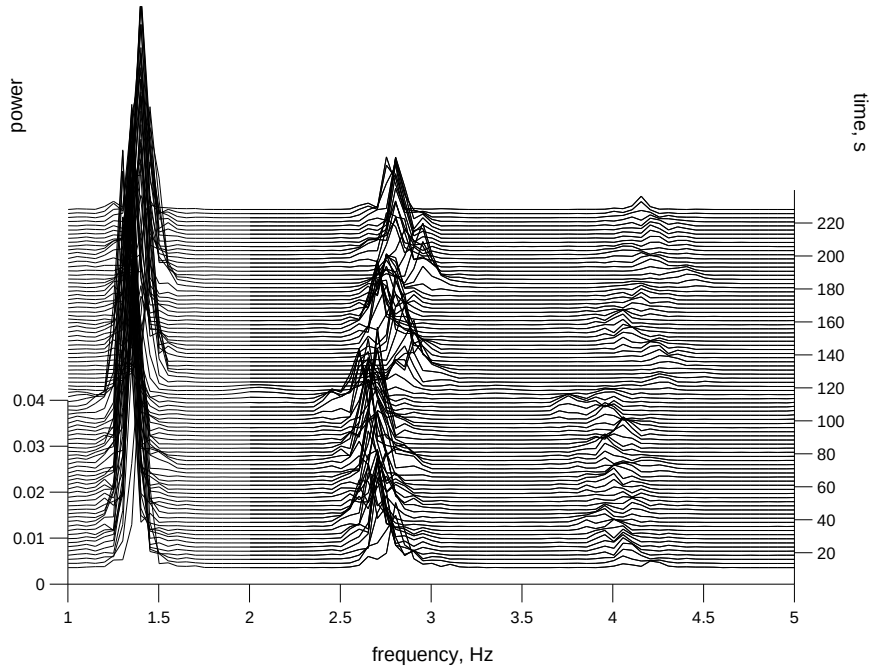

Figure 3.11: Spectrogram of the arterial pulsations. Note the variation in the heart rate and its second and third harmonic.

of PH-signals (not shown) contain mainly noise.

Fig. 3.11 shows the spectrogram of the arterial pulsations of subject 9. The variation in the heart rate is clearly visible, especially in the second and third harmonic.

Fig. 3.12 shows the spectrogram of the tapping signal (finger movement) of subject 3, shown in Fig. 3.8(f). Note that although the subjects were instructed to follow a metronome, the tapping frequency is not perfectly constant.

3.3.4 Filtering

As shown in the previous section, the fast neuronal signal is so small compared to other physiological signals that it can not be observed directly in the NIRS signals. The physiological interferences in the low frequency region (below 1 Hz, respiration and Mayer waves) as well as the high frequency noise can be removed with a conventional bandpass filter. An eighth order Butterworth filter with cut-off frequencies at 1 Hz and 10 Hz was used. The signals were filtered both in forward and backward direction to obtain zero phase distortion.

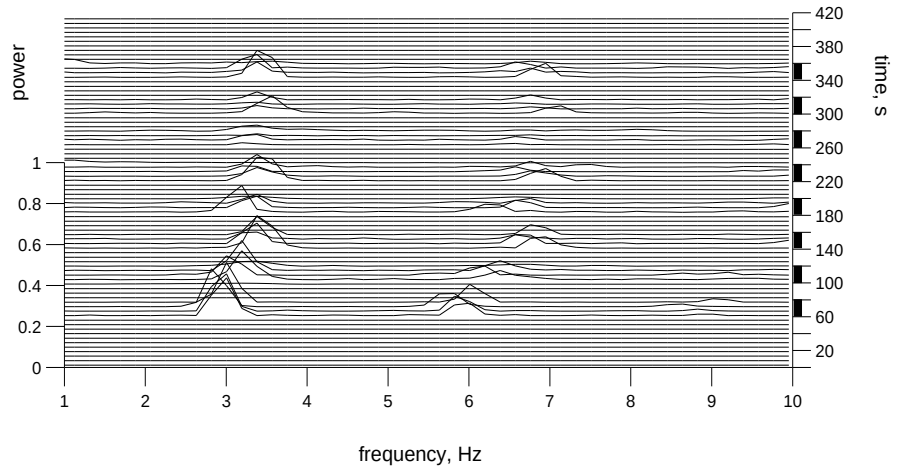

Figure 3.12: Spectrogram of the tapping signal (finger movement). The tapping periods are marked by the black squares parallel to the time axis.

However, the largest alterations in the optical signals are at the heart rate and its harmonics due to the arterial pulsations. Therefore, specific filters were used to reduce the effect of the arterial pulsations on the optical signals. Two different types of filters were used.

In most cases, a conventional adaptive noise canceller (ANC), as shown in Fig. 3.13, based on the normalized least-mean-square (NLMS) algorithm was used. The primary signal, which serves as desired response for the adaptive filter, is in our case the NIRS-signal containing the signal of interest (tapping) and noise (arterial pulsations). The pulse oximeter signal, which contains the arterial pulsations but not the tapping signal, is used as input to the adaptive filter (noise reference) in order to reduce the noise in the NIRS signal. The principles underlying this NLMS-based adaptive noise canceller are summarized in the first subsection.

In some measurements, however, the pulse oximeter signal was saturated, resulting in a distorted waveform -resembling a square wave- of the arterial pulsations. In those cases, a filter was used that only uses the NIRS signals and not the pulse oximeter signal [73]. In short, it extracts a mean shape of the pulse by screening each trace separately for pulses, whose period is adjusted before the averaging. This mean shape corresponds to the best estimate of each pulse and is used to remove each pulse from the data. This again requires adjusting the period of the mean shape to the one of each pulse and by scaling the shape by linear regression. In the remainder of this paper, this filter is referred to

as “HF”.

NLMS-based adaptive noise canceller

The structure of a basic adaptive noise canceller is shown in Fig. 3.13. The

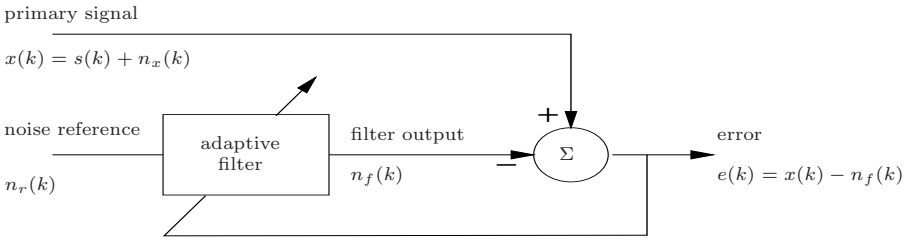

Figure 3.13: Interference canceller: primary signal = NIRS signal (DC or PH), noise reference = pulse oximeter signal.

primary signal $x(k)$ contains the signal of interest $s(k)$ plus (uncorrelated) noise $n_x(k)$. Adaptive filtering requires a second signal, the so-called noise reference $n_r(k)$, which is uncorrelated with the signal of interest $s(k)$ but correlated in some unknown way with the noise $n_x(k)$. This noise reference is filtered to obtain a signal $n_f(k)$ which is close to the noise $n_x(k)$. The output of the filter $n_f(k)$ is then subtracted from the primary input to estimate the error signal $e(k)$.

$$e(k) = s(k) + n_x(k) - n_f(k) \tag{3.15}$$

The filter is optimized according to a certain cost function. A common cost function is the mean-squared error (MSE) criterion, defined as the mean-squared value of the estimation error.

$$\begin{aligned} \mathcal{E}\{e(k)^2\} &= \mathcal{E}\{(s(k) + n_x(k) - n_f(k))^2\} && (3.16) \\ &= \mathcal{E}\{s(k)^2\} + \mathcal{E}\{(n_x(k) - n_f(k))^2\} + 2\mathcal{E}\{s(k)(n_x(k) - n_f(k))\} && (3.17) \end{aligned}$$

Assuming that $s(k)$ is uncorrelated with $n_x(k)$ and $n_f(k)$, and all of them are statistically stationary and have zero means, yields:

$$\mathcal{E}\{e(k)^2\} = \mathcal{E}\{s(k)^2\} + \mathcal{E}\{(n_x(k) - n_f(k))^2\}. \tag{3.18}$$

Note that the signal power $\mathcal{E}\{(s(k))^2\}$ is unaffected as the filter is adjusted to minimize the $\mathcal{E}\{e(k)^2\}$. Hence, if the cost function $J_{MSE} \equiv \mathcal{E}\{(n_x(k) - n_f(k))^2\}$ is minimized, then $e(k)$ is the best least-squares estimate of the signal of interest $s(k)$.

For a transversal finite impulse response (FIR) filter, also denoted as tapped-delay line filter, the filter output is formed as a linear combination of delayed

input samples, i.e.:

$$n_f(k) = w_0 n_r(k) + w_1 n_r(k-1) + \ldots + w_{M-1} n_r(k-M+1) \tag{3.19}$$

where $n_f(k)$ represents the filter output at time k, $n_r(k)$ the filter input at time k and $w_i,\ i = 0 \ldots M-1$ the filter weights, or tap weights. This can also be written using vector notation:

$$n_f(k) = \sum_{i=0}^{M-1} w_i n_r(k-i) = \mathbf{w}^T \mathbf{n}_r(k) \tag{3.20}$$

with $\mathbf{w}^T = [w_0\ w_1 \ldots w_{M-1}]$ and $\mathbf{n}_r(k)^T = [n_r(k)\ n_r(k-1) \ldots n_r(k-M+1)]$. The number of filter weights M, also referred to as the filter order, determines the length of the impulse response. The filter weights w_i, which determine the shape of the filter response, are calculated in order to minimize the chosen cost function.

Using Eq. (3.20), the function to be minimized J_{MSE} can be written as:

$$J_{MSE} = \mathcal{E}\{(n_x(k) - \mathbf{w}^T \mathbf{n}_r(k))^2\}, \tag{3.21}$$

which can be manipulated further to give:

$$J_{MSE} = \mathcal{E}\{n_x(k)^2\} - \mathbf{w}^T \mathcal{E}\{\mathbf{n}_r(k)\mathbf{n}_r(k)^T\}\mathbf{w} - 2\mathbf{w}^T \mathcal{E}\{\mathbf{n}_r(k) n_x(k)\}. \tag{3.22}$$

This function can be minimized by applying an iterative procedure such as the steepest-descent method:

$$\mathbf{w}(k) = \mathbf{w}(k-1) + \mu \mathcal{E}\{\mathbf{n}_r(k) n_x(k)\} - \mathcal{E}\{\mathbf{n}_r(k)\mathbf{n}_r(k)^T\}\mathbf{w}(k-1)) \tag{3.23}$$

where μ is the so-called step-size parameter. For this iteration, however, knowledge of the statistical parameters, i.e. the correlation matrix $\mathcal{E}\{\mathbf{n}_r(k)\mathbf{n}_r(k)^T\}$ and the cross-correlation vector $\mathcal{E}\{\mathbf{n}_r(k) n_x(k)\}$, is required. Since in our case only data sequences are given, the statistics have to be estimated from these data. Substituting the statistical parameters with instantaneous estimates, i.e. leaving out the expectation operators, leads to the so-called least mean squares (LMS) algorithm.

$$\mathbf{w}(k) = \mathbf{w}(k-1) + \mu \mathbf{n}_r(k)(n_x(k) - \mathbf{n}_r(k)^T \mathbf{w}(k-1)) \tag{3.24}$$

Note that the error between the noise in the primary signal and the filter output $(n_x(k) - \mathbf{n}_r(k)^T \mathbf{w}(k-1))$ is used to steer the adaptation. This makes sense because if the error is small, the filter weights do not need to be altered, but if the error is large, they need to be changed a lot. The step-size parameter μ controls the speed of adaptation. The stable range for μ is inversely proportional to power of the input signal $\mathbf{n}_r(k)$. An alternative algorithm which is robust with respect to power variations, is the normalized LMS algorithm

(NLMS). It uses a normalization of the step-size by means of a quantity that behaves roughly as the power of the input signal, i.e. $\mathbf{n}_r(k)\mathbf{n}_r(k)^T$

$$\mathbf{w}(k) = \mathbf{w}(k-1) + \frac{\mu}{(\alpha^2 + \mathbf{n}_r(k)^T\mathbf{n}_r(k))}\mathbf{n}_r(k)(n_x(k) - \mathbf{n}_r(k)^T\mathbf{w}(k-1)) \quad (3.25)$$

where α is a small constant to prevent overflow in case that $\mathbf{n}_r(k)\mathbf{n}_r(k)^T = 0$. For time-varying systems, μ should be sufficiently large to track the variations. On the other hand, a large step-size may result in a high excess mean squared error. Furthermore, in order to ensure a stable filter, μ must be smaller than 2.

Reduction of arterial pulsations with adaptive filtering

In this subsection, the performance of the ANC for the given application with optical data is briefly discussed. Both the NIRS-signals (primary signal) and the pulse oximeter signal (noise reference) were preprocessed with the above mentioned bandpass filter. An adaptive filter with 300 taps was used and the adaptation constant of the NLMS algorithm was set to 0.1.

A segment of the CDC3-signal of Fig. 3.8(a) is enlarged in Fig. 3.14(a). The filtered signal (bandpass and adaptive NLMS) is shown in Fig. 3.14(b). Fig-

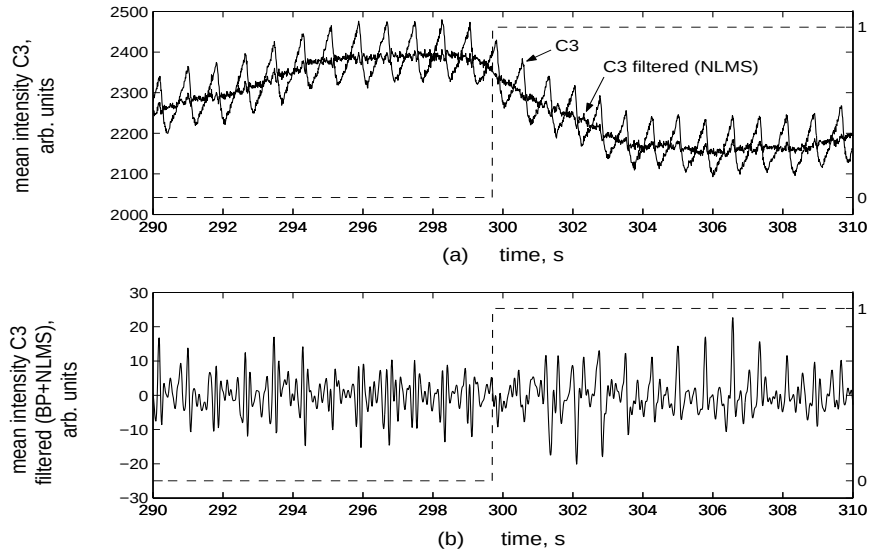

Figure 3.14: Representative (filtered) signals. The solid lines, corresponding to the left axes, are: (a) CDC3 signal of subject 3 before and after adaptive filtering (NLMS) to reduce the arterial pulsations, (b) CDC3 signal of subject 3 filtered with an eighth order Butterworth bandpass filter (1-10Hz) and NLMS to reduce arterial pulsations. The dotted line, which corresponds to the right axes, indicates when the subject is tapping: 1 means tapping, 0 means rest.

ure 3.14(a) also shows the CDC3-signal after adaptive filtering only (no bandpass filtering) to clearly illustrate the reduction of the arterial pulsations.

Comparing the power spectra of both signals, as shown in Fig. 3.15, illustrates the effect of the ANC more clearly. The power spectra were estimated using Welch's method with non-overlapping windows of 1920 samples (20 s), corresponding to the tapping- and rest-periods. The peaks at the heart rate and its harmonics are strongly reduced in the filtered signal. Some residual of the arterial pulsations can be observed in the power spectrum of the filtered CDC3-signal as peaks at higher harmonics of the heart rate. This is probably due to a somewhat different shape of the pulse in the pulse-oximeter signal, which is measured in a finger, than that in the optical signals in the brain.

The tracking performance of the ANC is illustrated in Fig. 3.16, which shows the frequency responses of the ANC at different time instants. In order to estimate the frequency responses of the ANC, the transfer function of the system with the primary signal $x(k)$ as input and the error $e(k)$ as output was calculated. The transfer functions are estimated using Welch's averaged periodogram method on windows of 12 s. The signals of subject 9 between 100 s and 140 s seconds were used because there was a clear variation in heart rate during this period, as shown in Fig. 3.11. Fig. 3.16(a) shows the estimates of the frequency response of the ANC in the beginning (100 s - 112 s) and at the end (124 s - 136 s) of this period. Fig. 3.16(b) shows the power spectra, also estimated using Welch's method with the same parameters, of the pulse oximeter signal during the same periods. The frequency response of the ANC

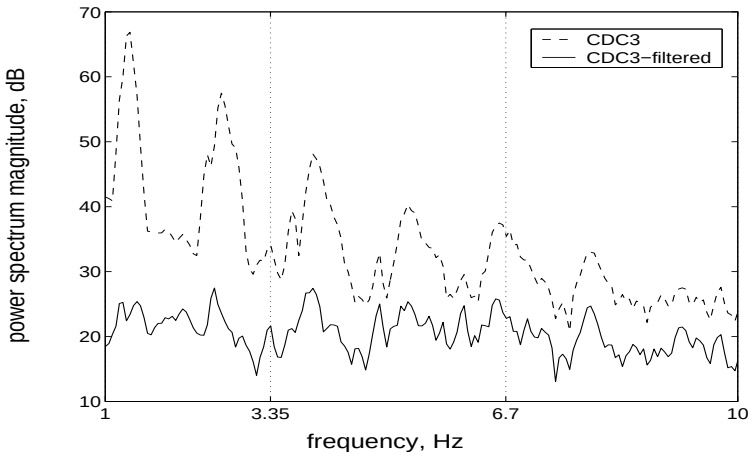

Figure 3.15: Power spectra of the signals in Fig. 3.14: the CDC3-signal of subject 3 and the filtered CDC3-signal (bandpass and adaptive). Note: the spectra were shifted vertically in order to obtain a clear figure.

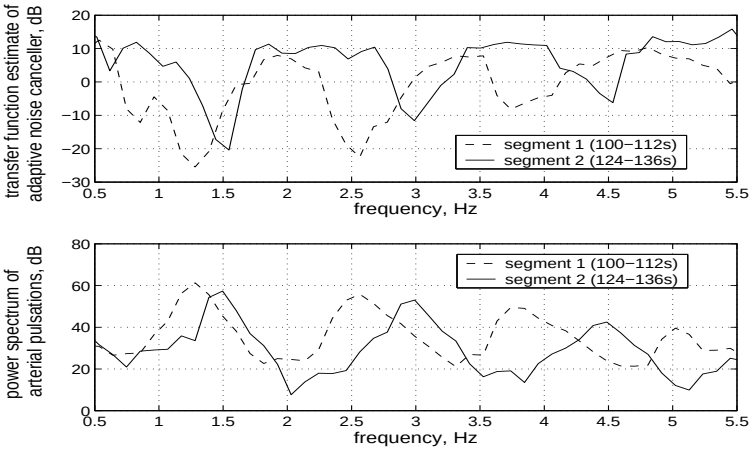

Figure 3.16: (a) Estimate of the frequency response of the ANC at different time instants (b) Power spectra of the arterial pulsations at the corresponding time instants.

consists of stopbands around the heart rate and its harmonics, as can be inferred from comparison with the spectra of the pulse oximeter signal. The heart rate increases from approximately 75 bpm (1.25Hz) during the first segment to 90 bpm (1.50 Hz) during the second segment. Therefore, the third harmonic of the heart rate during the first segment (3.75 Hz) is right in the middle between the second (3 Hz) and third (4.5 Hz) harmonic of the heart rate during the second segment. Remember that also the tapping frequency was between 2 and 3 times the heart rate, implying that, in this case, it would not be possible to remove the heart rate and its harmonics with fixed filters without also removing the tapping signal. Furthermore, using an adaptive filter makes the methodology more general in the sense that it is not necessary to have prior knowledge about the tapping frequency. On the other hand, the pulse oximeter signal or another signal which can be used as noise reference must be available.

Since the arterial pulsations are much smaller, or can not be observed at all, in the PH-signals due to the higher noise, the effect of the ANC on the PH-signals is smaller.

Detection of the tapping signal in the filtered optical signals

As shown in Fig. 3.15, a very small peak at the tapping frequency can be observed in the power spectra of the filtered signals. However, this peak is so small that it would not be possible to identify it without prior knowledge of the tapping frequency. To determine whether the observed peaks in the power are actually caused by the stimulation, the power at the tapping frequency during

consecutive tapping- and rest-periods was compared. The power spectra were calculated in this case for each tapping- and rest-period with 3 overlapping windows whose length was half the considered period. For each stimulation period, the tapping period was determined from the spectrum of the tapping (finger movement) signal; the same frequency was used to calculate the power during the following rest period. The Wilcoxon rank-sum test was used to determine whether the power at the tapping frequency during tapping-periods was significantly different from that during rest-periods [114]. This test, which calculates the probability that the given data (or more extreme) are observed if both populations would have the same mean, allows to compare and summarize the results of the different measurements in a simple way. The results are summarized in Table 3.2, which gives the lowest p-value among all channels for each measurement together with the number of channels with a p-value less than 0.05. In some measurements, one or two optical signals were saturated and

Table 3.2: Overview of the subjects and summary of the significance of the filtered DC- and PH-signals.

subj. no.	filter	detected harmonic	DC rank-sum minimum p-value	DC no. channels with $p < 0.05$	PH rank-sum minimum p-value	PH no. channels with $p < 0.05$
1	NLMS	3rd	0.0002	4/14	X	0/14
2	NLMS	1st	0.0030	7/15	0.0019	2/15
3	NLMS	1st	0.0003	11/16	0.0379	1/16
4	NLMS	2nd	0.0002	9/16	0.0148	2/16
5	HF	1st	0.0104	2/14	0.0281	1/14
6	NLMS	3rd	X	0/14	0.0047	2/14
7	NLMS	3rd	0.0002	4/16	X	0/16
8	NLMS	1st	0.0499	1/14	0.0379	1/14
9	NLMS	2nd	0.0002	4/16	X	0/16
10	HF	2nd	0.0011	1/14	X	0/14
11	HF	2nd	0.0019	1/15	X	0/15
12	NLMS	1st	0.0022	4/14	X	0/14
13	NLMS	1st	0.0207	1/14	X	0/14
14	NLMS	3rd	X	0/14	0.0281	1/14

X: not significant ($p > 0.05$)

therefore excluded from the analysis. For each significant signal, it was verified that the difference was in the right direction, i.e. that the power during tapping-periods was larger than that during rest-periods. In some measurements, where the peaks at the 2nd or 3rd harmonic were more clear in the power spectrum than the peak at the tapping frequency itself, the respective harmonic was used for the detection, as indicated in Table 3.2.

In 49 DC-signals (24%) out of 206, the power at the tapping frequency during tapping-periods is significantly different from that during rest-periods at a level of $p < 0.05$. In 8 subjects (out of 14), more than one channel with $p < 0.05$ is found. For the smallest p-value among all channels for each measurement, the significance level was lowered to $p < 0.003$ according to multiple testing corrections. Note that this is a conservative approach based on the Bonferroni inequalities, although the channels are not independent (since they interrogate the same tissue) and that it is actually not expected to see a fast signal in all channels (localized fast signal). In 9 (out of 14) subjects a significant DC channel is found at the $p < 0.003$ level, 7 of these correspond to subjects where more than one channel with $p < 0.05$ was found.

In 10 PH-signals out of 206 (5%) a p-value below 0.05 was observed. One channel (subject 2) is significant at the level of $p < 0.003$. The 2 channels in this subject that are significant at the $p < 0.05$ level, are also significant at the $p < 0.05$ level in the corresponding DC channels (same source-detector pair). It was also noted that in subject 9, when the 3rd harmonic is analyzed (not shown in the Table 3.2), 6 DC-channels and 8 PH-channels are significant at the $p < 0.05$ level; 5 of those channels are significant in both DC and PH.

For the detection of the tapping using the rank-sum test, prior knowledge of the tapping frequency and the beginning and end of the tapping periods was used. In order to determine if tapping periods can be detected in the filtered signals without this prior knowledge, the spectrogram of the filtered signals were calculated. The spectrogram of the filtered CDC3-signal is shown in Fig. 3.17. Compared to Fig. 3.10, the reduction of the arterial pulsations is clearly visible, especially for the first three harmonics. The higher harmonics are the dominant peaks in the spectra. No peaks at the tapping frequency can be observed during tapping periods.

3.3.5 Independent component analysis (ICA)

Filtering allowed us to reduce the physiological interferences and the noise in the individual optical signals, and to detect the tapping-related fast signal by using prior knowledge about the tapping frequency and periods. Without this prior knowledge, however, the fast signal can not be observed in individual NIRS signals. Therefore, we will try to exploit the information in different NIRS signals (light bundles) simultaneously by applying a multichannel technique. One such method which has been used to separate weak signals contaminated with artifacts and noise is independent component analysis (ICA). The goal of ICA, also referred to as 'blind source separation' (BSS), is the decomposition of a set of multichannel data in a linear mixture of statistically independent source signals. Assuming that the tapping is statistically independent from other physiological sources (arterial pulsations, respiration), it is expected that ICA is able to separate the fast signal. ICA was thus applied to the set of

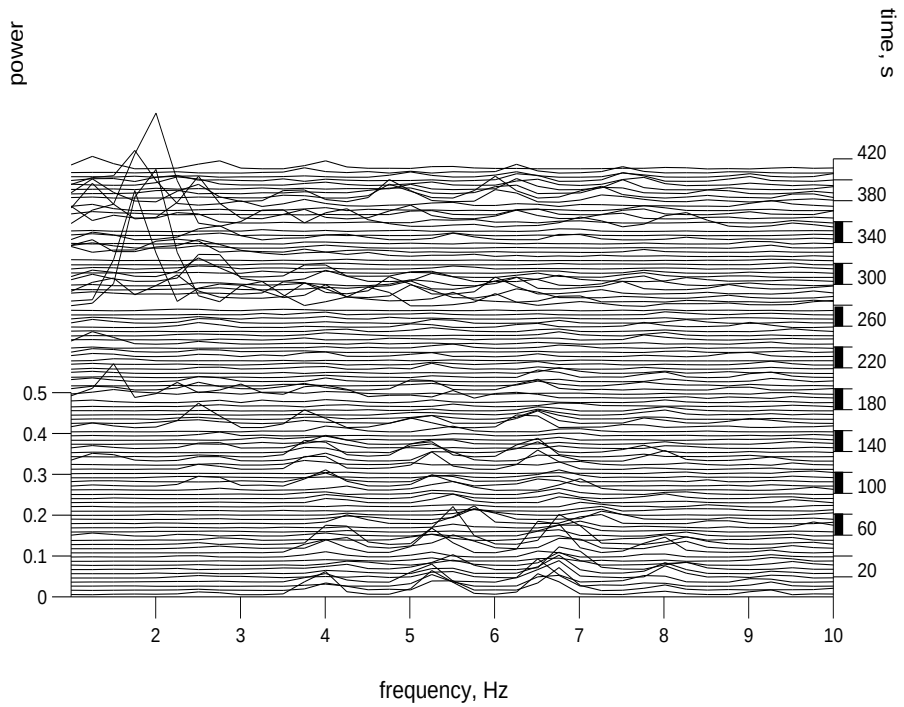

Figure 3.17: Spectrogram of the filtered CDC3-signal. The tapping periods are marked by the black squares parallel to the time axis.

NIRS signals in order to extract a signal component where the fast signal can be detected more clearly than in the (filtered) optical signals themselves. In this section, the principles of ICA are first briefly discussed, and the ICA-algorithm we used presented. Then, the application of ICA to the NIRS signals is discussed.

Basic ICA

The goal of ICA is to find linear combinations of a set observed signals that are statistically independent. Assuming that the observed signals are linear mixtures of statistically independent source signals, ICA allows to recover blindly the source signals from the observed signals. Blindly, because both the mixing matrix as well as the source signals are a priori unknown.

Each observed variable $x_i, i = 1, \ldots, m$ is modelled as a linear combination of n sources $s_i, i = 1, \ldots, n$:

$$x_i = a_{i1}s_1 + a_{i2}s_2 + \ldots + a_{in}s_n, \qquad \forall i = 1, \ldots, m \tag{3.26}$$

or, using matrix notation:

$$\mathbf{x} = \mathbf{A}\mathbf{s} \tag{3.27}$$

where $\mathbf{x}$ is a vector of size m representing the observations, $\mathbf{A}$ the $m \times n$ mixing matrix and $\mathbf{s}$ a vector of size n representing the n sources. Without loss of generality, it can be assumed that both $\mathbf{x}$ and $\mathbf{s}$ have zero mean: if this is not true, $\mathbf{x}$ can always be centered by subtracting the sample mean. The goal is to identify the mixing matrix $\mathbf{A}$ and/or the source vector $\mathbf{s}$, only from the corresponding observations $\mathbf{x}$. The effect of noise, which is not included in this basic ICA model, will be considered later.

The basic assumption used to solve this problem is that the components of $\mathbf{s}$ are mutually statistically independent. Random variables s_i and s_j are said to be independent if information on the value of s_i does not give any information on the value of s_j for $i \neq j$. Technically, random variables s_i are independent if and only if the joint probability density function (pdf) can be factorized, i.e. $p(s_1, s_2, \ldots, s_n) = p_1(s_1)p_2(s_2)\ldots p_n(s_n)$ where $p_i(s_i)$ represents the marginal pdf of s_i, i.e. the pdf of s_i when it is considered alone. A second assumption is that the sources must have non-gaussian distributions, except for one source. This assumption is necessary if the estimation of the ICA model relies on the higher order cumulants, which are zero for gaussian distributions. However, in a specific class of ICA methods, this assumption is replaced by an assumption on the time structure of the signals. Third, it is often assumed that the number of observations is at least equal to the number of sources, i.e. that the mixing matrix is at least square, and invertible. Under the preceding three assumptions, the ICA model is identifiable, meaning that the mixing matrix and the sources can be estimated up to some trivial indeterminacies [40]. Since both $\mathbf{A}$ and $\mathbf{s}$ are unknown, the variances and the order of the sources can not be determined. It is easy to see that any change in the magnitude or the order of the sources can always be cancelled by a corresponding change in the mixing matrix.

ICA can be seen as a fine-tuning of the well-known principal component analysis (PCA), also referred to as whitening, which decomposes the observed signals in a linear mixture of uncorrelated components. Since uncorrelatedness is a weaker form of independence (considering only second order statistics), it is not sufficient to estimate the ICA model. The weaker condition results in a rotational indeterminacy of the solution, i.e. the mixing matrix remains unknown up to an orthogonal transformation [47]. To overcome this indeterminacy, one has to rely on information not contained in the covariance matrix, typically higher-order statistics. However, as PCA is a standard procedure and simplifies the problem of ICA, it is the first step in most ICA algorithms. PCA reduces the determination of the $m \times n$ mixing matrix $\mathbf{A}$ to that of an orthogonal $n \times n$ matrix. Furthermore, PCA can be used to reduce the dimension of the data.

The unknown orthogonal matrix can be determined in several ways, usually involving some kind of higher-order information. One approach, followed for example in the fastICA-algorithm [99], consists of finding linear combinations of maximum non-gaussianity, as measured by kurtosis or (approximations of) negentropy. Closely related methods are based on maximum likelihood estimation or the minimization of mutual information, as for example in the 'Infomax'-algorithm [18]. An algebraic approach is based on tensors, generalizations of matrices to more than two dimensions. As a generalization of the eigenvalue decomposition of the covariance matrix to perform PCA, the diagonalization of higher-order cumulant tensors can be used for ICA estimation, as for example in the 'JADE'-algorithm [34, 47]. All these methods are based on the assumption that the sources are non-gaussian. For temporally correlated signals, on the other hand, this assumption can be replaced by assumptions on the time structure of the sources. In this class, several methods exist, based on assumptions regarding the covariance matrices or the nonstationarity of the sources [19, 234, 133]. Since the optical signals are temporally correlated, we used an algorithm that exploits this time structure, namely SOBI [19]. The SOBI-algorithm, in which the determination of the matrix $\mathbf{U}$ is based on the simultaneous diagonalization of a set of covariance matrices at different lags, is described in the next subsection.

So far, we assumed that the data were noiseless, which is not correct when dealing with real-life data such as the optical signals considered. Most methods taking noise into account explicitly assume that the noise is additive and gaussian. Two types of additive noise can be distinguished. Sensor noise leads to the following noisy ICA model $\mathbf{x} = \mathbf{A}\mathbf{s} + \mathbf{n}$, where $\mathbf{n} = (n_1, \ldots, n_m)$ is the noise vector. If the noise has some particular, known covariance structure, the mixing matrix can still be estimated using ordinary ICA methods. The sources $\mathbf{s}$ however can no longer be identified, because they cannot be completely separated from the noise. The same holds for source noise, leading to the corresponding noisy ICA model $\mathbf{x} = \mathbf{A}(\mathbf{s} + \mathbf{n})$ with $\mathbf{n} = (n_1, \ldots, n_n)$. In this case, ordinary ICA methods yield the mixing matrix $\mathbf{A}$ and the noisy independent components $\tilde{s}_i = s_i + n_i, i = 1, \ldots, m$. Another special case that reduces to the basic ICA model is found when the sum of the number of sources k and noise components l is smaller than the number of observations m. In this case, the noise variables can be considered as extra sources and ordinary ICA methods will find the real sources as the k most non-gaussian sources. In more general cases, however, little is known about the effect of noise on the performance of ICA algorithms. One observation is that noise tends to 'smear' the sources over several estimated independent components, i.e. that ICA is not able to completely separate all sources anymore [68]. In practice, it is therefore usually helpful to filter the observed signals in order to reduce the noise, when dealing with temporally correlated signals.

Anyway, ICA has turned out to be useful in many real-life applications. Ap-

plications can be found in many different areas such as audio processing (cocktail party problem), biomedical signal processing and telecommunications. In the biomedical field, ICA has been used to analyze electrical (EEG, ECG), magnetic (MEG) and hemodynamic (fMRI) signals [105]. In EEG and MEG analysis, ICA has been used to separate artifacts, i.e. signals not generated by brain activity but by some external disturbances such as eye muscle artifacts [216, 217]. ICA has also been used to decompose event-related evoked potentials in EEG signals [13, 217]. In ECG analysis, ICA has been used for the separation of maternal and fetal ECGs recorded simultaneously from cutaneous electrodes placed on the mother's abdomen [48]. In fMRI, ICA has been used to separate independent spatial and/or temporal activity patterns [128, 33].

ICA for temporally correlated signals: SOBI

Since we are specifically considering time signals in this section, the time index k will be explicitly mentioned. Let us consider the noisy ICA model

$$\mathbf{x}(k) = \mathbf{y}(k) + \mathbf{n}(k) = \mathbf{A}\mathbf{s}(k) + \mathbf{n}(k), \tag{3.28}$$

where $\mathbf{n}(k)$ is assumed to be additive, spatially and temporally white noise, i.e. $\mathcal{E}\{\mathbf{n}(t+\tau)\mathbf{n}^*(k)\} = \sigma^2\delta(k)\mathbf{I}_m$ where σ is the noise variance, $\delta(k)$ is the Kronecker delta and $\mathbf{I}_m$ the identity matrix. The covariance matrix $\mathbf{R}_x(0)$ of the observations $\mathbf{x}$ at zero lag can then be written as:

$$\begin{aligned} \mathbf{R}_x(0) &= \mathcal{E}\{\mathbf{x}(k)\mathbf{x}^*(k)\} && (3.29)\\ &= \mathbf{A}\mathbf{R}_s(0)\mathbf{A}^T + \sigma^2\mathbf{I}_m && (3.30)\\ &= \mathbf{A}\mathbf{A}^T + \sigma^2\mathbf{I}_m. && (3.31) \end{aligned}$$

As the sources are assumed to be independent, the covariance matrix of the sources is positive and diagonal. As the variance of the source signals can not be determined, they are assumed to be normalized, and hence $\mathbf{R}_s(0) = \mathbf{I}_m$.

The first step of the algorithm consists of whitening the signal part $\mathbf{y}(k)$ of the observations, i.e. calculating an $n \times m$ matrix $\mathbf{W}$ such that transformed signals $\mathbf{W}\mathbf{y}(k)$ are 'white', meaning that its components are uncorrelated and their variances equal unity (hence $\mathcal{E}\{\mathbf{W}\mathbf{y}(k)\mathbf{y}^*(k)\mathbf{W}^T\} = \mathbf{I}_n$). Using the ICA model, it follows that:

$$\mathcal{E}\{\mathbf{W}\mathbf{y}(\mathbf{k})\mathbf{y}^*(\mathbf{k})\mathbf{W}^T\} = \mathbf{W}\mathbf{A}\mathbf{A}^T\mathbf{W}^T = \mathbf{I}_n. \tag{3.32}$$

Together with Eq. (3.31), this shows that a whitening matrix $\mathbf{W}$ can be determined from the covariance matrix $\mathbf{R}_x(0)$, provided the noise covariance matrix is known or can be estimated. This can be achieved using the eigenvalue decomposition of $\mathbf{R}_x(0)$, i.e. $\mathbf{R}_x(0) = \mathbf{E}\mathbf{D}\mathbf{E}^T$ with $\mathbf{E}$ the orthogonal matrix of

eigenvectors and $\mathbf{D}$ the diagonal matrix of its eigenvalues $\lambda_i, i = 1, \ldots, m$. Under white noise assumptions, the noise variance σ^2 can be estimated as the average of the $m - n$ smallest eigenvalues of the covariance matrix $\mathbf{R}_x(0)$. The whitening matrix can then be written as $\mathbf{W} \equiv (\mathbf{D}_n - \sigma^2\mathbf{I}_n)^{-1/2}\mathbf{E}_n^T$, where $\mathbf{D}_n$ represents the $n \times n$ submatrix of $\mathbf{D}$ containing the n largest eigenvalues, $\mathbf{E}_n$ the $m \times n$ submatrix of $\mathbf{E}$ containing the corresponding n eigenvectors and where the matrix $(\mathbf{D}_n - \sigma^2\mathbf{I}_n)^{-1/2}$ is computed by an element-wise operation as $(\mathbf{D}_n - \sigma^2\mathbf{I}_n)^{-1/2} = diag\{(\lambda_1 - \sigma^2)^{-1/2}, \ldots, (\lambda_n - \sigma^2)^{-1/2}\}$. It is easy to check that the whitened signals $\mathbf{W}\mathbf{y}(k)$ satisfy $\mathcal{E}\{\mathbf{W}\mathbf{y}(k)\mathbf{y}^*(k)\mathbf{W}^T\} = \mathbf{I}_n$.

From Eq. (3.32), it also follows that any orthogonal transformation of $\mathbf{W}$ to the right is also a whitening matrix. So, there are an infinity of different matrices $\mathbf{W}$ that give uncorrelated, but not necessarily independent, components. The indeterminacy can be expressed as follows:

$$\mathbf{A} = \mathbf{W}^\dagger\mathbf{U} \tag{3.33}$$

where $\mathbf{U}$ is an unknown $n \times n$ orthogonal matrix and the superscript † denotes the Moore-Penrose pseudoinverse. So, whitening is not sufficient to obtain independent components, but it reduces the determination of the $m \times n$ mixing matrix $\mathbf{A}$ to that of an orthogonal $n \times n$ matrix $\mathbf{U}$.

To overcome the above mentioned indeterminacy, in basic ICA usually higher order information is used. In the SOBI algorithm, however, the temporal correlations of the observations are exploited to determine the matrix $\mathbf{U}$. The idea is to find a matrix that, in addition to making the instantaneous covariances (at zero lag) of the transformed observations go to zero, also nullifies the covariances at non-zero lags. The rationale is that also the lagged covariances should be zero due to the independence of the sources. Using Eq. (3.27) and Eq. (3.33), the covariance matrix of the whitened observations $\mathbf{z}(k) = \mathbf{W}\mathbf{x}(k)$ at lag τ can be written as:

$$\begin{aligned}
\mathbf{R}_z(\tau) &= \mathcal{E}\{\mathbf{z}(t+\tau)\mathbf{z}^*(k)\} && (3.34)\\
&= \mathbf{W}\mathbf{R}_x(\tau)\mathbf{W}^T && (3.35)\\
&= \mathbf{W}\mathbf{A}\mathbf{R}_s(\tau)\mathbf{A}^T\mathbf{W}^T && (3.36)\\
&= \mathbf{U}\mathbf{R}_s(\tau)\mathbf{U}^T \qquad \forall\tau \neq 0 && (3.37)
\end{aligned}$$

Since $\mathbf{R}_s(\tau)$ is diagonal, the orthogonal matrix $\mathbf{U}$ can be obtained as an orthogonal diagonalizing matrix of a whitened covariance matrix for some non-zero lag τ. More robust results are obtained by calculating a matrix that simultaneously diagonalizes a set of L whitened covariance matrices at different lags $\tau_i, i = 1, \ldots, L$. Note that this method also works for gaussian sources, while ICA using higher order information does not. On the other hand, a limitation of this method is that sources with identical autocovariances (power spectra), can not be estimated.

In summary, the SOBI algorithm consists of the following steps:

1. Estimate the sample covariance matrix $\hat{\mathbf{R}}(0)$ from N data samples.
2. Calculate the eigenvalue decomposition of $\hat{\mathbf{R}}(0) = \hat{\mathbf{E}}\hat{\mathbf{D}}\hat{\mathbf{E}}^T$ and estimate the whitening matrix as $\hat{\mathbf{W}} \equiv (\hat{\mathbf{D}}_n - \hat{\sigma}^2\mathbf{I}_n)^{-1/2}\hat{\mathbf{E}}_n^T$
3. Form sample estimates $\hat{\mathbf{R}}_z(\tau_i)$ by computing the sample covariance matrices of $\hat{\mathbf{z}}(k) = \hat{\mathbf{W}}\mathbf{x}(k)$ for a fixed set of time lags $\tau_i, \quad i = 1, \ldots, L$.
4. Calculate an orthogonal matrix $\hat{\mathbf{U}}$ as the matrix that simultaneously diagonalizes the set $\{\hat{\mathbf{R}}(\tau_i)|i = 1, \ldots, L\}$.
5. Estimate the mixing matrix as $\hat{\mathbf{A}} = \hat{\mathbf{W}}^\dagger\hat{\mathbf{U}}$ and/or the independent components as $\hat{\mathbf{s}}(k) = \hat{\mathbf{U}}^T\hat{\mathbf{W}}\mathbf{x}(k)$.

For each subject, the SOBI-algorithm was applied to the set of DC-signals and to the set of PH-signals. The optical signals used as input for SOBI consisted of 40000 samples, comprising all tapping- and rest-periods. Both raw and filtered signals were analyzed and the results are compared in the next subsections. We always estimated as many independent components as there were observations, i.e. 16. In some subjects, one or two optical signals were saturated and therefore excluded from the analysis. In this case ($m = n$), the estimation of the whitening matrix reduces to $\hat{\mathbf{W}} \equiv \hat{\mathbf{D}}^{-1/2}\hat{\mathbf{E}}^T$. The number L of lagged covariance matrices to be diagonalized was set to 10. This value was based on simulations showing that the performance of SOBI increases with increasing L, especially in difficult environments (poor SNR, small spectral difference, etc.) [19]. For $L > 6$, however, the additional performance gain is very small. The time lags τ_i used were equally spaced with a difference of 10 samples between consecutive lags, i.e. $\tau_1 = 10, \tau_2 = 20, \ldots, \tau_{10} = 100$ samples. Experiments with various other lags showed that these values yield the best results for our data, although the differences were relatively small.

SOBI applied to raw signals

SOBI was applied to the set of raw DC-signals of each subject, as well as to the set of raw PH-signals. Assuming that the fast signal is independent of other physiological interferences such as the arterial pulsations and the noise, SOBI is be expected to separate the fast signal, or at least -since the noise will hamper the separation- a component containing mainly the fast signal together with reduced physiological interferences and noise.

Figure 3.18 shows the power spectrum of an IC calculated from the raw DC-signals of the subject 3. A peak can be observed at the tapping frequency (3.35 Hz). Also the arterial pulsations can be observed as peaks at the heart

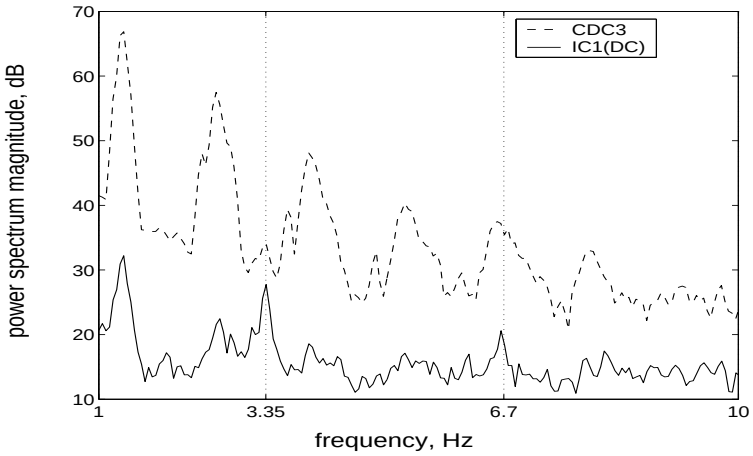

Figure 3.18: Power spectra of the CDC3-signal of subject 3, and the IC containing the fast signal, calculated with SOBI from the set of raw DC-signals. Note: the spectra were shifted vertically in order to obtain a clear figure.

rate and its harmonics, although they are much smaller than in the spectrum of the raw DC-signals. Compared to the power spectrum of the filtered CDC3-signal shown in Fig. 3.15, it is noted that, although the residual of the arterial pulsations is larger, the peak at the tapping frequency can more clearly be observed in the power spectrum of the IC. This shows the ICA can be useful for separating the fast signal, although the separation is not perfect. Usually, many ICs contain the arterial pulsations and possibly some other signals such as the fast signal or respiration.

As with the filtered signals, the Wilcoxon rank-sum test was used to identify independent components (ICs) where the power at the tapping frequency is higher during tapping periods than during rest-periods. For each subject, the lowest p-value, obtained with the rank-sum test, among all ICs is given in Table 3.3. The number of significant ICs is not mentioned as the fast signal is not expected to be present in every IC. The p-values are similar to those of filtered signals in Table 3.2. In 5 subjects, a significant IC is found at the $p < 0.003$ level. Most of these subjects also had one or more significant DC-signals. In the PH-signals, few significant ICs are found.

The spectrogram of the IC containing the fast signal of subject 3 is shown in Fig. 3.19. The heart rate is the dominant frequency in this IC. However, also small peaks at the tapping frequency can be observed during several tapping periods that are not present during the rest-periods. This shows that the peak at the tapping frequency in the power spectrum of Fig. 3.18 is indeed due to the fast signal and that the fast signal can be observed without using prior knowledge about the tapping frequency or periods.

Table 3.3: Significance of the independent components calculated from the raw DC- and PH-signals.

subj. no.	detected harmonic	SOBI(DC) rank-sum minimum p-value	SOBI(PH) rank-sum minimum p-value
1	3rd	0.0070	X
2	1st	0.0002	0.0006
3	1st	0.0002	0.0499
4	2nd	0.0002	X
5	1st	0.0379	X
6	3rd	X	X
7	3rd	0.0002	X
8	1st	0.0070	0.0379
9	2nd	0.000003	X
10	2nd	0.0379	X
11	2nd	X	X
12	1st	0.0411	X
13	1st	X	X
14	3rd	0.0499	X

X: not significant ($p > 0.05$)

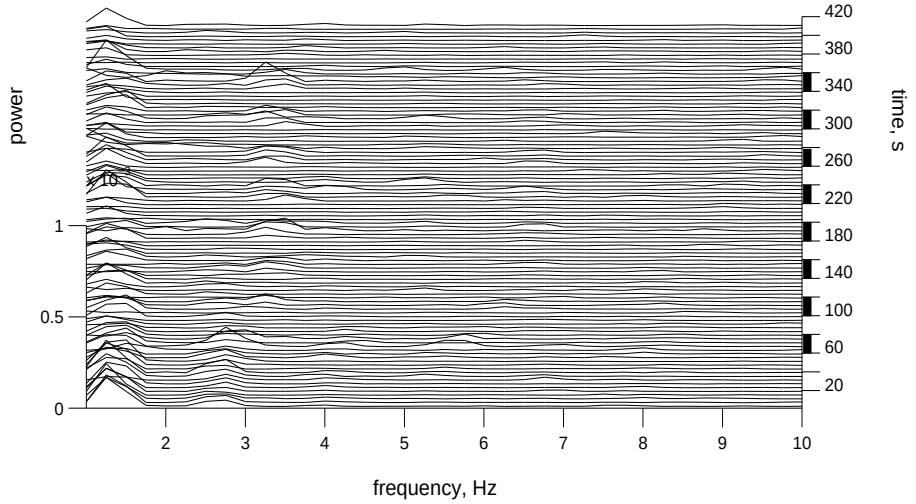

Figure 3.19: Spectrogram of the first IC calculated from the raw DC-signals of subject 3. The tapping periods are marked by the black squares parallel to the time axis.

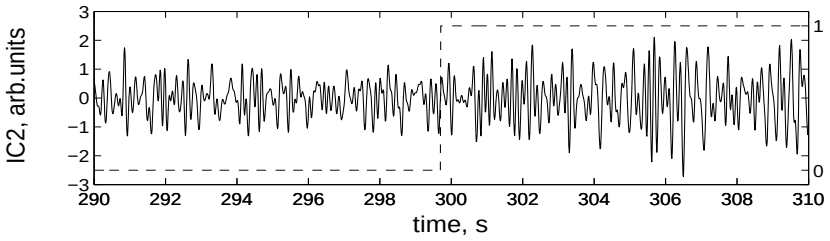

Figure 3.20: Time course of IC2, calculated from the set of all filtered DC-signals of subject 3. The dotted line, which corresponds to the right axes, indicates when the subject is tapping: 1 means tapping, 0 means rest.

SOBI applied to filtered signals

As the separation of the fast signals is hampered by noise and the arterial pulsations, SOBI was also applied to the filtered optical signals (filtering as described in section 3.3.4). Fig. 3.20 shows the second independent component (IC2) calculated from the set of all filtered DC-signals of subject 3. This IC looks somewhat different during the tapping-period than during the rest-period, although it is not possible to directly identify a tapping-related fast signal in this time series.

The power spectrum of IC2, on the other hand, as shown in Fig. 3.21, clearly shows that this IC contains the fast signal. The dominant peaks in the power

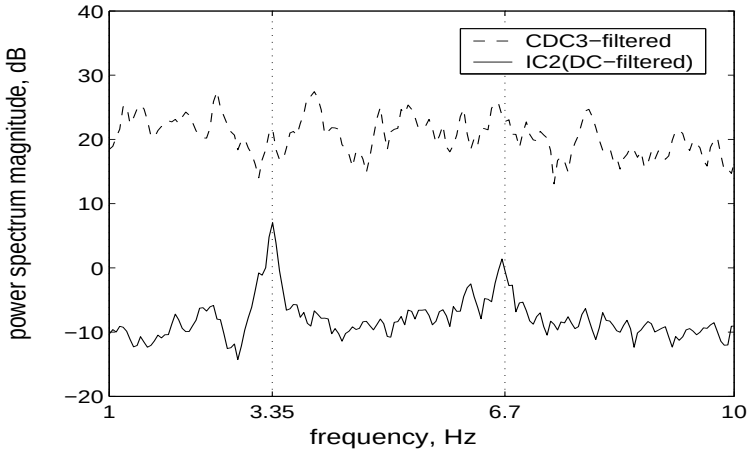

Figure 3.21: Power spectra of the filtered CDC3-signal of subject 3, and the IC containing the fast signal, calculated with SOBI from the set of filtered DC-signals. Note: the spectra were shifted vertically in order to obtain a clear figure.

spectrum of this IC are at the tapping frequency (3.35 Hz) and its second harmonic (6.7 Hz). This IC only contains the fast signal, while the other ICs contain the (residual) arterial pulsations and/or noise. The peak at the tapping frequency is much larger in the power spectrum of IC2 than in that of the filtered signals itself. Comparison with the power spectrum of the ICs calculated from the raw signals, shown in Fig. 3.18, shows that filtering the signals before applying ICA, improves the separation.

The power at the tapping frequency during consecutive tapping- and rest-periods is shown in Fig. 3.22. The large difference in power between tapping- and rest-periods, shows that the peak observed in the power spectrum is caused by the finger tapping.

The Wilcoxon rank-sum test was used to determine whether the difference in power at the tapping frequency during tapping- and rest-periods was statistically significant. For IC2 of subject 3, the spectrum of which is shown in Fig. 3.21, the p-value is 0.0002. This is actually the lowest possible value that can be obtained with the rank-sum test for the given sample size (16 data points), meaning that the power at the tapping frequency during any tapping period is larger than the power during all rest-periods, as shown in Fig. 3.22. In Table 3.4 the lowest p-value among the ICs is given for each measurement. The used filters and harmonics are the same as given in Table 3.2. Considering the DC-signals, in 9 subjects a significant IC is found at the $p < 0.003$ level. It is noted that for all these subjects, the significance of the ICs is higher than that of the DC-channels (lower p-value), reflecting the improved separation of the tapping signal by applying ICA. Concerning the PH-signals, in 4 subjects the lowest p-value among all ICs was lower than 0.05, among which the subject with a significant PH-channel at the $p < 0.003$ level. Considering the 3rd harmonic of subject 9 (not shown in Table 3.4), which has 8 PH-channels with a p-value below 0.05, the lowest p-value observed among the ICs was $p = 0.0001$.

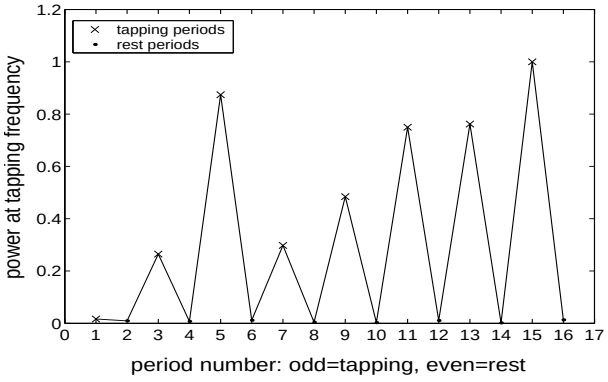

Figure 3.22: Power of IC2, calculated from the set of all filtered DC-signals of subject 3, at the tapping frequency during consecutive tapping- and rest-periods.

Table 3.4: Significance and the number of detected tapping periods of the independent components from the filtered DC- and PH-signals.

subject no.	DC: p-value rank-sum test (20 s-windows)	DC: detected tapping-periods (4 s-windows)	PH: p-value rank-sum test (20 s-windows)	PH: detected tapping-periods (4 s-windows)
1	0.0002(*)	6/8	X	0/8
2	0.0002(*)	7/8	0.0379	0/8
3	0.0002(*)	7/8	X	0/8
4	0.0002(*)	7/8	X	0/8
5	0.0003	7/8	X	0/8
6	0.0379	0/8	X	0/8
7	0.0002(*)	8/8	0.0104	0/8
8	0.0148	0/8	0.0281	0/8
9	0.000003	15/16	X	0/8
10	0.0006	5/8	X	0/8
11	0.0499	0/8	0.0047	0/8
12	0.0022(*)	5/6	X	0/8
13	0.0207	0/8	X	0/8
14	0.0379	0/8	X	0/8

(*): lowest possible p-value for rank-sum test of given sample size
X: not significant ($p > 0.05$)

The independent component containing the fast signal allow us to identify the tapping periods individually. Figure 3.23 shows the spectrogram of the IC containing the fast signal. All tapping periods except the first can clearly be distinguished in the spectrogram of the IC. Even the shift of the tapping frequency in each tapping period and between tapping periods can be observed (compare with Fig. 3.12).

Figure 3.24 shows the power at the tapping frequency, as in Fig. 3.22 but for 'arbitrary' (not perfectly coinciding with tapping- and rest-periods) time windows of 4 s. The tapping frequency was determined in this case from the spectrogram of the IC (optical signal) itself, by selecting, for each instant in time, the maximum of the STFT over the frequency range of interest. In order to determine in a more objective way which tapping periods can be detected, the following simple procedure was followed. The mean plus twice the standard deviation of the power at the tapping frequency during the baseline period (the first minute of the measurement, without stimulation) was used as threshold level. A tapping period (of 20 s) was considered as detected when the threshold was exceeded three or more times (out of 5, for non-overlapping

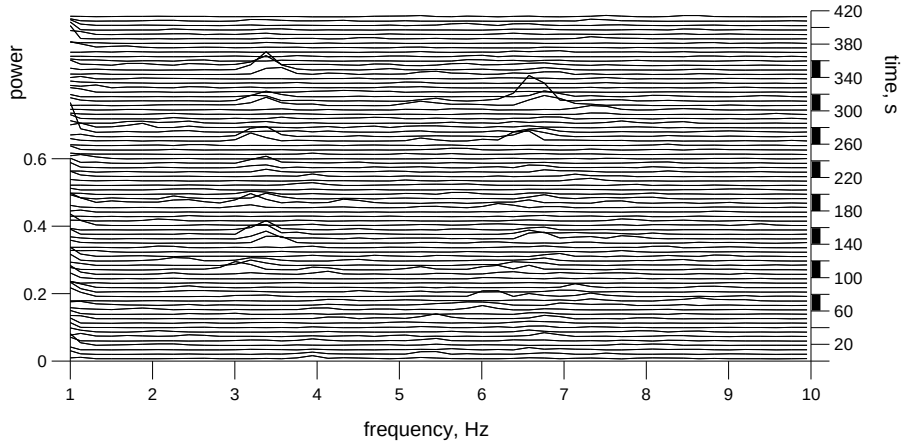

Figure 3.23: Spectrogram of IC2 calculated from the set of filtered DC-signals of subject 3. The tapping periods are marked by the black squares parallel to the time axis.

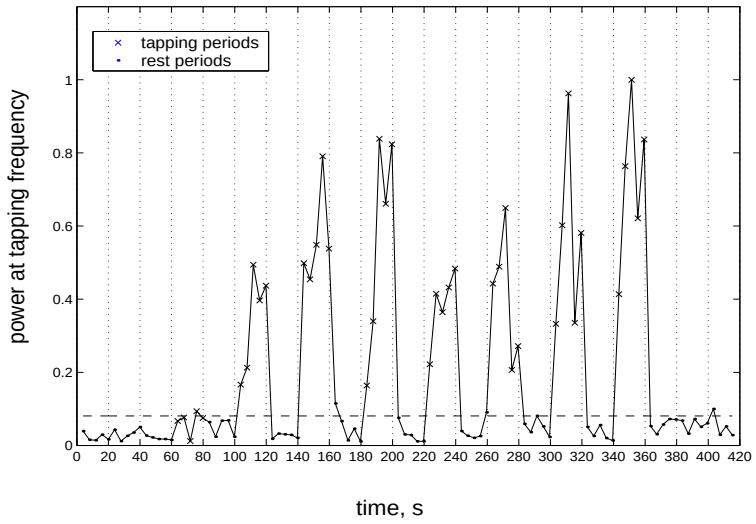

Figure 3.24: Power of IC2, calculated from the set of all filtered DC-signals of subject 3 at the tapping frequency as a function of time (non-overlapping windows of 4 s). The dashed line represents the threshold level used for the detection of tapping.

windows of 4 s) during that tapping period. As shown in Fig. 3.24, all except the first tapping period in the spectrogram of Fig. 3.12 are detected in this way. Also for the other measurements, the tapping periods detected in this way agree very well with those that can be distinguished by visual inspection in the corresponding spectrograms. As this procedure does not use the tapping signal in any way, it allows us to quantify which tapping periods can be detected using only the optical signals, as shown in Table 3.4. Considering the 9 subjects with significant ICs at the $p < 0.003$ level (calculated from the DC-channels), 67 out of 78 tapping periods (85%) are detected individually.

3.3.6 Discussion

Considering the DC-signals, in 9 subjects an IC was found in which the power during tapping-periods was significantly larger than during rest-periods (subjects 1-5,7,9,10,12). The used significance level of $p < 0.003$ is a conservative value taking into account multiple testing corrections. Furthermore, the 9 subjects include all 8 subjects where several significant DC-channels at the $p < 0.05$ level were found; the remaining subject with an IC with a p-value below 0.003, had one DC-channel which was also significant at the $p < 0.003$ level. In 6 of these 9 subjects, the p-value of the IC was actually the lowest possible value that can be obtained with the rank-sum test for the given sample size (16 or 12 data points), meaning that the power at the tapping frequency during any tapping period is larger than the power during all rest-periods. Considered together, these findings show that the considered ICs contain a fast signal related to the finger tapping. In these 9 subjects where the fast signal was detected in the DC-signals, 67 out of 78 tapping periods could be identified individually in the spectrogram of the IC containing the fast signal. Since the fast signal is expected to be very localized, the most likely reason for not finding the fast signal in all subjects, is that the sensor, which is relatively small, was not precisely in the right position. Measurements with larger sensors, with more sources and detectors, could answer this question. In the same context, localization of brain activity based on the fast optical signal could be an interesting topic for further research. As the fast signal is expected to be more localized, this technique could have a higher spatial resolution than techniques based on the slow signal, at least for the more superficial cortical areas (the penetration of NIR light is limited to a few centimeters from the skull). As the weights of the ICA mixing matrix corresponding to the IC containing the fast signal, can be considered as a measure of the contribution of the fast signal to each light bundle, ICA could be useful for localization.

There was one subject with a significant PH-channel at the $p < 0.003$ level. The fact that the 2 channels in this subject which are significant at the $p < 0.05$ level are also significant at the $p < 0.05$ level in the corresponding DC channels (same source-detector pair), suggests that the observed low p-values are not due to chance. The same could be assumed for the 3rd harmonic in subject 9, where

5 (out of 16) channels are significant in both DC and PH at the $p < 0.05$ level, and the lowest p-value among the ICs was $p = 0.0001$. In general, however, the fast signal could not be reliably detected in the PH-signals, probably because there is too much noise in the PH-signals.

Our statistical analysis shows that the described fast signal in the DC signals is not due to random noise. Furthermore, it cannot be a movement artifact caused by direct mechanical coupling between the finger tapping and the optical sensors because it is localized. Therefore, we conclude that the observed fast signal originates from neuronal activity. These findings confirm and extend the results of a previous study, in which a subset of these measurements were analyzed using a method based on the cross-correlation function of the optical signals with the tapping signal (finger movement) over the complete measurement period of 5 minutes [227]. In 54 AC-, 174 DC- and 10 PH-signals (always out of 367) fast changes were found that were significant at the $p < 0.05$ level (25 AC-, 134 DC- and 1 PH-signal at the $p < 0.001$ level respectively). In the latter study, it was also shown that the localization of the fast signal is in reasonable agreement with the slow signal. So, in the data presented here (from the motor cortex) as well as in other data (from the visual cortex) recorded in the same laboratory with frequency-domain NIRS, a significant fast signal is observed in the DC- but not in the PH-signals [227, 228]. We only found indications of the fast signal in the phase in 2 out of 14 subjects, which is probably due to the high noise in the phase signals.

Relatively few other studies describing the non-invasive detection of a fast neuronal signal in humans using NIRS have been published so far. The possibility of measuring non-invasively fast optical signals related to neuronal activity in humans was first reported by G. Gratton et al. in 1995 [74, 79]. Since then, his research group, the cognitive neuroimaging lab (CNL) of the Beckman Institute at the University of Illinois at Urbana-Champaign (UIUC), has run several additional studies in which a fast neuronal signal was measured by NIRS in response to various stimuli [78, 177, 50, 77]. In their publications, the fast signal is referred to as "event-related optical signal"(EROS). Another, independent research group at UIUC, the laboratory for fluorescence dynamics (LFD) of the Department of Physics, from which the data described here were obtained, and a group from Berlin, the Berlin Neuro-Imaging Center (BNIC), also reported fast neuronal signals measured by NIRS [227, 228, 193]. Very recently, Franceschini at al., from the Anthinoula A. Martinos Center for Biomedical Imaging, Massachusetts General Hospital, Harvard Medical School, reported the detection of the fast optical signal with CW NIRS during finger-tapping, tactile stimulation, and electrical median nerve stimulation [66]. Comparing these studies is difficult, however, because they differ in several aspects such as the type of stimulation, the instrumentation, source-detector distance, the kind of signal processing etc. The type of stimulation for example determines which area of the brain is activated. This in turn affects the fast signal because

its amplitude is dependent on the depth of the origin of the signal.

The first studies of Gratton et al. in 1995 described increases in the phase of a frequency-domain NIRS instrument in a small number of subjects (3 and 4) respectively in the visual [74] and the motor cortex [79]. The latter study describes fast changes in the optical parameters of brain tissue during a tapping exercise. In this study, the power at the tapping frequency (0.8 Hz) was compared in NIRS measurements contralateral and ipsilateral to the hand performing the tapping. Significant fast optical changes were observed in the PH-signals but not in the DC-signals, while slow, hemodynamic effects were observed both in PH- and DC-signals. Simulations were performed which showed that the PH-signal is more sensitive to changes in deeper layers than the DC-signal, thereby suggesting that the fast effects may occur in deeper layers than the slow effects. Several other studies in the visual [74, 78, 77], auditory [177] and motor [50] cortex, were conducted by the same group. In all these studies, only fast neuronal changes in the PH-signals are reported but not in the DC-signals, as opposed to the present study.

The BNIC-group failed to detect a change in the phase in the visual cortex [199], although they used a similar experimental set-up as Gratton et al. in 1995 [74]. According to Gratton, this can be explained by the fact that the study did not include any systematic mapping of occipital areas, nor contralateral control of stimulated areas or averaging across subjects [77]. The BNIC-group also conducted a study using continuous-wave NIRS instrumentation where a decrease in the intensity of the reflected light was observed following somatosensory stimulation [193].

Franceschini et al. detected fast intensity changes during functional activation using CW NIRS instrumentation with 8 source and 16 detector positions, covering both the contralateral and ipsilateral cortex simulatenously. A fast signal was detected in 43% (9/21) of the measurements during finger-tapping, 60% (12/20) of those during tactile stimulation, and 22% (4/18) during electrical median nerve stimulation [66]. The robustness and validity of the detected fast signals was assessed using 5 criteria to avoid misinterpretation due to possible measurement artifacts. One of these criteria required spatial localization of the fast signal in a small area contralateral to the stimulated hand to avoid false detection of the fast signal due to motion artifacts. Additionally, the authors report Monte Carlo simulations showing that a focal scattering change in the cortex that causes a 0.1% change in intensity only causes a 0.008° phase shift [66]. This could also explain the higher detection rate of the fast signal in DC-signals relative to PH-signals observed in our data.

Based on studies conducted in single neurons [195], in populations of neurons at the macroscopic level [176] and (invasively) in animals [123], all authors of the cited literature assume that the fast signal originates from changes in light scattering. However, it can not be excluded that the reported fast signals in

human subjects are related to changes in light absorption. From the phase relationship between the fast DC signal and the fast PH signal, it could be deduced whether the changes are caused by absorption or by scattering. However, as we could not reliably detect the fast signal in the phase, we are not able to clarify this aspect. Further research should aim at detecting fast signals in both DC and PH signals in order to determine whether the observed fast neuronal changes are due to absorption or to scattering effects.

An important methodological difference between the present work and the cited studies on the fast neuronal signal, concerns the signal processing techniques. Most other studies use a folding average approach which is not effective in our case because the tapping frequency is not perfectly constant, contrary to the stimulation frequency in the case of visual or somatosensory stimulation. Using adaptive filtering and ICA, however, we were able to separate a component from the optical signals in which individual stimulation periods can be identified. The advantage of the presented approach, which can be applied as well in other cases such as visual stimulation, is that less measurement time is required per subject or more types of tests can be carried out within the measurement period. Furthermore, new effects such as habituation can be studied.

3.4 Conclusions

Near infrared spectroscopy (NIRS) is an optical technique that can be used to analyze human tissue non-invasively due to the relatively good transparency of biological tissue in the near-infrared range. The two most important types of interaction of NIR light with biological tissue are absorption and scattering. The most important absorbing compounds in tissue are oxygenated (HbO_2) and deoxygenated (Hb) hemoglobin. The variation in concentration of these compounds results in changes in absorption, and hence in the light attenuation that is measured. Compared to absorption, the light attenuation due to scattering is high but relatively constant in time. Different models can be used to determine concentration changes or other parameters from the measured light attenuation. Using the modified Beer-Lambert law, absolute concentration changes can be calculated from light intensity measurements at different wavelengths. Using the diffusion approximation describing the propagation of photons in a highly scattering medium, absolute quantification is possible. Time-resolved methods (TRS), either in time- or in frequency-domain, allow to determine absolute concentrations. Spatially resolved spectroscopy (SRS), allows to calculate the tissue oxygenation index (TOI), a measure of (cerebral) hemoglobin oxygen saturation. Our research contributed to two applications of NIRS.

The first application is the monitoring of cerebral circulation and oxygenation

in neonates. In collaboration with the Department of Paediatrics at University Hospitals Leuven (Gasthuisberg), different studies regarding the clinical use and validation of NIRS have been conducted. A commercial NIRS device was used to measure concentration changes of HbO_2, Hb, cerebral blood flow (CBF) and volume (CBV), and TOI. In the first study, cerebral TOI was measured in prematurely born infants. It was found that TOI is a stable parameter reflecting the cerebral venous oxygen saturation and that TOI increases during the first three days of life. In the second study, the effect of rewarming on the cerebral circulation and oxygenation of very preterm infants with hypothermia was investigated. No negative effects of rewarming on the cerebral oxygenation were found. In the third study, the assessment of cerebral autoregulation based on NIRS measurements was investigated. Concordant changes in mean arterial blood pressure (MAP) and cerebral intravascular oxygenation (HbD) measured non-invasively with NIRS, are assumed to reflect impaired cerebral oxygenation. A new method to quantify the concordance of MAP and HbD was proposed and compared to correlation and coherence analysis. The first measurements suggest that the new method and the correlation coefficient are better parameters to detect impaired cerebral autoregulation. A larger follow-up study is necessary, however, to confirm the performance of the parameters and to evaluate the predictive value of the different parameters with respect to possible brain damage statistically.

The second application was functional monitoring of brain activity using NIRS. Functional NIRS relies on the changes of the optical properties of the brain tissue related to functional activation. Two types of changes can be observed: the fast signal, with a response time on the order of milliseconds, which is directly related to neuronal activity, and the slow signal, with a response time on the order of seconds, which is related to hemodynamic changes in the activated area. The fast signal is much smaller than the slow signal (and other physiological signals) and is therefore difficult to detect, but it is more localized than the slow signal because it is directly related to neuronal activity. Our research contributed to the detection of the fast signal in the motor cortex. Low-noise frequency-domain NIRS instrumentation, using 4 crossed source-detector pairs, was used to study the fast neuronal signal related to a finger tapping exercise. The arterial pulsatility, which was the main source of physiological noise, was first reduced using an adaptive filter. On the filtered signals, independent component analysis was applied to separate a signal component due to the neuronal activity. In 9 out of 14 subjects, an independent component could be extracted from the intensity signals where the power at the tapping frequency during stimulation was significantly larger than during rest. In those 9 subjects, 67 out of 78 tapping periods could be identified individually in a time-frequency plot of the independent component. In the phase signals, we only found indications of the fast signal in 2 out of 14 subjects.

Chapter 4

Heart rate variability of neonates

In this chaper, the heart rate variability of neonates is analyzed. The main goal of this study is to investigate if abnormal cardiorespiratory events can be predicted from the heart rate recorded during a polysomnography. Standardized HRV parameters as well as recently introduced methods are used to quantify different aspects of HRV. Special attention is paid to detrended fluctuation analysis (DFA), a method which characterizes the scaling behaviour of a time series. The methodology for calculating all HRV measures is fine-tuned for our neonatal heart rate data. All HRV measures are calculated for a number of preterm neonates, divided in three age-matched groups according to the occurrence of abnormal cardiorespiratory events during the polysomnography and the eventual home monitoring. The values of the HRV parameters obtained in the present study as well as the differences between behavioural states, are compared to results reported in literature.

4.1 Introduction

4.1.1 Polysomnography and evaluation of cardiorespiratory control in neonates

Polysomnography is the continuous, simultaneous recording of physiological parameters such as ECG, respiration, peripheral oxygen saturation (SaO_2), EMG, EEG and EOG during several hours. With respect to neonates, clinicians

gained interest in polysomnographies after a controversial [1] study describing an association between central apneas and the sudden infant death syndrome (SIDS) [194]. Prospective studies, however, did not confirm the predictive value of polysomnographies, and in particular apneas, for determining which infants are at risk of SIDS [1]. Nevertheless, instead of being used as a diagnostic tool for SIDS, polysomnography has become a well established method to evaluate the cardiorespiratory control. In the neonatal intensive care unit (NICU), polysomnographies are usually performed in prematurely born infants to determine the degree of maturation in cardiorespiratory control, or in infants having experienced an apparent life threatening event (ALTE). ALTE is characterized by a combination of apnea (temporally not breathing), color change (cyanotic or pallid), decreased muscle tone (limpness), choking or gagging and requires significant intervention (vigourous shaking, mouth-to-mouth breathing, or full cardiopulmonary resuscitation) [1]. Epidemiological studies indicate that both groups, preterms and ALTE, are at increased risk of extreme cardiorespiratory events compared to normal, term infants [174]. As it has been shown that subsequent life threatening events can be predicted with a single polysomnography, this can be used for the identification of high risk infants who need cardiorespiratory home monitoring, the continuous bedside measurement of heart rate, respiration and eventually SaO_2 [44].

In the University Hospitals Leuven (Gasthuisberg), every year several hundreds of polysomnographies are recorded, in survivors of ALTE and in preterm infants with possibly immature cardiorespiratory control. The criteria for an abnormal polysomnography are central or obstructive apnea for more than 15 s combined with a bradycardia below 60 bpm and/or oxygen desaturation below 80%, or a bradycardia below 50 bpm for > 4 s. Cardiorespiratory home monitoring is prescribed for infants with an abnormal polysomnography. The home monitoring is also evaluated with bradycardia below 50 bpm for > 4 s as criterium for abnormal follow-up [44]. According to the results of the polysomnographies (PS) and the follow-up (FU), the infants can thus be divided in 3 groups: NN (normal PS, normal FU), AN (abnormal PS, normal FU), AA (abnormal PS, abnormal FU).

The goal of our study is to investigate if life threatening cardiorespiratory events can be predicted from the fluctuations of the heart rate during periods without abnormal bradycardia (below 50 bpm for > 4 s). More specifically, it will be investigated if the aforementioned groups (NN, AN, AA) can be distinguished using measures of heart rate variability calculated on segments without abnormal bradycardia. If this is possible, the identification of risk infants could be done using shorter recordings, and the eventual misclassification of risk infants

[1] The study was based on the observation of apnea, documented by cardiorespiratory monitoring during prolonged hospitalization, in 2 infants who died unexpectedly after discharge from the hospital. Both infants were siblings of 3 infants who had died suddenly at home earlier. More than 2 decades later, evidence of infanticide for all 5 infants in the original report became known.

as normal because no abnormal event occurred during the polysomnography could be avoided. Furthermore, it could provide insight in the mechanisms causing life threatening events. The underlying hypothesis is that the deficiencies in the autonomic nervous system that cause the life-threatening events are reflected in the heart rate not only by abnormal bradycardia but also by more subtle, latent changes.

4.1.2 Heart Rate Variability

It is well known that the heart rate (HR) of a normal healthy individual is not entirely regular but fluctuates constantly over time as a result of counteracting influences of the autonomic nervous system [121]. The cardiac parasympathetic (vagus) nerves decrease the heart rate, whereas the sympathetic nerves accelerate it. As the heart rate is primarily controlled by the autonomic nervous system, the analysis of the fluctuations in instantaneous heart rate, referred to as heart rate variability (HRV), represents a non-invasive marker of autonomic activity.

The first documented observation of HRV is often credited to Hales in 1733, who described fluctuations in the heart rate of a horse synchronous to the respiration [23]. The clinical relevance of HRV was acknowledged in 1965 when Hon and Lee noted that fetal distress was preceded by alterations in HRV before any appreciable change occurred in the heart rate itself [91]. Since then, HRV has been extensively studied in various investigations. Reduction in HRV is often associated with pathological conditions of the heart and nervous system [120]. Several studies confirmed the clinical potential of HRV for the assessment of diabetic neuropathy and the prognosis of risk after acute myocardial infarction in adults [201]. Although HRV has been the subject of numerous clinical studies investigating several other diseases and clinical conditions, the practical use of HRV is hitherto mainly oriented towards the two aforementioned clinical scenarios [10, 17, 152, 188, 16, 201, 96].

Given a sequence of RR intervals, the durations between consecutive heart beats, several methods can be used to quantify the variations in the heart rate. Perhaps the simplest measures are time-domain statistics such as the standard deviation. Better separation between short- and long-term variability is obtained in the frequency-domain: spectral analysis provides information of how the power (variance) is distributed as a function of frequency of the fluctuations. Different frequency bands can be associated with different physiological mechanisms such as respiration (high frequencies), baroreceptor reflex (low frequencies) and thermoregulation (very low frequencies). The time- and frequency-domain measures are the most commonly used HRV parameters in clinical studies. In order to facilitate the comparison and interpretation of the results of different investigations, standards for the measurement and calculation of these HRV parameters were proposed in 1996 by the Task Force of

the European Society of Cardiology and the North American Society of Pacing and Electrophysiology [201]. Although these (second-order) measures are also often referred to as 'linear' (since they can be used to (fully) describe linear systems), we will use the term 'standard' HRV measures. During the last decade, various other methods, often originating from non-linear dynamical and/or chaotic system theory, such as Lyapunov exponents, entropy measures, fractal analysis and correlation dimensions have been applied to HRV data [71, 26, 169, 35, 233, 165, 16]. Among these newer methods, fractal analysis, which aims at quantifying the statistical self-similarity (scaling behaviour) of the time series, is a promising tool [26, 233, 165, 97, 184, 118, 3]. While the calculation and interpretation of the standard HRV measures is relatively straightforward, advances in understanding of the performance and interpretation of the newer methods are necessary before they can be used in a clinical setting.

Since the emergence of continuous monitoring of the electrocardiogram in neonatal intensive care units, neonatal HRV data has been used in various clinical studies. The maturation of the autonomic nervous system of infants has been studied by investigating the changes in HR and HRV during postnatal development and with behavioural state [83, 187, 160, 144, 143]. Heart rate variability of neonates has also been investigated in various pathophysiological conditions, often related but not restricted to SIDS or respiratory abnormalities. The investigation of the HR and/or HRV in relation to SIDS and ALTE is based on the hypothesis that there is a deficiency in autonomic cardiorespiratory control in SIDS victims and infants who experienced an ALTE. Several studies compared HR and HRV between SIDS victims or ALTE infants and normal infants (for an overview see [161, 181]). Since the standards for HRV proposed by the Task Force [201] are not directly applicable to neonates (see section 4.2) and many studies were performed before these standards were published anyhow, most studies used different methodologies for HRV calculation. Although comparison of different studies is difficult due to differenes in methodology, however, inconsistent or even conflicting results have been found [161, 181]. Specifically with respect to ALTE infants, two studies reported significantly decreased HRV and increased HR during quiet sleep in ALTE infants compared to normal infants [115, 162]. A recent study, on the other hand, found significantly increased HRV during quiet sleep in ALTE infants as compared to normals and no significant differences in HR [56].

4.2 Neonatal heart rate data

Physiological influences such as respiration, baroreceptor reflex and thermoregulation introduce rhythmical fluctuations in the heart rate. Heart rate and HRV are also affected by other factors such maturation [108, 36, 58], behavioural

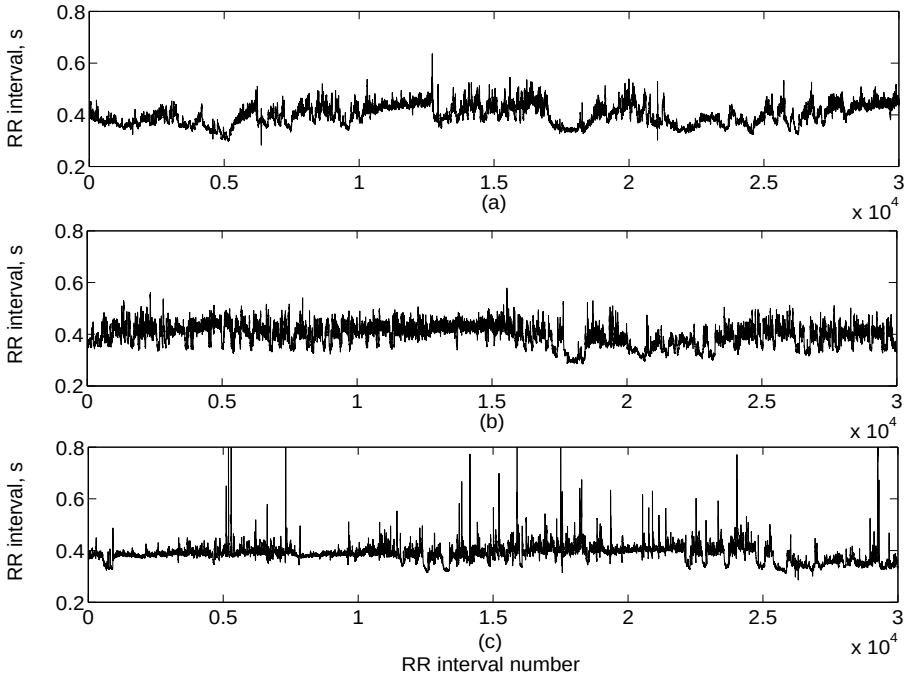

Figure 4.1: Examples of neonatal RR interval series.

state [175, 192], sleeping position [72, 8] and body movements. In this section, properties of HR and HRV that are specific for neonates are addressed [42]. A few representative examples of neonatal RR interval series are shown in Fig. 4.1. Note that the mean heart rate of these neonates is approximately 150 bpm (2.5 Hz), corresponding to a mean RR interval of 0.4 s.

Respiratory sinus arrhythmia (RSA) is a periodic fluctuation in the heart rate associated with respiration: an increase in heart rate during inspiration and a corresponding decrease during expiration [205, 191, 161]. Since the sampling frequency of the RR interval series is inherently equal to the heart rate, only fluctuations with a frequency lower than half the HR can be observed in the RR interval series (Nyquist theorem). Since the respiration rate in neonates, around 40-80 breaths/minute, is sometimes larger than half the heart rate, around 120-160 bpm, RSA can not always be observed in neonates. The strength of RSA (power of HRV at the respiratory frequency) depends on the respiratory frequency: the lower and more regular the respiratory frequency, the stronger RSA [175, 11]. As a consequence, RSA is stronger during quiet sleep than during active sleep or wakefulness. Other respiratory events such as sighs [59], respiratory pauses (apneas) [41] or periodic breathing also influence the heart rate. During periodic breathing periods of normal respiration are alternated

with periods without respiration, and this period is reflected in the heart rate. The duration of these periods, at birth usually in the range between 5 and 10 s, decreases with postnatal age [156, 223]. Periodic breathing is a very common respiratory pattern in preterm infants that is usually not of pathologic significance [69]. As some infants breath periodically up to 40% of the time, it is important to take it into account when evaluating HRV [90].

Other rhythmical fluctuations can be observed at lower frequencies in Fig. 4.1(b), or more clearly in Fig. 4.12(a). These oscillations with a period around 30 heart beats (10 s) are present in most RR interval series, and not only during quiet sleep segments. The amplitude of the fluctuations is usually around 0.03 s (corresponding to HR changes of 10 bpm), but this varies throughout the RR interval series. Although this '10s-rhythm' has been described in many other studies, its origin is not exactly known. It is believed to be related to the Mayer waves observed in blood pressure and is attributed to baroreceptor reflex [161]. Similar low frequency rhythms are also observed in the heart rate of adults [122]. Some other phenomena cause similar rhythms in the RR interval series. The fluctuations introduced by non-nutritive sucking (NNS), for example, have a period of on average 12 s and an amplitude of approximately 10 bpm [140]. NNS is common in neonates, but usually the duration of NNS is only a fraction of the total recording time.

Besides RSA and the 10s-rhythm, in some RR interval series even slower rhythmical fluctuations are observed. Fluctuations with a period in the range between 20 s and 100s are often attributed to thermoregulation [102], although other physiological effects can cause similar HR fluctuations. This is the case in the RR interval series of Fig. 4.1(b) where fluctuations with a period of around 400 heart beats (2-3 min) are observed between beat number 5000 and 10000. From the other signals measured during the polysomnography, it was inferred that these were caused by body movement: 'bursts' of activity are alternated with rest periods.

Several studies investigated the effect of maturation, both gestational and postnatal age, on neonatal HR and HRV. The HR at birth decreases with gestational age [36], reaching approximately 120 bpm for healthy full-term infant at birth. During postnatal development, HR increases during the first weeks till about 160 bpm, and decreases continuously afterwards to 60-80 bpm in normal adults [144]. Total HRV increases with increasing gestational age [38, 192]. Upon reaching the age of term infants, HRV of prematurely born infants is often lower than in infants born at term suggesting delayed maturation [58]. With respect to the different spectral components of HRV, a relative increase of the power in the high frequency range with gestational age was reported in [36, 58] whereas a relative increase of the power in the low frequency range was found in [175]. Regarding the postnatal development of HRV, a longitudinal study found that HRV during quiet sleep decreases during the first postnatal weeks and increases afterwards [108]. On the other hand, increases in HRV

during the first postnatal days have also been reported [175, 32]. According to [2], this increase in HRV could mainly be attributed to the power in the low frequency range for full-term infants.

The behavioural state (awake, quiet sleep, active sleep) has an important effect on HR and HRV. Heart rate is lower during quiet sleep than during active sleep or wakefulness [161, 181]. Long term HRV is reported to be higher during active sleep than during quiet sleep, which can partly be explained by body movements. Short term HRV, on the other hand, is suggested to be higher during quiet sleep than during active sleep. The decreased (long-term) HRV during quiet sleep (QS) periods can be observed for example in Fig. 4.1(a) between RR intervals 10500 and 12500, and in Fig. 4.1(b) between RR intervals 13000 and 15000. Usually, QS periods can be identified in the RR interval series itself. Using other signals that were recorded during the polysomnography (EMG, EOG, respiration, EEG), it can be verified that those segments correspond to QS. The duration of the QS periods depends on age. For our recordings, the duration of QS periods is between 10 and 30 minutes, which corresponds to approximately 2000 to 4000 RR intervals.

Another specific heart rate pattern, which is not typical for preterm neonates but is also found in full-term neonates and sometimes in adults, can be observed Fig. 4.1(c). Throughout this RR interval series, a number of spikes can be observed. Two kinds of spikes can occur in RR interval series: spikes due to cardiac arrhythmias such as premature beats which affect only one or two RR intervals, and short HR decelerations. Faulty peak detection (missed RR peak or false detection) causes similar spikes as certain cardiac arrhythmias. As all faulty peak detection were manually corrected (based on the ECG recording), however, such spikes are not present in our RR interval series. The spikes shown in Fig. 4.1(c) are short decelerations in heart rate: an increase of the RR interval from 0.1 s to 0.4 s during 5 to 20 heart beats. In some cases, these decelerations are related to short apnea.

4.3 Standard time- and frequency-domain analysis of HRV

In this section, the standard time- and frequency-domain parameters of HRV as defined by the Task Force [201], and their application to neonatal data, are discussed.

4.3.1 Basic concepts

Time-domain analysis

The simplest parameters to evaluate HRV are time-domain, descriptive statistics such as the standard deviation. These statistics can be calculated on the RR intervals series itself or on the sequence of differences between consecutive RR intervals, emphasizing the short-term variability. A multitude of time-domain parameters has been used in various studies. Since many of these parameters are highly correlated with others, this study is limited to the parameters recommended in [201]:

1. SDNN: the standard deviation of the so-called normal-to-normal (NN) intervals, i.e. excluding ectopic beats, which is an estimate of overall HRV;
2. TI: the triangular index, defined as the total number of all NN intervals divided by the maximum of the density distribution (approximated on a discrete scale by the number of NN intervals in the modal bin). TI is a measure of overall HRV and is more influenced by the lower than the higher frequencies;
3. SDANN: the standard deviation of the average NN intervals calculated over periods of 5 minutes, which is an estimate of the changes in heart rate with periods longer than 5 minutes;
4. RMSSD: the square root of the mean of the squares of the differences between consecutive RR intervals, which is an estimate of the short-term HRV variability.

Frequency-domain (spectral) analysis

In 1981, the power spectral analysis of heart rate fluctuations was introduced providing more detailed information on the distribution of the power (variance) as a function of frequency and contributing to the understanding of the autonomic background of HRV [7]. Usually, three major peaks can be distinguished in the power spectrum of adult heart rate: a high-frequency (HF) peak at the respiratory frequency (RSA), a low-frequency (LF) peak synchronous to Mayer waves in blood pressure around 0.1 Hz, which is attributed to baroreceptor reflex, and very-low frequency (VLF) HR fluctuations presumably caused by thermoregulation [7]. As the distribution of the power and the central frequency of the LF and HF component may vary with changes in autonomic modulations of the heart period, the powers in three different frequency bands, each encompassing a spectral peak, are recommended as spectral HRV measures (VLF: 0.003 to 0.04 Hz, LF: 0.04 to 0.15 Hz, HF: 0.15 to 0.4 Hz). For long-term recordings sometimes an additional ultra low frequency band is used

(ULF: < 0.003 Hz). The power in the HF-band mainly reflects vagal or (parasympathetic) activity, while disagreement exists with respect to the LF component. The power in each band can also be expressed in normalized units, i.e. the ratio of the power in each band to the total power, in order to emphasize the balance of vagal and sympathetic activity and to minimize the effect of the changes in total power on the values of LF and HF power. Some studies suggest that LF, expressed in normalized units, is a quantitative marker of sympathetic modulations whereas others view it as reflecting both sympathetic and vagal activity. The ratio of LF power to HF power is recommended as a measure of sympathovagal balance.

4.3.2 Methodology

The methodology for calculating the standard HRV measures is based on the recommendations in [201]. In this section, the methodology we used to estimate the power spectrum of the inherently irregularly sampled heart rate is briefly discussed. In addition, two necessary modifications with respect to the recommendations of the Task Force [201] are proposed. First, the recommendations of the Task Force are intended for adults, and therefore certain aspects, especially regarding the spectral analysis, are inappropriate for neonatal data. Secondly, the sampling rate of our ECG recordings is lower than recommended by the Task Force. The effects of both aspects on the standard HRV measures are also discussed in this section.

Spectral analysis of HRV

Different time series can be used to represent heart rate variability: (1) the RR interval series, the sequence of consecutive RR interval durations, (2) the (instantaneous) heart rate (HR) sequence, the reciprocal of the RR interval series, (3) the recently introduced heart timing (HT) sequence, reflecting the deviation of the occurrence time of each beat from the mean RR interval [127] and (4) the event series consisting of a sequence of Dirac impulses placed at the beat occurrence times [127]. As each number of such a sequence corresponds to a single heart beat, these sequences are inherently irregularly sampled in time. Three different approaches can be used to estimate the power spectrum of such a sequence. By assuming that the signals are evenly sampled, standard methods for spectral estimation, such as the Fourier transform, can be used. In this case, the unit of the frequency variable of the spectrum is "cycles per beat", which can be converted to an average number of "cycles per second" (Hz) by multiplying it with the average heart rate. Alternatively, certain techniques such as the Lomb periodogram allow direct estimation of the power spectrum from irregularly sampled time series [113]. The third approach consists of using an interpolation method to recover an regularly sampled signal from the irregularly spaced samples prior to the power spectrum estimation. Depending

on the HR time series used and the spectral estimation method, slightly different power spectrum estimates are obtained. It was recently shown that the spectrum of an adequately interpolated HT signal more closely resembles the spectrum of the modulating signal according to the integral pulse frequency modulation (IPFM) model compared to the spectra of RR or HR series [127]. The IPFM model, which generates beat occurrence times by integrating a modulating signal, representing sympathetic and parasympathetic influences, up to a certain threshold, is assumed by many authors to explain the mechanism used by the autonomic system to control the heart rate [179]. Since the error is systematic, however, the results of comparative clinical studies are comparable for all methods. Furthermore, the differences obtained with the various methods are usually much smaller than the differences between patients in clinical studies. Therefore, in our study the spectrum was estimated from the regularly sampled interpolation of the HR signal following the recommendations of the Task Force [201]. A simple yet efficient algorithm was used for the derivation of the regularly sampled interpolation of the HR signal [22]. Whereas a sampling frequency of 4 Hz is mostly used for adults, we used a sampling rate of 8 Hz to account for the higher heart rate in neonates.

Effect of age on spectral analysis of HRV

Owing to the differences in heart and respiration rate between neonates and adults, the frequency ranges used to calculate the spectral HRV parameters as recommended by the Task Force for adults are inappropriate for neonates. As the respiration rate in neonates is usually between 40 and 80 breaths/minute (0.6-1.3 Hz), which is much higher than in adults (0.2-0.4 Hz), the upper frequency of the HF range must be increased to include the respiration frequency. Therefore, the frequency range 0.15-1.5 Hz was used for the HF power. As mentioned above, however, it should be noted that RSA can not always be observed in neonatal heart rate, i.e. when the respiration rate is higher than half the heart rate.

Effect of ECG sampling rate on standard HRV measures

The sampling frequency of the ECG determines the precision with which the occurrence times of the R-wave peaks, and hence the RR intervals, can be determined. Figure 4.2 illustrates the derivation of the an RR interval from a digitized ECG measurement. The solid line represents the (analog) ECG signal, and the crosses represent the exact occurrence times of two consecutive R-wave peaks, respectively $R(i-1)$ and $R(i)$. In the digitized ECG, represented by the dots, the samples closest to each R-wave peak are used to calculate the RR intervals. Assuming that the R-waves are symmetric, each of these samples corresponds to the highest data sample of an R-wave. If the errors on the occurrence times are denoted $\Delta R(i-1)$ and $\Delta R(i)$, the error on the

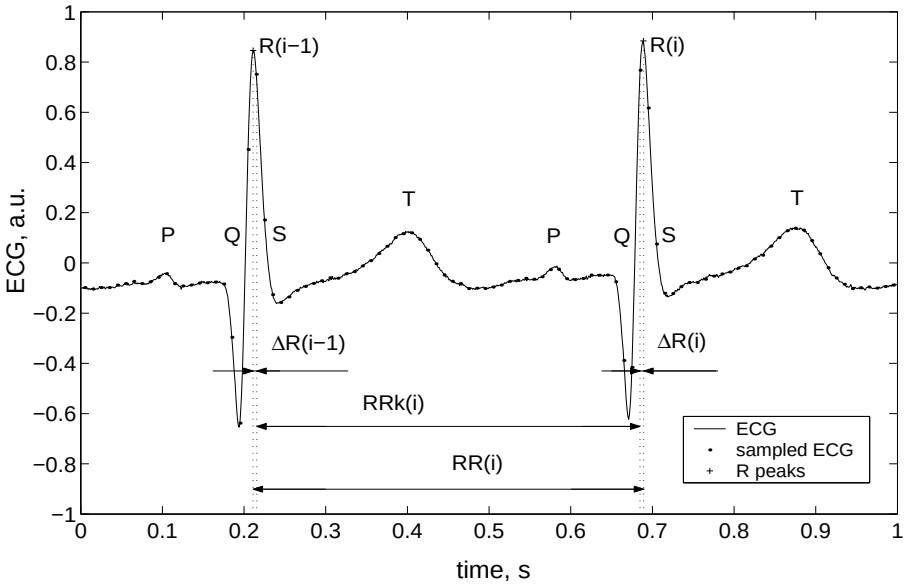

Figure 4.2: Effect of the ECG sampling frequency on the accuracy of the RR intervals.

RR interval, $\Delta RR(i)$, introduced by the finite ECG sampling frequency, can be written as:

$$\Delta RR(i) \equiv RRk(i) - RR(i) = \Delta R(i) - \Delta R(i-1) \tag{4.1}$$

where $RR(i)$ represents the exact RR interval and $RRk(i)$ the RR interval determined from the digitized ECG. Assuming that $\Delta R(i)$ is a sequence of independent, identically distributed random variables uniformly distributed on the interval $-1/(2f_s) \leq \Delta R(i) \leq 1/(2f_s)$, where f_s represents the ECG sampling frequency, the sequence of errors $\Delta RR(i)$ can be considered as a FIR-filtered white noise sequence (FIR-filter with transfer function $H(z) = 1 - z$). The addition of this error sequence $\Delta RR(i)$ to the exact RR interval series introduces a bias in the time- and frequency-domain HRV measures. As the statistics of the error sequence $\Delta RR(i)$ depend only on the ECG sampling frequency f_s, this bias can be compensated for. Since the variance of $\Delta RR(i)$ equals $1/(6f_s^2)$, the standard deviation of the exact RR interval series $R(i)$ can be estimated from the finite resolution RR interval series $RRk(i)$ as follows:

$$\sigma_{RR} \approx \sqrt{\sigma_{RRk}^2 - 1/(6f_s^2)} \overset{fs=100\ Hz}{=} \sqrt{\sigma_{RRk}^2 - (1/6).10^{-4}} \tag{4.2}$$

This correction was applied to the calculation of SDNN from RR interval series derived from ECGs sampled at 100 Hz. Similarly, a correction factor for the

RMSSD can be derived:

$$RMSSD_{RR} \approx \sqrt{RMSSD_{RRk}^2 - 1/(2f_s^2)} \overset{fs=100\ Hz}{=} \sqrt{\sigma_{RRk}^2 - 5.10^{-5}} \quad (4.3)$$

The accuracy of these corrections depend on the number of RR intervals used to calculate the HRV measures. The larger the number of RR intervals, the better the statistical properties of the sample distribution of the actual errors on the beat occurrence times $\Delta R(i)$ will match those of the assumed uniform distribution and the more accurate the corrections will be.

In order to verify if the proposed model for the error $\Delta RR(i)$ and the proposed corrections for the HRV measures hold, a sampling frequency of 1000 Hz was used for the ECG in 10 polysomnographies instead of the usual 100 Hz. From this 1000 Hz signal, two RR interval series with a resolution of respectively 0.001 s and 0.01 s were derived. For the '1000 Hz' RR interval series, the automatic peak detection algorithm was applied to the ECG signal, and the resulting RR interval series was manually corrected afterwards. The '100 Hz' RR interval series was obtained by rounding the occurrence times of all R wave peaks to 0.01 s precision and taking the differences. This 100 Hz RR interval series hence contains the same RR intervals as if the ECG was sampled at 100 Hz and the peak detection was perfect. Since the corrections for ECGs sampled at 1000 Hz are negligible, the accuracy of the corrections can be evaluated by comparing the HRV measures calculated using the 1000 Hz RR intervals series and those obtained from the corresponding 100 Hz RR interval series with correction. As the corrections for the standard time-domain HRV measures are only dependent on the ECG sampling rate, its relative importance increases with decreasing variability of the RR interval series. As shown in appendix , however, even for the segments with the lowest variability (quiet sleep) and the shortest RR interval segments considered, the corrections give accurate results. The mean relative error of the HRV measures calculated from the 100 Hz RR intervals with the correction, compared to the HRV measures calculated from the 1000 Hz RR intervals is always smaller than 4%.

Assuming that the sequences $RR(i)$ and $\Delta RR(i)$ are uncorrelated, a correction procedure for the power spectrum estimation can be determined. Due to the addition of the FIR filtered white noise error sequence $\Delta RR(i)$, the estimated power of a 100 Hz RR interval series is higher than that of the exact RR interval series. As the transfer function of the filter ($H(z) = 1 - z$) has a high-pass characteristic, this effect is most pronounced in the high frequency range. If the uneven sampling of the RR interval series is disregarded, the power spectrum of the error sequence can be calculated analytically:

$$S_{\Delta RR}(f_{RR}) = 1/(6f_s^2)(1 - cos(2\pi f_{RR})) \quad (4.4)$$

where f_{RR} represents the frequency variable in "cycles per beat". As mentioned above, however, the power spectrum estimated from the regularly sampled interpolation of the HR signal, which is used in this study, is slightly different

from that of the RR interval series itself. Therefore, the "correction"spectrum of Eq. (4.4) can not simply be subtracted from the spectrum estimated from the 100 Hz RR interval series. The distortion of the interpolated HR power spectrum not only depends on the ECG sampling rate but also on the instantaneous heart rate. Therefore, an artificial RR interval series was synthesized by adding a FIR filtered white noise sequence according to a given ECG sampling rate, simulating the error on the RR intervals, to a constant value equal to the mean of the RR interval series under analysis. The corresponding HR series of this artificial RR interval series was derived and interpolated in exactly the same way as the real RR interval series, i.e. using the algorithm presented in [22]. As the resulting artificial HR signal only contains variations due to the finite sampling rate of the ECG, its power spectrum can be used as a correction for the HR power spectra. In order to obtain a statistically meaningful correction spectrum, an artificial RR interval series was synthesized that was much larger than the actual RR interval series.

The correction procedure is illustrated in Fig. 4.3 using segments of a 1000 Hz RR interval series. Figure 4.3(a-b) shows two examples of an RR interval series derived from an ECG sampled at 1000 Hz, respectively during quiet (a) and active (b) sleep. Figure 4.3(c-d) shows the corresponding 100 Hz RR interval series. The estimated power spectra of the 1000 Hz (solid line) and 100 Hz (dashed line) RR interval series are shown in Fig. 4.3(e) and (f) for respectively the QS and AS segments. A logarithmic scale was used to obtain a clear figure. The "error"spectrum (solid line), the difference between the spectra of the 100 Hz and 1000 Hz spectra, is compared with the correction spectrum as estimated from the artificial RR interval series (dashed line) in Figure 4.3(g-h). The correction spectra resemble smoothed versions of the actual error spectra. Since there are relatively large differences between both spectra for the individual frequency components, however, the usefulness of the correction spectrum to improve the estimate of the power at a specific frequency is limited. But, as far as the power in the different frequency bands is concerned, the correction spectrum drastically improves the estimates, especially for the HF power. As the HF frequency band is relatively wide, the average power of the correction spectrum agrees well with the average power of the error spectrum in this band. For a given frequency resolution, the LF band contains less frequency components than the HF band. Therefore, the difference in power in this LF band between the actual error spectrum and the correction spectrum could be larger. However, as the correction for the power in the LF band (and ULF and VLF bands) is small compared to the power of the HRV, also the HRV measures in the lower frequency bands can be estimated fairly accurately. As shown in appendix , the mean relative error of the HF power and LF/HF-ratio calculated from the 100 Hz RR interval series with correction, compared to the HF power respectively LF/HF ratio calculated from the 1000 Hz RR interval series is smaller than 4%. The errors on ULF, VLF and LF power are negligible.

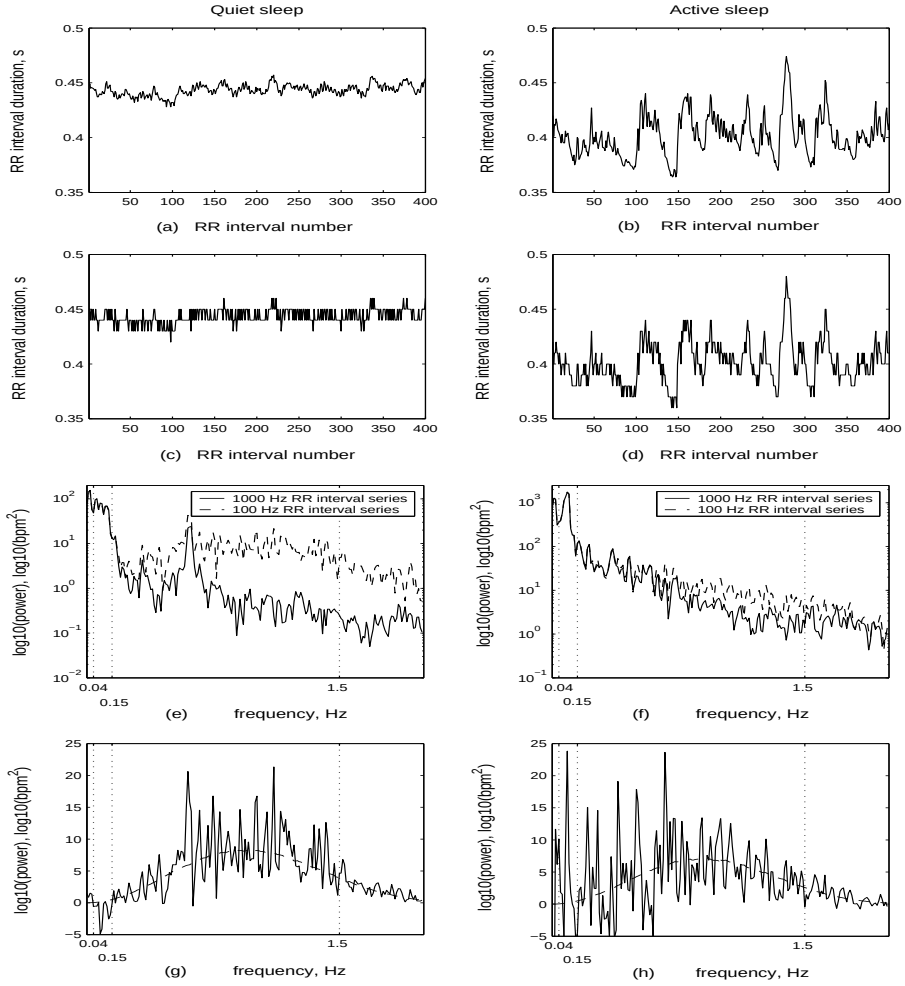

Figure 4.3: Effect of the ECG sampling rate on HRV power spectrum estimation: (a-b) 1000 Hz RR interval series during (a) quiet sleep and (b) active sleep, (c-d) 100 Hz RR interval series during (c) quiet sleep and (d) active sleep, (e-f) power spectrum estimates of 1000 Hz RR interval series (solid line) and 100 Hz interval series (dashed line) during (e) quiet sleep and (f) active sleep (logarithmic scale), (g-h) difference between power spectrum estimates of 100 Hz RR interval series and 1000 Hz RR interval series (solid line) and the "correction"spectrum calculated from an artificial RR interval series used to correct the spectrum of the 100 Hz spectrum during (g) quiet sleep and (h) active sleep. The dashed vertical lines in (e-h) represent the borders of the LF and HF frequency range.

4.3.3 Standard HRV parameters

In this section, an overview is given of the different standard HRV measures as used in this study.

Regarding the length of the recordings from which the HRV measures are obtained, it is recommended to use short-term recordings of 5 minutes made under physiologically stable conditions and/or nominal 24-hour recordings [201]. Therefore, for the short-term variability, the first 5 minute periods, free of artifacts and ectopic beats or arrhythmic events, from both quiet sleep (QS) and active sleep (AS) were selected for analysis. In addition, the HRV measures calculated on all 5 minute QS periods were averaged per subject, as well as the HRV measures of an equal number of AS periods. To assess the long term variability, the complete recordings of each subject are used because 24-hour recordings are not available. Since the average duration of our recordings is approximately 8 hours (between 6 and 14 hours), and the average heart rate in our recordings is approximately twice the heart rate rate of a normal adult, these recordings still contain a sufficient number of RR intervals to make a fair estimate of the long term variability. The HRV measures calculated on the complete RR interval series are referred to as "global"HRV measures. Abnormal bradycardias, according to the criteria discussed in 4.1.1, were removed from the long-term RR time series by linear interpolation prior to the calculation of the HRV measures.

The following parameters were calculated both globally and on the separate sleep states: SDNN, RMSSD, VLF, LF, HF, LFN (normalized), HFN (normalized) and (LF/HF). The superscripts "QS1", "AS1", "QSX"and "ASX"denote that the particular HRV parameter is calculated using respectively the first quiet sleep period, the first active sleep period, the average of all quiet sleep periods and the average of all active sleep periods. HRV measures without subscript refer to the global measures, calculated on the complete RR interval series. TI, SDANN and ULF were only calculated for the complete RR interval series because they can not be estimated accurately on short segments.

4.4 Fractal analysis of neonatal HRV

4.4.1 Basic concepts

In recent literature, a multitude of publications on the fractal character of physiological signals can be found. Terms such as 'fractal', 'self-similar', '(power-law) scaling', 'long-memory', 'long-range dependence' and '1/f noise' are often used in this context. In this section, these basic notions will be defined and their interrelationships will be clarified.

Long-range dependence, long-memory

A stationary time series $x(k)$ is long-range dependent (or has long-memory), if its autocorrelations $r_x(\tau) = \mathcal{E}\{x(k)x(k+\tau)\}$ decay so slowly with increasing τ that they are not summable:

$$r_x(\tau) \propto C_r\ \tau^{-\gamma},\ k \to \infty,\ 0 < \gamma < 1 \tag{4.5}$$

This definition is equivalent to $x(k)$ having a spectral density $P_{xx}(f)$ that tends to infinity at zero:

$$P_{xx}(f) \propto C_p\ f^{-\beta} = C_p\ (1/f)^{\beta},\ f \to 0,\ 0 < \beta < 1 \tag{4.6}$$

with $\beta = 1 - \gamma$ the spectral index. It is worth noting that the definition of long-range dependence by Eqs. (4.5) or (4.6) are asymptotic definitions. It does not specify the correlations for any specific lag, only the rate of convergence. Any individual correlation can be arbitrarily small. This makes the detection of slowly decaying correlations difficult, especially when dealing with small sample sizes. The effect of long-range correlations on statistical inference, however, is not negligible even for small sample sizes. The variance of the sample mean, for example, increases in the case of long-range dependence. Although each individual correlation can be very small, it is the slow decay, and thus the joint effect of all correlations together, that increases the variance of the sample mean.

Fractals, self-similarity, scaling

The concept of fractals [2] is usually associated with self-similar geometrical structures. Self-similar structures are similar at every scale of observation, i.e. they are composed of substructures that are similar to the larger structure, and hence lack any characteristic scale. If the substructures are identical, rescaled replicas of the larger structure, the fractal is *exact*. When the similarity is present only in between statistical populations of observations of a given feature made at different scales, the fractal is *statistical*. Examples of (spatial) statistical fractals in physiology include branching arteries and veins, the tubes of the systems and the lung tree and electrical network of the heart (His-Purkinje system) [14].

As an extension of this concept, time series are called fractal when the temporal fluctuations of the signal, of which the time series is the sampled representation, are self-similar. Strictly speaking, fractal time-series are self-affine rather than self-similar because the scaling is anisotropic, i.e. a segment of the time series

[2] The term fractal, from the Latin word 'fractus' (broken, fragmented), refers to an extension of the notion of dimension used to characterize these complex structures. Contrary to the Euclidean dimension D_E and the topological dimension D_T of an object, the *fractal dimension* D, for which multiple definitions exist, can have non-integer, fractional values. Mandelbrot defined fractals as structures with $D_T \leq D \leq D_E$ [124].

looks only similar to a rescaled segment if the time axis and amplitude axis are rescaled with different factors. Mathematically, a time series $x(k), k = 1, \ldots, N$, is said to be statistically self-affine with self-similarity parameter H if:

$$x(k) =_d c^H x(k/c), \forall c > 0 \tag{4.7}$$

where $=_d$ means equality in distribution. As a consequence, every statistical measure m_k of a self-affine time series of length k exhibits *(power-law)scaling*, i.e. it is proportional to k^H:

$$m_k =_d p\, k^H \tag{4.8}$$

where p is a constant factor. Taking logarithms yields:

$$log(m_k) =_d log(p) + Hlog(k) \tag{4.9}$$

In practical applications, usually only self-similar processes with stationary increments are considered, referred to as "H-sssi"-processes. A time series is said to have stationary increments $y(i,k)$ if:

$$\{y(i,k) \equiv y_i(k) \equiv x(i+k) - x(k), k = 1, \ldots, N\} =_d \{x(i) - x(0)\},\ \forall i \tag{4.10}$$

For an H-sssi process with finite second moment, the self-similarity parameter H necessarily falls in the range $0 < H < 1$. It can be shown that for $0 < H < 1/2$ the process has short-range dependence (the correlations sum up to zero), for $H = 1/2$ the observations are uncorrelated and for $1/2 < H < 1$ the process has long-range dependence [21].

Relation between self-similarity and long-range dependence

The relation between long-range dependence and self-similarity is most easily demonstrated using a specific, often used class of processes. It can be shown that for each H $(0 < H < 1)$, there is exactly one Gaussian H-sssi process, the so-called fractional Brownian motion (fBm). The increments of fBm, referred to as fractional Gaussian noise (fGn), are long range dependent if $H > 1/2$. If $H < 1/2$, the fGn is said to be anti-correlated (or anti-persistant). If $H = 1/2$ the fGn is uncorrelated, i.e. white Gaussian noise, and the corresponding fBm is ordinary Brownian motion.

The power spectrum of fGn is characterized by a slope $-1 < \beta = 2H - 1 < 1$ in the limit as $f \to 0$. Although fBm is nonstationary, it can be shown that the periodogram of a fBm obeys a power law with $1 < \beta = 2H + 1 < 3$ in the limit as $f \to 0$ [64]. Due to this property, the term '1/f-noise' is sometimes used for fGn and/or fBm. It is important to note, however, that whereas the spectra of continuous fGn or fBm processes exactly obey a power law over all frequencies, the spectral estimates of discrete fGn and fBm are only power law in the limit as $f \to 0$, a difference which is often disregarded in literature.

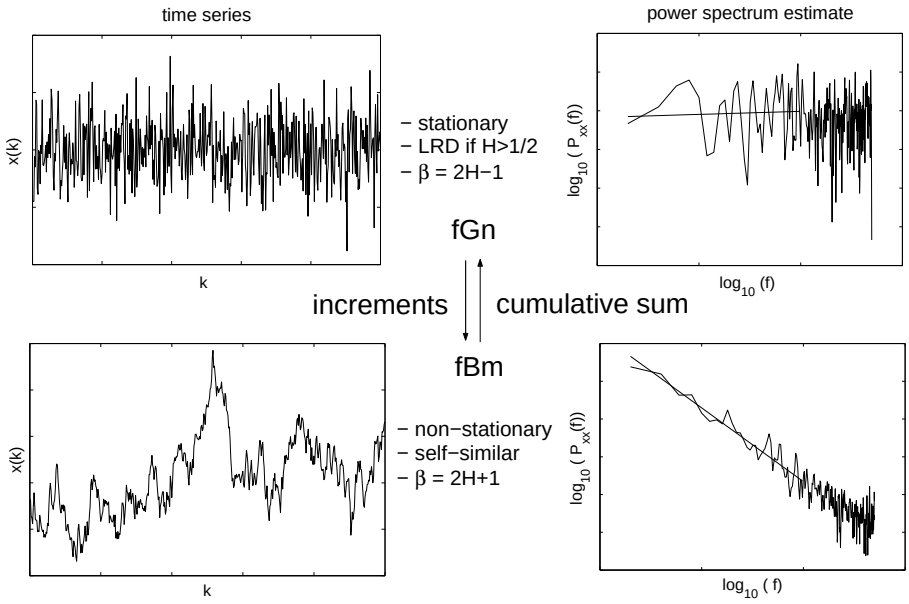

Figure 4.4: Realisations of fractional Gaussian noise (fGn) and fractional Brownian motion (fBm) with $H = 0.5$, the corresponding power spectra, and interrelationships between the properties

The spectra of correlated ($H > 1/2$) fGn exhibit a significant discrepancy from power-law behaviour only near the highest frequencies, while the spectra of anti-correlated fGn ($H < 1/2$) have more extensive regions of non power law behaviour [67]. Some examples of fGn and fBm, the corresponding spectra, properties and interrelationships are shown in Fig. 4.4.

Estimation of H or β

As shown above, fractal signals can be characterized by the self-similarity parameter H together with the classification of the signal as fGn or fBm or by the spectral index β which is almost equivalent. Various methods, either in time-domain, frequency-domain, and time-scale domain (wavelet-based), exist to estimate H, β or equivalent parameters from a time series (see also appendix B). The most commonly used methods employ the power-law scaling relationship (4.9) to make a linear fit between the estimates of a statistical measure, calculated from the time series under analysis, and the scales in a log-log plot. The scaling exponent, H or β, is determined as the slope of the regression line. Besides these somewhat heuristic approaches, several other methods exist based on for example maximum likelihood estimation [21].

4.4.2 Detrended fluctuation analysis (DFA)

The first method to estimate H was invented by Hurst in 1951 when confronting the question of how high the Aswan dam had to be built so that it would contain the greatly varying levels of the Nile within a given window of observation [98]. In Hurst's rescaled range analysis, the so-called R/S statistic, the rescaled adjusted range, is estimated as a function of the length of observation (scale) n and then Eq. (4.9) is solved for H by linear regression. The power law scaling relationship Eq. (4.9) of various statistical measures is the basis for several other methods such as dispersional analysis and scaled window variance analysis. Some of these methods are applicable to either fGn or fBm but not to both. Alternatively, H can be calculated from the estimated autocorrelation function by using Eq. (4.5).

Detrended fluctuation analysis (DFA), which is closely related to scaled window variance analysis, exploits the power law scaling relationship of the variance with the length of observation n [165]. The DFA algorithm consists of the following steps:

1. Integrate the time series $x(k)$, $k = 1, \ldots, N$: $y(k) \equiv \sum_{i=1}^{k} x(i)$, $k = 1, \ldots, N$.
2. Divide the integrated time series $y(k)$ into non-overlapping segments of equal length n.
3. Calculate the local trend in each segment by fitting a polynomial function of order l to $y(k)$, and subtract this local trend from $y(k)$ in order to obtain the detrended time series $y_d(k)$, $k = 1, \ldots, N$. (The corresponding algorithm is denoted as DFA-l.)
4. Calculate the variance $F(n)$ of the detrended time series for a given segment size n: $F(n) = \sqrt{\frac{1}{N} \sum_{i=k}^{N} (y_d(k))^2}$.
5. Repeat the previous steps for different segment sizes (or "scales") n in order to obtain the fluctuation function $F(n)$.

If the time series is self-similar, the fluctuation function $F(n)$ increases by a power-law: $F(n) \propto n^{\alpha}$. The scaling exponent α can be estimated by a linear fit on the log-log plot of $F(n)$ versus n. The scaling exponent α is related to the Hurst coefficient: for fGn $\alpha = H$, for fBm $\alpha = H + 1$. The fluctuation functions for fGn and fBm with $H = 0.5$ are shown in Fig. 4.5. At small scales, there is a deviation of the power law behaviour, which can be corrected for [106].

For experimental data, power-law scaling does not extend over all scales up to infinity, but only holds for a restricted range of scales. For a given signal,

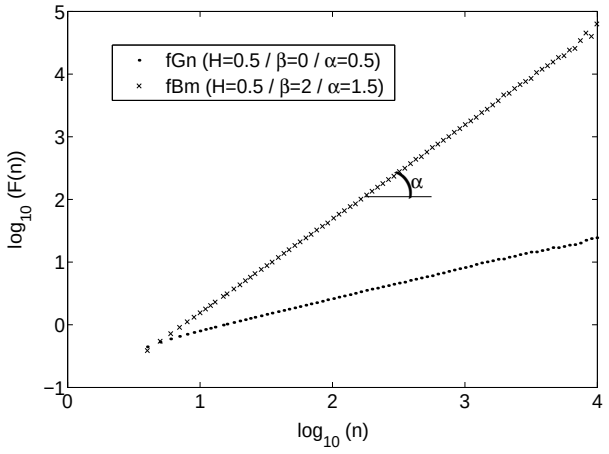

Figure 4.5: Fluctuation function of fractional Gaussian noise (fGn) and fractional Brownian motion (fBm) with $H = 0.5$ calculated with DFA on realisations of 100000 samples

this scaling range is the most important parameter that has to be set in order to estimate the scaling exponent with DFA. In some applications, where the fluctuation function resembles a broken line, two different scaling exponents are estimated over different scaling ranges. This issue will be addressed more into detail in the next section.

From the relationship between the Hurst coefficient and DFA scaling exponent α, it is clear that, for fGn and fBm, α is related to the spectral index as $\alpha = (\beta + 1)/2$. Also for arbitrary signals, however, it can be shown analytically and by numerical simulations that DFA and spectral analysis are related [224, 87]. In appendix A, it is shown that the DFA fluctuation function F(n) is equivalent to a frequency-weighted power spectrum [224]. Although the DFA scaling exponents are often presented is an independent HRV measure with respect to spectral measures, DFA does not provide any information that cannot be obtained through spectral analysis. So, despite often being presented as a 'nonlinear' measure, the DFA scaling exponent is actually a 'linear' statistic in the sense that it only uses information present in the power spectrum. This can also be demonstrated explicitly using the technique of surrogate data [168].

Another interesting property of DFA is the superposition rule for the fluctuation functions. Let $x_1(i)$ and $x_2(i)$ be two uncorrelated time series and their fluctuation functions respectively $F_{x_1}(n)$ and $F_{x_2}(n)$. The fluctuation function of the sum of these two time series is then equal to [93]:

$$F_{x_1+x_2}(n) = \sqrt{F_{x_1}(n)^2 + F_{x_2}(n)^2} \tag{4.11}$$

4.4.3 Methodology

DFA has been applied to heart rate variability data in several studies. [165, 97, 184, 118, 3]. The scaling exponents α obtained with DFA are reported to have diagnostic and prognostic value for patients with various types of cardiac diseases [119, 118, 116, 51]. Whereas the calculation and interpretation of the standard HRV parameters is relatively straightforward, the application of DFA to real (neonatal) heart rate data requires some methodological factors to be addressed. The signal length N (number of RR intervals) and the scaling range (over which the regression line is fitted) should be determined. Furthermore, the effects of the ECG sampling rate and the specific heart rate patterns discussed in section 4.2 on DFA are studied. These investigations contribute to the understanding of the performance of DFA and its interactions with physiological signals.

Time variation of the scaling behaviour

As shown in Fig. 4.1, RR interval series usually exhibit certain changes as a function of time, for example due to different behavioural states. The question can be raised whether the scaling behaviour of these RR interval series is constant in time, and which the optimal signal length N is. The difficulty in assessing the time variation of the scaling behaviour comes from a classical trade-off: to get reliable estimates (of the scaling behaviour) long data segments are necessary, but to track rapid changes short data segments are needed.

In order to distinguish the true time variation of the scaling exponent(s) describing the scaling behaviour, from statistical fluctuation of estimates across time of a constant exponent, an approach based on the technique of (amplitude adjusted) surrogate data is proposed [168]. Surrogate data have identical power spectra as the original data, but they stem from a linear and stationary process. Usually, surrogate data are used to detect possible nonlinear correlations in a given data set. When a test statistic that is sensitive to nonlinear correlations is used, differences between the original and the surrogate data point to nonlinearity of the original data. A test statistic that is only sensitive to linear correlations, does not allow to discriminate between original and surrogate data, but if the data is divided into shorter segments the linear test statistic will differ from segment to segment. Since the surrogate data reflect a linear, stationary process, the variability between segments reflects the sampling distribution of the test statistic. So, if the values of the linear test statistic from the segments of the original data do not fall in the sampling distribution of the surrogate data, the original data are not stationary with respect to the test statistic. Since the scaling exponent(s) α obtained with DFA is essentially a linear statistic [107, 224, 87], the latter approach can be used to test the time variation of α.

For the largest scales, of the order of the total length of the RR interval series, this method obviously can not be applied. Since these scales may contain interesting information as well as the shorter scales, the scaling behaviour will also be studied on large scales by applying DFA to the complete RR interval series. The time variation at these scales, however, can not be assessed.

Hence, in order to assess the time variation of the scaling exponents, the complete RR interval series were divided into shorter segments on which DFA was applied. The segment size was determined as a compromise between the need to track rapid changes (short segments) and the need for accurate estimates (longer segments). One possible source of nonstationarity in the fractal properties which is already described in literature is related to the behavioural state [31, 101, 203, 166]. Therefore, the choice of the segment size was based on the length of the quiet sleep segments, which is usually between 2000 and 4000 RR intervals for our recordings. Hence, segments of length $N = 2000$ were used for DFA, with an overlap of 1500 points between consecutive segments.

Visual inspection of the fluctuation functions revealed a downward crossover, a change from a steep slope to a smaller slope, around scale $n = 20$ in most segments irrespective of the behavioural state. Therefore, two scaling exponents were estimated as a linear fit over a specific scaling range for each segment: α_1 on short scales ($4 \leq n \leq 16$) and α_2 on intermediate scales ($32 \leq n \leq 200$).

Figure 4.6 shows a neonatal RR interval series consisting of 60000 RR intervals (a), together with the scaling exponents α_1 and α_2 as a function of time, respectively in (b) and (c). In each figure, the scaling exponents calculated on one surrogate data set are also shown (dashed line). The horizontal dotted lines represent the mean scaling exponent of the surrogate data, and the mean $\pm$ 2 $\times$ standard deviation. The range of both α_1 and α_2 calculated on the real data is much wider than that calculated on the surrogate data. For α_1, almost half the estimates on the real data are outside the mean $\pm$ 2 $\times$ standard deviation range. For α_2, the number of points outside this range is somewhat smaller, but there are some remarkable large decreases. Comparing these with the RR interval series, it is clear that these low α_2 values (around 0.5) correspond to the quiet sleep stages. This is in agreement with results presented in [31, 166], stating that the RR interval series is uncorrelated during quiet sleep in adults. However, a detailed analysis of the quiet sleep segments in section 4.4.3, shows that in our case, the observed scaling exponent does not characterize the correlations of a possible fractal component in the RR interval series. Since similar observations hold for the other RR interval series, it is clear that neither α_1 nor α_2 can be considered stationary over the whole RR interval series. The same approach applied to parts of RR interval series without quiet sleep segments suggests that the scaling exponents can not be considered stationary in between quiet sleep segments either.

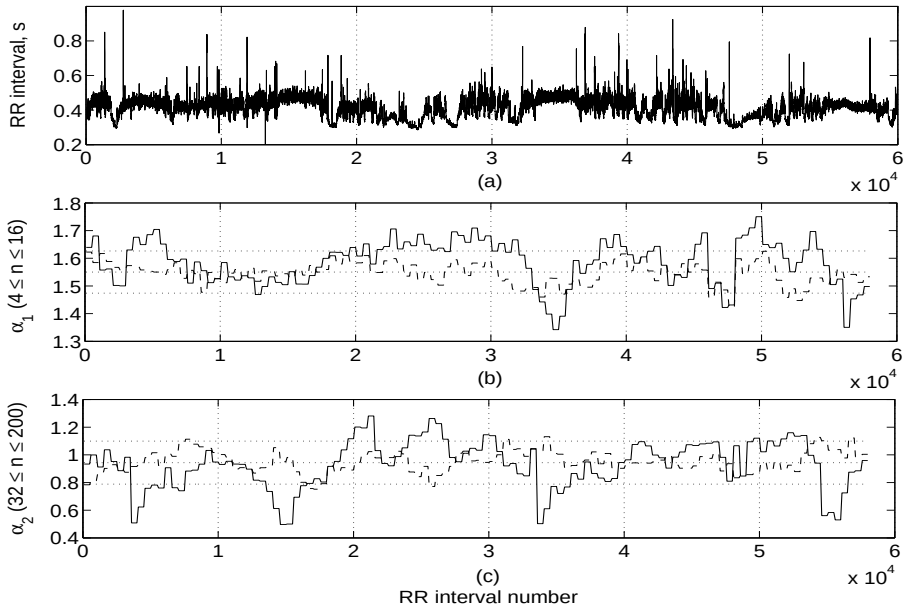

Figure 4.6: (a) RR interval series and scaling exponents (b) α_1 ($4 \leq n \leq 16$) and (c) α_2 ($32 \leq n \leq 200$) calculated over segments of length $N = 2000$ as a function of time. In each figure, the scaling exponents calculated on one surrogate data set are also shown (dashed line). The horizontal dotted lines in (b) and (c) represent the mean scaling exponent of the surrogate data, and the mean $\pm$ 2 $\times$ standard deviation.

As the quite sleep periods are the main cause of the time variation of the scaling behaviour, DFA will be applied separately to segments of different sleep states. This allows comparison of the scaling properties of different subjects in corresponding behavioural states, but makes the evaluation of the scaling behaviour at larger scales impossible. Therefore, DFA will also be applied to complete RR interval series. The time variation of the scaling behaviour at the largest scales, however, can not be assessed. It was also noted that, for all the RR interval series studied, the scaling exponents on short scales (α_1 and α_2) calculated on the complete RR interval series agree with the means of the scaling exponents calculated on consecutive segments of 2000 RR intervals. As they could represent useful parameters as well, these scaling exponents will also be considered. The scaling behaviour estimated from the complete RR interval series, and the corresponding scaling exponents, will be referred to as "global"scaling behaviour and exponents.

Spikes

As discussed in section 4.2, some (neonatal) RR interval series contain spikes, as shown in Fig. 4.1(c) and Fig. 4.6(a). Two kinds of spikes are considered: spikes due to faulty peak detection or certain cardiac arrhythmias and decelerations of the heart rate. An R-wave that is not detected by the peak detection algorithm causes a positive spike in the RR interval series whose amplitude is approximately twice the mean RR interval. A false detection on the other hand introduces two smaller values in the RR interval series. Certain cardiac arrhythmias such as premature beats introduce similar heart rate patterns. Therefore, these spikes, which affect only one or two RR intervals, will be considered together.

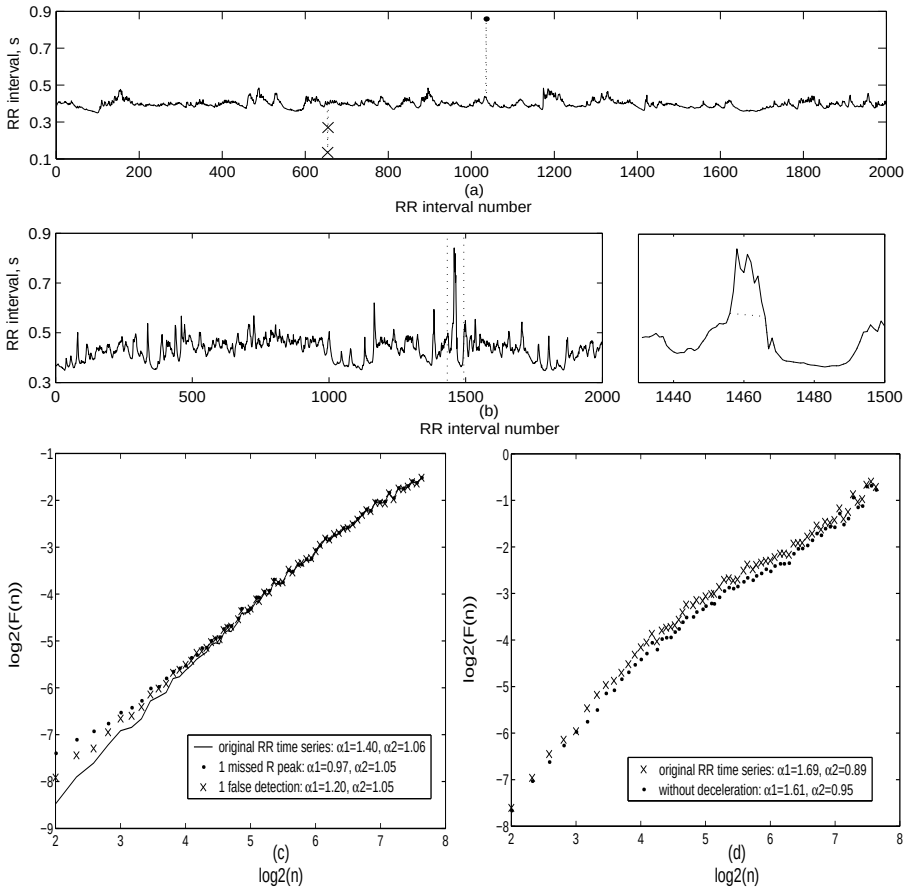

Figure 4.7: (a) RR interval series of length $N = 2000$ with one faulty peak detection (missed R peak or false detection), (b) Effect of 1 faulty peak detection on the scaling behaviour, (c) RR interval series of length $N = 2000$ containing 1 deceleration, (d) Effect of 1 deceleration on the scaling behaviour.

Figure 4.7(a/c) shows the effect of spikes due to faulty peak detection on the scaling behaviour calculated using DFA on a segment of 2000 RR intervals. Both missed R-peaks and false detections, which respectively result in one larger and two consecutive smaller data points in the time series, affect the scaling behaviour at the smallest scales ($n < 16$). One faulty peak detection lowers the estimate of α_1 strongly, but the α_2 estimate is not affected. Of course, for larger numbers of spikes (relative to the total number of RR intervals), the affected scaling range will increase. The effect of 0.1% missed peak on the scaling behaviour of the RR interval series of Fig. 4.6(a) is shown in Fig. 4.8. Hence, in order to get reliable estimates of the scaling exponents of RR interval series, especially on small scales, very good peak detection is necessary. Furthermore, since certain cardiac arrhythmias such as premature beats result in similar spikes, these should be removed before applying DFA.

As mentioned before, the spikes shown in Fig. 4.1(c) and Fig. 4.6(a) are not due to faults in the peak detection, but are actually short decelerations in heart rate, as shown in Fig. 4.7(c). Their effect on the smallest scales ($n < 16$) is smaller than that of the spikes due to faulty peak detections but they also affect larger scales (up to $n = 150$), as shown in Fig. 4.7(d).

In this example, the effect on both scaling exponents is quite large, increasing

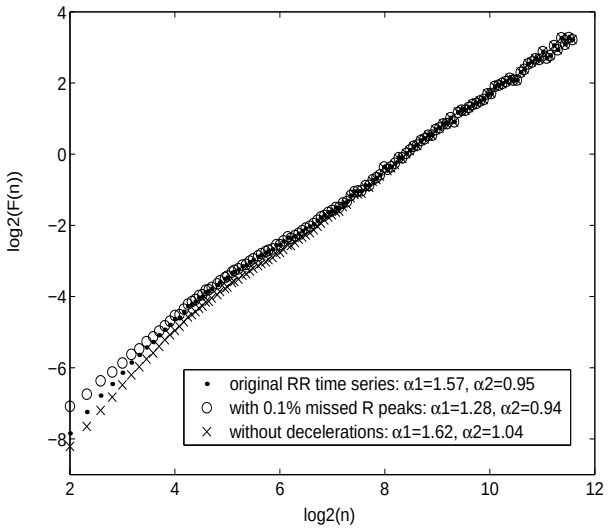

Figure 4.8: Effect of spikes and decelerations on the scaling behaviour of RR interval series. Comparison of the fluctuation functions calculated on the complete RR interval series of Fig. 4.6(a), the same time series with 0.1% spikes added and the same RR interval series where the decelerations have been removed (shown in Fig. 4.9(a)).

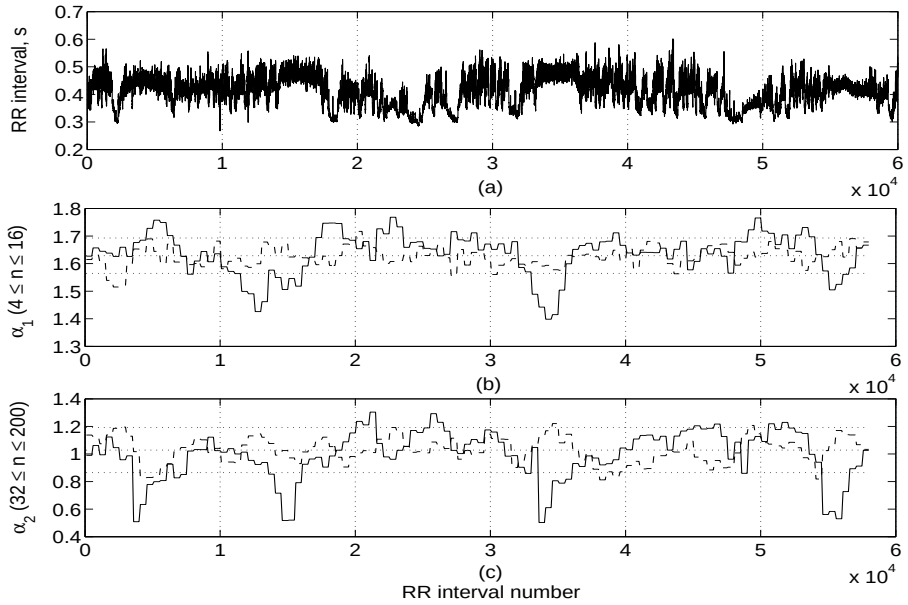

Figure 4.9: (a) RR interval series of Fig. 4.6 from which the decelerations were removed and the corresponding scaling exponents (b) α_1 ($4 \leq n \leq 16$) and (c) α_2 ($32 \leq n \leq 200$) calculated over segments of length $N = 2000$ as a function of time. In each figure, the scaling exponents calculated on one surrogate data set are also shown (dashed line). The horizontal dotted lines in (b) and (c) represent the mean scaling exponent of the surrogate data, and the mean $\pm$ 2 $\times$ standard deviation.

the estimate of α_1 (from 1.61 to 1.69) and decreasing the estimate of α_2 (from 0.95 to 0.89). This effect can be explained by the fact that this deceleration causes an increase in the fluctuation function $F(n)$ which is maximal at the scales somewhat larger than the length of the deceleration ($15 \leq n \leq 20$). The effects of decelerations on the scaling behaviour depend on a number of factors such as the amplitude and the duration of the decelerations, the number of decelerations, the variance of the RR interval series, etc. In some segments, decelerations have the opposite or a negligible effect on the scaling exponents.

To evaluate the average effect of the decelerations on the scaling exponents, the decelerations were removed from the RR interval series shown in Fig. 4.6(a). A simple algorithm that replaced the RR intervals exceeding 120% of the average of the surrounding RR intervals by interpolation was used. For the example of Fig. 4.6(a), this procedure resulted overall in 0.5% of 'corrected' RR intervals. The scaling exponents estimated on the 'corrected' RR interval series as a

function of time were compared to those estimated on the original time series, as shown in Fig. 4.6(b-c). It can be noted that, on average, the decelerations decrease the estimates of both scaling exponents α_1 (from 1.64 to 1.59) and α_2 (from 0.99 to 0.93). Other RR interval series with large numbers of decelerations yield comparable results, which can be explained qualitatively by the fact that, on average, the decelerations cause an increase in the fluctuation function $F(n)$ which is maximal at very small scales and decreases towards larger scales. This effect is also observed in Fig. 4.8, where the fluctuation functions, calculated on the complete RR interval series of Fig. 4.6(a) and Fig. 4.9(a) (where the decelerations have been removed) are compared. On very large scales ($n > 200$), the effect of the decelerations on the scaling behaviour is negligible. From these observations, we suggest that the decelerations should be removed before analyzing the scaling behaviour, despite the fact that they might contain useful physiological information. With respect to the fractal properties of the RR interval series however -which one tries to quantify using DFA- spikes can be considered as disturbances that hinder the estimation of the scaling exponents.

In order to determine to what extent these decelerations contribute to the observed variation of the scaling exponents, the RR interval series from which the decelerations were removed (shown in Fig. 4.9) and RR interval series without decelerations (not shown) were analyzed with the method presented in section 4.4.3. It was found that even without spikes, the scaling exponents can not be considered constant. Decelerations contribute to the variability of the estimates of the scaling exponents, but their effect is not enough to explain the observed variation.

Periodic fluctuations

To study the effect of periodic fluctuations on DFA, simulations with sinusoids and signals with known scaling properties, i.e. realizations of fGn and fBm, were performed. These 'exact fractal' signals were synthesized using the spectral synthesis method (or Fourier filtering method) [163], which consists of filtering the Fourier components of an uncorrelated sequence of random numbers with a suitable power-law filter in order to introduce the desired correlations among the variables. It has been shown that this method has the disadvantage that the correlations are valid only up to a certain fraction of the total time series [164]. In order to overcome this limitation, a larger time series than actually needed was generated, of which only a fraction (i.e. 10%) was used. Figure 4.10 shows the effect of a sinusoidal component on the fluctuation function of an exact fractal signal with $\beta = \alpha = 1$ (pink noise).

A sinusoidal component in an otherwise exact fractal signal leads to a (positive) deviation from the scaling behaviour of the exact fractal signal in a range of scales around the period of the fluctuation. The deviation can be characterized

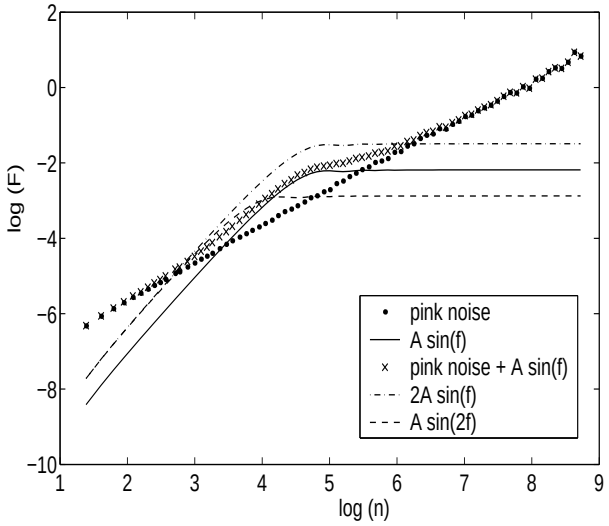

Figure 4.10: Effect of an additive sinusoidal component on the fluctuation function of an exact fractal signal (pink noise), for different amplitudes and frequencies of the sinusoid.

by two upward -indicating the beginning and the end of the deviation- and one downward crossover at a scale corresponding to the period of the fluctuation. This deviation can be explained by the superposition rule: the fluctuation function of the resulting signal is approximately equal to the sum of the fluctuation functions of the sinusoid and the exact fractal signal. It is noted that the fluctuation function of the sinusoid has a slope of 2 up to a scale inversely proportional to the frequency of the sinusoid, and is constant at larger scales. Using this superposition rule, the effect of sinusoids with different frequencies and/or amplitudes and of fractal signals with different scaling exponent α can be evaluated. The higher the frequency, the smaller the scales where the fluctuation function deviates from that of the underlying fractal signal. The larger the amplitude of the sinusoid relative to that of the fractal signal, the larger the range of scales where the fluctuation function deviates from that of the underlying fractal signal. Depending on the relative amplitude and frequency of the sinusoid, it is possible that only one upward crossover is observed in the fluctuation function of the resulting signal.

The effect of periodic fluctuations depends on the relative strength and the period of the fluctuations. Hence, realistic values for these parameters are needed to evaluate the effect of the periodic fluctuations observed in (neonatal) RR interval series. In the remainder of this section, the effect of the two most common periodic fluctuations described in section 4.2, RSA and 10s rhythm, on the scaling behaviour of neonatal RR interval series is discussed in detail.

As discussed in section 4.2, RSA is the periodic fluctuation of the heart rate related with the respiration. In order to study the effect of RSA on DFA, it is not possible to simply filter out RSA using a bandstop filter and compare the fluctuation function of the filtered RR interval series with that of the original. Since the respiratory rate nor the heart rate is perfectly constant, RSA usually shows up as a relatively broad peak in the power spectrum and therefore all the variability in a large frequency range would be removed by the filter, including that of an eventual underlying fractal component. Hence, we use the opposite approach and take a segment where RSA is not visible, add a periodic component corresponding to the respiratory rate and compare the scaling behaviour of the resulting signal with that of the original signal. The effect of RSA on two segments of different sleep stages is shown in Fig. 4.11. For this example, RSA was modeled as a sinusoid with a frequency of 0.92 Hz, corresponding to the main frequency of the respiratory signal, and an amplitude corresponding to an increase in heart rate of approximately 7 bpm, which is a realistic value for neonates [205, 191].

As expected, RSA affects the fluctuation function only at small scales ($n < 20$). Using the superposition principle, it can be seen how this effect varies with the strength and the frequency of RSA. Since RSA is not always present, the effect on the global scaling behaviour will in general be smaller than that on the segments of 2000 RR intervals shown in Fig. 4.11.

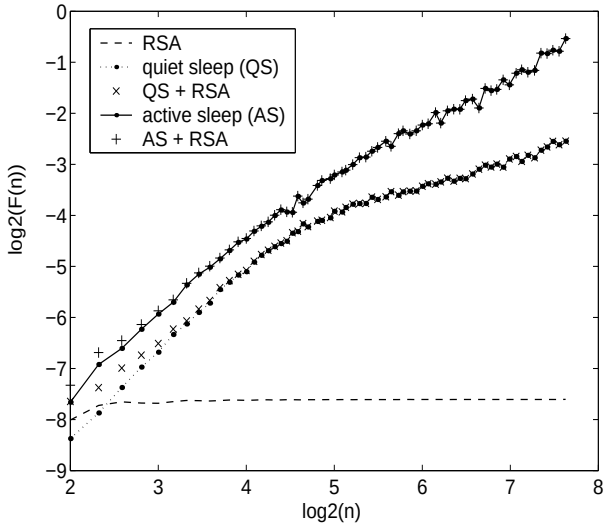

Figure 4.11: Effect of RSA on the scaling behaviour of RR interval series. Fluctuation function $F(n)$ calculated on segments of $N = 2000$ intervals from different sleep stages.

Figure 4.12(a) shows a quiet sleep segment of 2000 RR intervals from Fig. 4.6(a) where the '10s-rhythm', the cyclical fluctuations with a period around 30 RR intervals discussed in section 4.2, can be observed. Since we cannot simply filter these fluctuations out (this would remove the fractal content in the corresponding scaling region), the effect of the 10s-rhythm on the scaling behaviour was studied using a simulated RR interval series. An exact fractal signal, generated with the spectral synthesis method, with $\alpha = 0.95$ was superimposed onto a sinusoid with a period of 12 s. The amplitude of both components was adjusted so that the scaling behaviour of the resulting signal closely matches that

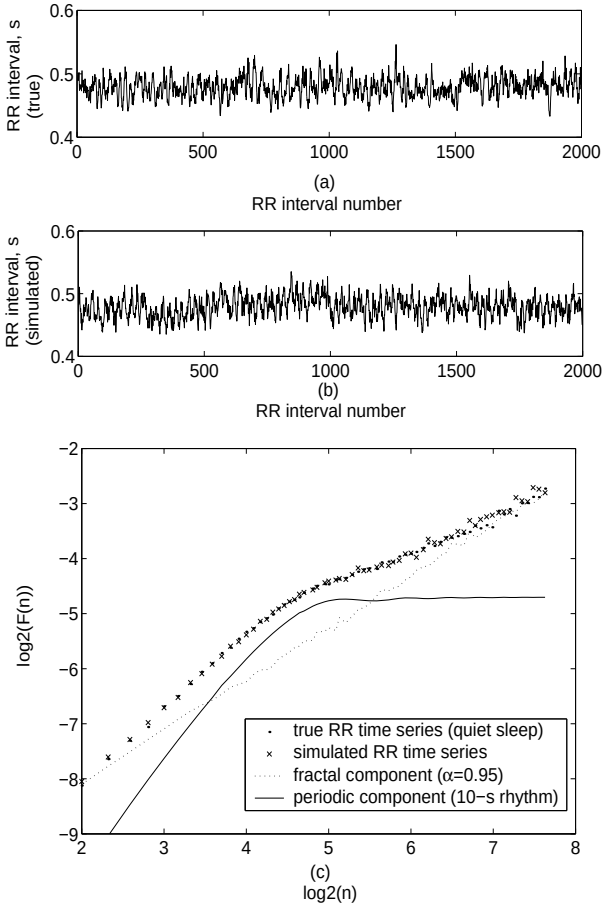

Figure 4.12: (a) segment of 2000 RR intervals during quiet sleep, (b) simulated RR interval series during quiet sleep, (c) scaling behaviour of the true RR interval series, the simulated RR interval series, and the fractal and periodic components of the simulation.

of the real RR interval series. Figure 4.12(b) shows that not only the scaling behaviour but also the simulated time series itself is very similar to the real RR interval series. Figure 4.12(c) shows the fluctuation functions of the real and the simulated RR interval series, and the two components of the simulated time series separately. The periodic component affects the scaling behaviour strongly at all scales. Despite the good linearity of the fluctuation function in the range $32 \leq n \leq 200$, the estimated scaling exponent $\alpha_2 = 0.65$ does not reflect the scaling properties of the underlying fractal signal ($\alpha = 0.95$). It is clear that, due to the 10s-rhythm, it is impossible to determine the scaling exponent of the fractal component by applying DFA on segments of $n = 2000$ RR-intervals, although the power (variance) of both components is approximately equal. According to the superposition principle, the scaling exponent can be expected to reflect the underlying fractal signal at larger scales ($n > 200$), but due to the limited length of the quiet sleep segments, this can not be verified on real data.

During other sleep stages, the 10s-rhythm is also present, but less marked since the variability on all scales is larger. A segment of 8000 RR intervals was analyzed in the same way as the quiet sleep segment, as shown in Fig. 4.13. By using a segment of 8000 RR intervals, the scaling behaviour at larger scales can also be observed. The scaling behaviour of the real RR interval series is well approximated by the superposition of a periodic component (10s-rhythm) and an exact fractal signal with scaling exponent $\alpha = 1.15$. The larger variability on all scales (in comparison to the 10s-rhythm) results in a smoother crossover

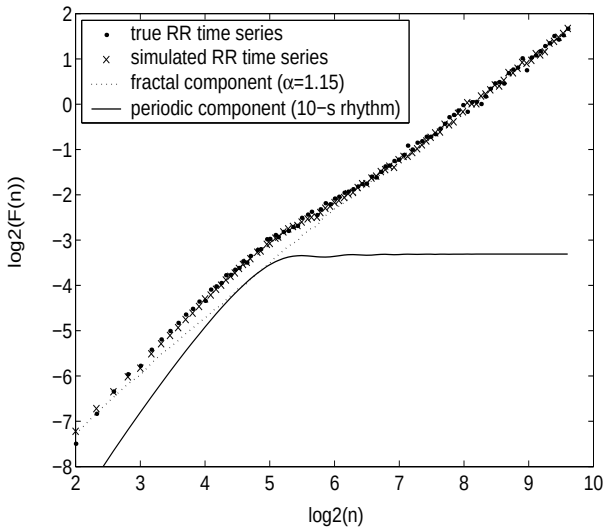

Figure 4.13: Scaling behaviour of a true RR interval series of 8000 RR intervals, a simulated RR interval series, and the fractal and periodic component of the simulation.

in the scaling behaviour (smaller difference between α_1 and α_2). However, although in this case the power of the periodic fluctuations is only 10% of the total power of the signal, the scaling behaviour is still affected by the periodic fluctuations up to large scales ($n = 200$). The scaling exponents $\alpha_1 = 1.44$ and $\alpha_2 = 0.92$ are clearly different from the scaling exponent of the underlying fractal signal ($\alpha = 1.15$). On very large scales ($n > 200$), the scaling exponent does correspond to the underlying fractal signal.

As mentioned in section 4.2, non-nutritive sucking (NNS) and periodic breathing (PB) both introduce periodic fluctuations in the RR interval series similar to the 10s-rhythm. They have a similar effect on the scaling behaviour, but NNS and PB are only present during a fraction of the total recording time, although this can be as high as 40% for PB [90].

Besides these periodic fluctuations with a period around 10 s, in some RR interval series even slower fluctuations are observed. Between RR interval number 5000 and 10000 in Fig. 4.1(b) for example, fluctuations with an average period of 400 RR intervals are observed. This introduces a second crossover in the fluctuation function around the scale $n = 400$, as shown in Fig. 4.14: the slope of the fluctuation function decreases (from 1.08 in the range $n = 32 - 200$ to 0.84 in the range $n = 300 - 2000$).

Our simulations show that the periodic fluctuations observed in (neonatal) RR interval series show up as a crossover in the fluctuation function. This can be explained using the spectral interpretation of DFA. Periodic fluctuations

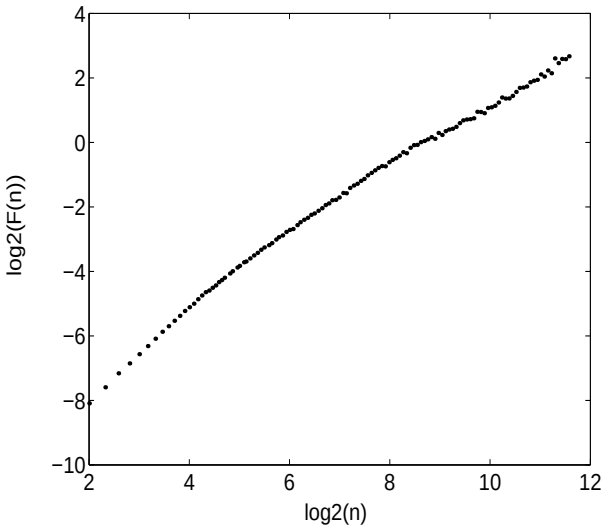

Figure 4.14: Scaling behaviour of the complete RR interval series shown in Fig. 4.1(b).

increase the power at a certain frequency or frequency range compared to the power-law distribution of the exact fractal signal. For the frequencies and amplitudes in our data, these spectral peaks show up as crossover in the fluctuation function at a scale corresponding to the period of the fluctuations. Scaling exponents estimated as the linear slope on scaling ranges near the crossover scale do not reflect the correlation properties of the fractal component of the signal. In order to characterize the fractal component of the signal, it is better to use all available scales.

Effect of ECG sampling frequency

As discussed in section 4.3.2, the error in the RR intervals introduced by the finite ECG sampling rate, $\Delta RR(i)$, can be modelled as a FIR-filtered white noise sequence which is only dependent on the ECG sampling rate. Hence, the DFA fluctuation function of $\Delta RR(i)$ is only dependent on the sampling frequency. Assuming that the sequences $RR(i)$ and $\Delta RR(i)$ are uncorrelated, the superposition principle can be used to correct the fluctuation function of the sampled RR interval series $RRk(i)$: the fluctuation function of true interval series can be approximated as:

$$F_{RR(i)}(n) \approx \sqrt{F_{RRk(i)}(n)^2 - F_{\Delta RR(i)}(n)^2} \tag{4.12}$$

where $F_{\Delta RR(i)}(n)$ is the fluctuation function of the errors $\Delta RR(i)$ which can be calculated from the filtered white noise sequence.

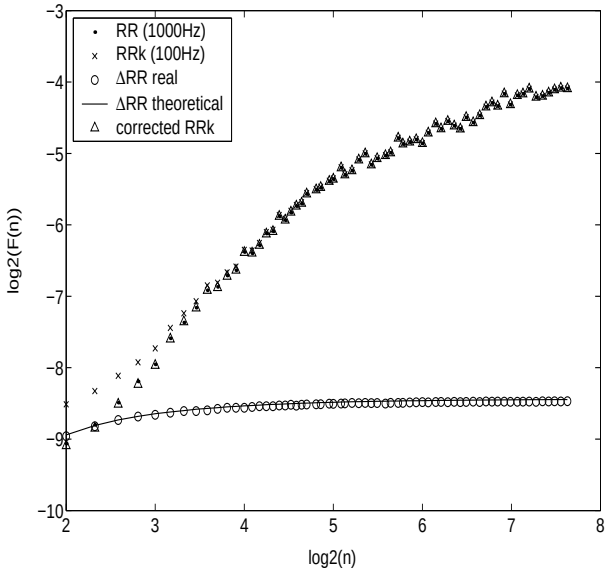

Figure 4.15: Effect of the ECG sampling frequency on the DFA fluctuation function of RR interval series.

The accuracy of the correction for the fluctuation function is evaluated using the ECGs sampled at 1000 Hz, similarly as for the standard HRV measures. Figure 4.15 compares the fluctuation functions of both RR interval series calculated on a quiet sleep segment of 2000 RR intervals. Due to the high-pass filter characteristic of the error sequence, the fluctuation function of the errors increases with increasing scale, and remains practically constant at scales larger than $n \geq 16$. The constant value of $F_{\Delta RR(i)}(n)$ at large scales is proportional to the variance of the (whole) RR interval series under analysis. It does not equal the variance, however, owing to the integration and detrending steps in the DFA algorithm. Despite the smaller value of the fluctuation function of the errors at small scales, the effect of the 100 Hz ECG sampling rate on the fluctuation function is most pronounced at small scales because the fluctuation function of the RR interval series decreases more than that of the errors with decreasing scale. At small scales, the fluctuation function of the 100 Hz RR interval series is larger than that of the 1000 Hz RR interval series. The fluctuation function of the error, of the 100 Hz RR interval series compared to the 1000 Hz RR interval series, agrees very well with the theoretical fluctuation function of the error introduced by 100 Hz ECG sampling, indicating that the error introduced by sampling the ECG at 1000 Hz is negligible. The corrected fluctuation function of the 100 Hz RR interval series is a good approximation of the fluctuation function of the 1000 Hz RR interval series.

For a given sampling rate of the ECG, the effect on the DFA fluctuation function of the RR interval series increases with decreasing variability of the RR interval series. The RR interval series used for Fig. 4.15 was a quiet sleep segment with relatively low variability. Figure 4.16 shows the effect on two other RR interval

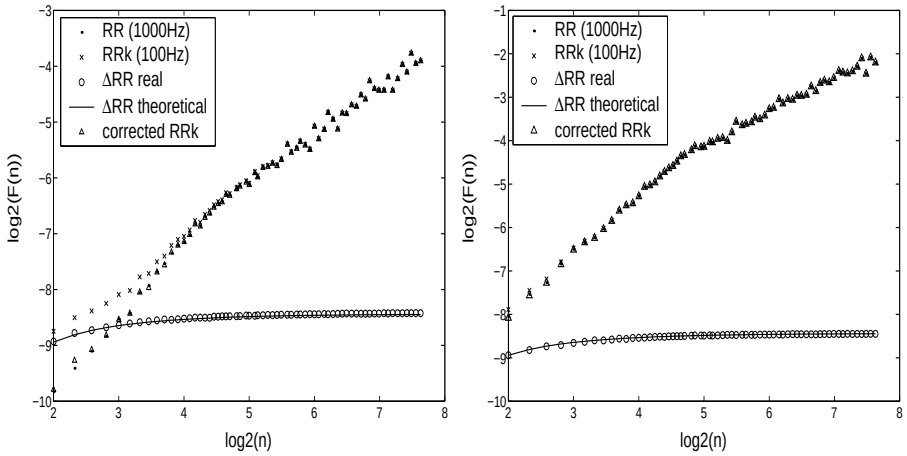

Figure 4.16: Effect of the ECG sampling frequency on the DFA fluctuation function of RR interval series with low (left) and high (right) variability.

series. For the left figure, the RR interval segment with the lowest variability of all 1000 Hz ECG recordings was used. In this case, which can be considered as an upper bound, the fluctuation function is affected up to scales $n \leq 16$. The right figure shows the fluctuation function of an RR interval segment with a high variability, which is hardly affected by the 100 Hz sampling. In both cases, the corrected fluctuation function is in good agreement with the fluctuation function calculated from the 1000 Hz RR interval series.

4.4.4 DFA parameters of HRV

As behavioural state has an important effect on the scaling properties of the RR interval series, DFA measures were calculated separately for quiet and active sleep segments. Two scaling exponents α_1 and α_2 were estimated as a linear fit over respectively short ($4 \leq n < 16$) and intermediate ($32 \leq n < 200$) scales. Similarly to the standard HRV measures, these scaling exponents were calculated on the first QS and the first AS segment, as well as on all QS segments and an equal number of AS segments. For the latter, the average fluctuation function of the different QS and AS segments were used to calculate the scaling exponents.

DFA was also applied to the complete RR interval series to determine the scaling exponent α_3 at large scales ($500 \leq n < 4000$). The scaling exponents α_1 and α_2 at small and intermediate scales were also calculated, as an estimate of the average scaling behaviour at these scales over time. Additionally, one global scaling exponent α_0 was calculated using the complete scaling range ($16 \leq n < 4000$).

4.5 Sample asymmetry analysis

As discussed in section 4.2, some neonatal RR interval series are characterized by a number of transient heart rate decelerations. These HR decelerations are usually relatively small and short: an average increase in RR interval between 0.1 s and 0.4 s during 5 to 20 heartbeats. Although most of these HR decelerations are therefore not considered as abnormal bradycardias according to the criteria described in section 4.1.1, they might be clinically relevant. In this section, sample asymmetry analysis (SAA) [111] is presented as a measure to quantify these HR decelerations.

4.5.1 Basic concepts

Sample asymmetry analysis was designed to quantify the contribution of accelerations and decelerations in heart rate recordings to detect early stages

of neonatal sepsis and systemic inflammatory response syndrome [111]. SAA quantifies the asymmetry of the histogram of RR intervals caused by reduced accelerations and/or transient decelerations. The sample asymmetry of a sequence of N RR intervals is calculated as follows:

1. Calculate the histogram $H(x)$ of all RR intervals (expressed in ms).
2. Define a reference point μ_{RR} in the histogram of the RR intervals (for example the median).
3. Define the left-weighting function $w_1(x) \equiv (x - \mu_{RR})^{\gamma_1}$ (with $\gamma_1 > 0$) whenever $x < \mu_{RR}$ and 0 elsewhere, and the right-weighting function $w_2(x) \equiv (x - \mu_{RR})^{\gamma_2}$ (with $\gamma_2 > 0$) whenever $x \geq \mu_{RR}$ and 0 elsewhere.
4. Calculate the sum of the weighted deviations to the left and to the right of the reference point μ_{RR} as follows: $R_1 = \sum H(x)w_1(x)$ and $R_2 = \sum H(x)w_2(x)$.
5. Calculate the sample asymmetry as the ratio $R \equiv R_2/R_1$.

It is clear that if $\gamma_1 = \gamma_2$ and the distribution is symmetric around the reference point that $R_1 = R_2$ and hence $R = 1$. If the distribution is asymmetric with more and/or larger deviations to the right (decelerations), then $R > 1$. The reference point can be any arbitrary central point such as the median or the mean. The sensitivity of R to left and right deviations can be controlled through the parameters γ_1 and γ_2, and separate quantification of left (accelerations) and right (decelerations) is possible through R_1 and R_2.

4.5.2 Methodology

SAA was applied to the RR interval series with a quadratic weighting function ($\gamma_1 = \gamma_2 = 2$) and using the median as reference point (μ_{RR}). This parameter choice was based on the simulations presented in [111] showing that SAA (with $\gamma_1 = \gamma_2 = 2$ and the median as reference point) is able to quantify in a graded fashion the number of decelerations in neonatal RR interval series. Note that for this parameter choice R is approximately equal to the ratio of the sum of squares of the RR intervals larger than μ_{RR} to the sum of squares of the RR intervals smaller than μ_{RR}.

As SAA is specifically used in the present study to quantify short decelerations -not asymmetry due to slower variations- the RR interval series was detrended prior to constructing the histogram. To this end, the RR interval series were high-pass filtered with a fourth order Butterworth filter with a cut-off frequency corresponding to 500 RR intervals. As a bin size of 10 ms was used, which is small enough to accurately describe the histogram, there were no difficulties with different ECG sampling rates (i.e. 1000 Hz or 100 Hz).

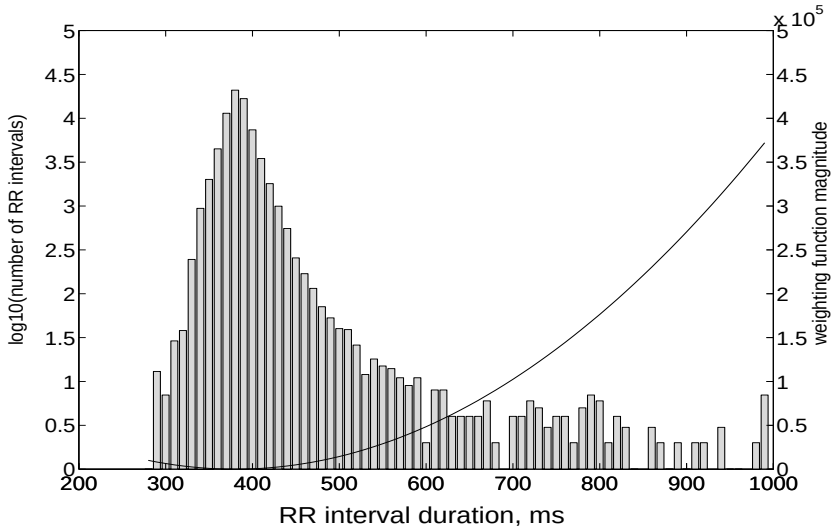

Figure 4.17: Sample asymmetry analysis of RR interval series of subject AA5 (R=6.09).

The SAA of the RR interval series of subject AA5, which is partly shown in Fig. 4.1(c), is illustrated in Fig. 4.17. The histogram is displayed with a logarithmic ordinate to clearly show the tail of the histogram. This RR interval series with a relatively large number of decelerations, is characterized by $R = 6.09$. The RR interval series of subject NN5, partly shown in Fig. 4.1(b), has less decelerations and a correspondingly lower value of $R = 1.87$.

An alternative, classical measure to quantify the asymmetry of a distribution is the skewness, which is defined as the third moment about the mean divided by the third power of the standard deviation. As it was observed in several RR interval series that SAA better represents the HR decelerations, SAA was preferred over skewness to quantify the decelerations.

4.6 Classification AA, AN, NN neonates

4.6.1 Subjects

For the present study, polysomnographies of ALTE infants and preterm neonates recorded in the University Hospitals Leuven (Gasthuisberg) between 2000 and 2003 were considered. The subjects were divided in three groups (NN, AA, AN) according to evaluation of the polysomnography and the follow-up using the criteria described in section 4.1.1. As there were only 9 ALTE infants

in our data set, the present study is limited to the preterm infants. Thirty-nine preterm infants with an abnormal polysomnography were included in the study. Fifteen of these 39 subjects experienced abnormal events during the follow-up. ECG recordings with large numbers of artifacts were excluded. As the maturation is an important determinant of heart rate, age-matched AN and AA-groups were composed, consisting of 10 subjects each. Ten age-matched preterm infants were retained from the NN group. The mean conceptional age (CA) at the time of the polysomnography was 36.4 weeks for the NN preterms, 36.3 weeks for the AN preterms and 36.4 weeks for the AA preterms. The mean gestational age (GA) was 32.3 weeks, 31.9 weeks and 32.3 weeks respectively for the NN, AN and AA preterms. A summary of the patient data is given in Table 4.1.

Table 4.1: Summary of patient data. The column headings refer to the evaluation of the polysomnography and the follow-up. Conceptional age at the time of the polysomnography and gestational age (between brackets) are expressed in weeks. An asterisk denotes ECG recordings sampled at 1000 Hz and "# RR"refers to the number of RR intervals.

normal/normal			abnormal/normal			abnormal/abnormal		
	age	# RR		age	# RR		age	# RR
NN1	32(30)	125639	AN1	36(30)	100407	AA1	36(34)	135284
NN2	40(28)	62767	AN2	38(36)	60414	AA2	37(34)	123652
NN3	37(33)	69267	AN3	37(32)	71812	AA3	37(35)	70191
NN4*	36(31)	75781	AN4	34(32)	74722	AA4	37(30)	72269
NN5*	36(33)	50952	AN5	36(32)	78310	AA5*	37(32)	72000
NN6*	38(35)	37752	AN6	37(34)	75303	AA6	35(28)	67907
NN7*	38(30)	60051	AN7	38(27)	63446	AA7	36(34)	71041
NN8*	35(33)	30405	AN8	36(34)	69990	AA8	37(32)	69197
NN9*	36(35)	57898	AN9	36(32)	94154	AA9	36(33)	65117
NN10*	36(35)	54420	AN10	36(30)	138643	AA10	36(27)	76474

4.6.2 Measurements

All heart rate data used in this study were obtained from polysomnographies. The physiological parameters measured during the polysomnographies included electrocardiogram (ECG), thoracic and abdominal respiratory movements, nasal flow (thermistor), SaO_2 (pulse oximeter), chin electromyogram (EMG) and electro-oculogram (EOG) to detect sleep states. All signals are analog and are

digitized and stored on a PC by the data acquisition system CODAS (Dataq Instruments, USA). The RR intervals were derived from the ECG signal, which was usually sampled at 100 Hz as were all other signals. Ten ECG signals were sampled at 1000 Hz in order to study the effect of the ECG sampling rate on the HRV measures. The R peaks were detected by an automatic peak detection algorithm based on the second derivative of the ECG signal. To avoid errors due to faulty peak detection, all RR interval series were manually checked for false and/or missed peaks, and corrected if necessary (based on the ECG signal). The mean duration of the ECG recordings was 8 hours, yielding RR interval series containing on average 75000 RR intervals.

Several signals recorded during the polysomnography were used to determine the behavioural states of the neonates. Quiet sleep periods were identified in the polysomnographies as periods characterized with regular respiration, low EOG amplitude (no eye movements), low EMG amplitude (no chin movement). Active sleep periods were defined by irregular breathing, limited EOG activity (bursts, isolated eye movements) and limited EMG activity. All quiet sleep segments in each polysomnography were analyzed. Following each quiet sleep segment, an active sleep segment was selected of approximately the same duration as the quiet sleep segment.

4.6.3 Results

For all HRV measures calculated on the complete RR interval series, the mean values ± standard deviations for each group of subjects is shown in Table 4.2.

The groups were compared pairwise for each HRV parameter individually. As the distribution of the HRV parameters is not known (and can not be estimated reliably due to the limited sample size) the Wilcoxon rank-sum test was used to assess the statistical significance of the differences between the groups. None of the global standard or DFA measures yielded significant differences between the three groups. SAA-R tends to be larger for AA than for NN and AN, although only the difference with AN is significant ($p < 0.05$). The SAA-R values of each subject are shown in Fig. 4.18. Note that there is a large overlap between the three groups.

The mean values of the HRV parameters calculated separately on QS and AS segments are shown in Table 4.3. With respect to the standard time-domain HRV parameters, no differences between groups can be observed in QS nor in AS. VLF and LF tend to be smaller for AA than for AN and NN, both in QS and in AS, although only the difference in LF during AS between AA and NN reaches a significance level of 0.05. With respect to HF, there are no significant differences between the groups in QS nor in AS. In QS, HFN tends to be larger for AA than for NN ($p < 0.05$) and AN (n.s.), while no differences

Table 4.2: Summary of global HRV measures calculated on the complete RR interval series. Significant differences ($p < 0.05$) between groups are indicated between brackets.

	NN mean ± std	AN mean ± std	AA mean ± std
RR (ms)	405 ± 21	401 ± 22	396 ± 15
SDNN (ms)	41.4 ± 9.5	42.4 ± 9.9	43.6 ± 8.7
TI	9.1 ± 2.6	8.7 ± 2.3	9.7 ± 2.2
SDANN (ms)	27.0 ± 8.2	26.0 ± 4.8	29.5 ± 6.8
RMSSD (ms)	10.3 ± 2.4	10.1 ± 3.2	10.8 ± 3.9
PWR ($10^6 bpm^2$)	2.8 ± 1.2	3.4 ± 0.8	3.1 ± 1.2
ULF ($10^6 bpm^2$)	1.17 ± 0.17	1.29 ± 0.68	1.27 ± 0.58
VLF ($10^6 bpm^2$)	1.11 ± 0.52	1.50 ± 1.00	1.24 ± 0.50
LF ($10^6 bpm^2$)	0.45 ± 0.17	0.49 ± 0.29	0.45 ± 0.14
HF ($10^6 bpm^2$)	0.12 ± 0.06	0.10 ± 0.06	0.11 ± 0.07
VLFN	39.8 ± 11.1	42.8 ± 8.0	40.4 ± 4.0
LFN	17.0 ± 7.5	14.9 ± 4.3	15.5 ± 4.6
HFN	4.6 ± 2.6	3.2 ± 1.1	3.7 ± 2.2
α_0	1.02 ± 0.07	1.03 ± 0.04	1.06 ± 0.03
α_1	1.51 ± 0.09	1.53 ± 0.06	1.50 ± 0.12
α_2	1.06 ± 0.11	1.10 ± 0.10	1.08 ± 0.10
α_3	0.99 ± 0.16	0.95 ± 0.11	1.01 ± 0.11
SAA-R	2.27 ± 1.48	$1.90 \pm 0.86_{(AA)}$	$2.85 \pm 1.50_{(AN)}$

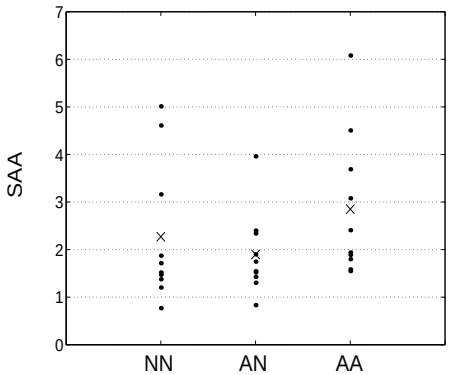

Figure 4.18: Global HRV measure with significant differences between groups: $SAA - R$. The values of each individual subject are denoted with dots ("·"); the mean of each group is denoted with a cross ("×").

Table 4.3: Summary of HRV measures calculated on quiet sleep segments and active sleep segments separately. Significant differences ($p < 0.05$) between groups are indicated between brackets.

	NN mean ± SD	AN mean ± SD	AA mean ± SD
RR^{QSX} (ms)	426 ± 31	419 ± 26	426 ± 24
$SDNN^{QSX}$ (ms)	12.6 ± 4.6	10.6 ± 3.0	10.4 ± 3.7
$RMSSD^{QSX}$ (ms)	6.9 ± 0.9	5.3 ± 1.6	6.7 ± 32
VLF^{QSX} $(10^3 bpm^2)$	1.46 ± 0.87	1.29 ± 0.41	1.01 ± 0.60
LF^{QSX} $(10^3 bpm^2)$	3.50 ± 2.40	2.13 ± 0.72	1.78 ± 1.11
HF^{QSX} $(10^3 bpm^2)$	1.30 ± 0.92	0.78 ± 0.42	1.16 ± 0.98
LFN^{QSX}	52.3 ± 10.0	50.1 ± 7.4	45.4 ± 6.8
HFN^{QSX}	21.6 ± 10.0	$18.1 \pm 7.1_{(AA)}$	$27.1 \pm 10.4_{(AN)}$
$(LF/HF)^{QSX}$	2.98 ± 1.42	$3.59 \pm 1.84_{(AA)}$	$2.04 \pm 0.80_{(AN)}$
α_1^{QSX}	1.34 ± 0.15	$1.35 \pm 0.17_{(AA)}$	$1.20 \pm 0.16_{(AN)}$
α_2^{QSX}	0.75 ± 0.12	0.74 ± 0.06	0.76 ± 0.13
RR^{ASX} (ms)	411 ± 23	407 ± 24	402 ± 18
$SDNN^{ASX}$ (ms)	29.4 ± 6.3	27.5 ± 9.5	26.3 ± 6.5
$RMSSD^{ASX}$ (ms)	8.8 ± 1.5	7.8 ± 2.6	7.7 ± 3.3
VLF^{ASX} $(10^3 bpm^2)$	19.5 ± 8.5	18.7 ± 12.8	14.8 ± 6.6
LF^{ASX} $(10^3 bpm^2)$	$11.2 \pm 4.0^{(AA)}$	10.2 ± 6.2	$8.1 \pm 2.3^{(NN)}$
HF^{ASX} $(10^3 bpm^2)$	2.5 ± 1.0	2.1 ± 1.3	2.1 ± 1.6
LFN^{ASX}	34.3 ± 8.5	33.8 ± 6.6	33.5 ± 4.2
HFN^{ASX}	8.0 ± 3.5	7.0 ± 1.3	8.6 ± 4.5
$(LF/HF)^{ASX}$	4.82 ± 1.42	5.10 ± 0.86	4.84 ± 1.78
α_1^{ASX}	1.55 ± 0.08	1.57 ± 0.04	1.53 ± 0.12
α_2^{ASX}	1.03 ± 0.14	1.03 ± 0.12	1.08 ± 0.09

are observed in AS. In QS, (LF/HF) tends to be smaller for AA than for NN (n.s.) and AN ($p = 0.05$), while no differences are observed in AS. Regarding the scaling exponents, α_1 tends to be lower in AA than in NN (n.s.) and in AN ($p < 0.05$) during QS. There are no differences for α_1 in AS or for α_2 in either state. For the HRV measures for which a significant difference between the groups was observed, the values of each subject are shown Fig. 4.19. Note that the difference between the mean values of each group is small compared to the intersubject variability in each group.

For each subject, the differences in HRV measures between behavioural states

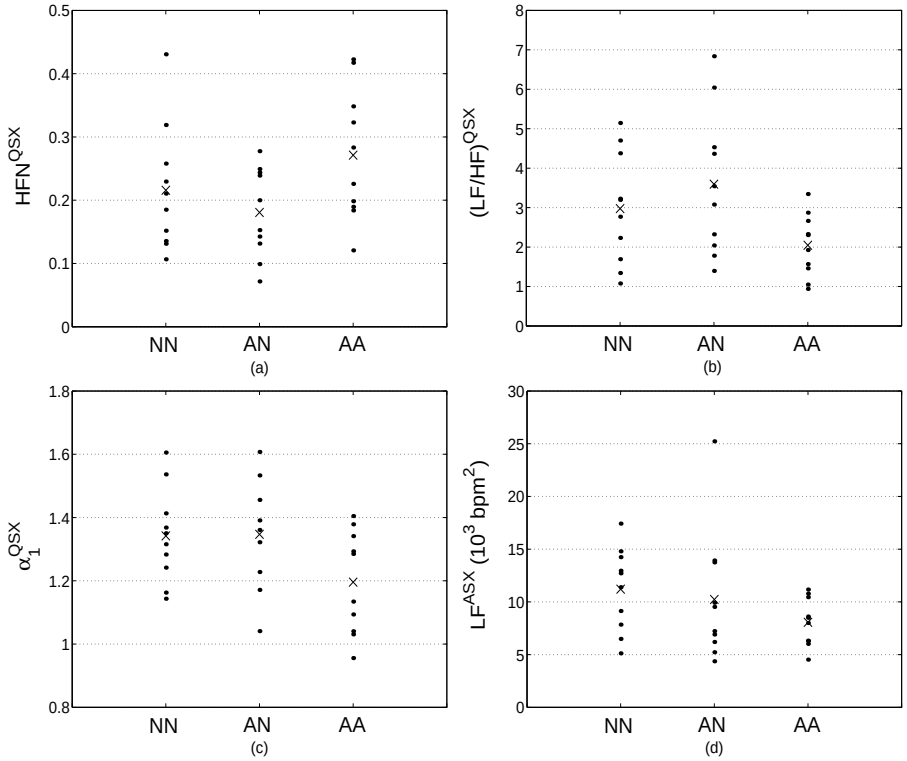

Figure 4.19: HRV measures with significant differences between groups: (a) HFN^{QSX}, (b) $(LF/HF)^{QSX}$, (c) α_1^{QSX}, (d) LF^{ASX}. The values of each individual subject are denoted with dots ("·"); the mean of each group is denoted with a cross ("×").

were evaluated using the Wilcoxon signed rank test for matched samples. Heart rate (1/RR) and all absolute HRV measures (SDNN, RMSSD, VLF, LF and HF) are significantly lower in QS than in AS ($p < 0.0001$). HFN is significantly larger in QS than in AS ($p < 0.00001$), while (LF/HF) is smaller in QS than in AS. Both scaling exponents α_1 and α_2 are significantly smaller in QS than in AS ($p < 0.00001$).

The mean values of the HRV parameters calculated on the first QS and AS segment are shown in Table 4.4. With respect to the standard time-domain HRV parameters, no differences between groups can be observed in QS1 or in AS1. The results for all spectral measures (VLF, LF, HF) are similar to the average values per behavioural state both for QS1 and AS1. There are no significant differences between the groups for any of the spectral parameters. The results for the scaling exponents α_1 and α_2 are comparable to the average

Table 4.4: Summary of HRV measures calculated on the first quiet sleep segment and the first active sleep segment. Significant differences ($p < 0.05$) between groups are indicated between brackets.

	NN mean ± std	AN mean ± std	AA mean ± std
RR^{QS1} (ms)	432 ± 32	426 ± 44	431 ± 25
$SDNN^{QS1}$ (ms)	12.2 ± 4.9	10.7 ± 5.4	9.9 ± 3.8
$RMSSD^{QS1}$ (ms)	7.2 ± 2.6	5.9 ± 3.0	6.8 ± 3.9
VLF^{QS1} $(10^3 bpm^2)$	0.95 ± 0.50	0.97 ± 0.70	0.67 ± 0.41
LF^{QS1} $(10^3 bpm^2)$	3.5 ± 2.6	2.3 ± 1.4	1.5 ± 0.9
HF^{QS1} $(10^3 bpm^2)$	1.2 ± 0.8	0.9 ± 0.6	1.2 ± 1.2
LFN^{QS1}	57.7 ± 12.4	52.6 ± 11.9	46.4 ± 8.5
HFN^{QS1}	$22.5 \pm 7.3^{(AA)}$	23.7 ± 12.6	$30.3 \pm 14.3^{(NN)}$
$(LF/HF)^{QS1}$	2.95 ± 1.45	3.15 ± 2.26	2.18 ± 1.80
α_1^{QS1}	1.33 ± 0.19	1.33 ± 0.21	1.23 ± 0.27
α_2^{QS1}	$0.61 \pm 0.15^{(AA)}$	$0.60 \pm 0.15_{(AA)}$	$0.75 \pm 0.15^{(NN)}_{(AN)}$
RR^{AS1} (ms)	408 ± 25	407 ± 33	412 ± 18
$SDNN^{AS1}$ (ms)	26.7 ± 5.8	27.1 ± 11.3	25.6 ± 9.5
$RMSSD^{AS1}$ (ms)	8.0 ± 1.6	7.7 ± 2.4	8.3 ± 3.5
VLF^{AS1} $(10^3 bpm^2)$	18.2 ± 12.0	16.0 ± 12.0	13.5 ± 7.7
LF^{AS1} $(10^3 bpm^2)$	9.4 ± 4.3	10.2 ± 4.9	8.5 ± 3.8
HF^{AS1} $(10^3 bpm^2)$	2.1 ± 1.1	2.1 ± 1.1	2.5 ± 2.0
LFN^{AS1}	33.2 ± 9.2	38.9 ± 10.7	37.1 ± 11.8
HFN^{AS1}	8.0 ± 3.9	8.2 ± 3.0	10.2 ± 4.5
$(LF/HF)^{AS1}$	4.70 ± 1.77	5.05 ± 1.76	4.26 ± 1.97
α_1^{AS1}	1.56 ± 0.08	1.60 ± 0.09	1.49 ± 0.11
α_2^{AS1}	1.02 ± 0.17	1.00 ± 0.17	0.99 ± 0.19

values per behavioural state. During QS1, α_2 is significantly larger for AA than for NN ($p < 0.05$) and AN ($p < 0.05$). The α_2 value of each subject during QS1 is shown Fig. 4.20. Note again the large overlap between the different groups.

With respect to the differences between behavioural state, the results obtained for QS1 and AS1 are in agreement with those obtained for the averaged QS and AS segments.

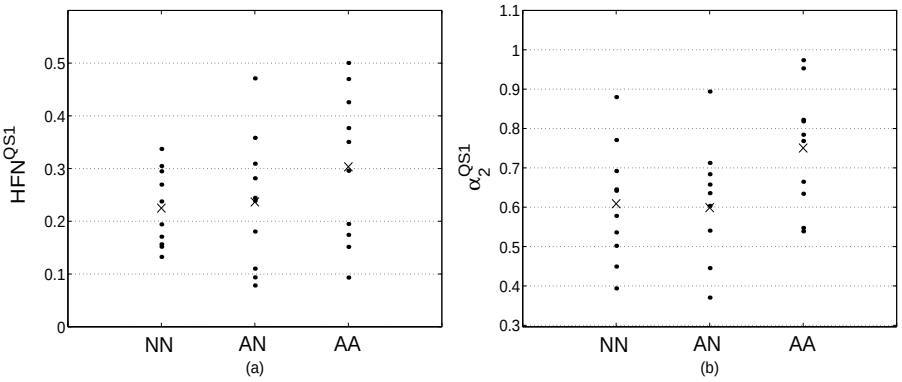

Figure 4.20: HRV measures with significant differences between groups: (a) HFN^{QS1} (b) α_2^{QS1}. The values of each individual subject are denoted with dots ("·"); the mean of each group is denoted with a cross ("×").

4.6.4 Discussion

The *mean heart rate* is not significantly different between NN-, AN- and AA-neonates, neither the overall mean neither in separated behavioural states (QS, AS). The heart rate during QS was found to be significantly lower than during AS. The mean heart rate values (both in QS and in AS) in this study are comparable to the values reported in literature for healthy preterm infants with similar gestational and postnatal age [108, 58, 36, 72].

No significant differences in *standard time-domain HRV measures* (SDNN, TI, SDANN, RMSSD) were found between NN-, AN- and AA-neonates, neither globally neither in QS or AS. To our knowledge, no comparative studies between similar groups of preterm neonates have been published. HRV of ALTE infants, whose cardiorespiratory control is evaluated using the same criteria, has been compared to normal neonates in several studies. Xu compared the HRV, obtained during polysomnography, of 102 healthy infants with that of 20 infants with future abnormal events, according to the event information on the home monitor [231]. No significant differences in SDNN or RMSSD were found between both groups, neither in QS nor in AS. The results of the latter study, however, might have been confounded by the wide range and differences in age (CA) in the control and event group [231]. Edner et al. found a significantly higher SDNN and RMSSD during QS in a group of 50 ALTE infants compared to an equally large group of sex- and age-matched control infants, while no significant differences in other standard time-domain measures or during AS were found [56]. In the latter study, HRV measures were determined from a polysomnography within a week after the ALTE had occurred [56]. Contrary to this, two other, smaller studies using similar -but not identical time-domain

HRV measures- reported smaller HRV in QS [162] or both in QS and AS [115] in ALTE infants compared to normal infants.

SDNN agrees with the values found in literature for comparable preterm infants (GA, CA) [108]. For the other standard time-domain HRV measures, to our knowledge, no comparative values are available in literature. Compared to normal full-term neonates with postnatal age less than 72 h, all standard time-domain parameters are smaller [130]. This finding agrees with results from studies on the maturation of the cardiac control in neonates [58, 108]. Both SDNN and RMSSD are found to be significantly smaller in QS than in AS. The difference in SDNN, which is relatively large, was also observed in several other studies [108, 72, 8]. Concerning the RMSSD in QS compared to AS, the results reported in literature are not consistent, but the differences are usually relatively small as in the present study [8, 56].

With respect to the *spectral HRV measures*, no significant differences between NN-, AN- and AA-infants were found when they were calculated on the complete RR interval series. VLF and LF tend to be smaller for AA infants than for NN or AN infants, both during QS and AS. Only the difference in LF averaged over all AS periods is significant. No differences in HF were observed between groups, neither globally nor in QS or AS. Xu did not find any significant differences in spectral HRV measures in infants with abnormal events during follow-up compared to normal infants [231]. In ALTE infants, VLF (and HF) were reported to be higher compared to normal age-matched infants [56]. It should be noted that there is considerable variation in the absolute spectral HRV measures between subjects (in each group) as well as within subjects (different segments of the same behavioural state), a finding which was also reported in other studies [11, 36]. Taking this into account, together with the small numbers of subjects in each group and the fact that multiple comparisons, albeit not independent, are made, the difference in LF^{ASX} is not convincing. A study on a larger population would be necessary to establish the statistical significance of this difference. However, due to the large overlap between the groups as shown in Fig. 4.19(d), it seems unlikely that the groups could be discriminated based on LF^{ASX}. As in the few studies that reported absolute spectral HRV measures of comparable infants, different spectral estimation methods were used, no direct comparison with our results is possible.

The distribution of HRV over the different frequency bands is better represented by the *normalized spectral HRV measures*. The normalized spectral HRV measures calculated on the complete RR interval series were not different between NN-, AN- and AA-infants. During QS, LFN tends to be smaller and HFN larger in AA- than in NN- or AN-infants. Hence, also LF/HF tends to be smaller in AA-infants. The differences in HFN^{QSX} and LF/HF^{QSX} between AA and AN, and in HFN^{QS1} between AA and NN are significant ($p < 0.05$). This could point to an increased vagal tone during QS in AA infants. Xu did not find significant differences in normalized spectral HRV measures in infants

with future abnormal events and normal infants [231]. In ALTE infants, LF/HF was found to be lower during AS than in otherwise comparable normal infants, suggesting that vagal tone dominates in ALTE infants [56]. Owing to the large overlap between all groups, shown in Fig. 4.19(a-b) and Fig. 4.20(a), the normalized spectral HRV measures are not useful for discriminating NN-, AN- and AA-infants. Comparison of normalized spectral HRV measures with the values obtained in other studies is hampered by the differences in frequency bands. From the data in [36], it can be derived that if the same frequency bands as in the present study were used, the LF/HF values are comparable for neonates with similar age. In [180], the spectral measures of HRV in full-term neonates were calculated using LF (0.03-0.15 Hz) and HF (0.15-1 Hz) frequency bands comparable to ours. The average values of LFN during QS (48 ± 17) is comparable to the value we obtained, but the LF/HF ratio is much larger (15.7 ± 15.4). Another study, in which the frequency bands recommended by the Task Force were used reported a lower LF/HF ratio (2.7) in full-term infants [130]. As the HF band (0.15-0.4 Hz) was not adjusted to account for the high respiration rate in neonates, however, the difference in LF/HF with our results should not only be attributed to maturation. Several studies using 0.2 Hz as the border between LF and HF typically report higher LF/HF ratios, especially during AS [161, 144]. Studies in which the spectra were calculated from the RR interval series itself (instead of the heart rate), yield roughly comparable values for LFN and HFN, although comparison is complicated by the fact that the frequency bands are expressed in cycles per beat [58, 38]. Regarding the differences in spectral measures between behavioural states, the absolute power in all three frequency bands is significantly larger during AS than during QS. Considering the normalized powers, a significant decrease of VLF power is observed, accompanied by significant increases in both LF and HF power, when going from AS to QS. The LF/HF ratio is significantly larger during AS than during QS. These differences between AS and QS are in accordance with several other results in preterm as well as in full-term neonates [58, 38, 175].

Neither the global *DFA scaling exponents*, nor the DFA scaling exponents during AS were significantly different between NN-, AN- and AA-infants. During QS, α_1 tended to be lower and α_2 higher in AA-infants compared to NN- and AN-infants. The difference in α_1^{QSX} between AA and AN was significant ($p < 0.05$). During the first QS segment, α_2^{QS1} was significantly higher in AA-infants compared to both NN- and AN-infants. Owing to the large overlap between the groups, however, discrimination of the different groups is not possible based on DFA scaling exponents. The differences in α_1 and α_2 can be related to differences in normalized spectral HRV measures in the corresponding frequency ranges. The LF range, where the normalized power was smaller in AA infants compared to NN- and AN-infants, corresponds approximately to the scaling range $16 < n < 60$ assuming a mean heart rate of 150 *bpm*. This scaling range corresponds approximately to the crossover range between the ranges used to calculate α_1 and α_2. The lower LF-power compared to VLF-

power in AA-infants could therefore explain the steeper slope in the fluctuation function (or in the spectrum) towards larger scales, i.e. larger α_2. Similarly, the lower LF/HF ratio in AA infants could explain the smaller scaling exponent on small scales α_1.

To our knowledge, scaling exponents of neonatal heart rate time series have so far only be reported by Bickel et al. [25]. Bickel et al. used dispersional analysis, a method which estimates the scaling exponents from the power law scaling of the standard deviation of the means of windowed data as a function of the window length [15]. The Hurst exponent in the scaling range ($4 < n < 16$), estimated on segments of 256 RR intervals, corresponds to a DFA scaling exponent between 1 and 1.5 [25]. Although no information on the behavioural state of the infants is provided in [25], this is in agreement with our results. Pikkujämsä et al. compared DFA and standard HRV measures in healthy children (< 15 years old), young ($15 - 39$ years old), middle aged($40 - 60$ years old) and elderly subjects (> 60 years old). Two DFA scaling exponents were calculated, respectively on scales $n < 11$ and $n > 11$, on 24 hour recordings and separately during night and day. Both short and long term scaling exponents tend to increase with increasing age during both day and night, although not all differences are significant. The short and long term scaling exponents reported for the young children (respectively, 0.91 ± 0.18 and 0.96 ± 0.10) are smaller than the values we obtained for neonates. This suggests a decrease in scaling exponents with age up to childhood or young adulthood followed by an increase towards senescence. The short term scaling exponent might have been underestimated, however, due to the relatively low sampling rate of the ECG (256 Hz).

Both α_1 and α_2 were found to be significantly lower during QS than during AS. Similar observations have been reported regarding differences between REM and deep sleep (to be compared to respectively active and quiet sleep in neonates) in adults. Penzel et al. compared DFA scaling exponents of healthy and sleep apnea patients in different sleep states [166]. For healthy adults, both short ($10 < n < 40$) and long term ($70 < n < 30$) scaling exponents were significantly larger during REM sleep (1.18 ± 0.24 resp. 0.81 ± 0.13) than during deep sleep (0.82 ± 0.19 resp. 0.55 ± 0.11) [166]. The long term scaling exponents are lower than the values we observed for α_2, which was estimated on a similar scaling range. As discussed in section 4.4.3, this can be explained by a relative increase in LF fluctuations compared to VLF fluctuations. The long term DFA scaling exponents ($30 < n < 70$) in healthy adults reported in [31] agree with those in [166], i.e. approximately 0.5 and 0.85 during respectively deep and REM sleep. Togo et al. investigated the fractal properties of HRV in healthy adults during different sleep states using coarse graining spectral analysis (CGSA)[3] in [203]. The scaling exponent, corresponding to the

[3]CGSA was designed to separate of the fractal component in a time series from harmonic components. The spectral index is estimated using the fractal component only. As shown in

reported spectral index estimated on segments of 128 s, was found to be higher in REM sleep (1.15) than during deep sleep (1.00). As the spectral indices were presumably estimated on the complete frequency range (corresponding to a scaling range of approximately $1 < n < 128s$), the values of the corresponding scaling exponents can not be directly compared to the results in [166, 31].

With respect to the sample asymmetry analysis, SAA-R tends to be higher in AA-infants compared to NN- and AN-infants, although only the difference between AA and AN is significant ($p < 0.05$). This suggests that AA infants have more and/or larger heart rate decelerations that are not considered as abnormal bradycardia according to the criteria presented in section 4.1.1. Owing to the large overlap between SAA-R values of the different groups, as shown in Fig. 4.18, discrimination of the different groups is not possibly using SAA-R only. In the only study reporting SAA-R values of HRV data (to our knowledge), SAA-R was used to detect early stages of neonatal sepsis in preterm infants (GA: 34 w) [111]. SAA-R was found to increase from approximately 3.3 ± 1.6 5 days before sepsis to 4.2 ± 2.3 1 day before sepsis.

4.7 Conclusion

Polysomnography, the continuous recording of physiological parameters such as ECG, respiration, SaO_2, EMG, EEG and EOG during several hours, is used to evaluate cardiorespiratory control of neonates. Home monitoring is prescribed for infants with abnormal cardiorespiratory events during the polysomnography. The main goal of the present study is to investigate if abnormal cardiorespiratory events can be predicted from the heart rate recorded during the polysomnography. The rationale for this investigation is the hypothesis that a deficiency in autonomic cardiorespiratory control is reflected in HRV. HRV, the analysis of the fluctuations in heart rate, is known to represent a non-invasive marker of autonomic activity.

The most important determinants of neonatal HR and HRV have been discussed. Respiration (RSA), baroreceptor reflex and thermoregulation introduce rhythmical fluctuations in the heart rate. Neonatal HR and HRV is also influenced by several other factors such as maturation and behavioural state. Another specific heart rate pattern, which was observed in our recordings are spikes, either due to ectopic beats or short HR decelerations.

Various parameters exist for the quantification of HRV. The standard time- and frequency domain HRV measures as defined by a consensus conference are the most commonly used [201]. The methodology for calculating these time-

the appendix B, however, the estimates of the spectral index obtained CGSA are not more accurate than those obtained with ordinary spectral analysis for real data.

domain HRV measures (SDNN, triangular index (TI), SDANN and RMSSD) and frequency-domain measures (ULF,VLF,LF,HF) is modified to account for the peculiarities of neonatal heart rate recordings. As the respiration rate is much higher in neonates than in adults, for which the standards in [201] were developed, the frequency ranges used to calculated the spectral HRV measures are adjusted. Another complication is caused by the relatively low sampling rate of our ECG recordings (100Hz), which limits the accuracy of the RR intervals. The effect of the ECG sampling rate on the RR intervals and the different standard HRV measures is analyzed. Based on the statistical properties of the errors in the RR intervals, correction factors are proposed to compensate for the bias introduced by the low ECG sampling rate. Using ECGs recorded at 1000 Hz, it is shown that these corrections allow us to accurately estimate all standard HRV measures from RR intervals series derived from ECGs sampled at 100 Hz.

During the last decade, various other methods have been used to assess HRV. Fractal analysis, which aims at quantifying the scaling behaviour of time series, proved to be a useful tool in several studies. Detrended fluctuation analysis (DFA) is a time-domain method that characterizes the scaling behaviour of a time series with one or more scaling exponents. The DFA method was analyzed and the relation with spectral analysis established. The methodology of applying DFA to neonatal RR interval series is investigated. It is shown that the DFA scaling exponents are not constant in time, but mainly dependent on behavioural state. Spikes (ectopic beats, HR decelerations) are shown to affect the scaling behaviour at small scales. It is suggested to remove them prior to applying DFA if one is interested at quantifying the scaling behaviour at small scales. Periodic fluctuations are shown to introduce a crossover in the scaling behaviour at a scale corresponding to the average period of the fluctuations. Therefore, scaling exponents estimated as the linear slope on scaling ranges near the crossover scale do not reflect the properties of a possible underlying fractal component. In order to characterize the latter, it is suggested to use all available scales. The effect of the ECG sampling rate on DFA is also investigated, and corrections are proposed based on the statistical properties of the errors on the RR intervals. It is shown that these corrections allow us to obtain accurate estimates of the scaling exponents from RR interval series derived from ECGs recorded with a sampling rate of 100 Hz .

In order to quantify the number and amplitude of the HR decelerations, which are not considered abnormal bradycardia, sample asymmetry analysis (SAA-R) was introduced. SAA-R is a measure based on the asymmetry of the histogram of the RR intervals around the median RR interval. As SAA-R is specifically used in the present study to quantify short HR decelerations, the RR interval series was detrended prior to constructing the histogram.

All HRV measures above were applied to RR interval series derived from the ECG recordings of preterm neonates. These ECGs were recorded during poly-

somnographies at the University Hospitals Leuven (Gasthuisberg). According to the results of the polysomnography (PS) and the eventual home monitoring (follow-up - FU), the infants can be divided into three groups: NN (normal PS, normal FU), AN (abnormal PS, normal FU) and AA (abnormal PS, abnormal FU). The goal of the present study was to investigate if these three groups can be distinguished using HRV parameters calculated on periods of the polysomnography without abnormal cardiorespiratory events. Three age-matched groups (both gestational and postnatal) of preterm neonates, each consisting of 10 infants, were composed. The statistical significance of the differences in HRV measures between the three groups was evaluated. Due to the small number of infants in each group, and the multiple comparisons, the results of the statistical tests should be interpreted cautiously. Of all HRV parameters calculated on the complete RR interval series, only a significant difference in SAA-R between AN and AA infants was observed. This might suggest that AA infants have more small HR decelerations. Due to the large overlap between groups, however, discrimination of the 3 groups is not possible using SAA. The HRV measures are also calculated on quiet (QS) and active sleep (AS) periods separately. During QS, a higher proportion of HF power is observed in the spectrum of AA infants compared to NN and AN infants (lower LFN, higher HFN, lower LF/HF). The observed differences in scaling exponents during QS in AA infants compared to NN and AN neonates (lower α_1, higher α_2) can be attributed to the relatively smaller proportion of LF power. Due to the large overlap between groups, however, none of these HRV measures allows discrimination of the 3 groups. Although comparison was often difficult due to differences in methodology and subjects, the values of the HRV measures reported in the present study as well as the differences between behavioural states, are in agreement with the literature.

Chapter 5

Conclusions and further research

Three biomedical applications of signal processing have been discussed. In this final chapter, the conclusions are summarized and some directions for further research are pointed out.

Subspace-based parameter estimation using data decimation

The problem of estimating the parameters of exponentially damped sinusoidal signals in the presence of noise was considered. It was shown how, in the case of oversampled signals, data decimation can be employed to reduce the computational complexity of subspace-based algorithms while retaining the same statistical accuracy. Three variants of the HTLS algorithm using data decimation were derived. HTLSDstack uses a concatenation of Hankel matrices constructed from different decimated sequences as data matrix. HTLSDsum uses the average of the Hankel matrices of each decimated sequence as data matrix. HTLSDdese uses the original, not decimated data matrix to estimate the decimated signal poles by exploiting the shift invariance property between its D order lower shift (top D rows deleted) and D order upper shift (bottom D rows deleted) equivalents (where D represents the decimation factor). The computational complexity of the three decimative HTLS variants is analyzed. The optimal matrix dimensions were determined for each method. The statistical accuracy and the robustness of the methods were compared using Monte Carlo simulations on reference signals and simulated MRS signals. It was concluded that decimation as applied in HTLSDstack yields as good estimates as the best possible ones without decimation at a much lower computational cost. The reduction in computational cost increases with increasing decimation

factor. For a given decimation factor, the computational cost of HTLSDsum is even lower, but the statistical accuracy of the parameter estimates of the peaks close to the Nyquist frequency is also lower. The decimative approach HTLSDdese does not offer any computational advantage, while its statistical accuracy did not prove to be higher than that of the other algorithms.

Near-infrared spectroscopy

Different studies regarding the clinical use and validation of NIRS with respect to the monitoring of cerebral circulation and oxygenation in neonates have been conducted in collaboration with the University Hospitals Leuven. A commercial NIRS device was used to measure concentration changes of HbO_2 and Hb, cerebral blood flow (CBF) and volume (CBV), and TOI. In the first study, cerebral TOI was measured in prematurely born infants. It was found that TOI is a stable parameter reflecting the cerebral venous oxygen saturation and that TOI increases during the first three days of life. In the second study, the effect of rewarming on the cerebral circulation and oxygenation of very preterm infants with hypothermia was investigated. No negative effects of rewarming on the cerebral oxygenation were found. In the third study, the assessment of cerebral autoregulation based on NIRS measurements was investigated. Concordant changes in mean arterial blood pressure (MAP) and cerebral intravascular oxygenation (HbD) measured non-invasively with NIRS, are assumed to reflect impaired cerebral autoregulation. A new method to quantify the concordance of MAP and HbD was proposed and compared to correlation and coherence analysis. The first measurements suggest that the new method and the correlation coefficient are better parameters to detect impaired cerebral autoregulation. A larger follow-up study is needed, however, to confirm the performance of the methods and to evaluate the predictive value of the different parameters with respect to possible brain damage in the clinic.

In another study, in collaboration with the University of Illinois at Urbana-Champaign, NIRS was used for the monitoring of brain activity. Functional NIRS relies on the changes of the optical properties of the brain tissue related to functional activation. Two types of signals can be observed: the fast neuronal signal, presumably caused by light scattering, which is directly related to neuronal activity, and the slow hemodynamic signal, due to light absorption, related to hemodynamic changes in the activated area. The aim of this study was to detect the fast signal in the motor cortex during a finger tapping exercise. As the amplitude of the fast neuronal signal is small compared to the slow hemodynamic signal and other physiological noise, it is difficult to detect. On the other hand, it is more localized than the slow signal because it is directly related to neuronal activity. Using advanced signal processing techniques, we were able to detect the fast neuronal signal in the motor cortex during a finger-tapping exercise. Low-noise frequency-domain NIRS instrumentation with 4 crossed source-detector pairs was used. The arterial pulsatility, which was the

main source of physiological noise, was first reduced using an adaptive filter. On the filtered signals, independent component analysis was applied to separate a signal component due to the neuronal activity. In 9 out of 14 subjects, an independent component could be extracted from the light intensity signals where the power at the tapping frequency during stimulation was significantly larger than during rest. In those 9 subjects, 67 out of 78 tapping periods could be identified individually in a time-frequency plot of the independent component. In the phase signals, we only found indications of the fast signal in 2 out of 14 subjects.

NIRS is a promising tool for monitoring hemodynamic and neuronal changes in the brain. It is not used to monitor brain circulation and oxygenation in clinical practice, so far, due to the limited accuracy and reproducibility of the quantified parameters. To overcome these limitations advances in both hardware and signal processing are necessary. New near-infrared spectroscopy devices that incorporate measurement of the optical pathlength factor can contribute to this, as well as technical details such as optode designs which reduce sensitivity to movement and the effect of ambient light. On the other hand, also in the signal processing and modelling aspects, there is potential for improvement. The use of more sophisticated computer modelling will allow to take into account effects such as scattering and inhomogeneities, thereby providing more accurate quantification. Furthermore, before NIRS could be introduced in routine clinical practice, proper large scale studies should be performed to validate its reliability and to define critical values of the different oxygenation parameters. Advances in hardware and modelling would be beneficial for functional NIRS too. Regarding the measurement of fast neuronal signals with NIRS, further research is needed to address some specific issues:

- Measurements with larger sensors, with more sources and detectors, could allow localization of brain activity based on the fast optical signal. As the fast signal is expected to be more localized, this technique could have a higher spatial resolution than techniques based on the slow signal, at least for the more superficial cortical areas (the penetration of NIR light is limited to a few centimeters from the skull).
- As the fast signal was observed in different studies, either in intensity or in phase signal, efforts should be made to combine the necessary hardware and signal processing tools to detect the fast signal in both the intensity and the phase signal at the same time. From the relationship between both signals, the origin of the fast signal, absorption or scattering, could be determined.
- Larger studies with different stimuli are needed to study the reproducibility of the fast signal in different conditions.

Heart rate variability of neonates

The heart rate variability (HRV) of neonates was analyzed to predict abnormal cardiorespiratory events. The properties and determinants of neonatal HR and HRV were discussed, and the differences in comparison with adults were pointed out. Several measures were used to quantify different aspects HRV, standard HRV measures as well as recently introduced methods. As the standard HRV measures were defined for adults, the methodology was adapted to account for the differences between neonatal and adult heart rate. Besides the standard HRV measures, the application of two recently introduced signal analysis methods to neonatal heart rate data, was studied. Detrended fluctuation analysis (DFA) is a time-domain method that characterizes a time series with one or more scaling exponents estimated as the slope of the so-called fluctuation function, which represents the scaling behaviour of the variance of the time series. The DFA method was analyzed and the relation with spectral analysis established. The methodology of applying DFA to neonatal RR interval series was investigated. It was shown that the DFA scaling exponents are not constant in time, but mainly dependent on behavioural state. As spikes (ectopic beats, HR decelerations) were shown to affect the fluctuation function at small scales, it is suggested to remove them prior to applying DFA if one is interested at quantifying the scaling behaviour at small scales. It was shown that periodic fluctuations introduce a crossover in the scaling behaviour at a scale corresponding to the average period of the fluctuations. Therefore, the slope of the fluctuation function in the neighborhood of the crossover scale do not reflect the properties of a possible underlying fractal component. In order to characterize the latter, it is better to use a wider scaling range. In order to quantify the number and amplitude of the HR decelerations, sample asymmetry analysis (SAA) was used. SAA is a measure based on the asymmetry of the histogram of the RR intervals around the median RR interval. Another methodological aspect that needed consideration was the relatively low sampling rate of the ECG recordings during normal polysomnographies. As the heart rate was determined from the R-peaks in the ECG, the accuracy of the heart rate is limited by the sampling frequency of the ECG. The effect of the ECG sampling rate on the HRV measures was analyzed. Based on the statistical properties of the errors in the RR intervals, correction factors were introduced to compensate for the bias introduced by the low ECG sampling rate. Using a set of ECGs that were recorded at a higher sampling rate, the accuracy of the proposed corrections was verified.

All aformentioned HRV parameters were applied to RR interval series derived from the ECG recording of preterm neonates. These ECGs were recorded during polysomnographies at the University Hospitals Gasthuisberg. According to the results of the polysomnography (PS) and the eventual home monitoring (follow-up - FU), the infants can be divided into three groups: NN (normal PS, normal FU), AN (abnormal PS, normal FU) and AA (abnormal PS, abnormal

FU). The goal of the present study was to investigate if these three groups can be distinguished using HRV parameters calculated on periods of the polysomnography without abnormal cardiorespiratory events. Three age-matched groups (both gestational and postnatal) of preterm neonates, each consisting of 10 infants, were composed. The statistical significance of the differences in HRV parameters between the three groups was evaluated. Due to the small number of infants in each group, and the multiple comparisons, the results of the statistical tests should be interpreted cautiously. Of all HRV measures calculated on the complete RR intervals series, only a significant difference in SAA between AN and AA infants was observed. This might suggest that AA infants have more small HR decelerations. Due to the large overlap between groups, however, discrimination of the 3 groups is not possible using SAA. The HRV measures were also calculated on quiet (QS) and active sleep (AS) periods separately. During QS, an higher proportion of HF-power was observed in the spectrum of AA infants compared to NN and AN infants (lower LFN, higher HFN, lower LF/HF). The observed differences in scaling exponents during QS in AA infants compared to NN and AN neonates (lower α_1, higher α_2) can be attributed to the relatively smaller proportion of LF-power. Due to the large overlap between groups, however, none of these HRV parameters allows discrimination of the 3 groups. Although comparison was often difficult due to differences in methodology and subjects, the values of the HRV measures reported in the present study as well as the differences between behavioural states, are in agreement with the literature.

Further research on this topic should include a study with larger groups to assess the statistical significance of the differences in HRV parameters. If more patients are available, classification techniques such logistic regression or neural networks, could provide a better discrimination by combining different HRV parameters. In addition, other parameters could be used to quantify other aspects of HRV. Approximate entropy, for example, was suggested to be different in ALTE-infants compared to normals [169]. As we could not reliably estimate approximate entropy from 100 Hz RR interval series, however, either a higher ECG sampling rate should be used or the method should be adjusted to compensate for the effect of the ECG sampling rate. On the other hand, a larger study that compared approximate entropy of HRV between ALTE infants and normals could not find a significant difference between the two groups [231]. A potentially more powerful approach consists in analyzing additional signals such as respiration or oxygen saturation. Further research is needed, for example, to improve the understanding of the variability of the respiration of preterm infants, which is higher than in fullterm infants. Furthermore, the analysis of the interaction between the heart rate, respiration and oxygen saturation could reveal information regarding cardiac flow, lung volume, metabolism, vasomotor response, etc. Such physiological information could provide a better basis for discrimination between the different groups.

Bibliography

[1] National institutes of health consensus development conference on infantile apnea and home monitoring, sept 29 to oct 1, 1986. *Pediatrics*, 79(2):292–299, 1987.

[2] Antila K Valimaki I. Aarimaa T, Oja R. Interaction of heart rate and respiration in newborn babies. *Pediatric Research*, 24(6):745–750, 1988.

[3] P.-A. Absil, R. Sepulchre, A. Bilge, and P. Gérard. Nonlinear analysis of cardiac rhythm fluctuations using DFA method. *Physica A*, 272(1-2):235–244, 1999.

[4] L. Adcock, L. Wafelman, S. Hegemier, A. Moise, M. Speer, C. Contant, and J. Goddard-Finegold. Neonatal intensive care applications of near-infrared spectroscopy. *Clinics in perinatology*, 26(4):893–903, Dec 1999.

[5] H. Akaike. Information theory and an extension of the maximum likelihood principle. In *Proc. of the 2nd International Symposium on Information Theory*, page 267.

[6] M. Akay, editor. *Time frequency and wavelets in biomedical signal processing*. IEEE Press, Piscataway, NJ, USA, 1998.

[7] S. Akselrod, D. Gordon, F.A. Ubel, D.C. Shannon, A.C. Barger, and R.J. Cohen. Power spectrum analysis of heart rate fluctuation: a quantitative probe of beat to beat cardiovascular control. *Science*, 213(4504):220–222, 1981.

[8] R.L. Ariagno, M. Mirmiran, M.M. Adams, A.G. Saporito, A.M. Dubin, and R.B. Baldwin. Effect of position on sleep, heart rate variability, and qt interval in preterm infants at 1 and 3 months' corrected age. *Pediatrics*, 111(3):622–625, 2003.

[9] S.R. Arridge and J.C. Hebden. Optical imaging in medicine ii: Modelling and reconstruction. *Physics in Medicine and Biology*, 42(5):841–853, 1997.

[10] A. Aubert, B. Seps, and F. Beckers. Heart rate variability in athletes. *Sports Med.*, 33(12):889–919, 2003.

[11] K. Baldzer, F.D. Dykes, S.A. Jones, M. Brogan, T.A. Carrigan, and D.P. Giddens. Heart rate variability analysis in full-term infants: spectral indices for study of neonatal cardiorespiratory control. *Pediatric Research*, 26(3):188–195, 1989.

[12] C.P. Barfield, V.Y. Yu, O. Noma, J. Kukita, L.J. Cussen, A. Oates, and A.M. Walker. Cerebral blood volume measured using near-infrared spectroscopy and radiolabels in the immature lamb brain. *Pediatric Research*, 46(1):50–56, 1999.

[13] A.K. Barros, R. Vigario, V. Jousmäki, and N. Ohnishi. Extraction of event-related signals from multichannel bioelectrical measurements. *IEEE Trans Biomed Eng.*, 47(5):589–593, 2000.

[14] J.B. Bassingthwaighte, L.S. Liebovitch, and B.J. West. *Fractal physiology.* Oxford University Press, New York, 1994.

[15] J.B. Bassingthwaighte and G.M. Raymond. Evaluation of dispersional analysis method for fractal time series. *Ann Biomed Eng.*, 23:491–505, 1995.

[16] F. Beckers. *Linear and non-linear dynamics of cardiovascular variability: validation and clinical applications.* PhD thesis, K.U. Leuven, 2002.

[17] F. Beckers, D. Ramaekers, J. Van Cleemput, W. Droogne, J. Vanhaecke, F. Van de Werf, and A.E. Aubert. Association between restoration of autonomic modulation in the native sinus node and hemodynamic improvement after cardiac transplantation. *Transplantation*, 73(10):1614–1620, 2002.

[18] A.J. Bell and T.J. Sejnowski. An information-maximisation approach to blind separation and blind deconvolution. *Neural Computation*, 7:1129–1159, 1995.

[19] A. Belouchrani, K. Abed-Meraim, J.-F. Cardoso, and E. Moulines. A blind source separation technique using second order statistics. *IEEE Trans Signal Process.*, 45(2):434–444, Feb 1997.

[20] D.A. Benaron, C.D. Kurth, J.M. Steven, M. Delivoria-Papadopoulos, and B. Chance. Transcranial optical path length in infants by near-infrared phase-shift spectroscopy. *J. Clin. Monit.*, 11(2):109–117, 1995.

[21] J. Beran. *Statistics for long-memory processes.* Chapman & Hall, 1994.

[22] R.D. Berger, S. Akselrod, D. Gordon, and R.J. Cohen. An efficient algortihm for spectral analysis of heart rate variability. *IEEE Trans Biomed Eng.*, 33(9):900–904, September 1986.

[23] G.G. Berntson, J.T. Bigger, D.L. Eckberg, P. Grossman, P.G. Kaufmann, M. Malik, N.H. Nagaraja, S.W. Porges, J.P. Saul, P.H. Stone, and M.W. van der Molen. Heart rate variability: origins, methods, and interpretive caveats. *Psychophysiology*, 34(6):623–648, 1997.

[24] D.V. Bhaskar Rao and K.S. Arun. Model based processing of signals: a state space approach. *Proceedings IEEE*, 80:283–309, 1992.

[25] D.R. Bickel, M.T. Verklan, and J. Moon. Detection of anomalous diffusion using confidence intervals of the scaling exponent with application to preterm neonatal heart rate variability. *Phys Rev. E*, 58:6440–6448.

[26] J.T. Bigger, R.C. Steinman, L.M. Rolnitzky, J.L. Fleiss, P. Albrecht, and R.J. Cohen. Power law behavior of RR-interal variability in healthy middle-aged persons, patients with recent myocardial infarction, and patients with heart transplants. *Circulation*, 93:2142–2151, 1996.

[27] D.A. Boas, T. Gaudette, G. Strangman, X. Cheng, J.J.A. Marota, and J.B. Mandeville. The accuracy of near infrared spectroscopy imaging during focal changes in cerebral hemodynamics. *NeuroImage*, 13:76–90, 2001.

[28] R.F. Bonner, R. Nossal, S. Havlin, and G.H.J. Weiss. Model for photon migration in turbid biological media. *J Opt Soc Am.*, 4:423–432, 1987.

[29] N.C. Brun, A. Moen, K. Borch, O.D. Saugstad, and G. Greisen. Near-infrared monitoring of cerebral tissue oxygen saturation and blood volume in newborn piglets. *Am J Physiol.*, 273(2 Pt 2):H682–686, 1997.

[30] H.U. Bucher, A.D. Edwards, A.E. Lipp, and G. Duc. Comparison between near-infrared spectroscopy and 133-xenon clearance for estimation of cerebral blood flow in critically ill preterm infants. *Pediatric Research*, 33(1):56–60, 1993.

[31] A. Bunde, S. Havlin, J.W. Kantelhardt, T. Penzel, J.-H. Peter, and K. Voigt. Correlated and uncorrelated regions in heart-rate fluctuations during sleep. *Phys Rev Lett*, 85(17):3736–3739, 2000.

[32] L.A. Cabal, B. Siassi, B. Zanini, J.E. Hodgman, and E.E. Hon. Factors affecting heart rate variability in preterm infants. *Pediatrics*, 65(1):50–56, 1980.

[33] V.D. Calhoun, T. Adali, L.K. Hansen, J. Larsen, and J.J. Pekar. Ica of functional MRI data: an overview. *4th international symposium on ICA and BSS (ICA2003)*, pages 281–287, 2003.

[34] J.F. Cardoso. High-order contrasts for independent component analysis. *Neural Computation*, 11(1):157–192, Jan 1999.

[35] A. Casaleggio, S. Cerutti, and M.G. Signorini. Study of the lyapunov exponents in heart rate variability signals. *Methods Inf Med.*, 36(4-5):274–277, Dec 1997.

[36] U. Chatow, S. Davidson, B.L. Reichman, and S. Akselrod. Development and maturation of the autonomic nervous system in premature and full-term infants using spectral analysis of heart rate fluctuations. *Pediatric Research*, 37(3):294–302, 1995.

[37] P.S. Churchland and T.J. Sejnowski. Perspectives in cognitive neuroscience. *Science*, 242:741–745, 1988.

[38] J. Clairambault, L. Curzi-Dascalova, F. Kauffmann, C. Medigue, and C. Leffler. Heart rate variability in normal sleeping full-term and preterm neonates. *Early Human Dev.*, 28(2):169–183, 1992.

[39] L.B. Cohen. Changes in neuron structure during action potential propagation and synaptic transmission. *Physiological Reviews*, 53(2):373–418, 1973.

[40] P. Comon. Independent component analysis, a new concept? *Signal Processing*, 36(3):287–314, April 1994.

[41] L. Curzi-Dascalova, E. Christova, P. Peirano, B.B. Singh, and C. Gaultier G. Vicente. Relationship between respiratory pauses and heart rate during sleep in normal premature and full-term newborns. *J Dev Physiol.*, 11(6):323–330, 1989.

[42] L. Curzi-Dascalova, F. Kauffmann, C. Gaultier, and R.H. Caldas de Amorim. Heart rate modifications related to spontaneous body movements in sleeping premature and full-term newborns. *Pediatric Research*, 45(4 Pt 1):515–518, 1999.

[43] A.M. Dale and E. Halgren. Spatiotemporal mapping of brain activity by integration of multiple imaging modalities. *Curr Opin Neurobiol.*, 11:202–208, 2001.

[44] H. Daniëls, G. Naulaers, F. Deroost, and H. Devlieger. Polysomnography and home documented monitoring of cardiorespiratory pattern. *Archives of disease in childhood*, 81(5):434–436, Nov 1999.

[45] R.B. Davies and D.S. Harte. Test for hurst effect. *Biometrika*, 74:95–101.

[46] R.A. De Blasi, M. Cope, C. Elwell, F. Safoue, and M. Ferrari. Noninvasive measurement of human forearm oxygen consumption by near infrared spectroscopy. *Eur J Appl Physiol Occup Physiol.*, 67(1):20–25, 1993.

[47] L. De Lathauwer. *Signal Processing based on Multilinear Algebra*. PhD thesis, K.U.Leuven, 1997.

[48] L. De Lathauwer, B. De Moor, and J. Vandewalle. Fetal electrocardiogram extraction by blind source subspace separation. *IEEE Trans Biomed Eng.*, 47(5):567–572, May 2000.

[49] D.T. Delpy, M. Cope, P. van der Zee, S. Arridge, S. Wray, and J.S. Wyatt. Estimation of optical pathlength through tissue from direct time of flight measurement. *Physics in Medicine and Biology*, 33(12):1433–1442, 1988.

[50] M.C. DeSoto, M. Fabiani, D.C. Geary, and G. Gratton. When in doubt, do it both ways: brain evidence of the simultaneous activation of conflicting motor responses in a spatial stroop task. *J Cogn Neurosci.*, 13(4):523–536, 2001.

[51] J.O. Diaz, Mäkikallio, H.V. Huikuri, G. Lopera, R.D. Mitrani, A. Castellanos, R.J. Myerburg, P. Rozo, F. Pava, and C.A. Morillo. Heart rate dynamics before the spontaneous onset of ventricular tachyarrhythmias in chagas' heart disease. *Am J Cardiol.*, 87(9):1123–1125, 2001.

[52] M.Y. Dincsoy, Y.M. Kim, F. Siddiq, M.G. Garcia, and H. Williams. Intracranial hemorrhage in small-for-gestational-age neonates: comparison with weight-matched appropriate-for-gestational-age infants. *Clin Pediatr.*, 27(1):21–26, 1988.

[53] A.J. du Plessis, J. Newburger, R.A. Jonas, P. Hickey, H. Naruse, M. Tsuji, A. Walsh, G. Walter, D. Wypij, and J.J. Volpe. Cerebral oxygen supply and utilization during infant cardiac surgery. *Ann Neurol.*, 37(4):488–497, 1995.

[54] A. Duncan, J.H. Meek, M. Clemence, C.E. Elwell, P. Fallon, L. Tyszczuk, M. Cope, and D.T. Delpy. Measurement of cranial optical-path length as a function of age using phase-resolved near-infrared spectroscopy. *Pediatric Research*, 39(5):889–894, 1996.

[55] A. Duncan, J.H. Meek, M. Clemence, C.E. Elwell, L. Tyszczuk, M. Cope, and D.T. Delpy. Optical pathlength measurements on adult head, calf and forearm and the head of the newborn-infant using phase-resolved optical spectroscopy. *Physics in Medicine and Biology*, 40(2):395–304, 1995.

[56] A. Edner, M. Katz-Salamon, H. Lagercrantz, M. Ericson, and J. Milerad. Heart rate variability in infants with apparent life-threatening events. *Acta Paediatr*, 89:1329–1329, 2000.

[57] A. Edwards, J. Wyatt, C. Richardson, D. Delpy, M. Cope, and E. Reynolds. Cotside measurements of cerebral blood flow in ill newborn infants by near infrared spectroscopy. *The Lancet*, (8614):770–771, 1988.

[58] M. Eiselt, L. Curzi-Dascalova, J. Clairambault, F. Kauffmann, C. Medigue, and P. Peirano. Heart-rate variability in low-risk prematurely born infants reaching normal term: a comparison with full-term newborns. *Early Human Dev.*, 32(2-3):183–195, 1980.

[59] M. Eiselt, L. Curzi-Dascalova, C. Leffler, and E. Christova. Sigh-related heart rate changes during sleep in premature and full-term newborns. *Neuropediatrics*, 23(6):286–291, 1992.

[60] A. Eke, P. Herman, L. Kocsis, and L.R. Kozak. Fractal characterization of complexity in temporal physiological signals. *Physiol Meas.*, (23):R1–R38, 2002.

[61] P. Fallon, I. Roberts, F.J. Kirkham, M.J. Elliott, A. Lloyd-Thomas, R. Maynard, and A.D. Edwards. Cerebral hemodynamics during cardiopulmonary bypass in children using near-infrared spectroscopy. *Ann Thorac Surg.*, 56(6):1473–1477, 1993.

[62] S. Fantini, M.A. Franceschini, J.B. Fishkin, B. Barbieri, and E. Gratton. Quantitative determination of the absorption spectra of chromophores in strongly scattering media: a light-emitting-diode based technique. *Applied Optics*, 33(22):5204–5213, 1994.

[63] S. Fantini, M.A. Franceschini, and E. Gratton. Semi-infinite-geometry boundary problem for light migration in highly scattering media: a frequency-domain study in diffusion approximation. *J Opt Soc Am. B*, 11(10):2128–2138, 1994.

[64] P. Flandrin. On the spectrum of fractional brownian motions. *IEEE Trans Info Th.*, 35:197–199, 1989.

[65] S.-E. Fotinea, Y.Dologlou, and G. Carayannis. Decimation and SVD to estimate exponentially damped sinusoids in the presence of noise. In *Proc. of 2001 IEEE International Conference on Acoustics, Speech, and Signal Processing ICASSP*, volume V, pages pp. 3073–3076, Salt Lake City, Utah, USA, 7-11 May 2001.

[66] M.A. Franceschini and D.A. Boas. Noninvasive measurement of neuronal activity with near-infrared optical imaging. *NeuroImage*, 21:372–386, 2004.

[67] D. B. Percival G. M. Raymond and J. B. Bassingthwaighte. The spectra and periodograms of anti-correlated discrete fractional gaussian noise. *Physica A*, 322:169–179, 2003.

[68] X. Giannakopoulos, J. Karhunen, and E. Oja. Experimental comparison of neural algorithms for independent component analysis and blind separation. *Int. J. of Neural Systems*, 9(2):651–656.

[69] S.F. Glotzbach, R.B. Baldwin, N.E. Lederer, P.A. Tansey PA, and R.L. Ariagno. Periodic breathing in preterm infants: incidence and characteristics. *Pediatrics*, 84(5):785–792, 1989.

[70] J. Goddard-Finegold, P.T. Louis, D.L. Rodriguez, Y. David, C.F. Contant, and P. Rolfe. Correlation of near infrared spectroscopy cerebral blood flow estimations and microsphere quantitations in newborn piglets. *Biol. Neonate*, 74(5):376–384, 1998.

[71] A.L. Goldberger. Non-linear dynamics for clinicians: chaos theory, fractals, and complexity at the bedside. *Lancet*, 347(9011):1312–4, May 1996.

[72] K. Goto, M. Mirmiran, M.M. Adams, R.V. Longford, R.B. Baldwin, M.A. Boeddiker, and R.L. Ariagno. More awakenings and heart rate variability during supine sleep in preterm infants. *Pediatrics*, 103(3):603–609, 1999.

[73] G. Gratton and P. M. Corballis. Removing the heart from the brain: Compensation for the pulse artifact in the photon migration signal. *Psychophysiology*, 32(3):292–299, May 1995.

[74] G. Gratton, P.M. Corballis, E. Cho, M. Fabiani, and D.C. Hood. Shades of gray matter: noninvasive optical images of human brain responses during visual stimulation. *Psychophysiology*, 32(5):505–509, 1995.

[75] G. Gratton and M. Fabiani. The event-related optical signal: a new tool for studying brain function. *Int J Psychophysiol.*, 42(2):109–121, 2001.

[76] G. Gratton and M. Fabiani. Shedding light on brain function: the event-related optical signal. *Trends in cognitive sciences*, 5(8):357–363, 2001.

[77] G. Gratton and M. Fabiani. The event-related optical signal (eros) in visual cortex: replicability, consistency, localization, and resolution. *Psychophysiology*, 40(4):561–571, 2003.

[78] G. Gratton, M. Fabiani, P.M. Corballis, D.C. Hood, M.R. Goodman-Wood, J. Hirsch, K. Kim, D. Friedman, and E. Gratton. Fast and localized event-related optical signals (eros) in the human occipital cortex: comparisons with the visual evoked potential and fmr. *NeuroImage*, 6(3):168–180, 1997.

[79] G. Gratton, M. Fabiani, D. Friedman, M.A. Franceschini, S. Fantini, P.M. Corballis, and E. Gratton. Rapid changes of optical parameters in the human brain during a tapping task. *J Cogn Neurosci.*, 1995.

[80] G. Gratton, J.S. Maier, M. Fabiani, W.W. Mantulin, and E. Gratton. Feasibility of intracranial near-infrared optical scanning. *Psychophysiology*, 31:211–215, 1994.

[81] A. Grinvald, E. Lieke, R.D. Frostig, C.D. Gilbert, and T.N. Wiesel. Functional architecture of cortex revealed by optical imaging of intrinsic signals. *Nature*, 324:361–364, 1986.

[82] B. Halder and T. Kailath. Efficient estimation of closely spaced sinusoidal frequencies using subspace-based methods. *IEEE Signal Processing Letters*, 4(2):49–51, February 1997.

[83] R.M. Harper, D.O. Walter, B. Leake, H.J. Hoffman, G.C. Sieck, M.B. Sterman, T. Hoppenbrouwers, and J. Hodgeman. Development of sinus arrhythmia during sleeping and waking states in normal infants. *Sleep*, 1:33–48, 1978.

[84] D.J. Hawrysz and E.M. Sevick-Muraca. Developments toward diagnostic breast cancer imaging using near-infrared optical measurements and fluorescent contrast agents. *Neoplasia*, 2(5):388–417, 2000.

[85] J.C. Hebden. Advances in optical imaging of the newborn infant brain. *Psychophysiology*, 40(4):501–510, 2003.

[86] H. Helmholtz. Ueber einige gesetze der vertheiliung elektrischer strome in korperlichen leitern, mit anwendung auf die thierisch-elektrischen versuche. *Ann Phys Chem*, 89:211–233, 353–377, 1853.

[87] C. Heneghan and G. McDarby. Establishing the relation between detrended fluctuation analysis and power spectral density analysis for stochastic processes. *Phys Rev E*, 62(5):6103–6110, 2000.

[88] T. Higuchi. Relationship between the fractal dimension and the power law index for a time series: a numerical investigation. *Physica D*, 46:254–264, 1990.

[89] E. Hillman. *Experimental and theoretical investigations of near infrared tomographic imaging methods and clinical applications.* PhD thesis, University College London, 2002.

[90] J.E. Hodgman, F. Gonzalez, T. Hoppenbrouwers, and L.A. Cabal. Apnea, transient episodes of bradycardia, and periodic breathing in preterm infants. *Am J Dis Child.*, 144(1):54–57, 1990.

[91] E.H. Hon and S.T. Lee. Electronic evaluations of the fetal heart rate patterns preceding fetal death: further observations. *Am. J. Obstet. Gynecol.*, 87:817–826, 1965.

[92] Y. Hoshi. Functional near-infrared optical imaging: utility and limitations in human brain mapping. *Psychophysiology*, 40(4):511–520, 2003.

[93] K. Hu, P. Ch. Ivanov, Z. Chen, P. Carpena, and H. E. Stanley. Effect of trends on detrended fluctuation analysis. *Phys Rev E*, 64:011114, 2001.

[94] Y. Hua and T.K. Sartkar. Matrix pencil method for estimating parameters of exponentially damped sinusoids in noise. *IEEE Trans Acoust Speech Signal Process.*, 38(5):814–824, May 1990.

[95] A.G. Hudetz, B.B. Biswal, H. Shen, K.K. Lauer, and J.P. Kampine. Spontaneous fluctuations in cerebral oxygen supply. an introduction. *Adv Exp Med Biol.*, 454:551–9, 1998.

[96] H.V. Huikuri, T. Mäkikallio, K.E. Airaksinen, R. Mitrani, A. Castellanos, and R.J. Myerburg. Measurement of heart rate variability: a clinical tool or a research toy? *J Am Coll Cardiol.*, 34(7):1878–1883, 1999.

[97] H.V. Huikuri, T.H. Mäkikallio, C.K. Peng, A.L. Goldberger, U. Hintze, and M. Moller. Fractal correlation properties of R-R interval dynamics and mortality in patients with depressed left ventrical function after an acute myocardial infarction. *Circulation*, 101:47–53, 2000.

[98] H. Hurst. Long-term storage capacity of reservoirs. *Trans Am Soc Civ Eng.*, 116:770–808, 1951.

[99] A. Hyvärinen and E. Oja. Independent component analysis: Algorithms and applications. *Neural Networks*, 13(4-5):411–430, 2000.

[100] A. Ishimaru. Diffusion of a pulse in densely distributed scatters. *J Opt Soc Am.*, 68:1045–1050, 1978.

[101] P.Ch. Ivanov, A. Bunde, L.A. Amaral, S. Havlin, J. Fritsch-Yelle, R.M. Baevsky, H.E. Stanley, and A.L. Goldberger. Sleep-wake differences in scaling behavior of the human heartbeat. *Europhys Lett.*, 48(5):594–600, 1999.

[102] T. Jahnukainen, C. Van Ravenswaaij-Arts, J. Jalonen, and I. Valimaki. Dynamics of vasomotor thermoregulation of the skin in term and preterm neonates. *Early Human Dev.*, 33(2):133–143.

[103] H.H. Jasper. Report of the committee on methods of clinical examination in electroencephalography. *Electroencephalography and clinical neurophysiology*, 10:370–375, 1957.

[104] F. F. Jöbsis. Noninvasive, infrared monitoring of cerebral and myocardial oxygen sufficiency and circulatory parameters. *Science*, 198(4323):1264–1267, Dec 1977.

[105] T.P. Jung, S. Makeig, T.W. Lee, M.J. McKeown, G. Brown, A.J. Bell, and T.J. Sejnowski. Independent component analysis of biomedical signals. *2nd International Workshop on Independent Component Analysis and Signal Separation*, pages 633–644, 2000.

[106] J.W. Kantelhardt, E. Koscielny-Bunde, H.H.A. Rego, S. Havlin, and A. Bunde. Detecting long-range correlations with detrended fluctuation analysis. *Physica A*, 295:441–454, 2001.

[107] D.T. Kaplan. Nonlinearity and nonstationarity: the use of surrogate data in interpreting fluctuations. Frontiers in blood pressure and heart rate analysis, pages 486–495. IOS Press, 1997.

[108] P.G. Katona, A. Frasz, and J. Egbert. Maturation of cardiac control in full-term and preterm infants during sleep. *Early Human Dev.*, 4(2):145–159, 1980.

[109] S.M. Kay. *Modern Spectral Estimation*. Prentice Hall, 1988.

[110] M. Kohl, R. Watson, and M. Cope. Optical properties of highly scattering media determined from changes in attenuation, phase, and modulation depth. *Applied Optics*, 36(1):105–115, 1996.

[111] B.P. Kovatchev, L.S. Farhy, H. Cao, M.P. Griffin, D.E. Lake, and R.J. Moorman. Sample asymmetry analysis of heart rate characteristics with application to neonatal sepsis and systemic inflammatory response syndrome. *Pediatric Research*, 54(6):892–898, 2003.

[112] R. Kumaresan and D.W. Tufts. Estimating the parameters of exponentially damped sinusoids and pole-zero medeling in noise. *IEEE Trans Acoust Speech Signal Process.*, 30(6):833–840, 1982.

[113] P. Laguna, G.B. Moody, and R.G. Mark. Power spectral density of unevenly sampled data by least-squares analysis: performance and application to heart rate signals. *IEEE Trans Biomed Eng.*, 45(6):698–715, 1998.

[114] E.L. Lehmann. Nonparametric statistical methods based on ranks, 1975.

[115] H.L. Leistner, G.G. Haddad, R.A. Epstein, T.L. Lai, M.A. Epstein, and R.B. Mellins. Heart rate and heart rate variability during sleep in aborted sudden infant death syndrome. *J Pediatr.*, 97(1):51–55, 1980.

[116] L.Y. Lin, J.L. Lin JL, C.C. Du, L.P. Lai, Y.Z. Tseng, and S.K. Huang. Reversal of deteriorated fractal behavior of heart rate variability by beta-blocker therapy in patients with advanced congestive heart failure. *J Cardiovasc Electrophysiol.*, 12(1):26–32, 2001.

[117] H.C. Lou, N.A. Lassen, and B. Friis-Hansen. Impaired autoregulation of cerebral blood flow in the distressed newborn infant. *J Pediatr*, 94(1):118–121, 1979.

[118] T.H. Mäkikallio, H.V. Huikuri, U. Hintze, J. Videbæk, R.D. Mitrani, A. Castellanos, R.J. Myerburg, and M. Möller; DIAMOND Study Group. Fractal analysis and time- and frequency-domain measures of heart rate variability as predictors of mortality in patients with heart failure. *Am J Cardiol.*, 87(2):178–182, 2001.

[119] T.H. Mäkikallio, T. Ristimäe, K.E.J. Airaksinen, C.K. Peng, A.L. Goldberger, and H.V. Huikuri. Heart rate dynamics in patients with stable angina pectoris and utility of fractal and complexity measures. *Am J Cardiol.*, 81(1):27–31, 1998.

[120] M. Malik. Heart rate variability. *Curr Opin Cardiol.*, 13:36–68, 1998.

[121] M. Malik and A.J. Camms, editors. *Heart Rate Variability.* Futura Publishing Company, 1995.

[122] A. Malliani, M. Pagani, F. Lombardi, and S. Cerutti S. Cardiovascular neural regulation explored in the frequency domain. *Circulation*, 84(2):482–492, 1991.

[123] D. Malonek and A. Grinvals. Vascular regulation at submillimeter range. *Adv. Exp. Med. Biol.*, 413:215–219, 1997.

[124] B. Mandelbrot. *Fractals: form, chance, and dimension.* Freeman San Francisco (Calif.), 1977.

[125] S.J. Matcher, P. Kirkpatrick, K. Nahid, M. Cope, and D.T. Delpy. Absolute quantification methods in tissue near infrared spectroscopy. volume 2389 of *Proceedings of SPIE*, pages 486–495, 1995.

[126] S.J. Matcher, K. Nahid, M. Cope, and D.T. Delpy. Absolute $S0_2$ measurements in layered media. *OSA TOPS on Advances in Optical Imaging and Photon Migration*, 3:83–91, 1996.

[127] J. Mateo and P. Laguna. Improved heart rate variability signal analysis from the beat occurrence times according to the ipfm model. *IEEE Trans Biomed Eng.*, 47(8):985–996, 2000.

[128] M. McKeown, S. Makeig, G. Brown, T.-P. Jung, S. Kindermann, A. Bell, and T. Sejnowski. Analysis of fMRI data by blind separation into independent spatial components. *Human Brain Mapping*, (6):160–188, 1998.

[129] J.H. Meek, L. Tyszczuk, C.E. Elwell, and J.S. Wyatt. Cerebral blood flow increases over the first three days of life in extremely preterm neonates. *Arch Dis Child Fetal Neonatal.*, 78(1):F33–F37, 1998.

[130] S.K. Mehta, D.M. Super, D. Connuck, A. Salvator, L. Singer, L.G. Fradley, R.A. Harcar-Sevcik, H.L. Kirchner, and E.S. Kaufman. Heart rate variability in healthy newborn infants. *Am J Cardiol.*, 89(1):50–53, 2002.

[131] M. Misra, J. Stark, M. Dujovny, R. Widman, and J.I. Ausman. Transcranial cerebral oximetry in random normal subjects. *Neurol Res.*, 20(2):137–141, 1998.

[132] M.J. Van de Ven MJ, W.N. Colier, M.C. van der Sluijs, D. Walraven, B. Oeseburg B, and H. Folgering. Can cerebral blood volume be measured reproducibly with an improved near infrared spectroscopy system? *J Cereb Blood Flow Metab.*, 21(2):110–113, 2001.

[133] L. Molgedey and H.G. Schuster. Separation of a mixture of independent signals using time delayed correlations. *Phys Rev Lett.*, 72(23):3634–3637, June 1994.

[134] G. Morren, P. Lemmerling, H. Daniëls, G. Naulaers, and S. Van Huffel. Sensitivity of detrended fluctuation analysis applied to heart rate variability data. *Internal Report 03-158, ESAT-SCD-SISTA, in review.*

[135] G. Morren, P. Lemmerling, H. Daniëls, G. Naulaers, and S. Van Huffel. Sensitivity of detrended fluctuation analysis applied to heart rate variability data - simulations. *Internal Report 02-184, ESAT-SCD-SISTA.*

[136] G. Morren, P. Lemmerling, and S. Van Huffel. Decimative subspace-based parameter estimation techniques applied to magnetic resonance spectroscopy signals'. In *Proc. of 23rd Annual International Conference of the IEEE Engineering in Medicine and Biology Society (EMBC2001)*, volume 3, pages 2319–2322, Istanbul, Turkey, 25-28 Oct 2001.

[137] G. Morren, P. Lemmerling, and S. Van Huffel. Decimative subspace-based parameter estimation techniques'. *Signal Processing*, 83(5):1025–1033, 2003.

[138] G. Morren, P. Lemmerling, S. Van Huffel, G. Naulaers, H. Devlieger, and P. Casaer. Detection of autoregulation in the brain of premature infants using a novel subspace-based technique'. In *Proc. of 23rd Annual International Conference of the IEEE Engineering in Medicine and Biology Society (EMBC2001)*, pages 2064–2067, Istanbul, Turkey, 25-28 Oct 2001.

[139] G. Morren, G. Naulaers, P. Lemmerling, S. Van Huffel, P. Casaer, and H. Devlieger. Quantitation of the concordance between cerebral intravascular oxygenation and mean arterial blood pressure for the detection of impaired autoregulation. *Adv Exp Med Biol.*, 510:403–408, 2003.

[140] G. Morren, S. Van Huffel, I. Helon, G. Naulaers, H. Daniëls, H. Devlieger, and P. Casaer. Effects of non-nutritive sucking on heart rate, respiration and oxygenation: a model-based signal processing approach. *Comp Biochem Physiol. A*, 132:97–106, 2002.

[141] G. Morren, M. Wolf, P. Lemmerling, U. Wolf, J.H. Choi, E. Gratton, L. De Lathauwer, and S. Van Huffel. Extraction of fast neuronal changes from multichannel, functional near-infrared spectroscopy signals using independent component analysis. In *Progress in biomedical optics and imaging*, volume 4623 of *Proceedings of SPIE*, pages 68–76. SPIE-BiOS, 2002.

[142] G. Morren, M. Wolf, P. Lemmerling, U. Wolf, J.H. Choi, E. Gratton, L. De Lathauwer, and S. Van Huffel. Detection of fast neuronal signals in the motor cortex from functional near infrared spectroscopy measurements using independent component analysis. *Medical and Biological Engineering and Computing*, 42(1):92–99, 2004.

[143] R. Mrowka, A. Patzak, and P.B. Persson. The complexity of heart rate in its postnatal development. *IEEE Engineering in medicine and biology*, (88-91), March/April 2001.

[144] R. Mrowka, A. Patzak, E. Schubert, and P.B. Persson. Linear and nonlinear properties of heart rate in postnatal maturation. *Cardiovasc Res.*, 31:447–454, 1996.

[145] G. Naulaers. *Non-invasive measurement of the neonatal cerebral and splanchic circulation by near-infrared spectroscopy.* PhD thesis, Katholieke Universiteit Leuven, 2003.

[146] G. Naulaers, B. Meyns, V. Leunens, S. Van Huffel, P. Casaer, and H. Devlieger. Continuous measurement of cerebral oxygenation (TOI) with NIRO 300 during rewarming of piglets. *ISOTT annual meeting*, 24-28 August, 2002. Manchester, UK.

[147] G. Naulaers, G. Morren, A. Debeer, V. Cossey, C. Vanhole, S. Van Huffel, P. Casaer, and H. Devlieger. Continuous measurement of cerebral blood volume and oxygenation during rewarming of neonates. *Accepted for publication in Acta Paediatrica.*

[148] G. Naulaers, G. Morren, A. Debeer, C. Vanhole, S. Van Huffel, P. Casaer, and H. Devlieger. Continuous measurement of ΔHbD and (TOI) during rewarming of neonates. *ISOTT annual meeting*, 24-28 August, 2002. Manchester, UK.

[149] G. Naulaers, G. Morren, S. Van Huffel, P. Casaer, and H. Devlieger. Cerebral tissue oxygenation index in very premature born infants. *Arch Dis Child Fetal Neonatal.*, 87(3):F189–F192, 2002.

[150] G. Naulaers, G. Morren, S. Van Huffel, P. Casaer, and H. Devlieger. Measurement of tissue oxygenation index during the first three days in premature born infants. *Adv Exp Med Biol.*, 510:379–383, 2003.

[151] H.B. Nielsen, R. Boushel, P. Madsen, and N.H. Secher. Cerebral desaturation during exercise reversed by O_2 supplementation. *Am J Physiol*, 277(3 Pt 2):H1045–1052, 1999.

[152] J. Nolan, P.D. Batin, R. Andrews anbd S.J. Lindsay, P. Brooksby, M. Mullen, W. Baig, A.D. Flapan, A. Cowley, R.J. Prescott, J.M. Neilson, and K.A. Fox. Prospective study of heart rate variability and mortality in chronic heart failure: results of the united kingdom heart failure evaluation and assessment of risk trial (uk-heart). *Circulation*, 98(15):1510–1516, 1998.

[153] H. Obrig and A. Villringer. Beyond the visible - imaging the human brain with light. *J Cereb Blood Flow Metab*, 23(1):1–18, 2003.

[154] E. Okada and D. Delpy. Investigation of the effect of discrete scatterers in CSF layer on optical path length in the brain. *Proceedings SPIE*, Vol. 4160:196–203.

[155] E. Okada, M. Firbank, M. Schweiger, S.R. Arridge, M. Cope, and D.T. Delpy. Theoretical and experimental investigation of near-infrared light propagation in a model of the adult head. *Applied Optics*, 36(1):21–31, 1997.

[156] K. Otto, R. Mrowka, E. Schubert, W. Orlow, R.R. Wauer, and A. Patzak. Low-frequency respiratory rhythms in infants during the first six months of life. *Clin Physiol.*, 20(3):200–211, 2000.

[157] C.K. Papadopoulos and C.L. Nikias. Parameter estimation of exponentially damped sinusoids using higer order statistics. *IEEE Trans Acoust Speech Signal Process.*, 38(8):1424–1436, 1990.

[158] J. Patel, K. Marks, I. Roberts, D. Azzopardi, and A.D. Edwards. Measurement of cerebral blood flow in newborn infants using near infrared spectroscopy with indocyanine green. *Pediatric Research*, 43(1):34–39, 1998.

[159] M.S. Patterson, B. Chance, and B.C. Wilson. Time resolved reflectance and transmittance for the non-invasive measurement of tissue optical properties. *Applied optics*, 28(12):2331–2336, 1989.

[160] A. Patzak, K. Lipke, W. Orlow, R. Mrowka, H. Strauss, E. Windt, P.B. Persso, and E Schubert. Development of heart rate power spectra reveals neonatal peculiarities of cardiorespiratory control. *Am J Physiol. (Reg, Int, Comp Physiol.)*, 271:R1025–R1032, 1996.

[161] A. Patzak, R. Mrowka, S. Springer, T. Eckard, O. Ipsiroglu, T. Erler, and S. Hofmann. Herzfrequenzvariabilität - methoden, physiologie und applikation im pädiatrischen schlaflabor. *Wien Klim Wochenschr.*, 112(5):234–250, 2000.

[162] P. Peirano, J. Lacombe, B. Kastler, G. Guillon, G. Vicente, and N. Monod. Night sleep heart rate patterns recorded by cardiopneumography at home in normal and at-risk for sids infants. *Early Hum Dev.*, 17(2-3):175–186, 1988.

[163] H.-O. Peitgen and D. Saupe, editors. *The science of fractal images.* Springer-Verlag, 1988.

[164] C.-K. Peng, S. Havlin, M. Schwartz, and H.E. Stanley. Directed polymer and ballistic deposition growth with correlated noise. *Phys Rev. A*, 44:2239, 1991.

[165] C.K. Peng, S. Havlin, H.E. Stanley, and A.L. Goldberger. Quantification of scaling exponents and crossover phenomena in nonstationary heartbeat time series. *Chaos*, 5(1):82–87, 1995.

[166] T. Penzel, J.W. Kantelhardt, L. Grote, J.H. Peter, and A. Bunde. Comparison of detrended fluctuation analysis and spectral analysis for heart rate variability in sleep and sleep apnea. *IEEE Trans Biomed Eng.*, 50(10):1143–1151, 2003.

[167] B. Pilgram and D. Kaplan. A comparison of estimators for 1/f noise. *Physica D*, 114:108–112, 1998.

[168] B. Pilgram and D. Kaplan. Nonstationarity and 1/f noise characteristics in heart rate. *Am J Physiol. 276 (Reg, Int, and Comp Physiol.)*, 45(1):R1–R9, 1999.

[169] S.M. Pincus, T.R. Cummins, and G.G. Haddad. Heart rate control in normal and aborted-sids infants. *Am J Physiol*, 264(3Pt2):R638–646, 1993.

[170] V. Pisarenko. The retrieval of harmonics from a covariance function. *Geophys. J. Roy. Astron. Soc.*, 33:347–366, 1973.

[171] O. Pryds, G. Greisen, H. Lou, and B. Friis-Hansen. Heterogeneity of cerebral vasoreactivity in preterm infants supported by mechanical ventilation. *J Pediatr*, 115(4):638–645, 1989.

[172] V. Quaresima, R. Lepanto, and M. Ferrari. The use of near infrared spectroscopy in sports medicine. *J Sports Med Phys Fitness*, 43(1):1–13, 2003.

[173] V. Quaresima, S. Sacco, R. Totaro, and M. Ferrari. Noninvasive measurement of cerebral hemoglobin oxygen saturation using two near infrared spectroscopy approaches. *J Biomed Opt*, 5(2):201–205, 2000.

[174] R. Ramanathan, M.J. Corwin, C.E. Hunt, G. Lister, L.R. Tinsley, T. Baird, J.M. Silvestri, D.H. Crowell, D. Hufford, R.J. Martin, M.R. Neuman, D.E. Weese-Mayer, L.A. Cupples, M. Peucker, M. Willinger, and T.G. Keens TG; Collaborative Home Infant Monitoring Evaluation (CHIME) Study Group. Cardiorespiratory events recorded on home monitors: Comparison of healthy infants with those at increased risk for sids. *JAMA*, 285(17):2199–2207.

[175] C. Van Ravenswaaij-Arts, J. Hopman, L. Kollee, G. Stoelinga, and H. Van Geijn. Spectral analysis of heart rate variability in spontaneously breathing very preterm infants. *Acta Paediatr.*, 83(5):473–480, 1994.

[176] D.M. Rector, G.R. Poe, M.P. Kristensen, and R.M. Harper. Light scattering changes follow evoked potentials from hippocampal schaeffer collateral stimulation. *J. Neurophysiol.*, 78(3):1707–1713, 1997.

[177] T. Rinne, G. Gratton, M. Fabiani, N. Cowan, E. Maclin, J. Sinkkonen A. Stinard, K. Alho, and R. Naatanen. Scalp-recorded optical signals make sound processing in the auditory cortex visible? *NeuroImage*, 10(5):620–624, 1999.

[178] J. Rissanen. A universal prior for the integers and estimation by minimum description length. *Annals of Statistics*, 11:417–431, 1983.

[179] O. Rompelman, J.B.I.M. Snijders, and C.J. van Spronsen. The measurement of heart rate variability spectra with the help of a personal computer. *IEEE Trans Biomed Eng.*, 29(7):503–510, 1982.

[180] H. Rosen, W. Craelius, D. Curcie, M. Hiatt, and T. Hegyi. Spectral analysis of heart variability in the newborn infant. *Biol Neonate*, 77(4):224–229, 2000.

[181] E.G. Rosenstock, Y. Cassuto, and E. Zmora. Heart rate variability in the neonate and infant: analytical methods, physiological and clinical observations. *Acta Paediatr*, 88:477–482, 1999.

[182] R. Roy and T. Kailath. Esprit - estimation of signal parameters via rotational invariance techniques. *IEEE Trans Acoust Speech Signal Process.*, 37(7):984–995, July 1989.

[183] R. Roy, A. Paulraj, and T. Kailath. ESPRIT - a subspace rotation approach to estimation of parameters of cisoids in noise. *IEEE Trans Acoust Speech Signal Process.*, 34(4):1340–1342, 1986.

[184] K. Saermark, M. Moeller, U. Hintze, H. Moelgaard, P.E. Bloch Thomsen, H. Huikuri, T. Mäkikallio, J. Levitan, and M. Lewkowicz. Comparison of recent methods of analyzing heart rate variability. *Fractals*, 8(4):315–322, 2000.

[185] B.M. Salzberg, A.L. Obaid, and H. Gainer. Large and rapid changes in light scattering accompany secretion by nerve terminals in the mammalian neurohypophysis. *J Gen Physiol*, 86(3):395–411, 1986.

[186] S.K. Samra, P. Dorje, G.B. Zelenock, and J.C. Stanley. Cerebral oximetry in patients undergoing carotid endarterectomy under regional anesthesia. *Stroke*, 27(1):49–55, 1996.

[187] V.L. Schechtman, R.M. Harper, and K.A. Kluge. Development of heart rate variation over the first 6 months of life in normal infants. *Pediatr. Res.*, 26:343–346, 1989.

[188] B. Seps, F. Beckers, and A. Aubert. Heart rate variability during gravity transitions. *Comput Cardiol.*, 29:433–436, 2002.

[189] I. Simonsen and A. Hansen. Determination of the hurst exponent by use of wavelet transform. *Phys Rev. E*, 58:79–87, 1998.

[190] L. Skov, O. Pryds, and G. Greisen. Estimating cerebral blood flow in newborn infants: comparison of near infrared spectroscopy and Xe clearance. *Pediatric research*, 30(6):570–573, Dec 1991.

[191] P. Sleight and B. Casadei. *Heart Rate Variability*, chapter 24: Relationships between heart rate, respiration and blood pressure variability, pages 311–327. Futura Publishing Company, 1995.

[192] L. Spassov, L. Curzi-Dascalova, J. Clairambault, F. Kauffmann, M. Eiselt, C. Medigue, and P. Peirano. Heart rate and heart rate variability during sleep in small-for-gestational age newborns. *Pediatric Research*, 35(4 Pt 1):500–505, 1994.

[193] J. Steinbrink, M. Kohl, H. Obrig, G. Curio, F. Syré, F. Thomas, H. Wabnitz, H. Rinneberg, and A. Villringer. Somatosensory evoked fast optical intensity changes detected non-invasively in the adult human head. *Neurosci Lett.*, 291(2):105–108, 2000.

[194] A. Steinschneider. Prolonged apnea and the sudden infant death syndrome. *Pediatrics*, 50:646–655, 1972.

[195] R.A. Stepnoski, A. LaPorta, F. Raccuia-Behlig, G.E. Blonder, R.E. Slusher, and D. Kleinfeld. Noninvasive detection of changes in membrane potential cultured neurons by light scattering. *Proc Natl Acad Sci.*, 88(21):9382–9386, 1991.

[196] P. Stoica and A.E. Nordsjö. Subspace-based frequency estimation in the presence of moving-average noise using decimation. *Signal Processing*, 63:211–220, 1997.

[197] P. Stoica and K.C. Sharman. Maximum likelihood methods for direction-of-arrival estimation. *IEEE Trans Acoust Speech Signal Process.*, 38(7):1132–1143, 1990.

[198] P. Stoica and T. Söderström. Statistical analysis of music and subspace rotation estimates of sinusoidal frequencies. *IEEE Trans Acoust Speech Signal Process.*, 39:1836–1847, August 1991.

[199] F. Syré, H. Obrig, J. Steinbrink, M. Kohl, R. Wenzel, and A. Villringer. Are VEP correlated fast optical changes detectable in the adult by non-invasive near infrared spectroscopy (NIRS)? *Adv. Exp. Med. Biol.*, 530:421–31, 2003.

[200] I. Tasaki. Rapid structural changes in nerve fibers and cells associated with their excitation processes. *Jpn J Physiol*, 49(2):125–138, 1999.

[201] Task Force of the European Society of Cardiology and the North American Society of Pacing and Electrophysiology. Heart rate variability. standards of measurement, physiological interpretation and clinical use. *Circulation*, 93:1043–1065, 1996.

[202] J. Teller, K. Schwendener, M. Wolf, M. Keel, H.U. Bucher, S. Fanconi, and O. Baenziger. Continuous monitoring of liver oxygenation with near infrared spectroscopy during naso-gastric tube feeding in neonates. *Schweiz Med Wochenschr.*, 130(18):652–656, 2000.

[203] F. Togo and Y. Yamamoto. Decreased fractal component of human heart rate variability during non-rem sleep. *Am J Physiol Heart Circ Physiol*, 280:H17–H21, 2000.

[204] V. Toronov, A. Webb, J.H. Choi, M. Wolf, A. Michalos, E. Gratton, and D. Hueber. Investigation of brain hemodynamics by simultaneous near-infrared spectroscopy and functional magnetic resonance imaging. *Med Phys.*, 28(4):521–527, 2001.

[205] J.K. Triedman, M.H. Perrott, J.P. Cohen, and R.J. Saul. Respiratory sinus arrhythmia: time domain characterization using autoregressive moving average analysis. *Am. J. Physiol.*, 268(6 Pt 2):H2232–2238, 1995.

[206] B.J. Tromberg, N. Shah, R. Lanning, A. Cerussi, J. Espinoza, T. Pham, L. Svaasand, and J. Butler. Non-invasive in vivo characterization of breast tumors using photon migration spectroscopy. *Neoplasia*, 2(1-2):26–40, 2000.

[207] M. Tsuji, A. du Plessis, G. Taylor, R. Crocker, and J. Volpe. Near infrared spectroscopy detects cerebral ischemia during hypotension in piglets. *Pediatr. Res.*, 44:591–595, 1998.

[208] M. Tsuji, J. Saul, A. du Plessis, E. Eichenwald, J. Sobh, R. Crocker, and J. Volpe. Cerebral intravascular oxygenation correlates with mean arterial pressure in critically ill premature infants. *Pediatrics*, 106(4):625–632, October 2000.

[209] R. Turner and T. Jones. Techniques for imaging neuroscience. *British Medical Bulletin*, 65:3–20, 2003.

[210] M. Van Bel, C.A. Dorrepaal, M.J. Benders, P.E. Zeeuwe, M. van de Bor M, and H.M. Berger. Changes in cerebral hemodynamics and oxygenation in the first 24 hours after birth asphyxia. *Pediatrics*, 92(3):365–372, 1993.

[211] S. Van Huffel, H. Chen, C. Decanniere, and P. Van Hecke. Algorithm for time-domain NMR data fitting based on total least squares. *J Magn Reson. A*, 110:228–237, Sept 1994.

[212] S. Van Huffel and J. Vandewalle. *The Total Least Squares Problem: Computational Aspects and Analysis.*, volume 9 of *Frontiers in Applied Mathematics*. SIAM, Philadelphia, Pennsylvania, 1991.

[213] L. Vanhamme, T. Sundin, S. Van Huffel, and P. Van Hecke. MR spectroscopy quantitation: a review of time-domain methods. *NMR in Biomedicine*, 14(4):233–246, June 2001.

[214] L. Vanhamme and S. Van Huffel. Multichannel quantification of biomedical magnetic resonance spectroscopy signals. In *Proc. 43rd Annual Meeting SPIE, Advanced Signal Processing Algorithms, Architectures and Implementations VIII*, volume 3461, pages 237–248, San Diego, USA, July 22-24 1998.

[215] D. Veitch and P. Abry. A wavelet-based joint estimator of the parameters of long-range dependence. *IEEE Trans Info Th.*, 45(3):878–897, 1999.

[216] R. Vigario. Extraction of ocular artifacts from EEG using independent component analysis. *Electroenceph clin neurophysiol.*, 103(3):395–404, 1997.

[217] R. Vigario, J. Särelä, V. Jousmäki, M. Hämäläinen, and E. Oja. Independent component approach to the analysis of EEG and MEG recordings. *IEEE Trans Biomed Eng.*, 47(5):589–593, 2000.

[218] A. Villringer and B. Chance. Non-invasive optical spectroscopy and imaging of human brain function. *Trends Neurosci.*, 20(10):435–442, 1997.

[219] K. Villringer, S. Minoshima, C. Hock, H. Obrig, S. Ziegler, U. Dirnagl, M. Schwaiger, and A. Villringer. Assessment of local brain activation. a simultaneous pet and near-infrared spectroscopy study. *Adv Exp Med Biol.*, 413:149–153, 1997.

[220] D. Vitacco, D. Brandeis, R. Pascual-Marqui, and E. Martin. Correspondence of event-related potential tomography and functional magnetic resonance imaging during language processing. *Hum Brain Mapp.*, 17(1):4–12, 2002.

[221] K. von Siebenthal, G. Bernert, and P. Casaer. Near-infrared spectroscopy in newborn infants. *Brain Dev.*, 14(3):135–143, 1992.

[222] M. Weiss, G. Schulz, M. Fasnacht, C. Balmer, J.E. Fischer, A.C. Gerber, H.U. Bucher, and O. Baenziger. Transcutaneously measured near-infrared spectroscopic liver tissue oxygenation does not correlate with hepatic venous oxygenation in children. *Can J Anaesth.*, 49(8):824–829, 2002.

[223] M.H. Wilkinson, S. Cranage, P.J. Berger, N. Blanch, and T.M. Adamson. Changes in the temporal structure of periodic breathing with postnatal development in preterm infants. *Pediatric Research*, 38(4):533–538, 1995.

[224] K. Willson, D.P. Francis, R. Wensel, A.J.S. Coats, and K.H. Parker. Relationship between detrended fluctuation analysis ans spectral analysis of heart rate variability. *Physiol Meas.*, 23:385–401, 2002.

[225] M. Wolf, N. Brun, G. Greisen, M. Keel, K. von Siebenthal, and H. Bucher. Optimising the methodology of calculating the cerebral blood flow of newborn infants from near infrared spectrophotometry data. *Medical and Biological Engineering and Computing*, 34(3):221–226, May 1996.

[226] M. Wolf, O. Weber, M. Keel, X. Golay, M. Scheidegger, H.U. Bucher, S. Kollias, P. Boesiger, and O. Banziger. Comparison of cerebral blood volume measured by near infrared spectroscopy and contrast enhanced magnetic resonance imaging. *Adv Exp Med Biol.*, 471:767–773, 1999.

[227] M. Wolf, U. Wolf, J.H. Choi, R. Gupta, L.P. Safonova, L.A. Paunescu, A. Michalos, and E. Gratton. Functional frequency-domain near-infrared spectroscopy detects fast neuronal signal in the motor cortex. *NeuroImage*, 17:1868–1875, 2002.

[228] M. Wolf, U. Wolf, J.H. Choi, V. Toronov, L.A. Paunescu, A. Michalos, and E. Gratton. Fast cerebral functional signal in the 100-ms range detected in the visual cortex by frequency-domain near-infrared spectrophotometry. *Psychophysiology*, 40(4):521–528, 2003.

[229] J. Wyatt, M. Cope, D. Delpy, C. Richardson, A. Edwards, S. Wray, and Reynolds E. Quantitation of cerebral blood volume in human infants by near infrared spectroscopy. *Journal of Applied Physiology*, 68(3):1086–1091, Mar 1990.

[230] J.S. Wyatt, M. Cope, D.T. Delpy, P. van der Zee, S. Arridge, A.D. Edwards, and E.O.R. Reynolds. Measurement of optical pathlength for cerebral near infrared spectroscopy in newborn infants. *Dev. Neuroscience*, 12(2):140–144, 1990.

[231] Xueyan Xu. *Prediction of life-threatening events in infants using heart rate variability measures.* PhD thesis, West Virginia University, 2002.

[232] Y. Yamamoto and R.L. Hughson. Coarse-graining spectral analysis: new method for studying heart rate variability. *J. Appl. Physiol.*, 71:1143–1150, 1991.

[233] Y. Yamamoto and R.L. Hughson. Extracting fractal components from time series. *Physica D*, 68:250–264, 1993.

[234] A. Ziehe and K.-R. Müller. TDSEP - an efficient algorithm for blind separation using time structure. In L. Niklasson, M. Boden, and T. Ziemke, editors, *Proc. of the 8th International Conference on Artificial Neural Netwerks (ICANN98), Perspectives in Neural Computing*, pages 675–680. Springer Verlag, 1998.

Appendix

A Relationship between detrended fluctuation analysis (DFA) and spectral analysis

As discussed in section 4.4, for fractional Gaussian noises and fractional Brownian motions, there is a simple relationship between the spectral index β and the DFA scaling exponent α, i.e. $\beta = 2\alpha - 1$. Note that, in principle, this equation only holds for large scales, or equivalently low frequencies. In this appendix, the relationship between DFA and spectral analysis for arbitrary signals is established. The derivation and final result are a correction of the results presented in [224]. The aim is to obtain the DFA fluctuation function in terms of the power spectrum of the signal. First, the fluctuation function of a single sinusoidal component is considered. The fluctuation function of an arbitrary function can then be determined based on its Fourier transform.

A.1 Fluctuation function of a single sinusoid

The consecutive steps of the DFA algorithm are applied to a sinusoid with amplitude A and frequency ω:

$$s_1(t) = A\,cos(\omega t) \tag{A.1}$$

Cumulation

Integrating $s_1(t)$ from time τ_0 to τ, yields the cumulative function $C(t)$:

$$C(t) = \frac{Af_s}{\omega}\,sin(\omega\tau) - \frac{Af_s}{\omega}\,sin(\omega\tau_0) \tag{A.2}$$

The factor f_s accounts for the discrete sampling of the signal: higher sampling rates result in greater cumulative sums.

Detrending

In order to investigate the effect of detrending, the Taylor series expansion of $C(t)$ around a particular value of $\omega\,\tau$ is used:

$$\begin{aligned} C(\tau+\delta) &= \frac{Af_s}{\omega}\sum_{p=0,2,\ldots}^{\infty}\frac{(-1)^{p/2}\omega^p sin(\omega\tau)}{p\,!}\,\delta^p \\ &+ \frac{Af_s}{\omega}\sum_{p=1,3,\ldots}^{\infty}\frac{(-1)^{(p-1)/2}\omega^p cos(\omega\tau)}{p\,!}\,\delta^p - \frac{Af_s}{\omega}sin(\omega\tau_0) \end{aligned} \tag{A.3}$$

To detrend $C(\tau)$ on an interval $[-\Delta/2, \Delta/2]$, the least squares regression line is subtracted:

$$D(\tau+\delta) = C(\tau+\delta) - aC(\tau+\delta) - b \tag{A.4}$$

As the last term of Eq. (A.3) is independent of δ, it is removed in the detrending step. The regression line is calculated for each term of the Taylor expansion in Eq. (A.3) separately.

For even p, the terms in the Taylor expansion in Eq. (A.3) are even functions of δ, and therefore the detrending reduces to subtracting the mean of the polynomial of even degree p on the interval $[-\Delta/2, \Delta/2]$:

$$a = 0 \tag{A.5}$$

$$b = \frac{1}{\Delta}\int_{-\Delta/2}^{\Delta/2} \delta^p \, d\delta = \frac{\Delta}{2^p\,(p+1)} \tag{A.6}$$

For odd p, the terms in the Taylor expansion in Eq.(A.3) are odd functions of δ, and therefore the regression line goes through the origin and can be calculated on the interval $[0, \Delta/2]$. The factor a is obtained by minimizing the least-squares difference between a polynomial of order p and a linear function:

$$a = min_x \left(\int_0^{\Delta/2} (\delta^p - x\,\delta)^2 \, d\delta) \right) \tag{A.7}$$

$$= min_x \left(\int_0^{\Delta/2} (\delta^{2p} - 2x\delta^{p+1} + x^2\delta^2) \, d\delta \right) \tag{A.8}$$

$$= min_x \left(\frac{\Delta^{2p+1}}{(2p+1)\,2^{2p+1}} - \frac{2\Delta^{p+2}}{(p+2)\,2^{p+2}}\,x + \frac{\Delta^3}{3.2^3}\,x^2 \right) \tag{A.9}$$

Setting the derivative with respect to x to zero, yields:

$$\frac{2\Delta^{2p+2}}{(p+2)\,2^{p+2}} = \frac{2\Delta^3}{3.2^3}\,x \tag{A.10}$$

The resulting regression coefficients are thus:

$$a = \frac{3\,\Delta^{p-1}}{(p+2)\,2^{p-1}} \tag{A.11}$$

$$b = 0 \tag{A.12}$$

Combining Eqs. (A.3),(A.4),(A.5-A.6) and (A.11-A.12) yields:

$$D(\tau+\delta) = \frac{Af_s}{\omega}\left[\sum_{p=0,2,\ldots}^{\infty} \frac{(-1)^{\frac{p}{2}}\omega^p sin(\omega\tau)}{p\,!} \left(\delta^p - \frac{\Delta^p}{2^p\,(p+1)} \right) \right.$$
$$\left. + \sum_{p=1,3,\ldots}^{\infty} \frac{(-1)^{\frac{p-1}{2}}\omega^p cos(\omega\tau)}{p\,!} \left(\delta^p - \frac{3\,\Delta^{p-1}}{2^{p-1}\,(p+2)}\,\delta \right) \right] \tag{A.13}$$

Variance of the detrended function

The value of the fluctuation function for a segment length n is the variance, or the mean squared value, of the detrended function $D(\tau+\delta)$. Squaring the detrended function yields:

$$
\begin{aligned}
D(\tau+\delta)^2 \;=\; & \left(\frac{Af_s}{\omega}\right)^2 \Bigg[sin^2(\omega\tau) \sum_{p_1=0}^{\infty}\sum_{p_2=0}^{\infty} \frac{(-1)^{\frac{p_1+p_2}{2}}\omega^{p_1+p_2}}{p_1!\,p_2!} \times \\
& \left(\delta^{p_1+p_2} - \frac{\Delta^{p_1}}{2^{p_1}\,(p_1+1)}\,\delta^{p_2} - \frac{\Delta^{p_2}}{2^{p_2}\,(p_2+1)}\,\delta^{p_1} \right. \\
& \left. + \frac{\Delta^{p_1+p_2}}{2^{p_1+p_2}\,(p_1+1)(p_2+1)}\right) \qquad for\ p_1,\ p_2\ even \\
+ \;\; & cos^2(\omega\tau) \sum_{p_1=0}^{\infty}\sum_{p_2=0}^{\infty} \frac{(-1)^{\frac{p_1+p_2-2}{2}}\omega^{p_1+p_2}}{p_1!\,p_2!} \times \\
& \left(\delta^{p_1+p_2} - \frac{3\Delta^{p_1-1}}{2^{p_1-1}\,(p_1+2)}\,\delta^{p_2+1} - \frac{3\Delta^{p_2-1}}{2^{p_2-1}\,(p_2+2)}\,\delta^{p_1+1} \right. \\
& \left. + \frac{9\Delta^{p_1+p_2-2}}{2^{p_1+p_2-2}\,(p_1+2)(p_2+2)}\delta^2\right) \qquad for\ p_1,\ p_2\ odd \\
+ \;\; & sin(\omega\tau)cos(\omega\tau) \sum_{p_1=0}^{\infty}\sum_{p_2=0}^{\infty} \frac{(-1)^{\frac{p_1+p_2-1}{2}}\omega^{p_1+p_2}}{p_1!\,p_2!} \times \\
& \left(\delta^{p_1+p_2} - \frac{\Delta^{p_1}}{2^{p_1}\,(p_1+1)}\,\delta^{p_2} - \frac{3\Delta^{p_2-1}}{2^{p_2-1}\,(p_2+2)}\,\delta^{p_1+1} \right. \\
& \left. + \frac{3\Delta^{p_1+p_2-1}}{2^{p_1+p_2-1}\,(p_1+1)(p_2+2)}\right) \qquad for\ p_1\ even,\ p_2\ odd \\
+ \;\; & sin(\omega\tau)cos(\omega\tau) \sum_{p_1=0}^{\infty}\sum_{p_2=0}^{\infty} \frac{(-1)^{\frac{p_1+p_2-1}{2}}\omega^{p_1+p_2}}{p_1!\,p_2!} \times \\
& \left(\delta^{p_1+p_2} - \frac{3\Delta^{p_1-1}}{2^{p_1-1}\,(p_1+2)}\,\delta^{p_2+1} - \frac{\Delta^{p_2}}{2^{p_2}\,(p_2+1)}\,\delta^{p_1} \right. \\
& \left. + \frac{3\Delta^{p_1+p_2-1}}{2^{p_1+p_2-1}\,(p_1+2)(p_2+1)}\right)\Bigg] \qquad for\ p_1\ odd,\ p_2\ even
\end{aligned}
\tag{A.14}
$$

The mean squared value of the detrended function is obtained by integrating $D(\tau+\delta)^2$ on the interval $[-\Delta/2, \Delta/2]$:

$$
\bar{D^2} \;=\; \frac{1}{\Delta}\int_{-\Delta/2}^{\Delta/2} D(\tau+\delta)^2\,d\delta \tag{A.15}
$$

As the integration interval is symmetric around the origin, the integrals of all polynomials of odd degree are zero. Therefore, all terms in $sin(\omega\tau)cos(\omega\tau)$

in Eq. (A.14) are removed after integration. The variance of the detrended function $D(\tau+\delta)$ on a segment of length Δ centered around τ can then be written as:

$$\begin{aligned}
\bar{D^2}(\tau,\Delta) &= \frac{1}{\Delta}\left(\frac{Af_s}{\omega}\right)^2 sin^2(\omega\tau)\sum_{p_1=0}^{\infty}\sum_{p_2=0}^{\infty}\frac{(-1)^{\frac{p_1+p_2}{2}}\omega^{p_1+p_2}}{p_1!\,p_2!}\times \\
&\quad \left(\frac{\Delta^{p_1+p_2+1}}{2^{p_1+p_2}\,(p_1+p_2+1)}-\frac{\Delta^{p_1+p_2+1}}{2^{p_1+p_2}\,(p_1+1)(p_2+1)}\right. \\
&\quad \left.-\frac{\Delta^{p_1+p_2+1}}{2^{p_1+p_2}\,(p_1+1)(p_2+1)}+\frac{\Delta^{p_1+p_2+1}}{2^{p_1+p_2}\,(p_1+1)(p_2+1)}\right)\ p_1,\,p_2\ even \\
&+ \frac{1}{\Delta}\left(\frac{Af_s}{\omega}\right)^2 cos^2(\omega\tau)\sum_{p_1=0}^{\infty}\sum_{p_2=0}^{\infty}\frac{(-1)^{\frac{p_1+p_2-2}{2}}\omega^{p_1+p_2}}{p_1!\,p_2!}\times \\
&\quad \left(\frac{\Delta^{p_1+p_2+1}}{2^{p_1+p_2}\,(p_1+p_2+1)}-\frac{3\Delta^{p_1+p_2+1}}{2^{p_1+p_2}\,(p_1+2)(p_2+2)}\right. \\
&\quad \left.-\frac{3\Delta^{p_1+p_2+1}}{2^{p_1+p_2}\,(p_1+2)(p_2+2)}+\frac{3\Delta^{p_1+p_2+1}}{2^{p_1+p_2}\,(p_1+1)(p_2+1)}\right)\ p_1,\,p_2\ odd
\end{aligned} \tag{A.16}$$

Note that the last two terms in both $sin^2(\omega\tau)$ and $cos^2(\omega\tau)$ cancel each other.

$$\begin{aligned}
\bar{D^2}(\tau,\Delta) &= \left(\frac{Af_s}{\omega}\right)^2 sin^2(\omega\tau)\sum_{p_1=0}^{\infty}\sum_{p_2=0}^{\infty}\frac{(-1)^{\frac{p_1+p_2}{2}}\omega^{p_1+p_2}}{p_1!\,p_2!\,2^{p_1+p_2}}\times \\
&\quad \left(\frac{1}{p_1+p_2+1}-\frac{1}{(p_1+1)(p_2+1)}\right)\Delta^{p_1+p_2} \qquad for\ p_1,\,p_2\ even \\
&+ \left(\frac{Af_s}{\omega}\right)^2 cos^2(\omega\tau)\sum_{p_1=0}^{\infty}\sum_{p_2=0}^{\infty}\frac{(-1)^{\frac{p_1+p_2-2}{2}}\omega^{p_1+p_2}}{p_1!\,p_2!\,2^{p_1+p_2}}\times \\
&\quad \left(\frac{1}{p_1+p_2+1}-\frac{3}{(p_1+2)(p_2+2)}\right)\Delta^{p_1+p_2} \qquad for\ p_1,\,p_2\ odd
\end{aligned} \tag{A.17}$$

The mean squared residual of the complete time series is the mean of the variances of all segments of length Δ. For a large number of segments this is equivalent to multiplying each power term in Δ by the mean of its associated oscillatory term, i.e. 1/2 for both $sin^2(\omega\tau)$ and $cos^2(\omega\tau)$:

$$\begin{aligned}
\bar{D^2} &= \frac{1}{2}\left(\frac{Af_s}{\omega}\right)^2\sum_{p_1=0}^{\infty}\sum_{p_2=0}^{\infty}\frac{(-1)^{\frac{p_1+p_2}{2}}\omega^{p_1+p_2}}{p_1!\,p_2!\,2^{p_1+p_2}}\times \\
&\quad \left(\frac{p_1\,p_2}{(p_1+p_2+1)(p_1+1)(p_2+1)}\right)\Delta^{p_1+p_2} \qquad for\ p_1,\,p_2\ even
\end{aligned}$$

$$+ \quad \frac{1}{2}\left(\frac{Af_s}{\omega}\right)^2 \sum_{p_1=0}^{\infty}\sum_{p_2=0}^{\infty} \frac{(-1)^{\frac{p_1+p_2-2}{2}}\omega^{p_1+p_2}}{p_1!\,p_2!\,2^{p_1+p_2}} \times \left(\frac{(p_1-1)(p_2-1)}{(p_1+p_2+1)(p_1+2)(p_2+2)}\right)\Delta^{p_1+p_2} \qquad for\ p_1,\ p_2\ odd \tag{A.18}$$

Note that, as the mean and the linear trends are removed (respectively corresponding to $p_1+p_2=0$ and $p_1+p_2=2$ due to the squaring), and the odd values of (p_1+p_2) were cancelled out, the summing begins effectively at $p_1+p_2=4$. In a segment of length Δ, the behaviour of the residual sum of squares is dependent on whether the segment is longer or shorter than the period of the sinusoid.

If the segment is short in comparison to the period of the sinusoid, i.e. $\Delta\omega < 1$, then the residuals after detrending are dominated by the term in $(\Delta\omega)^4$. The mean squared residual reduces then to:

$$\bar{D^2} \approx \frac{1}{2}\left(\frac{Af_s}{\omega}\right)^2 \frac{(-1)^2\,\omega^4}{2!\,2!\,2^4}\frac{4}{45}\Delta^4 \tag{A.19}$$

By expressing the segment length Δ as a number of samples, i.e. $\Delta = n/f_s$, this can be written as:

$$\bar{D^2} \approx \frac{A^2}{1440}\left(\frac{\omega}{f_s}\right)^2 n^4 \tag{A.20}$$

If the segment is long in comparison to the period of the sinusoid, i.e. as the number of periods in one segment increases, the trend approaches zero. Hence, the mean squared residual is simply the mean square value of the cumulated sinusoid weighted by a frequency dependent factor, introduced by the cumulation, and by the sampling frequency.

$$\bar{D^2} \approx \frac{1}{2}\left(\frac{Af_s}{\omega}\right)^2 \tag{A.21}$$

In Fig. A.1, the fluctuation function of a sinusoid with frequency $\omega = 2\pi/100$ is shown together with the approximations at small $(n < 2\pi/\omega)$ and large $(n > 2\pi/\omega)$ scales $(n > 2\pi/\omega)$ using respectively Eq. (A.20) and Eq. (A.21). Note that the approximations are fairly accurate except in the scaling range corresponding to the period of the sinusoid, which is marked with an arrow.

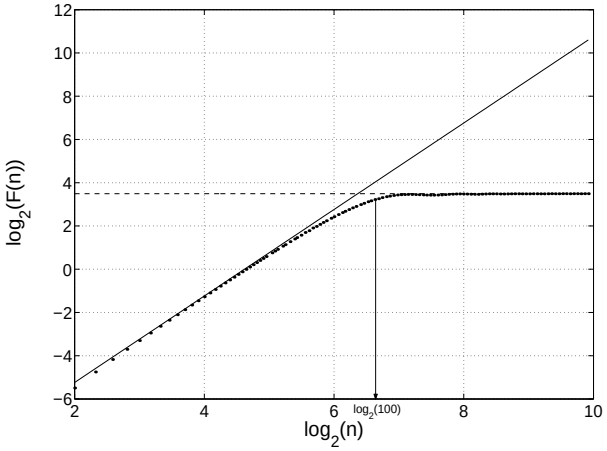

Figure A.1: Fluctuation function of a single sinusoid and its approximations at small ($n < 2\pi/\omega$) and large ($n > 2\pi/\omega$) scales ($n > 2\pi/\omega$) using respectively Eq. (A.20) and Eq. (A.21)

A.2 Fluctuation function of arbitrary signals

Using the Fourier transform, an arbitrary signal can be written as a linear combination of sinusoids. Since the Fourier components are orthogonal, and their cross-products are zero, the overall residual sum of squares of the complete signal is equal to the sum of contributions $\bar{D}^2$ of each Fourier component. For a given segment length n, the contributions of the low frequency components, for which $f < 1/n$, and the high frequency components, for which $f > 1/n$, can be found using respectively Eq. (A.20) and Eq. (A.21) where A^2 is replaced with $P(f)$. The fluctuation function $F(n)$ of a signal with power spectrum $P(f)$ can thus be written as:

$$F^2(n) \quad = \quad \frac{n^4}{1440\, f_s^2} \int_{1/N}^{1/n} (2\pi f)^2 P(f)\, df + \frac{f_s^2}{2} \int_{1/n}^{1} \frac{P(f)}{(2\pi f)^2}\, df \quad \text{(A.22)}$$

This shows how the DFA fluctuation function $F(n)$ can be calculated from a frequency-weighted spectral analysis. In order to calculate the value of the fluctuation function for a given segment length n, the power spectrum of the signal is multiplied by a frequency-weighting function proportional to f^2 up to the frequency corresponding to $1/n$, and proportional to $1/f^2$ for larger frequencies. The area under the frequency-weighted power spectrum is equal to $F^2(n)$. The procedure is illustrated in Fig. A.2. Note that, for a given segment length n, the weighting emphasizes the frequency components in the neighborhood of the frequency corresponding to the segment length, i.e. $1/n$.

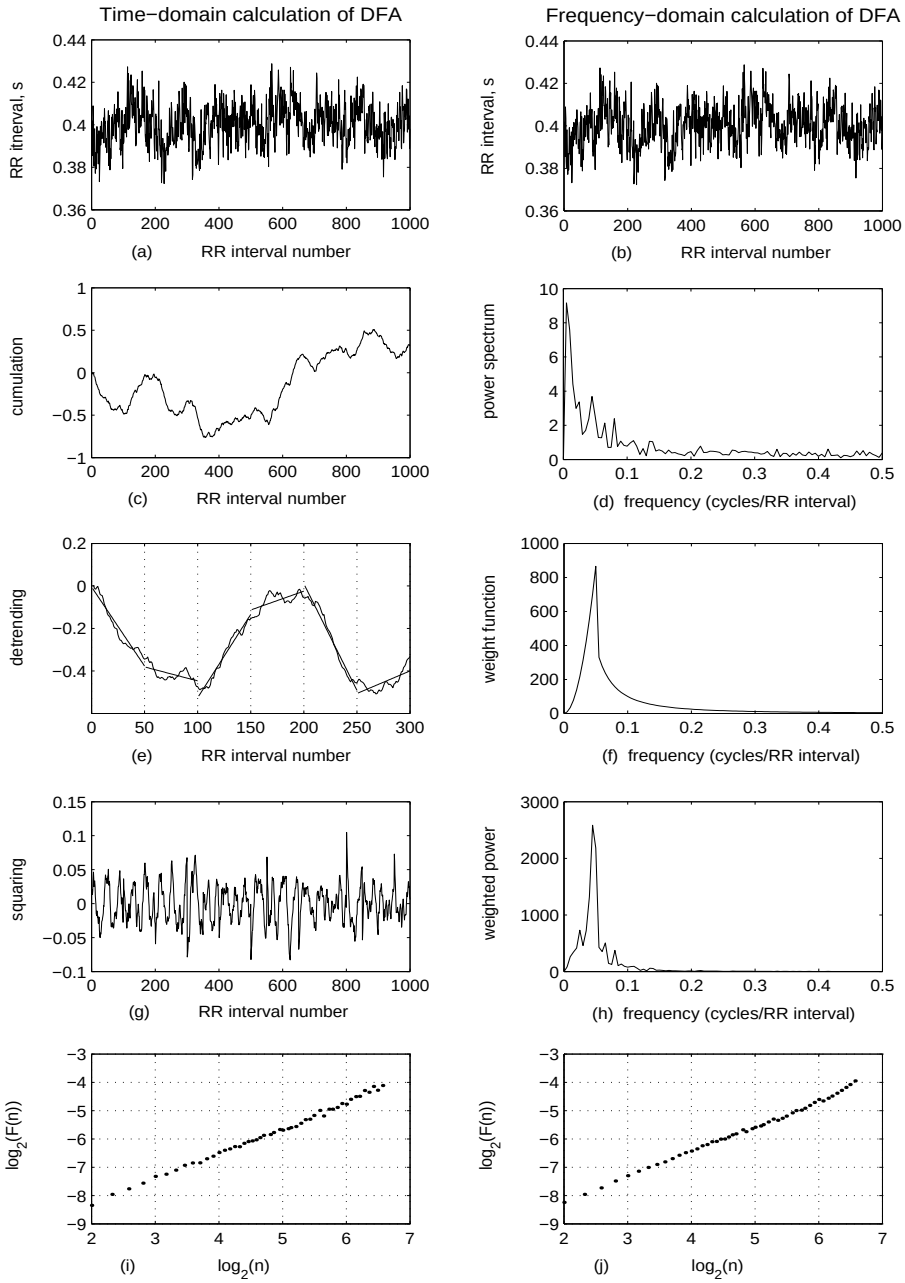

Figure A.2: Spectral interpretation of DFA algorithm: Calculation of DFA fluctuation function in time-domain (left) and frequency-domain (right).

B Alternative estimators of the fractal exponent

In this appendix, two alternative methods are presented that can be used to estimate the fractal exponent. The first alternative, coarse-graining spectral analysis (CGSA) is a frequency-domain method designed to be insensitive to harmonic components possibly present in otherwise fractal signals [232]. The choice for CGSA was motivated by the observation that the estimation of the scaling exponent with DFA is complicated by periodic fluctuations (see section 4.4.3). Our analysis shows, however, that in case of real-life signals the advantage of CGSA over ordinary spectral analysis is small. Another approach, which seems natural to characterize the scaling behaviour, consists of the estimation of the scaling exponent in the time-scale domain, i.e. by wavelet analysis. It is shown that, although differences in the performance are reported based on synthesized, exact fractal signals, these fractal estimators give similar results on the RR interval series under analysis.

B.1 Frequency domain methods

As discussed in section 4.4.1, fractal signals can be characterized by the spectral index β, the slope of the power spectrum in the limit as $f \to 0$. For fGn respectively fBm the spectral index is in the range $-1 < \beta < 1$ respectively $1 < \beta < 3$. The spectral index β can be estimated by least squares regression of the logarithm of the estimated power spectral density $P_{xx}(f)$ as a function of the logarithm of the frequency f. Preprocessing the signal, detrending and windowing, improves the power spectrum estimates obtained with the FFT. Since the power-law scaling only holds in the limit as $f \to 0$, the high frequencies should be excluded before fitting the regression line. Numerical experiments demonstrated that better estimates of β are obtained when frequencies larger than $f_N/4$, with f_N representing the Nyquist frequency, are excluded [60].

$$P_{xx}(f) =_d p\, f^{-\beta} \tag{B.1}$$

$$log(P_{xx}(f)) =_d log(p) - \beta\, log(f) \tag{B.2}$$

Coarse graining spectral analysis is an alternative frequency domain technique designed to be insensitive to harmonic components possibly present in otherwise fractal signals [232]. The idea is to separate the fractal and the harmonic components in the signal based on the cross-power spectrum of the original signal and the rescaled (coarse-grained) signal. If the original signal obeys the power law relationship, the cross power spectrum has the same slope as the power spectrum of the original signal. In the case of simple harmonics, on the other hand, the cross-power spectrum approaches zero. Based on these relations, a mixed signal yields a cross-power spectrum of the $1/f$ type. In

the case of multiple harmonic components, however, this approach does not always allow the separation of the harmonic from the fractal components. To overcome this limitation, an alternative algorithm was proposed taking into account the phase angle of the coarse-grained spectrum [233]. In addition to the calculation of the spectral index β without interference of possible harmonic components in the signal, this technique gives an estimate of the contribution of the fractal component to the total variance of the signal. Since we observed that periodic fluctuations hampered the estimation of the DFA scaling exponent (see section 4.4.3), CGSA was evaluated as an alternative that could possibly better characterize the scaling behaviour of the RR interval series. The CGSA algorithm consists of the following steps [233]:

1. Subtract the mean of the time series $x(k)$.

2. Calculate the 'coarse-grained', or resampled, time series $x_h(k) \equiv x(hk)$ for $h = 1/2, 1, 2$. Practically:

   - $x_{1/2}(k)$ is calculated by duplicating every data point of the first quarter of the original time series: $x_{1/2}(k) = x(fix(k/2)), k = 1, \ldots, N/2$, where $fix(k/2)$ represents the integer part of $k/2$;
   - $x_1(k)$ is the first half of the original time series: $x_1(k) = x(k), k = 1, \ldots, N/2$;
   - $x_2(k)$ is constructed by taking every other data point of the original time series: $x_2(k) = x(2k)$.

3. Divide the time series $x(k)$ into N_{sub} segments with overlap $\frac{N_{sub}N_{data}-N_{tot}}{N_{sub}-1}$.

4. Estimate the auto-power spectrum $P_{xx}(f)$ of $x(k)$ using the Welch method with the N_{sub} segments as defined above.

5. Estimate the cross-power spectra $S_{xx_h}(f)$ between the original signal $x(k)$ and the coarse-grained signals $x_h(k)$, using the Welch method with the N_{sub} segments as defined above. For self-affine time series with Hurst exponent H, $S_{xx_h}(f) = h^H S_{xx}(f)$. Therefore, the geometric mean of the cross-power spectra obtained with rescaling factors of respectively h and $1/h$, provides another estimate of the power spectrum of self-affine signals:

   $$S_{xx} = \sqrt{S_{xx_h} S_{xx_{1/h}}} \tag{B.3}$$

   Harmonic components, on the other hand, are suppressed in the cross-spectra due to the coarse-graining. Hence, for mixed signals, consisting of harmonic and fractal (self-affine) components, Eq. (B.3) gives an estimate of the spectrum of the fractal component.

6. The contribution of the fractal component to the power of the mixed signal, referred to as percent fractal power, can be calculated using:

$$\%fractal = 100 \frac{\sum_{f=0}^{f_s/2} S_{xx}}{\sum_{f=0}^{f_s/2} P_{xx}} \tag{B.4}$$

This algorithm, however, is not capable of discriminating multiple harmonic components of which the ratio of the frequencies is h. Therefore, the following improvement was proposed. The sample cross-spectra of each segment can be written as:

$$S_{xx}(h, f, k) \equiv G_{h,f,k} e^{-j\theta_{h,f,k}} \qquad k = 0, 1, \ldots, N_{sub} - 1 \tag{B.5}$$

For a sum of harmonic components with frequencies f_1 and $f_2 = hf_1$, $G_{h,f,k}$ is independent of k, and $\theta_{h,f,k}$ increases linearly with the increment of k. In fractal signals, however, this is not the case as any set of harmonics has random phase relationships [88]. Hence, the change in phase between consecutive sample cross-spectra $\delta\theta_{h,f,k}$, estimated from $S_{xx}(h, f, k-2)$ and $S_{xx}(h, f, k-1)$, can be used in an attempt to orthogonalize $S_{xx}(h, f, k)$ with respect to $S_{xx}(h, f, k-1)$:

$$S'_{xx}(h, f, k) \equiv G_{h,f,k} e^{-j\theta_{h,f,k} + \pi/2 + \delta\theta_{h,f,k}} \qquad k = 2, 3, \ldots, N_{sub} - 1 \tag{B.6}$$

If the orthogonalization succeeded, i.e. for harmonics with fixed phase relationships, the inner product $S_{xx}(h, f, k-1)S'_{xx}(h, f, k)$ is zero. The quantity

$$G'_{h,f,k} \equiv \frac{S_{xx}(h, f, k-1)S'_{xx}(h, f, k)}{S_{xx}(h, f, k-1)}, \tag{B.7}$$

with the same dimensions as the sample cross-spectrum can thus be used as an estimate of the sample spectrum of the fractal component. Using Schwartz's inequality, it can be shown that $G'_{h,f,k} \leq G_{h,f,k}$. As it was observed empirically that $G'_{h,f,k}$ distributes uniformly within the range $[0, G_{h,f,k}]$ [1], the estimate of the fractal spectrum obtained as:

$$S_{xx_h} \equiv \frac{2}{N_{sub} - 2} \sum_{k=2}^{N_{sub}-1} G'_{h,f,k} \tag{B.8}$$

can be used instead of Eq. (B.3).

To evaluate the performance of CGSA, a mixed signal consisting of the sum of fractional Brownian motion and a single harmonic component (sinusoid with frequency $f = 0.07\ Hz$) was considered. Fig. B.1 shows the power spectrum of the mixed signal (dashed line), the power spectrum of the fBm (dotted line) and the power spectrum of the fractal component estimated using CGSA from the mixed signal. In the power spectrum estimated using CGSA, the peak at

[1] private communications with Prof. Y. Yamamoto, the author of the CGSA algorithm

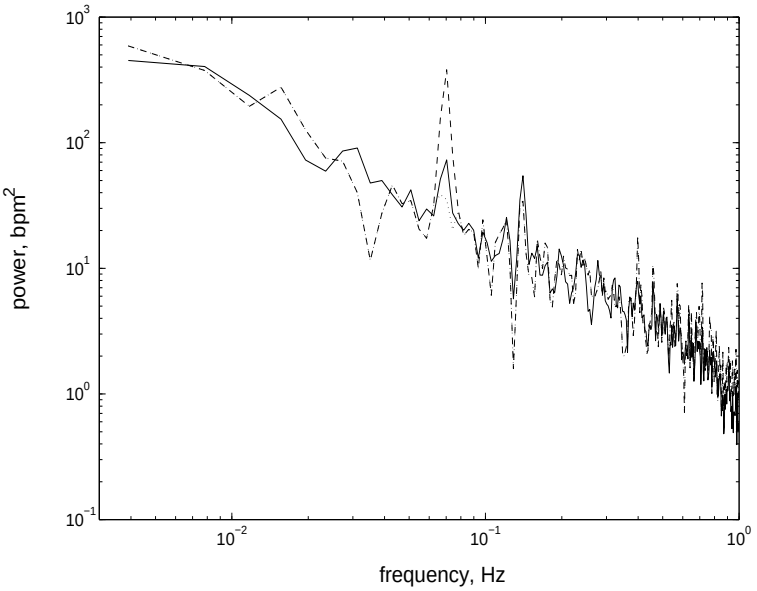

Figure B.1: Coarse graining spectral analysis of a signal consisting of the sum of fractional Brownian motion and a single harmonic component (sinusoid with frequency of 0.07 Hz): total spectrum (dashed line), spectrum of the fractal component estimated using CGSA (solid line) and the spectrum of the underlying fractional Brownian motion (dotted line).

the frequency of the harmonic component is reduced in comparison with the ordinary power spectrum. On the other hand, coarse graining introduces an additional peak at $2f = 0.14$. The effect on the estimates of the spectral index depends obviously on the frequency range used for the linear regression. If the frequency range mainly consists of lower frequencies than that of the harmonic component, CGSA results in a small reduction of the underestimation of the spectral index. In Fig. B.1, for example, the estimates of the spectral index in the range $0.004\ Hz < f < 0.1\ Hz$ obtained with ordinary spectral analysis and CGSA are $\hat{\beta}_{PSD} = 1.01$ respectively $\hat{\beta}_{CGSA} = 1.06$ compared to $\hat{\beta} = 1.18$ for the fBm estimated on the same frequency range. If the frequency range mainly consists of higher frequencies than that of the harmonic component, the effect of CGSA is similar, i.e. CGSA reduces the overestimation of the spectral index. If a larger frequency range is used for the linear regression, however, the improvement of CGSA compared to ordinary spectral analysis is almost negligible. If the frequency range $0.004\ Hz < f < 0.4\ Hz$ is used for the linear regression in the example of Fig. B.1, the estimates of the spectral index in the range $0.004\ Hz < f < 0.4\ Hz$ obtained with ordinary spectral analysis and CGSA are $\hat{\beta}_{PSD} = 1.04$ respectively $\hat{\beta}_{CGSA} = 1.03$ compared to $\hat{\beta} = 1.00$ for the fBm.

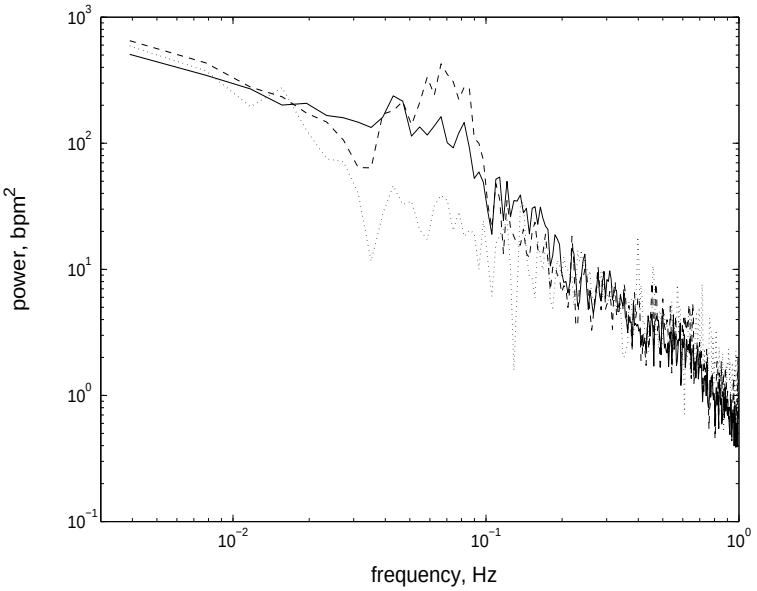

Figure B.2: Coarse graining spectral analysis of a signal consisting of the sum of fractional Brownian motion ($\beta = 1$) and periodic fluctuations with frequencies between 0.04 Hz and 0.1 Hz: total spectrum (dashed line), spectrum of the fractal component estimated using CGSA (solid line) and the spectrum of the underlying fractional Brownian motion (dotted line).

In the power spectrum of RR time series, typically broad peaks are observed instead of narrow peaks, owing to the nonstationarity of the underlying modulating signal. Therefore, broadband periodic fluctuations with a central frequency of 0.07 Hz were generated using a Butterworth bandpass filter with cut-off frequencies of respectively 0.04 Hz and 0.1 Hz. This periodic component was added to fBm, and the amplitudes of both components were chosen according to values observed in real RR time series. Fig. B.2 shows the power spectrum of the mixed signal (dashed line), the power spectrum of the fBm (dotted line) and the power spectrum of the fractal component estimated using CGSA from the mixed signal. In the power spectrum estimated using CGSA, the peak at the frequency of the harmonic component is reduced in comparison with the ordinary power spectrum. On the other hand, coarse graining introduces an increase in power in the range between $f/2$ and $2f$. Note that the reduction of the power at the central frequency of the periodic component is relatively smaller than in the case of a single harmonic component, which can be explained by the fact that the orthogonalization is not as good in this case. The effect on the estimates of the spectral index again depends on the frequency range used for the linear regression. As more frequency components are influenced by the periodic fluctuations, the accuracy of the estimated spectral components is

lower than in the case of a single harmonic component. In Fig. B.2, for example, the estimates of the spectral index in the range $0.004\ Hz < f < 0.1\ Hz$ obtained with ordinary spectral analysis and CGSA are $\hat{\beta}_{PSD} = 0.20$ respectively $\hat{\beta}_{CGSA} = 0.55$ compared to $\hat{\beta} = 1.18$ for the fGn estimated on the same frequency range. Although the error on $\hat{\beta}_{CGSA}$ is smaller, it is still larger than 100%. If the frequency range $0.004\ Hz < f < 0.4\ Hz$ is used for the regression, the estimates of the spectral index in the range obtained with ordinary spectral analysis and CGSA are $\hat{\beta}_{PSD} = 1.47$ respectively $\hat{\beta}_{CGSA} = 1.43$ compared to $\hat{\beta} = 1.00$ for the fGn.

So, in the case of broadband periodic fluctuations superposed on a fractal component, as observed in real RR interval series, neither ordinary spectral analysis neither CGSA allows accurate estimation of the true spectral index β of the fractal component. In the case of single harmonic components, on the other hand, it is better to simply disregard the frequencies of these components in the linear regression to find the slope of the spectrum. Therefore, it can be concluded that the advantage of CGSA over ordinary spectral analysis with respect to the estimation of the scaling exponent is small.

CGSA also gives an estimate of the contribution of the fractal component to the total spectral power of the signal, referred to as *% fractal*. As broadband periodic fluctuations are not completely removed from the fractal power spectrum by CGSA, the % fractal will be overestimated in general. More fundamentally, however, also in the case of a single harmonic component the estimates of the % fractal are not reliable, despite the high accuracies reported in [233]. In [233], quantitative results are presented for the % fractal of mixed signals consisting of a fractal component (fBm) and eventually one or two harmonic components. All signals had a length of 8500 data points, zero mean and unit variance [233]. For different values of β, the values of % fractal estimated using CGSA closely matches 100%, 50% and 33% for the mixed signals containing respectively 0, 1 and 2 harmonic components. In the CGSA algorithm, however, the % fractal is calculated on shorter segments (i.e. $Ndata = 4096$). Since the variance of fBm increases with increasing segment length according to Eq. (4.7), and the variance of the sinusoids, on the other hand, is independent of the segment length, the variance of the fractal signal on a segment of Ndata samples is on average a factor $(\frac{Ndata}{Ntotal})^H$ smaller than the variance of the complete signal consisting of Ntotal data points (where H denotes the Hurst coefficient). The variance of the sinusoids, on the other hand, is independent of the segment length. Therefore, the reported values of the % fractal actually do not match the theoretically expected values, which are thus smaller than 50% or 33% for one respectively two sinusoids (with a factor dependent on the spectral index β), but are overestimated. The fact that the estimated % fractal corresponds to the theoretical value of the complete set of Ntotal data points can be attributed to the detrending algorithm, in which the mean of each segment is added again after linear detrending, used in the CGSA implementation of the author. When

signals with different number of data points $Ntotal$, zero mean and unit variance, are considered, however, the estimated % fractal does not agree anymore with the theoretical value for the whole signal consisting of $Ntotal$ data points. Using linear detrending (without adding the mean afterwards), more consistent estimates of % fractal, with respect to the segment length $Ndata$, are obtained for different signal lengths $Ntotal$ while keeping $Ndata$ constant. It is, however, also observed that the ratio between the estimated and the theoretical % fractal depends on the spectral index β. This stems from the fact that the amplitude of the cross-spectrum of a fractal signal and its coarse-grained version depends on the spectral index β. Thus, to overcome this problem with the given algorithm, an iterative procedure would be required. Taking this into account together with the fact that broadband periodic fluctuations can not be separated very well anyhow, it can be concluded that the % fractal estimated using CGSA is not reliable.

In several studies the performance of different estimators of the fractal exponents are compared. Spectral analysis was found to be slightly more accurate than DFA with respect to the estimation of the Hurst exponent of fractal time series generated by the spectral synthesis method [167]. This is not surprising, as the spectral estimation method is based on the same algorithm, i.e. the FFT, as the method used to synthesize the exact fractal signal. Therefore, the better performance of in this specific case should not be generalized to arbitrary signals. In [60], for example, DFA proved more accurate and robust than the spectral analysis methods with respect to the estimation of the Hurst exponent of fractal time series generated by the Davies-Harte method [45], even if an optimized detrending method and frequency range was used. Anyhow, the differences in performance between DFA and spectral analysis methods are always relatively small. Therefore, the difference between estimates of the scaling exponents obtained with different methods is usually much smaller than the differences in scaling exponents estimated on different RR interval series (from the same or different subjects). This observation is confirmed by the correlation between estimates of the scaling exponents on different RR interval series obtained with DFA and spectral analysis. For all RR interval series derived from ECGs sampled at 1000 Hz, the scaling exponents were calculated using both DFA and spectral analysis. Considering all active and quiet sleep segments, the correlation coefficients were 0.81 and 0.94 for α_1 respectively α_2. The correlation coefficient of the global scaling exponent α_3 at very large scales was 0.88.

B.2 Wavelet-based methods

As fractal signals are characterized by power-law scaling, it seems natural to estimate the scaling exponent in the time-scale domain, i.e. by wavelet analysis. A wavelet is a function of limited duration (localized) with an average value of zero. The wavelet transform decomposes a signal into shifted and rescaled (stretched) versions of the original wavelet [6]. Note the difference with the Fourier transform, which decomposes the signal in sinusoids of different frequency. The wavelet basis functions can be constructed from a single function $\psi(t)$, also referred to as the mother wavelet:

$$\psi_{a,b} = \psi\left(\frac{t-b}{a}\right) \tag{B.9}$$

where a denotes the scale parameter and b the translation parameter. The continuous wavelet transform (CWT) of a signal $x(t)$ is defined as:

$$W[x](a,b) = \frac{1}{\sqrt{a}} \int_{-\infty}^{+\infty} \psi^*_{a,b}(t)x(t)dt \tag{B.10}$$

where $\psi^*_{a,b}(t)$ denotes the complex conjugate of $\psi_{a,b}(t)$.

Using Eq. (4.7), it can easily be shown that the wavelet coefficients exhibit the following scaling property:

$$W[x](ca,cb) = c^{H+1/2}W[x](a,b) \tag{B.11}$$

where H denotes the Hurst coefficient. As the scale rather than the translation parameter is of interest with respect to characterizing the fractal properties of the signal, the wavelet coefficients can be averaged across b, yielding $W[x](a)$. The scaling exponent $1/2 + H$ can then be estimated as the best linear fit of $W[x](a)$ versus a in logarithmic coordinates. This is the basis of the wavelet-based estimators of the scaling exponent [189]. Our implementation used the mean squared discrete wavelet transform coefficients, and included the bias correction proposed in [215].

It was again observed that the difference between estimates of the scaling exponents obtained with different methods is smaller than the differences in scaling exponents estimated on different RR interval series (from the same or different subjects). For all RR interval series derived from ECGs sampled at 1000 Hz, the scaling exponents were calculated using both DFA and the wavelet-based estimator. Considering all active and quiet sleep segments, the correlation coefficients were 0.88 and 0.89 for α_1 respectively α_2. The correlation coefficient of the global scaling exponent α_3 at very large scales was 0.96.

C Effect of ECG sampling rate on HRV parameters

In this appendix, the error on the HRV parameters introduced by the 100 Hz sampling rate of the ECG is quantified. To this end, 10 ECGs were recorded at 1000 Hz. From each of these ECGs, two RR interval series were derived with a resolution of respectively 0.001 s ("100 Hz RR interval series") and 0.01 s ("100 Hz RR interval series"), as explained in section 4.3.2. All HRV parameters were calculated on the 1000 Hz RR interval series and on the 100 Hz RR interval series, with and without the corrections presented in sections 4.3.2 and 4.4.3. The effect of the 100 Hz ECG sampling rate on the HRV parameters is mainly determined by the variance of the RR interval series under analysis. As the corrections are based on the statistical properties of the errors on the RR intervals due to the 100 Hz ECG sampling rate, the accuracy of the proposed corrections is mainly determined by the number of RR intervals considered. Therefore, the errors were calculated for all HRV parameters on the various RR interval segments used in the present study. The errors on the HRV parameters calculated from the 100 Hz RR interval series -with and without correction- are expressed in percentage compared to the HRV parameters calculated from the 1000 Hz RR interval series.

Table C.1: Effect of the 100 Hz ECG sampling rate on the HRV parameters calculated on the complete RR interval series: mean relative errors of the HRV parameters calculated from 100 Hz RR interval series with and without compensation, compared to the HRV parameters calculated from the 1000 Hz RR interval series.

	100 Hz mean relative error (%)	100 Hz with compensation mean relative error (%)
SDNN	0.5	-3.10^{-3}
SDANN	6.10^{-4}	6.10^{-4}
RMSSD	20	4.10^{-2}
PWR	1.3	3.10^{-3}
ULF	4.10^{-4}	4.10^{-4}
VLF	3.10^{-4}	3.10^{-4}
LF	3.10^{-2}	1.10^{-4}
HF	32.8	0.3
VLFN	-1.3	-3.10^{-3}
LFN	-1.3	-7.10^{-3}
HFN	31.0	0.3
α_0	-0.03	-1.10^{-4}
α_1	-7.9	-0.2
α_2	-0.8	-0.3
α_3	-0.1	-0.1

Table C.1 shows the relative errors on the HRV parameters calculated on the complete RR interval series. The HRV parameters quantifying short term fluctuations (RMSSD,HF,HFN,α_1) are strongly biased by the 100 Hz ECG sampling rate. Due to the large numbers of RR intervals in each recording, however, the accuracy of the corrections is very high, yielding errors smaller than 1% for all HRV parameters.

Table C.2: Effect of the 100 Hz ECG sampling rate on the HRV parameters calculated on quiet and active sleep sleep segments separately: mean relative errors of the HRV parameters calculated from 100 Hz RR interval series with and without compensation, compared to the HRV parameters calculated from the 1000 Hz RR interval series..

	100 Hz mean relative error (%)	100 Hz with compensation mean relative error (%)
SDNN^{QSX}	6.7	−0.2
RMSSD^{QSX}	57.9	−3.6
VLF^{QSX}	0.02	0.01
LF^{QSX}	0.16	0.05
HF^{QSX}	80.9	−1.9
LFN^{QSX}	−10.5	0.3
HFN^{QSX}	55.9	−1.7
$(\text{LF/HF})^{QSX}$	−36.4	2.3
α_1^{QSX}	−14.1	0.2
α_2^{QSX}	−0.24	−0.04
SDNN^{ASX}	1.6	0.6
RMSSD^{ASX}	32.3	1.3
VLF^{ASX}	0.4	0.4
LF^{ASX}	0.9	0.9
HF^{ASX}	32.5	2.8
LFN^{ASX}	−2.1	−0.1
HFN^{ASX}	28.6	1.7
$(\text{LF/HF})^{ASX}$	−23.6	−1.6
α_1^{ASX}	−7.0	0.3
α_2^{ASX}	−0.4	−0.2

Table C.2 shows the relative errors on the HRV parameters calculated on quiet and active sleep segments separately. The HRV parameters quantifying short term fluctuations (RMSSD,HF,HFN,α_1) are strongly biased by the 100 Hz ECG sampling rate. Owing to the lower variance of the RR interval series during QS, the 100 Hz ECG sampling rate also introduces a non-negligible bias in SDNN and LFN during QS, while this bias is relatively small during AS. Due to the relatively large numbers of RR intervals considered for the calculation of each measure, the accuracy of the corrections is good, yielding errors smaller than 4% for all HRV parameters.

List of publications

Reviewed papers

- G. Morren, P. Lemmerling and S. Van Huffel, "Decimative subspace-based parameter estimation techniques applied to magnetic resonance spectroscopy signals", *Proceedings of IEEE-EMBC 2001* (23rd Annual International Conference of the IEEE Engineering in Medicine and Biology Society), Vol. 3, p. 2319-2322 (CD-ROM paper No. 850), Istanbul, Turkey, October 25-28, 2001.
- G. Morren, P. Lemmerling, S. Van Huffel, G. Naulaers, H. Devlieger and P. Casaer, "Detection of autoregulation in the brain of premature infants using a novel subspace-based technique", *Proceedings of IEEE-EMBC 2001* (23rd Annual International Conference of the IEEE Engineering in Medicine and Biology Society), Vol. 2, p. 2064-2067 (CD-ROM paper No. 1014), Istanbul, Turkey, October 25-28, 2001.
- G. Morren, M. Wolf, P. Lemmerling, U. Wolf, J.H. Choi, E. Gratton, L. De Lathauwer and S. Van Huffel, "Extraction of fast neuronal changes from multichannel, functional near infrared spectroscopy signals using independent component analysis", *Proc. of SPIE Vol. 4623*, Progress in Biomedical Optics and Imaging, Vol. 3, No. 15, p 68-76, San Jose, California, USA, January 19-25, 2002.
- G. Naulaers, G. Morren, A. Debeer, C. Vanhole, S. Van Huffel, P. Casaer and H. Devlieger H., "Continuous measurement of ΔHbD and TOI during rewarming of neonates", in *Proceedings ISOTT 2002* (30th Annual Meeting of the International Society on Oxygen Transport to Tissue), Manchester, UK, August 24-28, 2002.
- G. Morren, S. Van Huffel, I. Helon, G. Naulaers, H. Daniëls, H. Devlieger and P. Casaer, "Effects of non-nutritive sucking on heart rate, respiration and oxygenation: a model-based signal processing approach", *Comparative Biochemistry and Physiology, Part A*, Vol. 132, No. 1, p. 97-106, 2002.

- G. Naulaers, G. Morren, S. Van Huffel, P. Casaer and H. Devlieger, "Cerebral tissue oxygenation index in very premature infants", *Archives of Disease in Childhood Fetal Neonatal*, Vol. 87, p. F189-192, 2002.
- G. Morren, G. Naulaers, P. Lemmerling, S. Van Huffel, P. Casaer and H. Devlieger, "Quantitation of the concordance between cerebral intravascular oxygenation and mean arterial blood pressure for the detection of impaired autoregulation", *Adv Exp Med Biol.* Vol. 510, p. 403-408, 2003
- G. Naulaers, G. Morren, S. Van Huffel, P. Casaer and H. Devlieger, "Measurement of tissue oxygenation index during the first three days in premature born infants" , *Adv Exp Med Biol.* Vol. 510, p. 379-383, 2003
- G. Morren, P. Lemmerling and S. Van Huffel, "Decimative subspace-based parameter estimation techniques", *Signal Processing*, Vol. 83, No. 5, p. 1025-1033, 2003.
- G. Morren, M. Wolf, P. Lemmerling, U. Wolf, J.H. Choi, E. Gratton, L. De Lathauwer and S. Van Huffel, "Detection of fast neuronal signals in the motor cortex from functional near infrared spectroscopy measurements using independent component analysis", *Medical and Biological Engineering and Computing*, Vol. 42, No. 1, p. 92-99, 2004.
- G. Naulaers, G. Morren, A. Debeer, V. Cossey, C. Vanhole, S. Van Huffel, P. Casaer and H. Devlieger, "Continuous measurement of cerebral blood volume and oxygenation during rewarming of neonates", Internal Report 02-218, ESAT-SCD/SISTA, K.U.Leuven (Leuven, Belgium), accepted for publication in *Acta Paediatrica*, 2003.

Submitted papers

- G. Morren, P. Lemmerling, H. Daniëls, G. Naulaers, S. Van Huffel, " Sensitivity of detrended fluctuation analysis applied to heart rate variability data", Internal Report 02-184, ESAT-SCD/SISTA, K.U.Leuven (Leuven, Belgium), 2003, *in review.*

Curriculum Vitae

Geert Morren was born in Leuven on June 14, 1974. He received the M.Sc. degree in electrical engineering (burgerlijk werktuigkundig-elektrotechnisch ingenieur) from the Katholieke Universiteit Leuven in 1997. From 1997 till 1999, he worked as project engineer with IMEC (Interuniversitair Micro-Electronica Centrum, Leuven) and as electrical design engineer with PEC (Project Engineering and Contracting, Leuven). From 2000 to 2004 he did research on biomedical signal processing at the SCD/SISTA division of department of electrical engineering (ESAT) at the Katholieke Universiteit Leuven.